UNIONE EUROPEA
Fondo Sociale Europeo

Ministero dell'Università e della Ricerca

PON RICERCA E INNOVAZIONE

UNIVERSITÀ DEGLI STUDI FIRENZE
Da un secolo, oltre.

# DOTTORATO DI RICERCA IN *SCIENZE CHIMICHE*

CICLO XXXVII - PON ex DM1061

## IMPROVING THE PROPERTIES OF HEXAGONAL FERRITES FOR THE REPLACEMENT OF RARE EARTH PERMANENT MAGNETS

Settore Scientifico Disciplinare
CHIM / 03


**Dottorando**
Dott. Gerace Alessandro

**Supervisori**
Prof. Totti Federico

Dott. Sangregorio Claudio

**Coordinatore**
Prof./Prof.ssa Papini Anna Maria

UNIONE EUROPEA
Fondo Sociale Europeo

Ministero dell'Università e della Ricerca

PON RICERCA E INNOVAZIONE 2014 - 2020

UNIVERSITÀ DEGLI STUDI FIRENZE
Da un secolo, oltre.

PhD in

*CHEMICAL SCIENCES*

CYCLE XXXVII - PON ex DM1061

# IMPROVING THE PROPERTIES OF HEXAGONAL FERRITES FOR THE REPLACEMENT OF RARE EARTH PERMANENT MAGNETS

Academic Discipline
CHIM / 03


**PhD Student**
Dott. Gerace Alessandro

**Supervisor**
Prof. Totti Federico

Dott. Sangregorio Claudio

**Coordinator**
Prof./Prof.ssa Papini Anna Maria

# *Improving the Properties of Hexagonal Ferrites for the Replacement of Rare Earth Permanent Magnets*

*Alessandro Gerace*

*PhD in Chemical Sciences*

*XXXVII Cycle*

*University of Florence*

# Abstract

The increasing demand for high-performance permanent magnets towards sustainable technologies is dominated by materials containing critical Rare Earth Elements (REEs). The latter suffer from significant supply-chain risks and create a large performance and cost gap above the valuable counterpart of hexaferrites. This thesis addresses this issue by investigating a multi-fold approach to enhance the magnetic properties of strontium hexaferrite, $SrFe_{12}O_{19}$ (SrM) nanomaterials, aiming to develop a sustainable "gap" magnet. This research integrates several strategies: optimizing green, cost-effective, and scalable synthesis for phase-pure SrM nanoparticles below 100 nm; tailoring the intrinsic properties via chemical modification of SrM structure with other non-REE elements (doping); consolidating powders into dense, anisotropic magnets using novel low-temperature compaction systems (Multi-Anvil, Piston Cylinder, Spark Plasma Sintering). The potential of hard-soft SrM/$Fe^0$ nanocomposites is also explored.

Key results include the synthesis of single-phase SrM nanoparticles with appropriate size and enhanced magnetic properties by modified solid-state and sol-gel methods. Efficient tuning of the magnetic and physical properties by aluminium and manganese doping allowed to reach coercivities up to 0.7 T and particle size down to 40 nm. Furthermore, advanced low-temperature compaction techniques were successfully employed to manufacture highly dense, aligned magnets, notably achieving up to 92% relative density with Multi-Anvil press and 97% relative density via Spark Plasma Sintering. Finally, an industrial-scale validation confirmed the viability of recycled hexaferrites in a circular economy, showing that bonded magnets fabricated from manufacturing waste exhibited competitive magnetic performance

comparable to commercial grades. This thesis aims to present a comprehensive framework for creating cost-effective, improved REE-free magnets that can bridge the critical performance gap and reduce reliance on strategic materials.

# List of contents

# Outline

The over-reliance on critical raw materials, particularly Rare Earth Elements (REEs), for high-performance permanent magnets poses significant environmental, economic, and geopolitical risks. Concurrently, a performance and cost gap exists between low-cost, low-performance ferrite magnets and high-cost, high-performance REE-based magnets. This doctoral thesis investigates strategies to enhance the magnetic and functional properties of nanosized strontium hexaferrite, $SrFe_{12}O_{19}$ (SrM), with the goal of developing a cost-effective, rare-earth-free "gap" permanent magnet, thus reducing reliance on critical REEs in specific applications.

SrM is a widely utilized magnetic material for numerous applications, owing to several advantages including high chemical stability, resistance to demagnetization, low cost, and natural abundance of its constituents. However, the lower magnetic strength and energy density compared to rare-earth magnets limit its use in high-performance or space-constrained applications. Specifically, the approaches adopted in this study to further improve ferrite properties rely on different principles. First, the improvement of hexaferrite's magnetic properties was explored by reducing its size to the nanoscale. Nanomaterials exhibit indeed unique properties which strongly differ from their bulk counterparts, arising from their finely controlled size, shape, composition and surface. The dimensions and shape of individual nanoparticles can significantly influence fundamental magnetic characteristics such as demagnetization resistance and magnetic anisotropy. The adopted synthetic strategies involved optimizing sustainable, scalable, and efficient procedures to produce SrM nanoparticles, eligible for industrial employment. Second, the magnetic properties can be potentially enhanced through the

substitution of its constituent ions with other non-REE elements. The synthesized powders were then employed in novel compaction techniques to increase the density and grain alignment while preserving the nanostructure, thus building a functional permanent magnet. Hexaferrites naturally tend to form a regular hexagonal thin platelet shape, with the easy magnetization c-axis perpendicular to the platelet plane. The mechanical shape-induced alignment leads to significant improvements in bulk magnetic properties, enhancing remanence and providing superior magnetic properties in the direction of the easy axis alignment. On the other hand, nanoparticles alignment can be realized applying a strong enough magnetic field as well.

Finally, the addition of a second nanomaterial with soft magnetic properties (namely, zero-valent iron nanowires) to realize hexaferrite-based nanocomposites was evaluated to leverage a beneficial magnetic interaction occurring at the interface of the two phases, through exchange or dipolar coupling.

The presented work will delve into how different synthesis methods, sintering processes, doping, particle size and morphology can exert various effects on microstructure and magnetic characteristics at the nanoscale. The objective is to provide a comprehensive overview of these strategies, offering relevant insights for the development of improved SrM permanent magnets.

The thesis is structured as follows:

- **Chapter 1** begins by introducing the central role of permanent magnets in modern technology, the dominance of rare-earth-based materials, and their associated challenges. It follows an analysis of current mitigation strategies, the research aims and specific objectives of this doctoral project; the chapter ends by describing the properties of SrM

which will be used as a main building block for the realization of promising nanocomposite for this purpose.

- **Chapter 2** will present the synthesis of nanosized SrM through low-temperature solid-state reaction, the investigation on various synthesis parameters and its structural and magnetic characterization. A further modification on the synthesis route will also be introduced.
- **Chapter 3** will show the obtainment of SrM nanoparticles by a modified sol-gel synthesis in NaCl matrix; the structural and magnetic investigation, and the evaluation of the influence of some synthesis parameters are discussed.
- **Chapter 4** will investigate the doping of SrM nanoparticles with selected cations ($Al^{3+}$ and $Mn^{3+}$) by adopting the modified sol-gel synthesis, and the related effects on morphology and magnetic characteristics.
- **Chapter 5** will display the densification process of nanosized SrM powders produced by various syntheses. The employment of different compaction techniques, namely Multi-anvil, Piston Cylinder press and Spark Plasma Sintering, and their efficacy to get dense and aligned samples will be presented.
- **Chapter 6** will show the synthesis of $Fe^0$ nanowires obtained by wet chemical approach through reduction of metal salts with sodium borohydride, and the effect of some strategies to reduce oxidation on their morphological and magnetic features; the nanocomposite with synthesized and commercial SrM to evaluate the exchange-coupling effect will also be discussed.
- **Chapter 7** will present the experience abroad in Kolektor KFH industry (Slovenia), with the explanation of the processing methodologies to obtain test samples for large-scale production. In the

context of the European INSPIRES project, the recycling strategies for permanent magnets will be discussed.

- **Chapter 8** will summarize the main findings of this research and draw overall conclusions, providing perspectives and recommendations for future research.
- **Appendix** details the experimental synthetic procedures employed to obtain the nanomaterials.

# **Chapter 1** | Introduction

## 1.1 Permanent magnets in modern technology

Magnetic materials are typically classified according to their chemical composition or magnetic characteristics. One criterion is on the stability of the magnetic field they generate when subjected to external influences. This stability is often referred to as the material's "hardness" [1]. Understanding the differences in magnetic hardness aids in selecting the appropriate type of magnetic material for a specific application, ensuring optimal performance and efficiency [2]. Soft magnetic materials have low magnetic hardness and can readily lose their magnetization when exposed to external fields. However, these materials can be easily magnetized due to their high permeability, and they are ideal in applications where rapid, reversable magnetization is beneficial, such as in transformers and inductors [3,4]. In contrast, hard magnetic materials possess a strong resistance to demagnetization, even when exposed to opposing magnetic fields [5]. This feature is essential for applications as electric motors and generators.

Permanent magnets (PMs) are fundamental to modern life, serving as vital components in a wide range of electromechanical and electronic devices. Their primary role in these applications is to create and sustain a magnetic field in a specific area, typically referred to as the "air gap" within a magnetic circuit [5–7]. The defining characteristic of PMs, which underscores their importance in various technologies, is the ability to retain their magnetization over time, generating a stable and persistent magnetic field without relying on any external power source or an induced magnetic field. This inherent quality arises from the anisotropy of their constituent hard magnetic materials [8,9]. Unlike

electromagnets, which depend on electrical energy to produce a magnetic field, PMs offer significant advantages, including a superior ratio of magnetic flux generated to the physical volume of the magnet itself [10]. This efficiency not only enhances their functionality but also contributes to the compactness and reliability of the devices that utilize them, making PMs an irreplaceable component in countless applications across different industries [11,12].

PMs possess the unique ability to store and convert electrical energy into mechanical energy and vice versa [5]. As such, they play a crucial role in various modern technologies focused on energy harvesting, generation, and conversion [13]. This attribute has positioned them at the forefront of advanced engineering applications, including electric motors, wind turbines, magnetic levitation transportation, data storage solutions, and biomedical devices [14–18]. The distinctive capability of PMs to interconvert motion and electricity forms the foundation for the operation of generators and motors used across a wide array of machinery [19]. Due to their physical properties, the shift towards green technologies, essential for a climate-resilient and sustainable future, relies heavily on PMs. Their ability to store, deliver, and convert energy makes PMs pivotal components in the technology used to harness renewable energy sources. As a result, they are prevalent in low-carbon energy applications such as wind turbines, wave park generators, and flywheels, as well as in future mobility solutions that do not rely on fossil fuels, including hybrid and electric vehicles (EVs) [20–22].

The first PM known to man was lodestone, based on the mineral magnetite $Fe_3O_4$. The natural magic of this material has intrigued people since ancient civilizations, and by manufacturing this material a precursor of the modern compass in navigation was created [23]. The growing use and significance of PMs can be primarily attributed to the notable advancements in their magnetic

properties. Nowadays, PMs are categorized into four primary types, each with unique properties that influence their suitability for various applications: Alnico, ferrite, samarium-cobalt (SmCo), and neodymium-iron-boron (NdFeB).

Alnico magnets (a composite of iron, aluminum, nickel, and cobalt) excel in high-temperature environments, withstanding temperatures up to 400°C without demagnetization, making them ideal for applications where heat dissipation is crucial [24]. Ferrite magnets, made from a composite of iron oxide and other metallic elements, are particularly popular due to their cost-effectiveness. They offer moderate magnetic strength, but their advantageous cost makes them suitable for various consumer products such as refrigerator magnets, loudspeakers, toys, and several other electronic devices. They are particularly useful in applications where a small volume is not strictly necessary, and their resistance to corrosion and high temperatures (up to about 250°C) also contributes to their widespread use in industrial applications, such as electric motors and magnetic assemblies [25,26]. SmCo magnets are known for their remarkable magnetic strength and durability, as they can maintain their magnetic properties even in extreme conditions, which makes them ideal for high-performance applications such as aerospace components, precision instruments, and high-end electric motors where reliability and performance are crucial [27]. NdFeB magnets, often called “Neo” magnets, are the most powerful type of PM available today. These magnets can produce extraordinarily strong magnetic fields, making them ideal for applications that require compact size with high strength, such as in modern electronics, medical imaging devices (like MRI machines), and advanced automotive technologies. However, NdFeB magnets have a sensibly lower resistance to corrosion and heat. They typically operate at temperatures under 100°C without significant loss of magnetic performance, which necessitates careful thermal management

in certain applications [28,29]. In the development of high-performance PMs, together with a desirable strong magnetic flux, maintaining good thermal or mechanical steadiness is also a must-have feature. It primarily enhances operational reliability and effectiveness across an extended range of industrial and commercial uses, ensuring optimal performance even under varying environmental conditions [30].

## 1.2 The core of PMs: the maximum energy product

The relevant figure of merit expressing the quality of a PM is its *maximum energy product*, or $(BH)_{max}$. This number describes the ability of a PM to withstand the influence of a counteracting magnetic field. Moreover, it measures the useful magnetic flux that can be produced by the magnet within a given volume. In other words, the $(BH)_{max}$ value (in $kJ/m^3$ or MGOe) provides an estimation of the magnetic energy density that can be stored in the magnet per volume unit and, therefore, the work that the magnet itself can do. This figure of merit is most frequently used to rate and compare the various families and grades of magnets, thus, PMs with large $(BH)_{max}$ values are highly sought after for all the previously mentioned technical applications [5].

Before proceeding with the discussion of the structural features that determine the hard magnetic properties, we must define the parameters that are generally used to specify the magnetic properties of PMs. Understanding these parameters is important for characterizing how a magnetic material responds to an *applied magnetic field* (*H*). When magnetic material is placed in an external field H, a *magnetic flux density* (*B*) is created, which is due to the polarization of the magnetic domains (small regions where the magnetic moments share a common direction). This polarization creates *magnetization*

($M$), which is related to B through the equation in SI units $B = \mu_0(H + M)$, where $\mu_0$ is the vacuum permeability ($\mu_0 = 4\pi \cdot 10^{-7}$ H/m), while in CGS units the relationship is $B = H + 4\pi M$.

To understand the $(BH)_{max}$, it is essential to describe the *hysteresis loop*, which defines the behaviour of a ferromagnetic or ferrimagnetic material in response to an applied magnetic field [1,31]. The hysteresis loop illustrates the irreversible and nonlinear relationship between B or M of a material as a function of H. Starting with an unmagnetized sample (H=0, M=0 or B=0), as H is increased, M or B in the material increases along the *initial magnetization* (or virgin) *curve*. When H is increased sufficiently, the material reaches a state of *saturation magnetization* ($M_S$) or *saturation induction* ($B_S$), where virtually all the magnetic domains are aligned with the applied field, and further increases in H produce a negligible increase in M or B. The minimum field necessary to achieve saturation is called the saturation field ($H_{SAT}$).

Once the external magnetic field H is suppressed, a residual magnetization ($M_R$) or remanent induction ($B_R$) remains in the material, the so-called *remanent magnetization* or *remanence*. This ability to retain magnetization after the field removal is a crucial property of PMs. While the residual magnetization in hard magnetic materials is significant, on the other hand, $M_R$ of soft magnetic materials is almost zero. The ratio of remanent to saturation magnetization ($M_R/M_S$) is sometimes denoted as the hysteresis loop *squareness ratio* in specific contexts or literature, reflecting the efficiency of the material in retaining magnetic properties [32]. For an efficient PM material, $M_R$ is usually 0.8-1.0 times $M_S$, resulting in a ratio closer to 1, which indicates the material keeps most of its magnetization. To reduce the remanence to zero, it is necessary to apply a field in the opposite direction. The magnitude of this reverse field required to accomplish that is called the *coercive force* ($H_C$) or

*coercivity*. Specifically, $H_{Ci}$ (intrinsic coercive field) is the reverse field needed to reduce the magnetization (M) to zero, while $H_{Cb}$ (normal coercivity) is the one reducing the magnetic flux density (B) to zero. These coercivities quantify the resistance of the material to demagnetization. For hard magnetic materials, $H_{Ci}$ is often a more critical parameter as it directly reflects the resistance at a fundamental level. A high coercive force is essential for a PM to maintain its magnetic flux against external influences, as it defines the necessary field to fully demagnetize the material [31]. As the negative field is further increased, the material becomes saturated in the opposite direction. If the applied field is then cycled back to the positive direction and increased again to the original saturation, the magnetization follows a symmetrical path, forming a closed loop – namely the hysteresis loop. This graphical representation is not a unique function of H but depends on the direction and magnitude of previously applied fields.

Regarding PMs, the second quadrant of the hysteresis loop is of particular interest. This quadrant, also known as the *demagnetization curve*, shows the relationship between the magnetic flux density (B) and the opposing magnetic field (H) within the magnet when it is operating in a demagnetizing condition, as is typical in most applications where the magnet produces an external field. The maximum energy product $(BH)_{max}$ is the largest value of the BH product that can be obtained from the demagnetization curve. It corresponds to the point on the B-H curve in the second quadrant where the rectangular area under the curve is maximized. This maximum area represents the optimum working point of the PM for many applications.

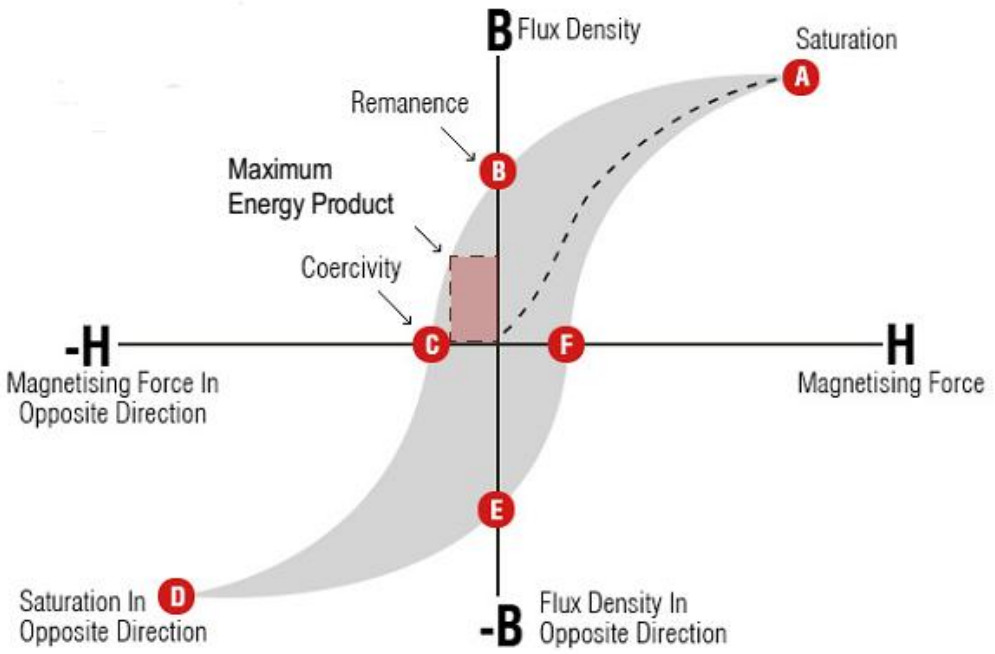


***Figure 1-1*** *Graphical representation of magnetic hysteresis loop in a B-H plot.*

The $(BH)_{max}$ is crucial for rating the performance of PM materials. A higher $(BH)_{max}$ value indicates that a smaller volume of magnetic material is required to produce a given magnetic field in a magnetic circuit. It is also proportional to the maximum energy that can be stored in a given volume of the magnet. Achieving a high $(BH)_{max}$ is a primary goal in the development of new and improved materials for PMs. Ideally, a PM material with a "square" hysteresis loop, characterized by high remanence and coercivity, will exhibit a larger $(BH)_{max}$. As this value represents the peak energy storage capability per unit volume, the development of PMs with higher $(BH)_{max}$ has been a historical trend, driven by the progressive discovery of new materials and improvements in processing techniques[33].

## 1.3 High-performance PMs based on Rare Earths

Noteworthy progress has been made in the fabrication of high-powered PMs during the last century, thanks to the discoveries of SmCo and NdFeB alloys. Rare Earth Elements (REEs) are comprised of the lanthanide elements plus scandium and yttrium, and they are generally classified into light REEs (LREEs) such as lanthanum, cerium, praseodymium, neodymium, samarium, europium, and the heavy REEs (HREEs) gadolinium, terbium, dysprosium, holmium, erbium, thulium, ytterbium, lutetium, scandium and yttrium.

REEs emerged as significant materials for PMs in 1967, with the discovery of magnets based on SmCo [34,35] at Philips Research Laboratories, and again in early 1982 with the even stronger NdFeB [36–38] at General Motors Research Laboratories and Sumitomo Special Metals Corporation. Today, a large fraction of the market depends on these kinds of PM due to their exceptional magnetic properties. These magnets are characterized by leading values of $(BH)_{max}$ and remarkable resistance to demagnetization, making them indispensable in all scenarios where peak performances are mandatory.

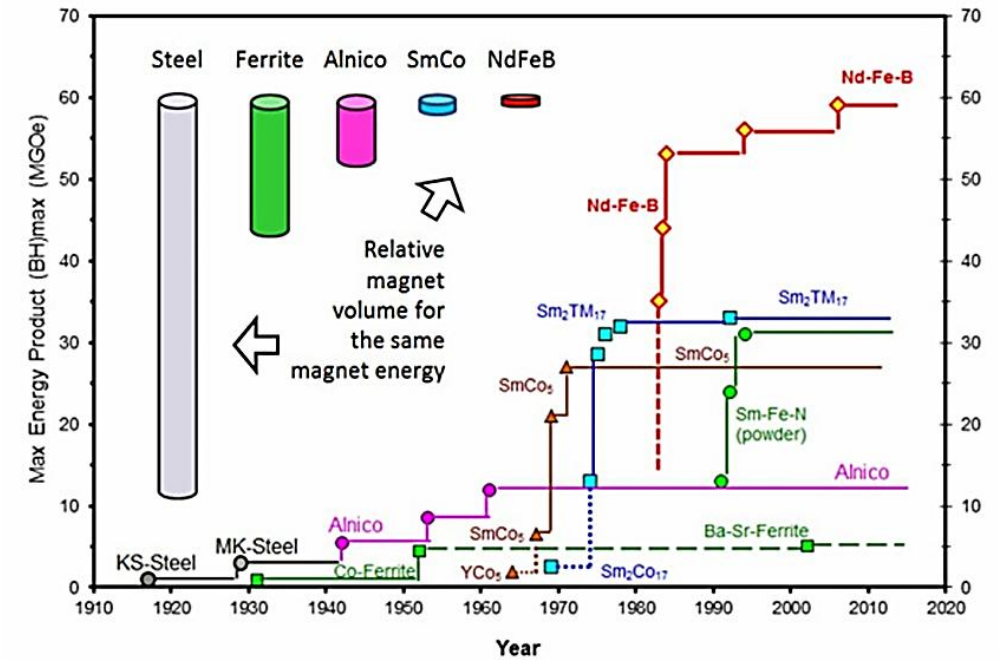


***Figure 1-2*** *Overview of the development of hard magnetic materials in the 20th century and relative $(BH)_{max}$. Modified from ref.* [33].

SmCo magnets, based on two main distinct phases, $SmCo_5$ and $Sm_2Co_{17}$, are still important due to their excellent thermal stability and corrosion resistance. These magnets can be used at temperatures up to 500 °C with a relevant $(BH)_{max}$ of about 239 kJ/m$^3$ (30 MGOe) [39]. SmCo formulations offer a lower $(BH)_{max}$ at room temperature compared to NdFeB, however, their $(BH)_{max}$ falls less dramatically with increasing temperature, so they are the preferred choice when operating temperatures are particularly elevated.

Currently, the NdFeB-type PMs dominate in terms of performance. They have attained increased $(BH)_{max}$ over 25 years after the discovery due to the excellent magnetic properties of its main phase, $Nd_2Fe_{14}B$, and the remarkable progress in the production process [40]. Commercial grades of strong magnets owing $(BH)_{max}$ over 400 kJ/m$^3$ (like N52 or N55, where the number refers to the corresponding $BH_{max}$ value in MGOe) are well-established [33,41], while the

current record value, 60 MGOe (474 kJ/m$^3$) [42] is close to the $(BH)_{max}$ theoretical limit of 512 kJ/m$^3$ for this kind of magnets. Higher $(BH)_{max}$, in conjunction with the cost advantage over SmCo, enabled the progressive growth of NdFeB in the spectrum of applications. These magnets usually contain four different REEs: neodymium (Nd), praseodymium (Pr), terbium (Tb), and dysprosium (Dy). The exact composition of REEs within a NdFeB-PM can vary, with different proportions leading to different magnetic properties. Although the $Nd_2Fe_{14}B$ phase provides the largest $(BH)_{max}$, its main disadvantage is that it suffers from significant declines in magnetic strength as temperature increases. However, the material's thermal stability can be improved by inserting other REEs such as Tb or Dy, but this also leads to a detriment of magnetic strength and a rise in cost, as HREEs are less abundant and thus more expensive.

Throughout the years, PMs based on REEs have become an essential component of countless high-tech products. The outstanding performances shown by these PMs, particularly NdFeB, have allowed the miniaturization of several devices, such as laptop computers and other consumer electronics. The reason relies on the fact that stronger magnets with larger $(BH)_{max}$ can furnish the same energy density in a much smaller volume than weaker magnets, as illustrated in **Figure 1-2**.

# 1.4 The "Rare Earth Challenge": supply, sustainability, and geopolitics

## 1.4.1 Escalating demand and market analysis

Studies from the International Energy Agency (IEA) in 2024 highlighted that global demand for magnet REEs (Nd, Pr, Dy, Tb) experienced a significant

jump (**Figure 1-3**) in recent years. It nearly doubled between 2015 and 2023, reaching ninety-three kilotonnes (kt). This increase is strongly correlated with the expanding embrace of clean energy technologies. Specifically, the proportion of magnet REE demand (share) deriving from clean energy applications rose from 8% to approximately 18% within the same timeframe, mainly driven by increased EV sales and wind turbine installations in order to support the efforts for climate change mitigation.

On the other hand, projections under the Announced Policies Scenario (APS) indicate a continued upward trend in total magnet REE demand, reaching 131 kt by 2030 and increasing to 181 kt by 2050. Within this overall growth, the demand for EV motors is expected to show the largest relative increase, escalating from 7% in 2023 to almost 30% by 2050. The Net Zero Emissions Scenario (NZE) assumes a more accelerated implementation of EV and wind turbine infrastructure between the present day and 2030 compared to the APS. Consequently, the NZE scenario projects total magnet REE demand in 2030 to be fifteen kilotonnes higher than the APS forecast for the same year. Stated Policies Scenario (STEPS) reflects the current policy environment without assuming additional measures or targets beyond the ones officially announced and legislated predicting a lower demand and growth compared to APS and NZE.

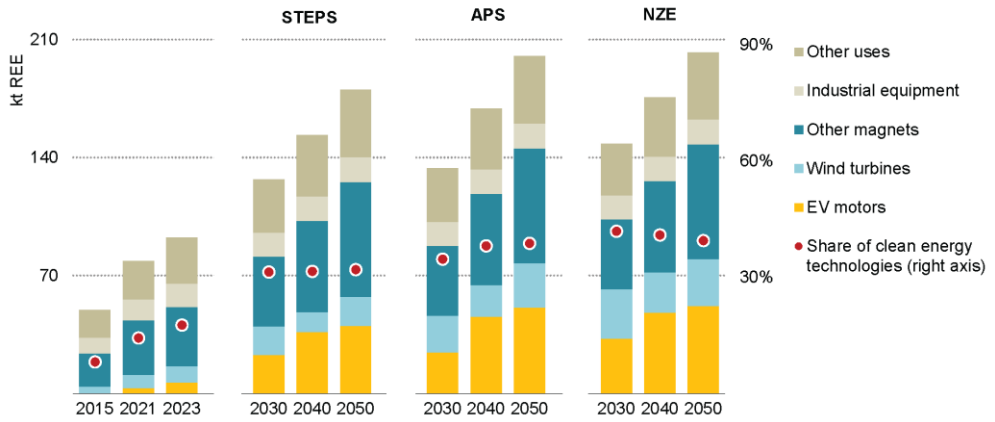


***Figure 1-3*** *Outlook for global magnet-REE (Nd, Pr, Dy, Tb) demand by sector and scenario: stated policies scenario (STEPS), announced policies scenario (APS), net zero emission scenario (NZE). From* [43]

The rising share of clean energy technologies in the total demand for REE-magnets indicates a shift towards more sustainable and environmentally friendly energy solutions, while the faster growth in the NZE scenario underscores the need for accelerated adoption of clean energy technologies to meet climate goals.

## 1.4.2 REEs - Environmental after-effects

As a result of the escalated demand for these elements, REEs became of concern to numerous industries, avidly looking around for them. Contrary to what the name suggests, REEs are relatively abundant in the Earth's crust. Nevertheless, their extraction processes pose significant environmental and economic challenges [44–48]. They gained the label "rare" because of the unusualness of finding them in a pure form, even though fairly plentiful in the entire Earth's crust. Their extraction is performed through several complex operations due to low concentrations in ores, which processing in copious amounts leads to increased energy consumption and $CO_2$ emissions, and the necessity of separation from other materials they are intimately mixed with. As

a result, REEs are often more resource-demanding and costlier to extract than standard ores like iron or coal [49]. The natural occurrence of radioactive elements such as thorium and uranium in rare earth-bearing minerals can lead to occupational and environmental radiation exposures during mining and processing, with a huge production of hazardous waste, the disposal of which must be rigorously managed. As IEA reports, very few countries outside China have the infrastructure and willingness to build solutions for managing these radioactive by-products. At the same time, only 17% of working REE miners align with the Global Industry Standard on Tailings Management. Conventional solvent leaching for separation of REEs contributes noticeably to environmental impacts, with considerable amounts of strong bases and acids employed, such as sodium hydroxide and sulfuric, oxalic, or hydrochloric acid [50]. Mining is the most detrimental activity, destroying the ecological environment and causing severe pollution. The overall procedure involves mechanical or chemical soil removal and erosion, leading to infertile lands; the release of dust and toxic gases inevitably pollutes the circumstantial air; the solvents used for extraction can leak and contaminate groundwater or sometimes entire waterways. Consequently, the destruction of habitats inevitably affects the surrounding local biodiversity and wildlife. This is the motivation of the blaming attribution of “not so green” technological transition.

### 1.4.3 REEs - Supply chain vulnerabilities and geopolitical concerns.

As previously stated, despite their name, REEs are not particularly scarce in the Earth's crust, but their economic viability for extraction is a critical limitation. Although these elements are reasonably abundant, REEs are typically found in dispersed, low-grade ores, rendering many potential sources

economically unprofitable for their mining and extraction [51] [52]. Moreover, REEs illustrate a clear example of a lack of geographical variety among the essential minerals for the energy transition. This geological and economic reality creates a fragile and unstable global supply chain, extremely vulnerable to geopolitical tensions and shifts in market demand. Therefore, even minor disruptions can have significant repercussions, affecting price volatility and the availability of these critical raw materials.

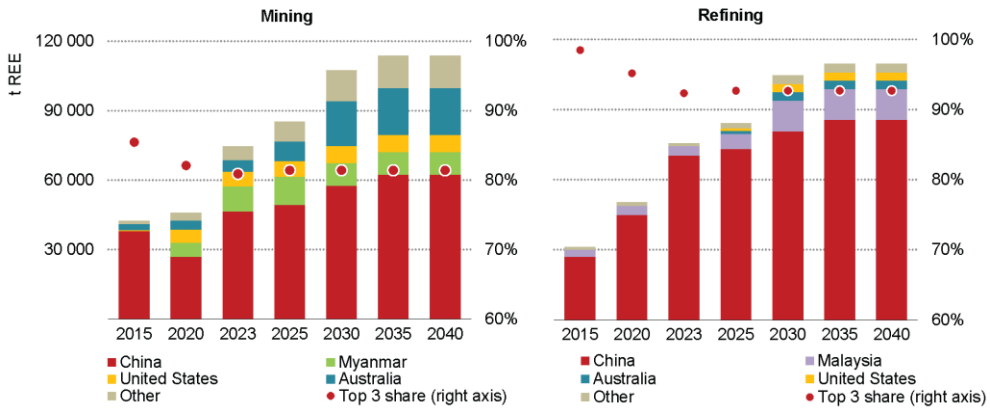


***Figure 1-4*** *Magnet-REE (Nd, Pr, Dy, Tb) production from operating and announced projects. From* [43]

A major strategic vulnerability arises from the heavy geographical concentration within the borders of China, which historically holds a dominant position in the REE production and market [53,54]. In 2023, just three countries accounted for 85% of magnet-REE mining, with China responsible for 62% of global production. However, the refining stage is even more concentrated, with China alone controlling 92% of global refined output in 2023 (**Figure 1-4**) in a near-monopolistic position. This extreme concentration of mining sites and key intermediate products in the hands of a single nation underscored a dangerous lack of diversification in the entire REE supply chain. Especially the refining is expected to remain highly concentrated, with China still holding a significant 77% share of global refined output by 2030. Consequently, it

could exert a strong influence on the international market of REE raw materials and REE-based PMs.

According to the USGS (2025), global Rare Earth Oxide (REO) mine production is estimated to have reached 390,000 metric tons in the past year. This growth was largely driven by increased output from China, Nigeria, and Thailand [55]. China itself produced 270,000 metric tons of REOs in 2024, a 15% rise from its 2023 production of 255,000 metric tons. These quantities are particularly notable considering China's domestic REO reserves, estimated at 44 million metric tons. Furthermore, official production statistics likely underestimate actual Chinese REO output as they do not account for undocumented mining. This unreported production further reinforces China's primary role in the global REE supply chain and likely augments REO resources at its disposal.

China built its monopoly over the global supply even on several policies the government adopted throughout the years. China’s leading position has reportedly been used as leverage in trade and political negotiations [56,57]. For example, the tightening of the Chinese export regulations caused the sharpest increase in REE prices between 2009 and 2011, as shown in **Figure 1-6**. The restrictions of China on REE raw materials, owning around 97% of global REE production at the time (**Figure 1-5**), caught general attention when the United States (US) and the European Union (EU) complained against China to the World Trade Organization (WTO) in 2009. They claimed that export restrictions imposed by China, including quotas and taxes, violated WTO rules. These geopolitical tensions were exacerbated by the territorial dispute with Japan over the Senkaku/Diaoyu Islands in 2010, where China took advantage of its dominance on REE supply and suspended exports towards Japan during the political conflict. In 2012, the US, the EU and Japan challenged China

again to the WTO for its policies. The countries further contested that the Chinese measures were principally aimed at satisfying internal demand and controlling the international price of REE minerals and raw materials.

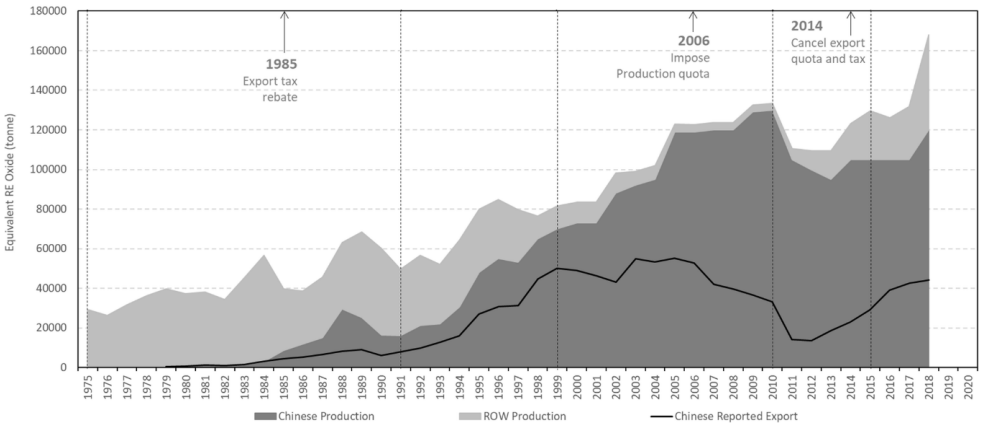


***Figure 1-5*** *Overview of Chinese and Rest of World (ROW) mine production of REEs throughout the years (1985-2018) and some policy variations. Modified from* [56].

As Wübbeke pointed out, the export restriction, the most controversial policy, needs to be considered in the context of other policies and regulations in the Chinese economy, including the reorganization of industries, resource conservation, and environmental protection [57]. Those points were the same reasons China moved and replied to its arguing contenders. The ambiguity that follows is inevitable. The shrinking of export quotas, the joint regard towards import trade, and the stricter control over internal industry and unregistered production all contributed to build the Chinese strategic stockpile and economic empire over REEs. The imposition of quotas is a powerful strategy that China holds tightly as it affirms its monopolistic grip on REEs. Not only in export trade but also internal production quotas can be a constraint in the long-term supply chain, as the disturbance can generate a positive influence, in other words, an increase, on international prices. The giant spike in RE prices became a major concern among REE stakeholders worldwide, making

evident the high susceptibility of supplies for REEs and the clear risk of a shortage in the future. Therefore, the period from 2010 to 2013, when China's adopted policies that heavily impacted REE prices and demand, defined the so-called "*Rare Earth Crisis*".

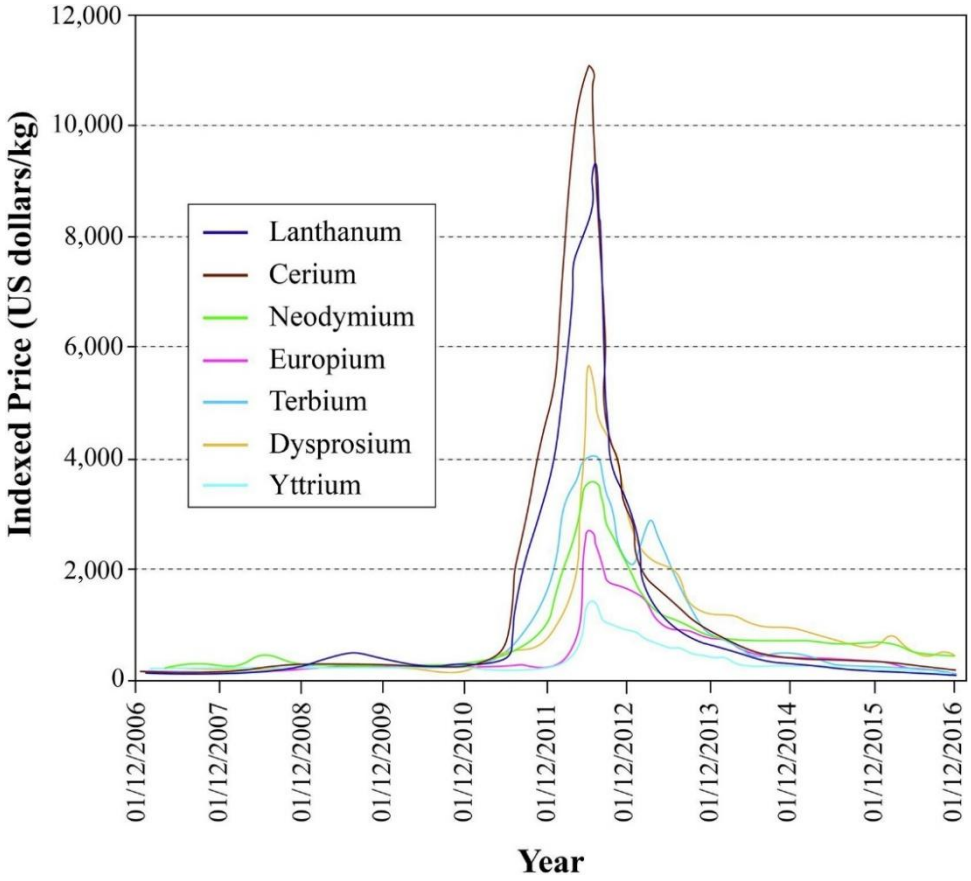


***Figure 1-6*** *Indexed prices for selected REOs from 2006 to 2016. From* [53].

The anxiety triggered by the precarious steadiness of the REE supply chain, manipulated by China's monopoly, represented the moving force for the other nations to find additional ways to reinforce their stocks. The balance between the increasing demand for a certain material and its availability is one factor defining its *criticality* [58]. The criticality of a resource is fundamentally defined

by two entangled factors. The potential for supply disruptions, comprising geopolitical instabilities, logistical challenges, and resource depletion, and the material's economic importance, which includes its role in technological advancements and its impact on overall economic stability. Having this in mind, the definition of *critical raw material* (*CRM*) fits perfectly with REEs [59,60]. These underlying reasons put pressure on the main economic entities, such as the US and EU, to find reliable and unhindered access to crucial raw materials. To address this challenge, in 2011, both created their list for the assessment of CRMs [61,62] to fulfil their objectives in the decarbonization processes toward a more environment-friendly future.

Therefore, the scrupulous analysis of all the possible bottlenecks through foresight studies is devoted to preventing disruption and helping build a resilient supply chain [63–65]. Consequently, a focus on fostering domestic production and processing facilities and forging resilient international partnerships is necessary and essential, as explicitly explained in the 2024 Critical Raw Materials Act [66]. This Act, in the frame of the Green Deal Industrial Plan, advances core arguments aimed at creating a secure and resilient supply chain, through the creation of a continuous monitoring system, the strategic diversification of imports by expanding the EU’s global network while actively tackling unfair trade practices, and the improvement of CRM sustainability and circularity across the European market.

## 1.5 The quest for alternatives: mitigation strategies and the "Performance Gap"

Within this broader context, another strong strategy to reduce the CRMs and REEs dependency and evolve the magnet technology is to operate, where possible, by substitution. The concerns over cobalt's criticality in SmCo PMs

and the need to identify alternatives led to the very development of the NdFeB alloy in 1984 [58]. As previously stated, today, most technological applications rely on REE-based PMs. The primary benefit is attributed to their superior performance-to-volume ratio. A notable trend is the employment of high-value PMs in numerous small-tech devices, even when the inherent high performance of these materials is not strictly essential for device functionality. This paradox suggests a potential over-specification, where the small volume may be favored over purely functional requirements, driven by factors such as miniaturization demands or market trends. The huge spike in prices as a consequence of the "*Rare Earth Crisis*", the still precarious and unpredictable value chain or REEs for all the aforementioned linked environmental and geopolitical motivations, is forcing attention on substitution, cost reduction and recycling of these materials for the PMs production.

In 2024, the global PM market, driven by the growing demand for energy-efficient technologies, is estimated to possess a value of $53.4 billion, and based on a Compound Annual Growth Rate (CAGR) projection of 8.57%, it is anticipated to reach $111.9 billion by 2033 [67]. The global market is essentially split between NdFeB and hard ferrite magnets. Over 90 per cent of all PMs produced and sold belong to these two magnet material types, which are undoubtedly different in terms of performance and cost. Average $(BH)_{max}$ values of NdFeB are almost 10 times higher than the counterpart Ba/Sr-ferrite (**Figure 1-2**), but their average price can jump even more. **Figure 1-7** displays the 2020 estimated magnet market, categorized by different types of materials. [11]. These charts reveal a significant contrast in magnet usage from a value versus weight perspective. Chart ***(a)*** demonstrates the dominance of NdFeB magnets in value terms, accounting for the majority of the total at 64%. This highlights the role of NdFeB as a high-value component, indicative of its superior magnetic strength per unit. On the other hand, chart ***(b)***, depicting

weight, shows ferrite magnets as the overwhelmingly dominant type, constituting 81.9% of the total production tonnage. This dominance underscores its position as a cost-effective, high-volume magnetic material suitable for applications where mass and economy are prioritized over extreme magnetic strength.

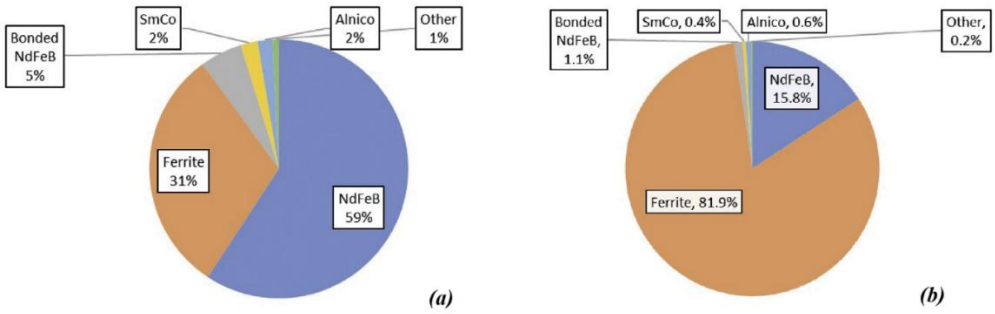


***Figure 1-7*** *2020 PM market by material type: on value basis (a) and weight basis (b). From* [11]

Based on magnetic property requirements and economic considerations, the dichotomy in the respective market roles of these two materials pushed the research forward in recent years. Most efforts have been devoted to refining NdFeB-type magnets to enhance their energy products or, even more, their thermal stability. Small additions of HREEs such as Dy or Tb gave the ability to withstand temperatures up to 200 °C, suitable for electric motors, but the criticality of these elements imposes to reduce or eliminate HREEs content in NdFeB magnets [68]. The hope of discovering a novel ultra-high-performance material to completely replace REE-based magnets is still not dismissed, but $Nd_2Fe_{14}B$ is a close-to-ideal-performance PM [28]. Additionally, while REEs are essential for high-performance applications, a considerable segment, especially in sectors like automotive and energy, requires magnets with only moderate strength within the 35-100 $kJ/m^3$ $(BH)_{max}$ range.

Seeking opportunities to mitigate reliance on REEs, a promising approach lies in targeting the performance range lying between REEs and ferrites. The existence of a substantial "*performance gap*", as previously shown (**Figure 1-2** and **Figure 1-7**), separates the lowest-performing REE magnets from cost-effective competitors like hard ferrites. Innovative pathways should, therefore, focus on developing a novel, economically viable magnetic material with a $(BH)_{max}$ capable of bridging this gap. Such functional material could not only offer enhanced performance and weight reduction in applications currently employing ferrites but also provide a more affordable alternative than REE magnets in less demanding applications, even if accompanied by a modest increase in weight [69].

# 1.6 Research aims, objectives and scope

Within this context, my doctoral project, is driven by the need to deal with the performance gap. On this prospect, we focused on the in-depth investigation of strategies to enhance the magnetic and functional properties of strontium hexaferrite, $SrFe_{12}O_{19}$ (SrM), with the objective of elevating the energy product, which rarely exceeds 38 $kJ/m^3$, to create a "gap magnet" solution. This advancement would offer a valuable alternative option for applications requiring lower-performing PMs, thus allowing for the potential replacement of current REE-based magnets and reducing dependency on critical materials. Moreover, if these "gap magnets" can be produced via a scalable and cost-efficient route, they would be eligible for industrial commercialisation. Thereby, REE-magnets would become more readily available and better allocated to high-performance applications, where their unique properties are truly essential.

As previously explained, to develop valuable magnetic materials for PMs, achieving high remanence and a coercivity large enough to sustain the

magnetization is crucial. Both parameters contribute to the squareness and the broadening of the hysteresis loop, and, indeed, to the $(BH)_{max}$ value[9]. The strategies to improve the properties of SrM are various and still largely under investigation, but they can be broadly categorized as physical and chemical modifications. Controlling the particle size and morphology at the nanoscale is a critical aspect of enhancing its magnetic properties [26]. Reducing the size of magnetic material to nanograins can increase its coercivity, transitioning from a multidomain to a single domain state below a critical size threshold[70]. Single domain, platelet shaped crystals of SrM having a certain degree of freedom can be mechanically or magnetically oriented, increasing both remanence and coercivity by the parallel alignment of the basal planes and thus of the magnetization easy axes, with reduced internal demagnetization[71,72]. Chemical modification, or doping, allows tuning the atomic structure by the strategic replacement of metal cations in specific sites, influencing the overall magnetization and the magnetocrystalline anisotropy[25,73]. The exchange-coupling with a soft phase can also to leverage the high $M_S$ of the soft phase to improve the remanence of the composite, while the hard phase provides the high coercivity[74]. For this strategy to work efficiently, the nanoparticles' high surface area to volume ratio is necessary to ensure optimal interaction.

The development of high-performance PMs faces a complex set of interconnected open questions, spanning fundamental theory, materials engineering, and industrial scalability. The intrinsic physics of intermetallic compounds works against discover an intermetallic phase owning better magnetic properties than NdFeB, and the challenge remains to engineer a microstructure that impedes reverse domain nucleation and growth. Reliable methods to control nanoparticle size, shape, and phase purity, and to assemble them into dense, well-aligned architectures, are lacking[75]. Realizing bulk nanocomposites that combine hard and soft phases with strong exchange

coupling continues to be hindered by phase separation, interface control, and grain boundary engineering. Achieving predictable magnetic properties (e.g., high coercivity, remanence, and energy product) in nanoparticles is hindered by issues like surface effects, dead layers, and defects[76]. From a processing perspective, achieving macroscopic texture with a preferred magnetization direction, while preserving nanoscale features that enhance coercivity, through synthesis and consolidation, is still unresolved[32]. At the industrial level, most high-performance nanoparticle synthesis routes are not yet scalable or environmentally sustainable, and the development of direct, one-step, green processes for air-stable, high-coercivity powders remains an urgent goal.

Therefore, the specific aims of this research were multiple: the first was to synthesize single-phase SrM nanoparticles with controlled morphologies, microstructures, and compositions using sustainable chemical synthesis routes and suitable to be scaled on industrial level such as low temperature solid state synthesis and modified sol-gel in NaCl matrix. Then, the effects of several processing parameters, sintering temperature, specific dopants (Al and Mn), on the morphological and main magnetic properties (saturation magnetization, remanence and coercivity) of synthesized SrM were examined. The densification and grain alignment techniques (Multi-anvil and Piston Cylinder press, Spark Plasma Sintering) were also investigated to obtain true samples of PMs. Furthermore, the synthesis of $Fe^0$ nanowires through wet chemical approach was performed to assess the coupling of this material with high $M_S$ and SrM. Additionally, in the framework of the European project INSPIRES, the sustainable and efficient strategies to recycle NdFeB magnets from end-of life appliances were assessed, with the purpose of contributing to the long-term circularity of this critical raw material and a greener forthcoming technology.

## 1.7 Hard hexagonal ferrites – a promising candidate

Within the hexaferrite family, strontium hexaferrite ($SrFe_{12}O_{19}$) is a material of significant interest for PM applications. Initially developed by Philips Research Laboratories in the 1950s, following the serendipitous discovery of barium hexaferrite ($BaFe_{12}O_{19}$), commercially known as Ferroxdure[77], $SrFe_{12}O_{19}$ has progressively gained market dominance. This is owed to several advantages, including improved magnetic properties over $BaFe_{12}O_{19}$ and its non-toxic nature. Both materials are isomorphous with the mineral magnetoplumbite ($PbFe_{12}O_{19}$), from which derives the name of the M-type hexagonal ferrite structure they belong (SrM, BaM).

The ferrite magnets have found widespread use in motors for household electronics, industrial equipment and automotive applications (integrated in DC motors for powering windows, mirrors, and headlight orientation). M-type hexaferrites offer several benefits over REE-based PMs, making them a preferred choice for specific applications and justifying their significant PM market share. While their magnetic performances were sensibly lower compared to REEs at room temperature, hexaferrites exhibit a notable advantage in retaining their magnetic flux at elevated temperatures (up to 300°C), better behaving than NdFeB in this regard. This is due to its higher *Curie temperature* ($T_c$), the upper limit of a PM operating temperature [31]. The value of $T_c$ sets the thermal limits of a PM's functionality, as its permanent magnetic properties are lost above this point. Sr-hexaferrite's $T_c$ is approximately 450°C (723 K), while in contrast, the $T_c$ of NdFeB magnets is lower, typically ranging from 310°C to 400°C (583-673 K). Although certain grades of SmCo offer even higher $T_c$ (700-850°C or 973-1123 K) and

maximum operating temperatures, SrM provides a beneficial balance of temperature performance at a more reasonable cost [12,69]. As ceramic oxides hexaferrites are electrical insulators, thus preventing eddy currents which is particularly relevant for dynamic operations in electrical motors. For the same reason, they are also chemically inert, rendering them resistant to corrosion and stable even when exposed to moisture or harsh environmental conditions, eliminating the need for protective surface coatings. This robust resistance to degradation thus reduces fabrication costs and enhances the long-term reliability of the device. Conversely, NdFeB magnets are known to be susceptible to rust and corrosion due to the presence of iron in their composition, often requiring protective coatings such as nickel plating to prevent degradation. While SmCo magnets generally exhibit better corrosion resistance than Neo magnets, they can still be brittle and prone to chipping [78].

A significant advantage of SrM over REE-magnets lies in the cost and availability of its constituent raw materials. The constituent elements of hexaferrites, such as strontium carbonate and iron oxide, are abundant and inexpensive raw materials compared to REEs. This is particularly relevant for large-scale applications where the material cost constitutes a significant portion of the overall expense. Ferrites have a reduced environmental impact throughout their lifecycle compared to REEs, from extraction to post-processing. This is primarily attributed to the abundance of its raw materials and the relatively simpler production involved. Furthermore, development efforts are focused on recycling their residues, ensuring the circularity of the whole manufacturing process [79,80]. The lower environmental mark of SrM aligns with the increasing global emphasis on sustainability and environmental regulations, making it a more ecologically responsible choice.

To fully appreciate the potential of SrM as a magnet, it is crucial to consider its crystallographic structure, from which derive its key magnetic properties.

## 1.7.1 The M-Type structure

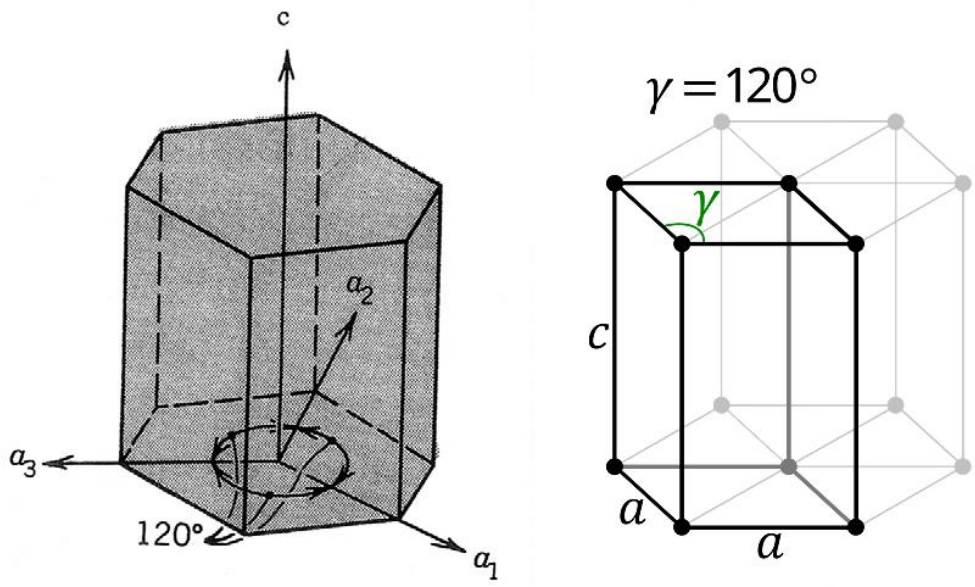


***Figure 1-8*** *Representation of the hexagonal unit cell, showing the two lattice parameters a (length of the edges in basal plane) and c (length of the edges along the c-axis). Modified from* [25]

SrM crystallizes in a hexagonal magnetoplumbite-type structure, belonging to the space group *P63/mmc*[81]. The hexagonal unit cell is characterized by two primary lattice parameters: *a*, which represents the length of the edges in the basal plane, and *c*, which denotes the length of the edge along the principal hexagonal axis [25].

Four Miller indices h, j, k and l are usually employed to indicate the planes. The last one indicates the principal *c*-axis and the three others the axes in the basal (0001) plane of the hexagonal polyhedron, at angles of 120° to each other (**Figure 1-8**) [26]. The unit cell of SrM comprises two formula units with 64 ions per unit cell (2 $Sr^{2+}$, 24 $Fe^{3+}$, and 38 $O^{2-}$). The hexagonal close-packed (*hcp*)

arrangement of oxygen ions forms the framework of the structure, with metal cations occupying specific interstitial positions[82]. This highly ordered array creates a complex magnetoplumbite structure which results in flat crystals with hexagonal facets that can be observed in microscopic examinations.

A way to visualize the structure is to consider it to be built from two different building blocks, *S* and *R*, packed along the c-axis (**Figure 1-9**). The S (for spinel) block presents two layer and the same occupancy of tetrahedral and octahedral sites as the spinel (cubic) crystal structure (1/3 in tetrahedral, $T_d$ cavities and 2/3 in octahedral, $O_h$ ones), thus having $(Fe_6O_8)^{2+}$ composition. The other block, R, is built from a three-layer *hcp* sequence, with a quarter of the oxygen anions substituted in the intermediate hexagonal layer by the large divalent cation ($Sr^{2+}$, $Ba^{2+}$). Considering the interstitial Fe atoms, the composition of this block is $(SrFe_6O_{11})^{2-}$. The full unit cell is obtained by ordering the blocks along the *c* direction, following the sequence $RSR^*S^*$, where the star indicates a rotation of 180°, giving a repeat distance of 2.2–2.3 nm [83,84]. This superstructure contains five distinct crystallographic sites for $Fe^{3+}$ ions, indicated by the Wickoff positions 2a, 2b, $4f_1$, $4f_2$ and 12k [82]. Each of these sites presents a unique local environment defined by the surrounding oxygen anions, important for understanding the magnetic properties of the compound. The 2b site hosts $Fe^{3+}$ ions in a trigonal bipyramidal coordination in the R block. Site $4f_1$ and 2a are the tetrahedral and octahedral sites of the S block. The $4f_2$ site features octahedrally coordinated $Fe^{3+}$ ions in the R block, but this environment is distorted due to the proximity of Sr atoms in the R block. Finally, $12_k$ site feature $Fe^{3+}$ in octahedral sites at the boundary between R and S blocks, which are also distorted (assigned to the R block).

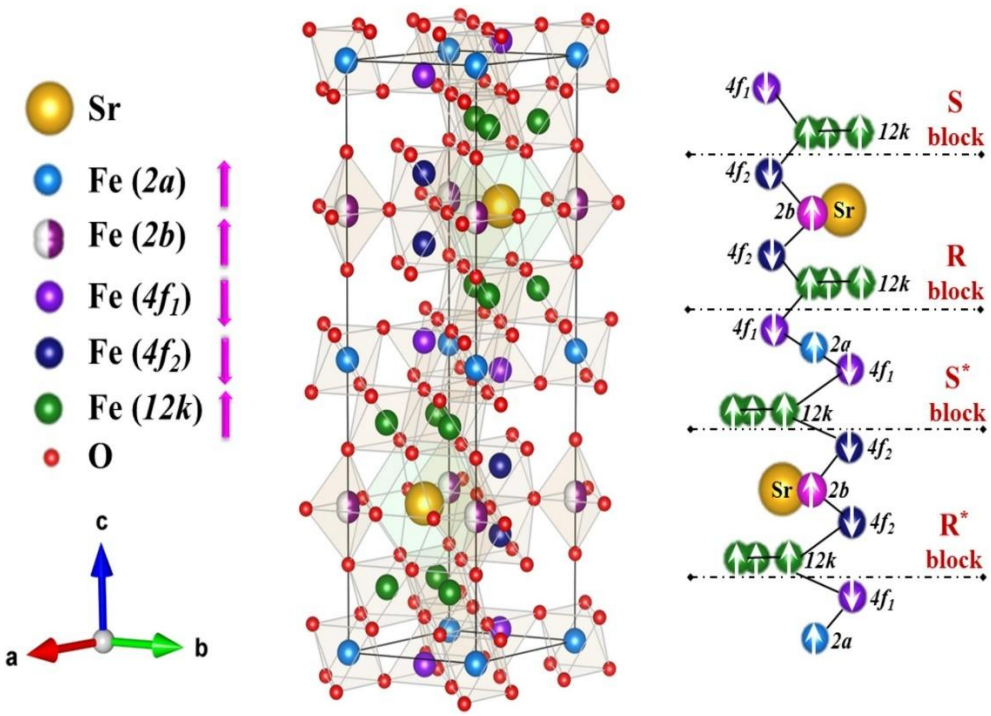


***Figure 1-9*** *Crystallographic structure of* $(SrFe_{12}O_{19})_2$. *From* [85].

SrM exhibits ferrimagnetic behaviour arising from the unequal and antiparallel alignment of magnetic moments of $Fe^{3+}$ ions along the c-axis [86]. The magnetic structure can be understood by examining the spin orientation of iron ions across the various sublattices formed by the different crystallographic sites. The spin orientation of each iron cation is coupled by super-exchange interaction through the oxygen anions [84]. The $Fe^{3+}$ cations have a spin-only magnetic moment of approximately 5 μB (Bohr magnetons) at 0 K, which arises from its five unpaired d electrons (S=5/2, high spin). The magnetic moments of $Fe^{3+}$ ions at 12k, 2a, and 2b sites are aligned parallel to the c-axis (spin up), while those at $4f_1$ and $4f_2$ sites are aligned antiparallel (spin down). Considering the site occupancy of the M-type ferrites (*n*12k =6, *n*2a = 1, *n*2b = 1, *n*4f1 = 2, *n*4f2 = 2), this configuration results in a net magnetic moment along the c-axis, as the number of $Fe^{3+}$ ions with up spins (8) exceeds those with down spins (4) and this unequal distribution leads to the ferrimagnetic

behavior, with a theoretical magnetic moment of 20 μB per formula unit [73]. Even if the $M_S$ at room temperature of M-hexaferrites is only slighty lower than other ferrimagnetic oxides, e.g. magnetite, however it is very low compared to the $M_S$ of most PM materials, like $Nd_2Fe_{14}B$. Their distinctive feature, which justify the employment as PMs, is the strong uniaxial *magnetocrystalline anisotropy* (*MCA*). This anisotropy primarily originates from the single-ion contribution of trigonal bipyramidal $Fe^{3+}$ ion at the 2b site, and, in minor extent, from the slight perturbation the large divalent metal cation ($Sr^{2+}$ or $Ba^{2+}$) induces in the lattice. The hexagonal crystallographic structure of the M-type ferrites makes the anisotropy lying along the *c*-axis [25]. At room temperature, the anisotropy constant ($K_1$) shows relatively high values, $3.2 \cdot 10^5$ J/m$^3$ for BaM and $3.5 \cdot 10^5$ J/m$^3$ for SrM. The strong anisotropy favors the alignment of magnetic moments along the c-axis, creating a preferred magnetization direction and stabilizing against demagnetizing fields and thermal fluctuations. A high MCA is a prerequisite for a high coercive field. Considering that the anisotropy is uniaxial, the *anisotropy field* ($H_A$) can be determined by the expression $2K_1/\mu_0 M_S$, reaching values of 1.35 MA/m and 1.47 MA/m for BaM and SrM, respectively [73].

This intricate relationship between crystal structure and magnetic properties provides a foundation for tailoring the characteristics of the material through strategic substitutions, processing techniques, and size control. Understanding these structure-property correlations is therefore essential for better optimizing the magnetic and functional properties of SrM, in order to further enhance its suitability for PM applications.

# References


(1) Skomski, R.; Sellmyer, D. J. Intrinsic and Extrinsic Properties of Advanced Magnetic Materials. In *Handbook of Advanced Magnetic Materials*; Springer, Boston, MA, 2006; Vol. 1, pp 1–57. https://doi.org/10.1007/1-4020-7984-2_1.

(2) Gutfleisch, O.; Willard, M. A.; Brück, E.; Chen, C. H.; Sankar, S. G.; Liu, J. P. Magnetic Materials and Devices for the 21st Century: Stronger, Lighter, and More Energy Efficient. *Advanced Materials* **2011**, *23* (7), 821–842. https://doi.org/10.1002/ADMA.201002180.

(3) Silveyra, J. M.; Ferrara, E.; Huber, D. L.; Monson, T. C. Soft Magnetic Materials for a Sustainable and Electrified World. *Science (1979)* **2018**, *362* (6413). https://doi.org/10.1126/SCIENCE.AAO0195/ASSET/44C5C08C-302D-48FB-89C2-82279D7C7C47/ASSETS/GRAPHIC/362_AAO0195_F10.JPEG.

(4) Périgo, E. A.; Weidenfeller, B.; Kollár, P.; Füzer, J. Past, Present, and Future of Soft Magnetic Composites. *Appl Phys Rev* **2018**, *5* (3), 31301. https://doi.org/10.1063/1.5027045/123950.

(5) Enz, U. Magnetism and Magnetic Materials: Historical Developments and Present Role in Industry and Technology. In *Handbook of Ferromagnetic Materials*; Elsevier, 1982; Vol. 3, pp 1–36. https://doi.org/10.1016/S1574-9304(05)80087-2.

(6) Imura, T.; Hori, Y. Maximizing Air Gap and Efficiency of Magnetic Resonant Coupling for Wireless Power Transfer Using Equivalent Circuit and Neumann Formula. *IEEE Transactions on Industrial Electronics* **2011**, *58* (10), 4746–4752. https://doi.org/10.1109/TIE.2011.2112317.

(7) Rasmussen, K. F.; Davies, J. H.; Miller, T. J. E.; McGilp, M. L.; Olaru, M. Analytical and Numerical Computation of Air-Gap Magnetic Fields in

Brushless Motors with Surface Permanent Magnets. *IEEE Trans Ind Appl* **2000**, *36* (6), 1547–1554. https://doi.org/10.1109/28.887205.

(8) Buschow, K. H. J. New Developments in Hard Magnetic Materials. *Reports on Progress in Physics* **1991**, *54* (9), 1123–1213. https://doi.org/10.1088/0034-4885/54/9/001.

(9) Coey, J. M. D. Hard Magnetic Materials: A Perspective. *IEEE Trans Magn* **2011**, *47* (12), 4671–4681. https://doi.org/10.1109/TMAG.2011.2166975.

(10) Zijlstra, H. Permanent Magnets; Theory. In *Handbook of Ferromagnetic Materials*; Elsevier, 1982; Vol. 3, pp 37–105. https://doi.org/10.1016/S1574-9304(05)80088-4.

(11) Ormerod, J. Permanent Magnet Markets and Applications. *Modern Permanent Magnets* **2022**, 403–434. https://doi.org/10.1016/B978-0-323-88658-1.00012-1.

(12) Coey, J. M. D. Permanent Magnet Applications. *J Magn Magn Mater* **2002**, *248* (3), 441–456. https://doi.org/10.1016/S0304-8853(02)00335-9.

(13) Lewis, L. H.; Jiménez-Villacorta, F. Perspectives on Permanent Magnetic Materials for Energy Conversion and Power Generation. *Metallurgical and Materials Transactions A 2012 44:1* **2012**, *44* (1), 2–20. https://doi.org/10.1007/S11661-012-1278-2.

(14) Chan, C. C.; Chau, K. T.; Jiang, J. Z.; Xia, W. Novel Permanent Magnet Motor Drives for Electric Vehicles. *IEEE TRANSACTIONS ON INDUSTRIAL ELECTRONICS* **1996**, *43* (2).

(15) Spooner, E.; Williamson, A. C. Direct Coupled, Permanent Magnet Generators for Wind Turbine Applications. *IEE Proceedings - Electric Power Applications* **1996**, *143* (1), 1. https://doi.org/10.1049/ip-epa:19960099.

(16) Beauloye, L.; Dehez, B. Permanent Magnet Electrodynamic Suspensions Applied to MAGLEV Transportation Systems: A Review. *IEEE Transactions*

*on Transportation Electrification* **2023**, *9* (1), 748–758. https://doi.org/10.1109/TTE.2022.3193296.

(17) Fastenau, R. H. J.; Van Loenen, E. J. Applications of Rare Earth Permanent Magnets. *J Magn Magn Mater* **1996**, *157–158*, 1–6. https://doi.org/10.1016/0304-8853(95)01279-6.

(18) Miyamoto, T.; Sakurai, H.; Takabayashi, H.; Aoki, M. A Development of a Permanent Magnet Assembly for MRI Devices Using Nd-Fe-B Material. *IEEE Trans Magn* **1989**, *25* (5), 3907–3909. https://doi.org/10.1109/20.42473.

(19) Melfi, M. J.; Evon, S.; McElveen, R. Induction versus Permanent Magnet Motors: For Power Density and Energy Savings in Industrial Applications. *IEEE Industry Applications Magazine* **2009**, *15* (6), 28–35. https://doi.org/10.1109/MIAS.2009.934443.

(20) Jing, L.; Tang, W.; Wang, T.; Ben, T.; Qu, R. Performance Analysis of Magnetically Geared Permanent Magnet Brushless Motor for Hybrid Electric Vehicles. *IEEE Transactions on Transportation Electrification* **2022**, *8* (2), 2874–2883. https://doi.org/10.1109/TTE.2022.3151681.

(21) Shao, L.; Navaratne, R.; Popescu, M.; Liu, G. Design and Construction of Axial-Flux Permanent Magnet Motors for Electric Propulsion Applications-A Review. *IEEE Access* **2021**, *9*, 158998–159017. https://doi.org/10.1109/ACCESS.2021.3131000.

(22) Yin, M.; Li, G.; Zhou, M.; Zhao, C. Modeling of the Wind Turbine with a Permanent Magnet Synchronous Generator for Integration. In *2007 IEEE Power Engineering Society General Meeting*; IEEE, 2007; pp 1–6. https://doi.org/10.1109/PES.2007.385982.

(23) Mills, A. A. The Lodestone: History, Physics, and Formation. *Ann Sci* **2004**, *61* (3), 273–319. https://doi.org/10.1080/00033790310001642812.

(24) Zhou, L.; Miller, M. K.; Lu, P.; Ke, L.; Skomski, R.; Dillon, H.; Xing, Q.; Palasyuk, A.; McCartney, M. R.; Smith, D. J.; Constantinides, S.; McCallum, R. W.; Anderson, I. E.; Antropov, V.; Kramer, M. J. Architecture and Magnetism of Alnico. *Acta Mater* **2014**, *74*, 224–233. https://doi.org/10.1016/J.ACTAMAT.2014.04.044.

(25) Pullar, R. C. Hexagonal Ferrites: A Review of the Synthesis, Properties and Applications of Hexaferrite Ceramics. *Prog Mater Sci* **2012**, *57* (7), 1191–1334. https://doi.org/10.1016/j.pmatsci.2012.04.001.

(26) de Julián Fernández, C.; Sangregorio, C.; de la Figuera, J.; Belec, B.; Makovec, D.; Quesada, A. Progress and Prospects of Hard Hexaferrites for Permanent Magnet Applications. *J Phys D Appl Phys* **2021**, *54* (15), 153001. https://doi.org/10.1088/1361-6463/ABD272.

(27) Yi, J. H. Development of Samarium–Cobalt Rare Earth Permanent Magnetic Materials. *Rare Metals* **2014**, *33* (6), 633–640. https://doi.org/10.1007/S12598-014-0405-1/FIGURES/10.

(28) Coey, J. M. D. Perspective and Prospects for Rare Earth Permanent Magnets. *Engineering* **2020**, *6* (2), 119–131. https://doi.org/10.1016/J.ENG.2018.11.034.

(29) Cooley, C. Z.; McDaniel, P. C.; Stockmann, J. P.; Srinivas, S. A.; Cauley, S. F.; Śliwiak, M.; Sappo, C. R.; Vaughn, C. F.; Guerin, B.; Rosen, M. S.; Lev, M. H.; Wald, L. L. A Portable Scanner for Magnetic Resonance Imaging of the Brain. *Nature Biomedical Engineering 2020 5:3* **2020**, *5* (3), 229–239. https://doi.org/10.1038/s41551-020-00641-5.

(30) McCallum, R. W.; Lewis, L.; Skomski, R.; Kramer, M. J.; Anderson, I. E. Practical Aspects of Modern and Future Permanent Magnets. *Annu Rev Mater Res* **2014**, *44* (1), 451–477. https://doi.org/10.1146/annurev-matsci-070813-113457.

(31) J. M. D. Coey. *Magnetism and Magnetic Materials*; Cambridge University Press, 2010.

(32) Granados-Miralles, C.; Saura-Múzquiz, M.; Andersen, H. L.; Granados-Miralles, C.; Saura-Múzquiz, M.; Andersen, H. L. Permanent Magnets Based on Hard Ferrite Ceramics. *Ceramic Materials - Present and Future* **2023**. https://doi.org/10.5772/INTECHOPEN.1002234.

(33) Gutfleisch, O. Controlling the Properties of High Energy Density Permanent Magneticmaterials by Different Processing Routes. *J Phys D Appl Phys* **2000**, *33* (17), R157. https://doi.org/10.1088/0022-3727/33/17/201.

(34) Strnat, K.; Hoffer, G.; Olson, J.; Ostertag, W.; Becker, J. J. A Family of New Cobalt-Base Permanent Magnet Materials. *J Appl Phys* **1967**, *38* (3), 1001–1002. https://doi.org/10.1063/1.1709459.

(35) Velge, W. A. J. J.; Buschow, K. H. J. Magnetic and Crystallographic Properties of Some Rare Earth Cobalt Compounds with CaZn5 Structure. *J Appl Phys* **1968**, *39* (3), 1717–1720. https://doi.org/10.1063/1.1656420.

(36) Croat, J. J.; Herbst, J. F.; Lee, R. W.; Pinkerton, F. E. Pr-Fe and Nd-Fe-Based Materials: A New Class of High-Performance Permanent Magnets (Invited). *J Appl Phys* **1984**, *55* (6), 2078–2082. https://doi.org/10.1063/1.333571.

(37) Sagawa, M.; Fujimura, S.; Togawa, N.; Yamamoto, H.; Matsuura, Y. New Material for Permanent Magnets on a Base of Nd and Fe (Invited). *J Appl Phys* **1984**, *55* (6), 2083–2087. https://doi.org/10.1063/1.333572.

(38) Croat, J. J.; Herbst, J. F.; Lee, R. W.; Pinkerton, F. E. High-Energy Product Nd-Fe-B Permanent Magnets. *Appl Phys Lett* **1984**, *44* (1), 148–149. https://doi.org/10.1063/1.94584.

(39) Ojima, T.; Tomizawa, S.; Yoneyama, T.; Hori, T. New Type Rare Earth Cobalt Magnets with an Energy Product of 30 MG·Oe. *Japanese Journal of Applied*

*Physics, Part 1: Regular Papers and Short Notes and Review Papers* **1977**, *16* (4), 671–672. https://doi.org/10.1143/JJAP.16.671/XML.

(40) Sugimoto, S. Current Status and Recent Topics of Rare-Earth Permanent Magnets. *J Phys D Appl Phys* **2011**, *44* (6), 064001. https://doi.org/10.1088/0022-3727/44/6/064001.

(41) Brown, D.; Ma, B. M.; Chen, Z. Developments in the Processing and Properties of NdFeb-Type Permanent Magnets. *J Magn Magn Mater* **2002**, *248* (3), 432–440. https://doi.org/10.1016/S0304-8853(02)00334-7.

(42) Matsuura, Y. Recent Development of Nd–Fe–B Sintered Magnets and Their Applications. *J Magn Magn Mater* **2006**, *303* (2), 344–347. https://doi.org/10.1016/J.JMMM.2006.01.171.

(43) International Energy Agency. *Global Critical Minerals Outlook 2024*; 2024. www.iea.org.

(44) Talan, D.; Huang, Q. A Review of Environmental Aspect of Rare Earth Element Extraction Processes and Solution Purification Techniques. *Miner Eng* **2022**, *179*, 107430. https://doi.org/10.1016/J.MINENG.2022.107430.

(45) Haque, N.; Hughes, A.; Lim, S.; Vernon, C. Rare Earth Elements: Overview of Mining, Mineralogy, Uses, Sustainability and Environmental Impact. *Resources 2014, Vol. 3, Pages 614-635* **2014**, *3* (4), 614–635. https://doi.org/10.3390/RESOURCES3040614.

(46) Lee, J. C. K.; Wen, Z. Rare Earths from Mines to Metals: Comparing Environmental Impacts from China's Main Production Pathways. *J Ind Ecol* **2017**, *21* (5), 1277–1290. https://doi.org/10.1111/JIEC.12491.

(47) Ali, S. H. Social and Environmental Impact of the Rare Earth Industries. *Resources 2014, Vol. 3, Pages 123-134* **2014**, *3* (1), 123–134. https://doi.org/10.3390/RESOURCES3010123.

(48) Navarro, J.; Zhao, F. Life-Cycle Assessment of the Production of Rare-Earth Elements for Energy Applications: A Review. *Front Energy Res* **2014**, *2* (NOV), 104175. https://doi.org/10.3389/FENRG.2014.00045/BIBTEX.

(49) Zaimes, G. G.; Hubler, B. J.; Wang, S.; Khanna, V. Environmental Life Cycle Perspective on Rare Earth Oxide Production. *ACS Sustain Chem Eng* **2015**, *3* (2), 237–244. https://doi.org/10.1021/SC500573B/SUPPL_FILE/SC500573B_SI_001.PDF.

(50) Vahidi, E.; Zhao, F. Environmental Life Cycle Assessment on the Separation of Rare Earth Oxides through Solvent Extraction. *J Environ Manage* **2017**, *203*, 255–263. https://doi.org/10.1016/J.JENVMAN.2017.07.076.

(51) Gupta, G. K.; Krishnamurthy, N. Extractive Metallurgy of Rare Earths. *https://doi.org/10.1179/imr.1992.37.1.197* **1992**, *37* (1), 197–248. https://doi.org/10.1179/IMR.1992.37.1.197.

(52) Ganguli, R.; Cook, D. R. Rare Earths: A Review of the Landscape. *MRS Energy and Sustainability* **2018**, *5* (1), 1–16. https://doi.org/10.1557/MRE.2018.7/METRICS.

(53) Dushyantha, N.; Batapola, N.; Ilankoon, I. M. S. K.; Rohitha, S.; Premasiri, R.; Abeysinghe, B.; Ratnayake, N.; Dissanayake, K. The Story of Rare Earth Elements (REEs): Occurrences, Global Distribution, Genesis, Geology, Mineralogy and Global Production. *Ore Geol Rev* **2020**, *122*, 103521. https://doi.org/10.1016/j.oregeorev.2020.103521.

(54) Mancheri, N. A.; Sprecher, B.; Bailey, G.; Ge, J.; Tukker, A. Effect of Chinese Policies on Rare Earth Supply Chain Resilience. *Resour Conserv Recycl* **2019**, *142*, 101–112. https://doi.org/10.1016/J.RESCONREC.2018.11.017.

(55) Geological Survey, U. *Mineral Commodity Summaries 2025*; 2025. https://doi.org/10.3133/mcs2025.

(56) Shen, Y.; Moomy, R.; Eggert, R. G. China's Public Policies toward Rare Earths, 1975–2018. *Mineral Economics* **2020**, *33* (1–2), 127–151. https://doi.org/10.1007/S13563-019-00214-2/FIGURES/18.

(57) Wübbeke, J. Rare Earth Elements in China: Policies and Narratives of Reinventing an Industry. **2013**. https://doi.org/10.1016/j.resourpol.2013.05.005.

(58) Binnemans, K.; Jones, P. T.; Müller, T.; Yurramendi, L. Rare Earths and the Balance Problem: How to Deal with Changing Markets? *Journal of Sustainable Metallurgy 2018 4:1* **2018**, *4* (1), 126–146. https://doi.org/10.1007/S40831-018-0162-8.

(59) Nassar, N. T.; Du, X.; Graedel, T. E. Criticality of the Rare Earth Elements. *J Ind Ecol* **2015**, *19* (6), 1044–1054. https://doi.org/10.1111/JIEC.12237.

(60) Smith Stegen, K. Heavy Rare Earths, Permanent Magnets, and Renewable Energies: An Imminent Crisis. *Energy Policy* **2015**, *79*, 1–8. https://doi.org/10.1016/J.ENPOL.2014.12.015.

(61) *EUR-Lex - 52011DC0025 - EN - EUR-Lex*. https://eur-lex.europa.eu/legal-content/EN/ALL/?uri=CELEX:52011DC0025 (accessed 2025-03-06).

(62) *2011 Critical Materials Strategy | Department of Energy*. https://www.energy.gov/node/349057 (accessed 2025-03-06).

(63) Carrara, S.; Bobba, S.; Blagoeva, D.; Dias, A.; Cavalli, P.; Georgitzikis, A.; Grohol, K.; Kuzov, A.; Latunussa, T.; Lyons, C.; Maury, G.; Somers, T. Supply Chain Analysis and Material Demand Forecast in Strategic Technologies and Sectors in the EU-A Foresight Study JRC Science for Policy Report; 2023. https://doi.org/10.2760/334074.

(64) Alves Dias, P.; Bobba, S.; Carrara, S.; Plazzotta, B. *THE ROLE OF RARE EARTH ELEMENTS IN WIND ENERGY AND ELECTRIC MOBILITY*; 2020. https://doi.org/10.2760/303258.

(65) *EUR-Lex - 52020DC0474 - EN - EUR-Lex*. https://eur-lex.europa.eu/legal-content/EN/TXT/?uri=CELEX:52020DC0474 (accessed 2025-03-10).

(66) *Regulation - EU - 2024/1252 - EN - EUR-Lex*. https://eur-lex.europa.eu/legal-content/EN/TXT/?uri=OJ:L_202401252 (accessed 2025-03-10).

(67) *Permanent Magnet Market Analysis and Forecasts, 2024-2033 with Hitachi Metals, Daido Steel, Shin-Etsu Chemical, TDK, Arnold Magnetic, Electron Energy and Adams Magnetic Products Dominating - ResearchAndMarkets.com | Business Wire*. https://www.businesswire.com/news/home/20241119445312/en/Permanent-Magnet-Market-Analysis-and-Forecasts-2024-2033-with-Hitachi-Metals-Daido-Steel-Shin-Etsu-Chemical-TDK-Arnold-Magnetic-Electron-Energy-and-Adams-Magnetic-Products-Dominating---ResearchAndMarkets.com (accessed 2025-03-10).

(68) Cui, J.; Ormerod, J.; Parker, D. S.; Ott, R.; Palasyuk, A.; McCall, S.; Paranthaman, M. P.; Kesler, M. S.; McGuire, M. A.; Nlebedim, C.; Pan, C.; Lograsso, T. Manufacturing Processes for Permanent Magnets: Part II—Bonding and Emerging Methods. *JOM* **2022**, *74* (6), 2492–2506. https://doi.org/10.1007/S11837-022-05188-1/FIGURES/1.

(69) Coey, J. M. D. Permanent Magnets: Plugging the Gap. *Scr Mater* **2012**, *67* (6), 524–529. https://doi.org/10.1016/j.scriptamat.2012.04.036.

(70) Cullity, B.; Graham, C. *Introduction to Magnetic Materials*; 2011.

(71) Stoner, E. C.; Wohlfarth, E. P. A Mechanism of Magnetic Hysteresis in Heterogeneous Alloys. *IEEE Trans Magn* **1991**, *27* (4), 3475–3518. https://doi.org/10.1109/TMAG.1991.1183750.

(72) Granados-Miralles, C.; Jenuš, P. On the Potential of Hard Ferrite Ceramics for Permanent Magnet Technology—a Review on Sintering Strategies. *J Phys D Appl Phys* **2021**, *54* (30), 303001. https://doi.org/10.1088/1361-6463/ABFAD4.

(73) Kojima, H. Fundamental Properties of Hexagonal Ferrites with Magnetoplumbite Structure. In *Handbook of Ferromagnetic Materials*; Elsevier, 1982; Vol. 3, pp 305–391. https://doi.org/10.1016/S1574-9304(05)80091-4.

(74) Kneller, E. F.; Hawig, R. The Exchange-Spring Magnet: A New Material Principle for Permanent Magnets. *IEEE Trans Magn* **1991**, *27* (4), 3588–3600. https://doi.org/10.1109/20.102931.

(75) Balamurugan, B.; Sellmyer, D. J.; Hadjipanayis, G. C.; Skomski, R. Prospects for Nanoparticle-Based Permanent Magnets. *Scr Mater* **2012**, *67* (6), 542–547. https://doi.org/10.1016/J.SCRIPTAMAT.2012.03.034.

(76) Ma, Z.; Mohapatra, J.; Wei, K.; Liu, J. P.; Sun, S. Magnetic Nanoparticles: Synthesis, Anisotropy, and Applications. *Chem Rev* **2023**, *123* (7), 3904–3943. https://doi.org/10.1021/ACS.CHEMREV.1C00860/ASSET/IMAGES/MEDIUM/CR1C00860_0036.GIF.

(77) Went, J. J.; Rathenau, G. W.; Gorter, E. W.; van Oosterhout, W. FERROXDURE, A CLASS OF NEW PERMANENT MAGNET MATERIALS. *PHILIPS TECHNICAL REVIEW* **1952**, *13* (7).

(78) Strnat, K. J. Modem Permanent Magnets for Applications in Electro-Technology. *Proceedings of the IEEE* **1990**, *78* (6), 923–946. https://doi.org/10.1109/5.56908.

(79) Bollero, A.; Rial, J.; Villanueva, M.; Golasinski, K. M.; Seoane, A.; Almunia, J.; Altimira, R. Recycling of Strontium Ferrite Waste in a Permanent Magnet Manufacturing Plant. *ACS Sustain Chem Eng* **2017**, *5* (4), 3243–3249. https://doi.org/10.1021/ACSSUSCHEMENG.6B03053/ASSET/IMAGES/LARGE/SC-2016-03053U_0008.JPEG.

(80) Berja, A.; Casaleiz, D.; Granados-Miralles, C.; Kosmač, K.; Saje, B.; Frangež, T.; Dvoršak, S.; Samardžija, Z.; Podmiljšak, B.; Fernández, J. F.; Quesada, A. A Simple and Industrially Scalable Process for Recycling Hexaferrite Ceramic

Magnets. *Open Ceramics* **2025**, *21*, 100724. https://doi.org/10.1016/j.oceram.2024.100724.

(81) Obradors, X.; Solans, X.; Collomb, A.; Samaras, D.; Rodriguez, J.; Pernet, M.; Font-Altaba, M. Crystal Structure of Strontium Hexaferrite SrFe12O19. *J Solid State Chem* **1988**, *72* (2), 218–224. https://doi.org/10.1016/0022-4596(88)90025-4.

(82) Tejera-Centeno, C.; Gallego, S.; Cerdá, J. I. An Ab Initio Study of the Magnetic Properties of Strontium Hexaferrite. *Sci Rep* **2021**, *11* (1), 1964. https://doi.org/10.1038/s41598-021-81028-7.

(83) Soria, G. D.; Jenus, P.; Marco, J. F.; Mandziak, A.; Sanchez-Arenillas, M.; Moutinho, F.; Prieto, J. E.; Prieto, P.; Cerdá, J.; Tejera-Centeno, C.; Gallego, S.; Foerster, M.; Aballe, L.; Valvidares, M.; Vasili, H. B.; Pereiro, E.; Quesada, A.; de la Figuera, J. Strontium Hexaferrite Platelets: A Comprehensive Soft X-Ray Absorption and Mössbauer Spectroscopy Study. *Scientific Reports 2019 9:1* **2019**, *9* (1), 1–13. https://doi.org/10.1038/s41598-019-48010-w.

(84) Smit, J.; Wijn, H. P. J.; Luton, G. E. *Ferrites : Physical Properties of Ferrimagnetic Oxides in Relation to Their Technical Applications*; Philips' Technical Library, Ed.; 1959.

(85) Gupta, A.; Roy, P. K. Improved Strontium Hexaferrites: An Overview of Current Progress in Synthesis, Properties, and Applications. *Materials Science and Engineering: B* **2024**, *306*, 117458. https://doi.org/10.1016/j.mseb.2024.117458.

(86) Fang, C. M.; Kools, F.; Metselaar, R.; De With, G.; De Groot, R. A. Magnetic and Electronic Properties of Strontium Hexaferrite SrFe12O19from First-Principles Calculations. *Journal of Physics: Condensed Matter* **2003**, *15* (36), 6229. https://doi.org/10.1088/0953-8984/15/36/311.

# **Chapter 2 |** Synthesis of SrM nanoparticles by Low-Temperature Solid-State Reaction (LTSSR)

Taking into account the need of selecting synthetic route suitable for industrial application, a low-temperature solid-state reaction (LTSSR), followed by calcination, was initially explored [1]. A typical synthesis involves mixing iron ($FeCl_3.6H_2O$) and strontium ($SrCl_2.4H_2O$) chlorides with sodium hydroxide (NaOH) in a mortar, yielding their respective oxo-hydroxides [details in Appendix]. The reaction is rapid and exothermic and produces minor fumes and results in a brownish, amorphous paste consisting of mixed $Fe^{3+}$ and $Sr^{2+}$ oxo-hydroxides. The resulting paste is washed thoroughly on a Büchner funnel with demineralized (DM) water until a chloride assay (using $AgNO_3/HNO_3$) confirms the absence of $Cl^-$ ions. This step removes excess NaOH and the NaCl by-product. The washed paste is then dried at 80 °C and ground into a fine powder prior to calcination. This methodology was selected as offering several advantages that align well with industrial scalability: it comprises few simple steps, and its solvent-free, solid-state nature allows for loading considerable amounts of reagents during the mixing stage. Furthermore, the process is cost-effective, utilizing room temperature conditions, low-cost precursors, and basic laboratory equipment. The employment of only water as solvent for the washing stage minimizes pollution and costs. The calcination step is also performed at a relatively low temperature (775 °C), significantly lower than conventional industrial procedures, which typically require temperatures exceeding 1000 °C [2–5]. Overall, this method is well suited for

industrial applications where large volumes are required. For the same purpose, cost optimization and pollution management are key considerations.

While the overall procedure is relatively straightforward, several processing parameters such as the $Fe^{3+}$/ $Sr^{2+}$ molar ratio, the $Na^{+}$/ $Sr^{2+}$ molar ratio, the calcination temperature, and the pH of the washing solution, were investigated to assess their impact on the size, structural and magnetic properties of the synthesized SrM nanoparticles. Powder X-ray Diffraction (PXRD) was employed to analyze the crystallographic phases and lattice parameters. Transmission Electron Microscopy (TEM) images were used to determine particle size, morphology, and size distribution. The effective metal content was verified by Inductively Coupled Plasma Atomic Emission Spectroscopy (ICP-AES). The key magnetic properties ($M_S$, $M_R$, and $H_C$) were determined from hysteresis loops measured at 300 K either from SQUID or PPMS magnetometer. Individual reaction parameters were systematically varied and tested, with the aim to obtain SrM nanoparticles with desirable magnetic properties and particle sizes within the nanometer range.

## 2.1 Temperature selection for controlled size of SrM nanoparticles

In the first series of experiments, the procedure reported by Kiani *et al* [1] was followed to obtain a single-phase compound after the heat treatment. Accordingly, the molar ratios between the metals in the reaction were set as $Fe^{3+}$/ $Sr^{2+}$ = 10 and $Na^{+}$/ $Sr^{2+}$ = 45, to limit the formation of the main contaminant they detected, namely hematite ($\alpha$-$Fe_2O_3$). The temperature used in the reference work, 750 °C for 3 hours, was determined based on differential thermal analysis (DTA) data, displaying at a temperature around 739 °C the formation of the SrM phase after dehydration of the hydroxides into metal

oxides [1]. In our case, to ensure the full conversion of the precursors into the desired product, the lowest temperature selected for the calcination stage was 775°C, slightly above the temperature designated for the proper SrM phase formation. Moreover, higher temperatures (837 °C and 900 °C) were investigated, to evaluate the effect on the size and aggregation of the nanoparticles [6].

The synthesized powders were evaluated by PXRD analysis to detect the presence of other phases outside SrM, and to estimate the crystallite size and the cell parameters of the resultant product. Moreover, TEM images were registered to check the morphology and the actual size of the nanoparticles, in combination with the size distribution. The results obtained are summarized in **Table 2-1**.

***Table 2-1*** *Crystallite size and cell parameters a and c obtained from PXRD, mean size and standard deviation obtained from TEM analysis of SrM samples produced by LTSSR at different calcination temperatures.*

| **Sample** | **Cry.size (nm)** | **a (Å)** | **c (Å)** | **Mean Size (nm)** | **Std. Dev. (nm)** |
|---|---|---|---|---|---|
| **3h, 775 °C** | 100(4) | 5.8855(3) | 23.074(2) | 63 | 20 |
| **3h, 837 °C** | 117(5) | 5.8825(3) | 23.059(2) | 100 | 31 |
| **3h, 900 °C** | 119(7) | 5.8837(4) | 23.064(2) | 129 | 41 |

As expected, at higher temperatures there was an increase in the mean particle size and its polydispersity, which was consistent with continuous and not homogeneous grain growth as the temperature rose [7]. A partial increase, although to a minor extent, was found in the crystallite size, while the cell parameters remained essentially unchanged and within the approximation of the cell refinement.

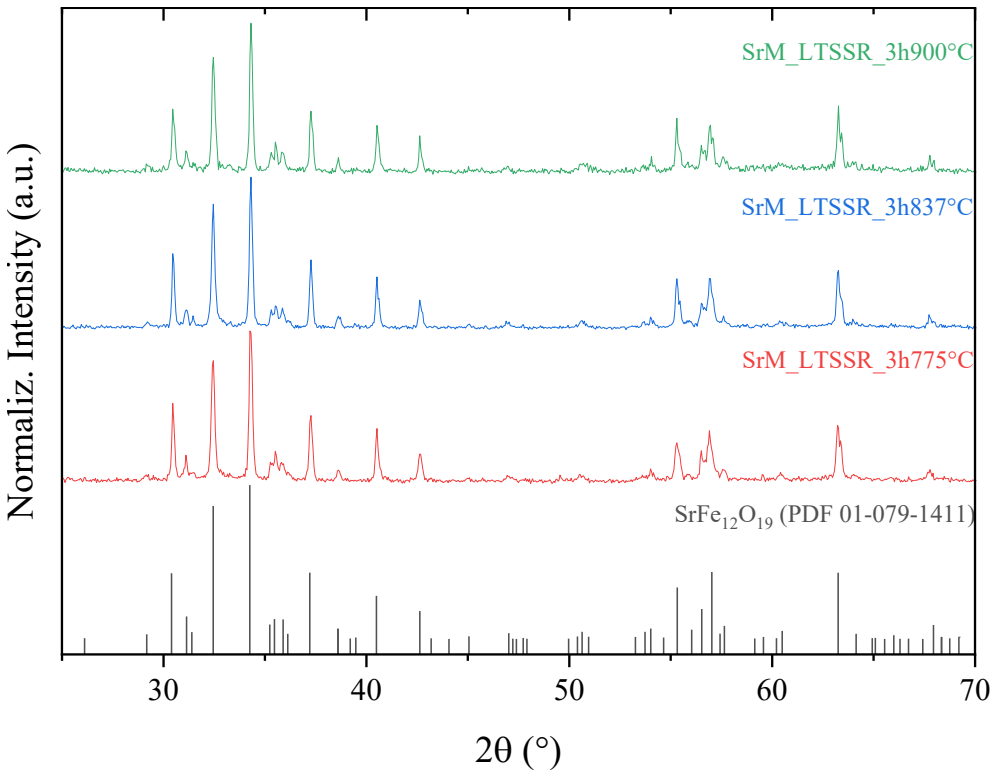


***Figure 2-1*** *PXRD diffraction patterns of SrM samples produced by LTSSR with different calcination temperatures: 775 °C for 3 h (red line), 837 °C for 3 h (blue line) and 900 °C for 3 h (green line).*

The diffraction patterns of the 3 samples displayed the typical reflections corresponding to the SrM profile without evidence of hematite impurities (the latter can be easily recognized by the presence of the most intense peak at 2θ = 33.2°). Thus, since no improvements were obtained by increasing temperature, in the following T = 775 °C was selected to get crystallite with size around 100 nm. TEM images revealed the formation of highly agglomerated nanoparticles. This assembly in large aggregates, even partially sintered in some points, could challenge the further orientation of the nanograins.

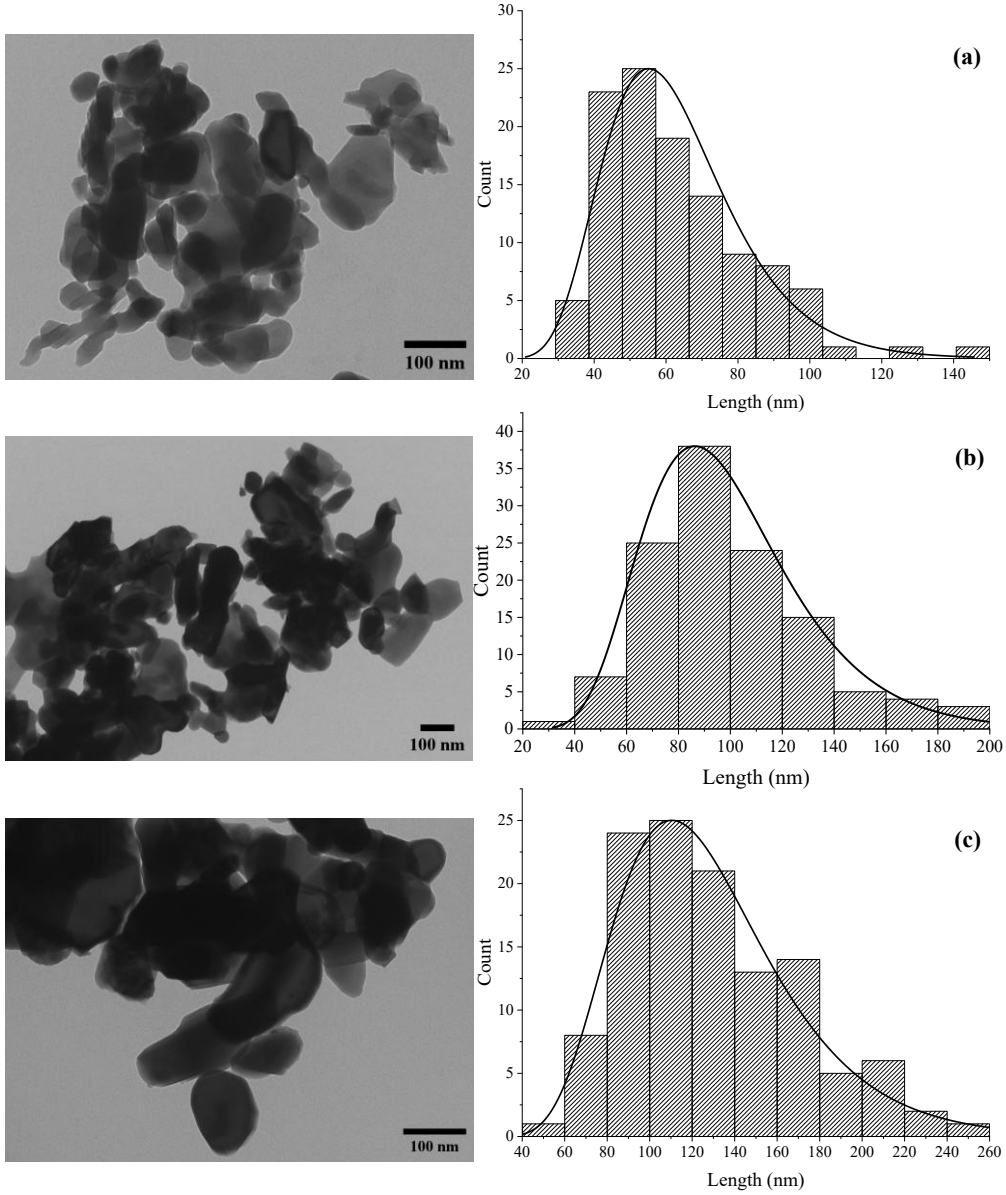


***Figure 2-2*** *TEM images and size distribution plots of SrM samples produced by LTSSR and different calcination temperature: (a) 775 °C, 3h; (b) 837 °C, 3h; (c) 900 °C, 3h.The histograms were estimated from over 100 particles and fitted to a lognormal function.*

## 2.2 Optimization of the washing stage through pH control

Attention was also paid to the pH of the water solution resulting from the washing stage. As reported by Kiani *et al.* [1], the amorphous paste, obtained from the reaction of metal chlorides precursors with NaOH to form metal hydroxides, is washed extensively with demineralized water until chloride ions are removed. Indeed, chloride ions can be potentially retained during the conversion of metal oxides precursors, hindering the correct formation of the hexaferrite phase [8].

As a further indication to the chloride assay, the pH in the washing solution was controlled to establish a relationship with the resultant product. Therefore, in this series of trials, the molar ratios between the reagents were adopted in order to obtain a single-phase product with respect to the reference ($Fe^{3+}$/ $Sr^{2+}$ = 10 and $Na^{+}$/ $Sr^{2+}$ = 45), washed until the chloride assay was negative, and the pH of the washing solution was kept under investigation, from neutral pH (around 6/7 of DM water) to basic (above 8). After that, the product was then dried and calcined at 775°C for 3 hours. The samples were named SrM_LTSSR_x, where the x indicates the pH found in the washing solution.

In **Figure 2-3** a comparison of the PXRD diffractograms of the obtained samples is shown. No dramatic change in the diffractograms was noticed, confirming that the main phase was the strontium hexaferrite, but moving towards basic pH some other low-intense peaks, at 2θ = 33.2° and 2θ = 32.8° not related to the main phase appeared. The first one was assigned to the presence of hematite (α-$Fe_2O_3$), while the other was more difficult to attribute, as it can be proper of cubic/orthorhombic mixed oxides $Sr_xFe_yO_z$ / $SrFe_xO_y$, which share really close diffraction peaks positioning in that frame. Even if not

in massive amounts, the presence of these additional phases could be related to an inhomogeneity in the quantities of precursors before the calcination step arising from incomplete mixing.

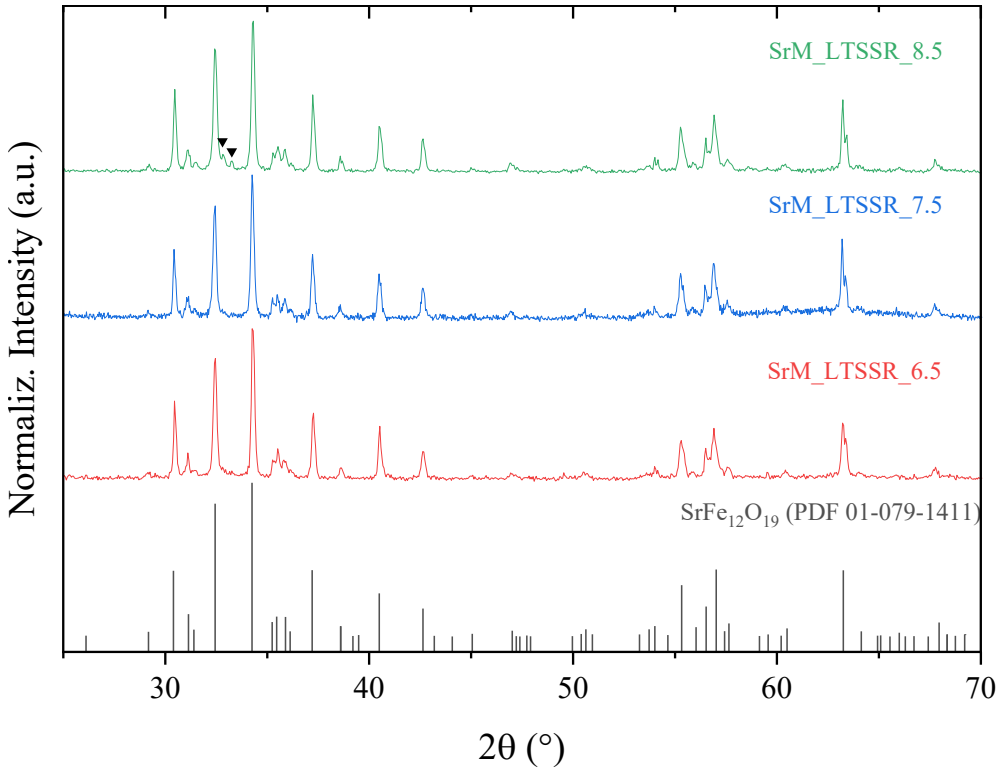


***Figure 2-3*** *PXRD diffraction patterns of SrM samples produced by LTSSR with different pH in washing solution. All samples were calcined at 775°C for 3 hours.*

The formation of these other phases can be attributed to the variation of the ratio between metal precursors before calcination: the SrO–$Fe_2O_3$ system in solid state reactions is depicted by a very narrow compositional range in which the single M-phase can form [2,3,9]. Accordingly, the presence of the second additional phase, besides hematite, can be justified by the shift of the relative amounts of precursors, necessary to develop single-phase SrM. The excess of iron can lead to iron oxides such as hematite, while an iron deficiency can result into Sr-rich phases [10,11]. However, since the two metal hydroxides are

soluble in water in different proportions [12], as shown by the corresponding solubility constant products:

- Iron (III) hydroxide: $K_{ps} = 2.79 \cdot 10^{-39}$
- Strontium (II) hydroxide: $K_{ps} = 3.2 \cdot 10^{-4}$

Therefore, this washing stage can be critical to have high control on the precursor molar ratio before calcination.

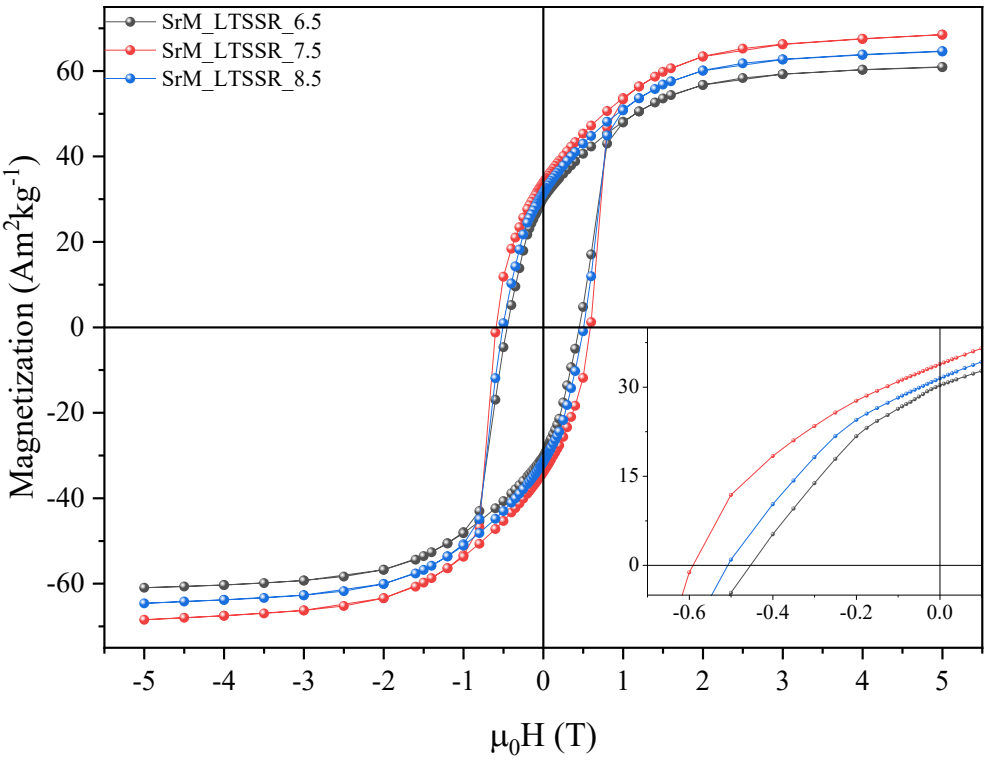


***Figure 2-4*** *Hysteresis loop at 300 K of SrM samples produced by LTSSR with different pH in the washing solution. All samples were calcined at 775°C for 3 hours.*

The magnetic properties, which are summarized in **Table 2-2**, were estimated from the hysteresis loops measured at 300 K (**Figure 2-4**). For the sample SrM_LTSSR_6.5 $M_S$, $M_R$ and $H_C$ were the lowest in the series. Conversely, the best features (higher $M_S$, $M_R$ and $H_C$) were found at slightly basic pH, in the sample SrM_LTSSR_7.5. The most relevant variation was found in the

coercivity value, while the saturation magnetization and especially the remanent magnetization seemed to be less affected. At higher pH (SrM_LTSSR_8.5) lower values in coercivity and magnetization with respect to the sample SrM_LTSSR_7.5 were observed, probably due to the presence of the secondary phases.

***Table 2-2*** *Magnetic parameters estimated from hysteresis at 300K of SrM samples produced by LTSSR with different pH in the washing solution.*

| | $M_s$ ($Am^2kg^{-1}$) | $M_r$ ($Am^2kg^{-1}$) | $M_r/M_s$ | $\mu_0H_c$ (T) |
|---|---|---|---|---|
| **SrM_LTSSR_6.5** | 61 | 30 | 0.50 | 0.45 |
| **SrM_LTSSR_7.5** | 69 | 34 | 0.49 | 0.59 |
| **SrM_LTSSR_8.5** | 65 | 32 | 0.49 | 0.51 |

Based on these results it was decided to stop the washing stage pH = 7.5 of the draining solution is reached.

## 2.3 The impact of metal ratios on the development of additional phases

Another factor that has been identified as having a major influence in the process is the relative proportions between the metals [1], particularly concerning the formation of spurious phases. In almost all the synthesis route developed so far for SrM, including conventional ceramic process, the iron to strontium molar ratio must be controlled in order to obtain a single-phase product [13]. In this synthesis, however, the sodium to strontium ratio must be also taken into consideration, since sodium hydroxide plays a decisive in converting the starting materials into the appropriate precursors. Thus, to identify the optimal

ratios to obtain a single-phase product and to determine which parameter has the greatest influence on the formation of secondary phases, small deviations from the ratios used in the reference reaction [1] were investigated: considering the molar ratios $Fe^{3+}/Sr^{2+}$ = 10 and $Na^{+}/Sr^{2+}$ = 45 as the starting point, a stoichiometric molar ratio $Fe^{3+}/Sr^{2+}$ = 12 was tested, then gradually reduced to discourage the hematite formation, which has been reported to be the main contaminant detected. Additionally, an increase in the $Na^{+}/Sr^{2+}$ ratio was explored to get smaller particle size and to assess the influence of sodium hydroxide on the process. During these experiments, the other processing parameters were kept constant at pH of the washing solution = 7.5 and calcination temperature at 775 °C for 3 hours. The conditions used to prepare the samples are summarized in **Table 2-3**. For clarity, the samples were named as SrM_LTSSR_Rx/y, indicating as x the $Fe^{3+}/Sr^{2+}$ ratio and y as the $Na^{+}/Sr^{2+}$ ratio. After the calcination, the samples were characterized by PXRD.

***Table 2-3*** *Summary of synthesis parameters for SrM samples produced by LTSSR with different metal ratios.*

| **Sample** | **$Fe^{3+}/Sr^{2+}$** | **$Na^{+}/Sr^{2+}$** | **pH** | **Calcination** |
|---|---|---|---|---|
| **SrM_LTSSR_R12/45** | 12 | 45 | 7.5 | 3h, 775°C |
| **SrM_LTSSR_R10/45** | 10 | 45 | 7.5 | 3h, 775°C |
| **SrM_LTSSR_R10/55** | 10 | 55 | 7.5 | 3h, 775°C |
| **SrM_LTSSR_R9/45** | 9 | 45 | 7.5 | 3h, 775°C |
| **SrM_LTSSR_R9.5/45** | 9.5 | 45 | 7.5 | 3h, 775°C |

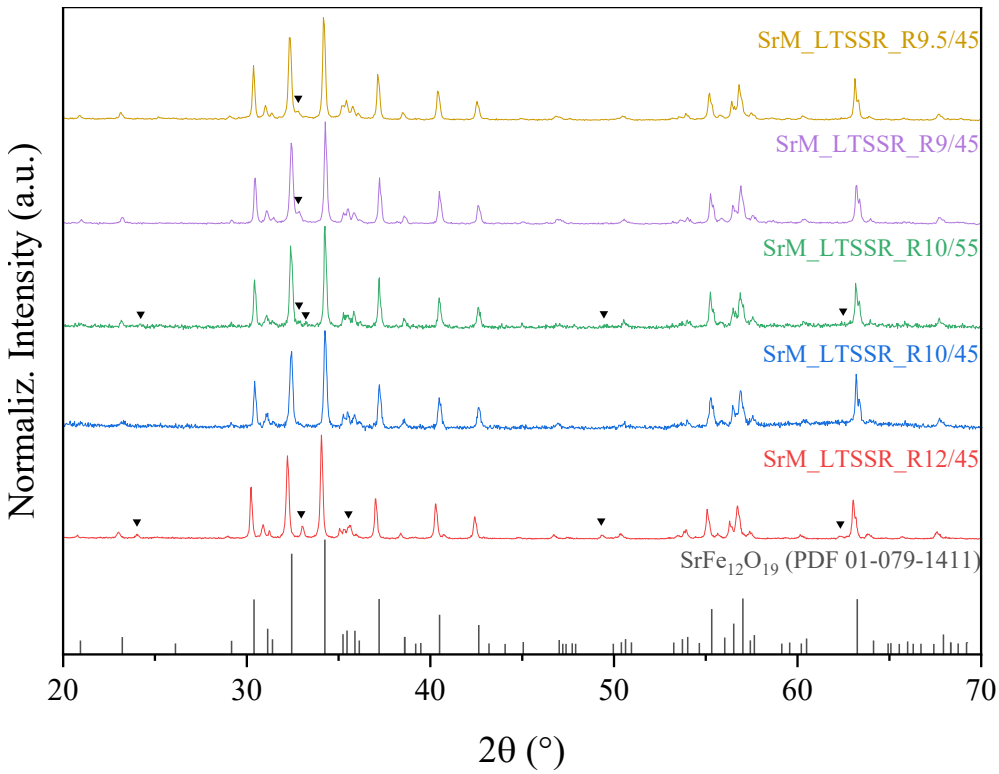


***Figure 2-5*** *PXRD diffraction patterns of SrM samples produced by LTSSR with different metal ratios.*

As it can be seen in the resulting powder diffractograms (**Figure 2-5**), even in this case, the main phase is still attributable to the Sr-hexaferrite. Nevertheless, when deviations from the molar ratios R10/45 were made, some additional peaks appeared. The most evident, recognizable from its high intense diffraction peak at 2θ = 33.2° accompanied by lower intensity peaks at 2θ = 24.2°, 35.6°, 49.5° and 62.5°, was the presence of about 8% of hematite (α-$Fe_2O_3$) when the molar ratio was shifted towards iron (R12/45). Even increasing the quantity of sodium hydroxide (sample R10/55) a low quantity of α-$Fe_2O_3$, noticeable by the same more intense diffraction peak at 33.2°. Moreover, increasing the sodium hydroxide content another small peak, placed at 2θ = 32.8°, was detected. This diffraction peak could correspond to a cubic/orthorhombic mixed oxides $SrFe_xO_y$ / $Sr_xFe_yO_z$. On the other hand,

lowering the $Fe^{3+}/Sr^{2+}$ ratio from 10 to 9 (R9/45), only this latter additional phase ($2\theta = 32.8°$) was detected, with no evident presence of hematite. This secondary phase appeared also for $Fe^{3+}/Sr^{2+} = 9.5$ (R9.5/45), and the intensity enhancement of the diffraction peak appeared to be proportional to the increase in strontium molar ratio.

The formation of these mixed oxides can be possibly ascribed to a variation of the molar ratio between iron and strontium precursors during the washing step [2,10]. Thereby, even in this case the washing process can have an influence in further changing the final proportion of the precursors before the calcination: starting with a stoichiometric molar ratio of $Fe^{3+}/ Sr^{2+} = 12$ can leave an excess of iron in the system, which, due to its minor water solubility, can lead to hematite formation. Instead with a larger amount of strontium, as in the case of $Fe^{3+}/ Sr^{2+} = 9$ and 9.5, strontium-rich oxides can form as secondary phases [11]. So, to limit the appearance of additional phases, the selected molar ratios between the metals were $Fe^{3+}/ Sr^{2+} = 10$ and $Na^{+}/ Sr^{2+} = 45$.

As a further step an assessment of the reproducibility of the synthesis was performed by preparing 3 samples using the best parameters identified ($Fe^{3+}/ Sr^{2+} = 10$ and $Na^{+}/ Sr^{2+} = 45$, pH = 7.5 for the washing solution, and calcination temperature at 775 °C for 3 hours).

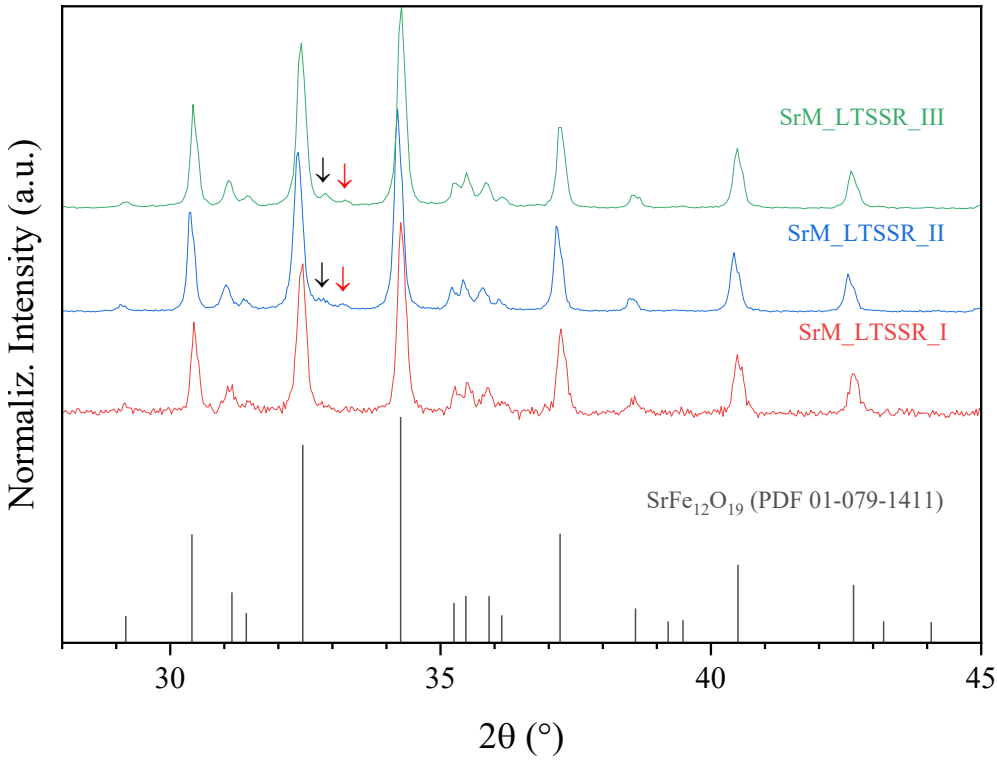


***Figure 2-6*** *PXRD diffraction patterns (close-up) of SrM samples produced LTSSR and synthesized using the same parameters: $Fe^{3+}$/ $Sr^{2+}$ = 10; $Na^{+}$/ $Sr^{2+}$ = 45; pH = 7.5 and calcination at 775°C, 3h. The arrows indicate the peaks of additional phases: red arrow for hematite, black arrow for mixed Sr-Fe oxides.*

The resultant PXRD diffractograms showed patterns confirming the prevalent presence of the $SrFe_{12}O_{19}$ phase in all the samples. The in-depth analysis of the region between the SrM diffraction peaks corresponding to (107) and (114) planes (**Figure 2-6**), however, revealed the main peaks of secondary phases. These peaks are very weak and dominate in intensity by the peak of SrM at 32.4°. Nevertheless, a minimal presence of mixed Sr-Fe oxides was also detected.

Overall, the structural and dimensional features (**Table 2-4**) of each sample were consistent, including the mean size and relative standard deviation

obtained by TEM analysis, as well as the structural parameters derived from the refinement of diffractograms.

***Table 2-4*** *Crystallite size and cell parameters (PXRD), mean size and standard deviation (TEM) of SrM samples produced by LTSSR and synthesized using the following parameters:* $Fe^{3+}/Sr^{2+} = 10$; $Na^{+}/Sr^{2+} = 45$; *pH = 7.5 and calcination 775°C, 3h.*

| Sample | Cry.size (nm) | a (Å) | c (Å) | Mean Size (nm) | Std.Dev. (nm) |
|---|---|---|---|---|---|
| **SrM_LTSSR _I** | 88(3) | 5.8845(4) | 23.056(2) | 77 | 22 |
| **SrM_LTSSR _II** | 94(1) | 5.8856(2) | 23.059 (1) | 78 | 27 |
| **SrM_LTSSR _III** | 92(1) | 5.8860(2) | 23.061(1) | 79 | 30 |

Also the magnetic properties were almost similar as shown by the hysteresis loops recorded at 300K shown in **Figure 2-7** (the main parameters of the loop are summarized in **Table 2-5**). One sample displayed slightly higher saturation magnetization while a decrease of the coercive force with Sr-content was observed.

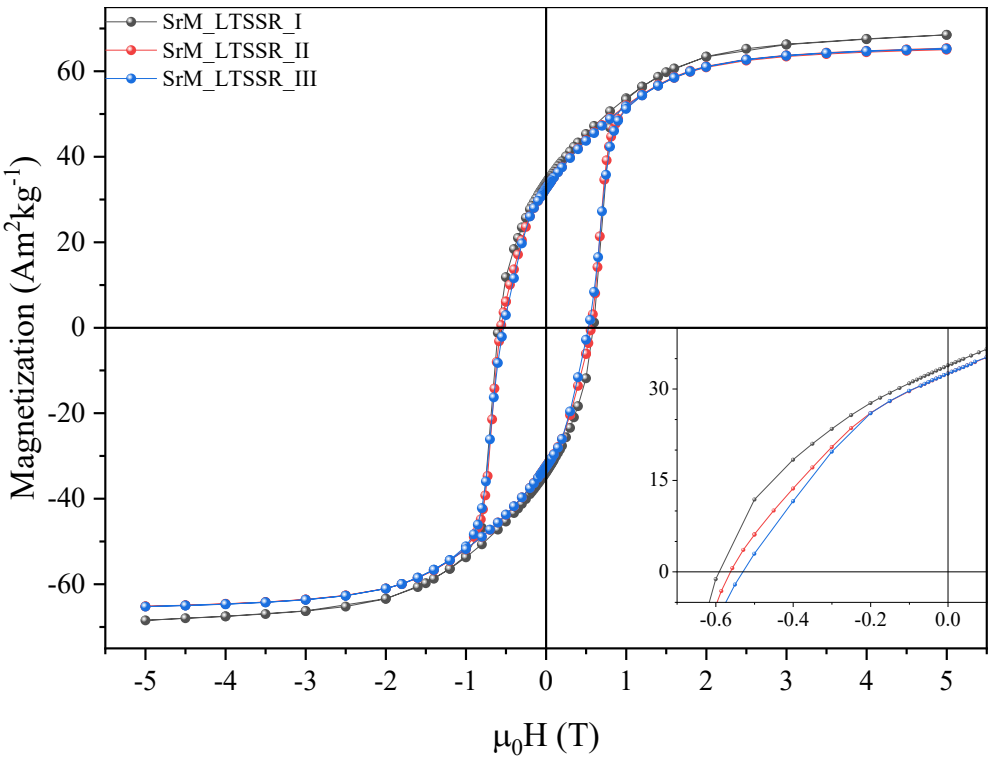


***Figure 2-7*** *Hysteresis loops at 300K of SrM samples synthesized using the same parameters: $Fe^{3+}/Sr^{2+}$ = 10; $Na^{+}/Sr^{2+}$ = 45; pH = 7.5 and calcination 775°C, 3h.*

The small presence of additional phases, especially the Sr-Fe mixed oxide, can explain the observed differences in the magnetic behavior. Hematite can affect magnetization, due to its antiferromagnetic nature [14]. Conversely, coercivity is the property most sensitive to variation in the microstructure, and it is strictly related to the magnetocrystalline anisotropy of the system [15,16]. The presence of a secondary Sr-rich phase can be responsible for the decrease in coercivity. This hypothesis was confirmed by ICP analysis which highlighted a small increase in strontium content.

***Table 2-5*** *Magnetic values obtained from hysteresis at 300K for SrM samples synthesized using the same parameters: $Fe^{3+}/Sr^{2+} = 10$; $Na^{+}/Sr^{2+} = 45$; pH = 7.5 and calcination 775°C, 3h.*

| Sample | $M_s$ ($Am^2kg^{-1}$) | $M_r$ ($Am^2kg^{-1}$) | $M_r/M_s$ | $\mu_0 H_c$ (T) |
|---|---|---|---|---|
| **SrM_LTSSR_I** | 69 | 34 | 0.49 | 0.59 |
| **SrM_LTSSR _II** | 65 | 33 | 0.50 | 0.56 |
| **SrM_LTSSR _III** | 65 | 33 | 0.50 | 0.53 |

# 2.4 An alternative optimized route: Modified Solid State Reaction (MSSR)

To optimize the synthesis process, a slight modification in the procedure was explored, based on conducting the washing step after the calcination step. This decision was mainly driven by two factors. The first was to prevent the premature loss of strontium hydroxide as observed during washing, thereby ensuring the appropriate precursor ratio in the mixed amorphous paste before calcination. The second was to leverage the NaCl formed after mixing the chlorides with sodium hydroxide to act as a matrix, analogous to the "molten salt" method, which limits particle growth and aggregation [17–20]. As the melting point of NaCl is 801°C [21], the matrix is assumed to be in a solid state when the amorphous mixture of hydroxides is dried, and even throughout the calcination step. Furthermore, such modification improved the feasibility of the reaction: the thick paste obtained in the mortar, indeed, can be directly transferred to dry, avoiding the long time usually required to drain the water through the filter paper and Büchner funnel. Moreover, the washing process is performed on a calcined powder which is more manageable than the wet precursor slurry and facilitates the more straightforward execution of additional assays (e.g. pH measurement, chloride assay with $AgNO_3/HNO_3$).

Considering the formation of strontium ferrite occurs according to the following the equation **(2-1)**:

$$12FeCl_3 + SrCl_2 \rightarrow 12Fe(OH)_3 + Sr(OH)_2 + 38NaCl \xrightarrow{\Delta}$$
$$SrFe_{12}O_{19} + 16H_2O \uparrow + 38NaCl$$

***(2-1)***

Four samples were prepared by:

- maintaining the stoichiometric molar ratio between iron and strontium of the hexaferrite, $Fe^{3+}/Sr^{2+}$ = 12, with sodium hydroxide also in stoichiometric proportion ($Na^{+}/Sr^{2+}$ = 38);
- decreasing the molar ratio $Fe^{3+}/Sr^{2+}$ = 10, while maintaining stoichiometric sodium hydroxide ($Na^{+}/Sr^{2+}$ = 32);
- $Fe^{3+}/Sr^{2+}$ = 12 but with an excess of sodium hydroxide ($Na^{+}/Sr^{2+}$ = 45);
- $Fe^{3+}/Sr^{2+}$ = 10 and $Na^{+}/Sr^{2+}$ = 45.

The reagents were mixed in the mortar, dried, and directly subject to thermal treatment at 775 °C for 3 hours. The calcination was conducted at 775°C for 3 hours. After the calcination, the resultant powder was washed multiple times with DM water to remove NaCl and eventual excess of not reacted reagents and then dried at 80°C. The efficacy of NaCl washing was monitored by the means of chloride assay ($AgNO_3/HNO_3$), and, assuming the complete reaction of the initial oxo-hydroxides, a neutral pH was targeted, without the concern of any precursor drainage. For clarity, the samples were named SrM_MSSR_Rx/y, where x represents the $Fe^{3+}/Sr^{2+}$ ratio and y the $Na^{+}/Sr^{2+}$ ratio.

## 2.4.1 MSSR - Stoichiometric sodium hydroxide

The ICP analysis of the two samples prepared using a stoichiometric amount of NaOH revealed an elemental composition close to the expected one ($Sr_{1.10}Fe_{11.90}O_{19}$ for SrM_MSSR_R12/38 and $SrFe_{12}O_{19}$ for SrM_MSSR_10/32). Moreover, the PXRD diffractograms (**Figure 2-8**) revealed a single-phase product in both samples, regardless of the variation in molar ratio between iron and strontium. All the observed sharp peaks, indeed, can be attributed to the hexagonal phase $SrFe_{12}O_{19}$, with a complete absence of any detectable secondary phases.

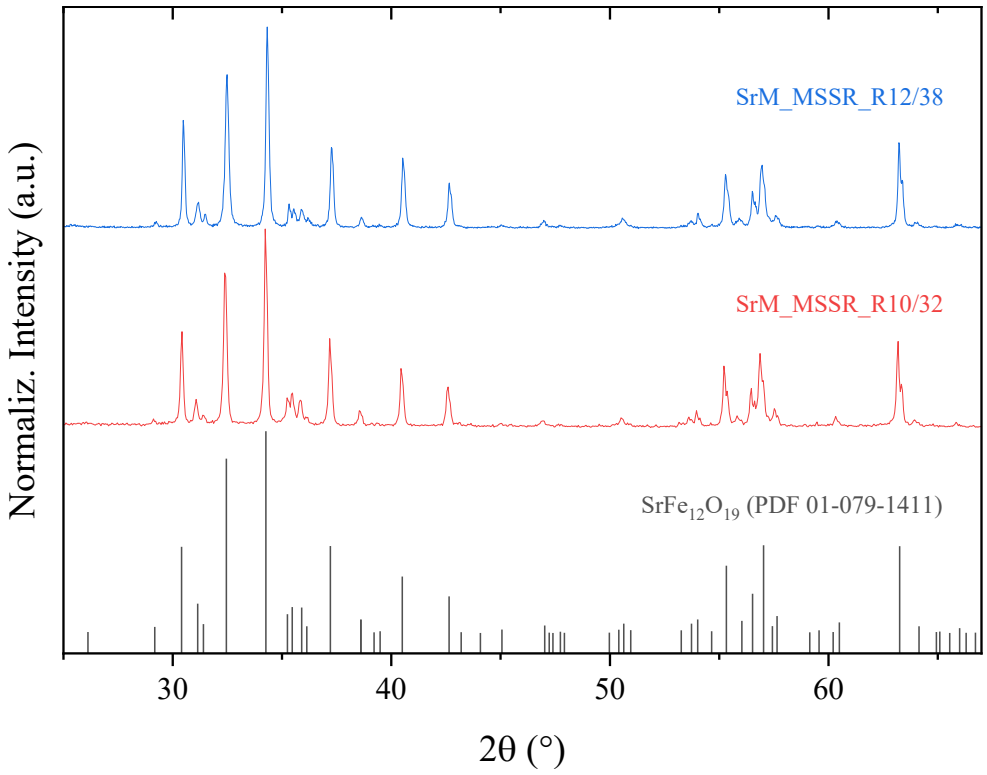


***Figure 2-8*** *PXRD diffractograms of SrM samples produced by MSSR with stoichiometric NaOH.*

***Table 2-6*** *Crystallite size and cell parameters (PXRD), mean size and standard deviation (TEM) of SrM samples produced by MSSR with stoichiometric NaOH.*

| **Sample** | **Cry.size (nm)** | **a (Å)** | **c (Å)** | **Mean Size (nm)** | **Std.Dev. (nm)** |
|---|---|---|---|---|---|
| **SrM_MSSR_ R12/38** | 122(3) | 5.8854(2) | 23.055(1) | 112 | 48 |
| **SrM_MSSR_ R10/32** | 99(1) | 5.8883(2) | 23.067(1) | 72 | 31 |

The structural parameters estimated from the refinement of the PXRD diffractograms (**Table 2-6**) showed SrM_MSSR_R12/38 has bigger crystallite size and smaller lattice parameters. TEM images (**Figure 2-8**) indicated this sample has average particle size over 100 nm, while the molar ratio $Fe^{3+}/Sr^{2+}$ = 10 brought to a mean size below that limit. In both cases, the mean particle size and standard deviation from TEM nicely agree with the crystallite size from XRD. This fact suggested that a significant portion of the particles can be predominantly single-crystals. Moreover, the TEM images suggested well crystallized platelets, with a much smaller number of interparticle aggregates with respect to LTSSR synthesis.

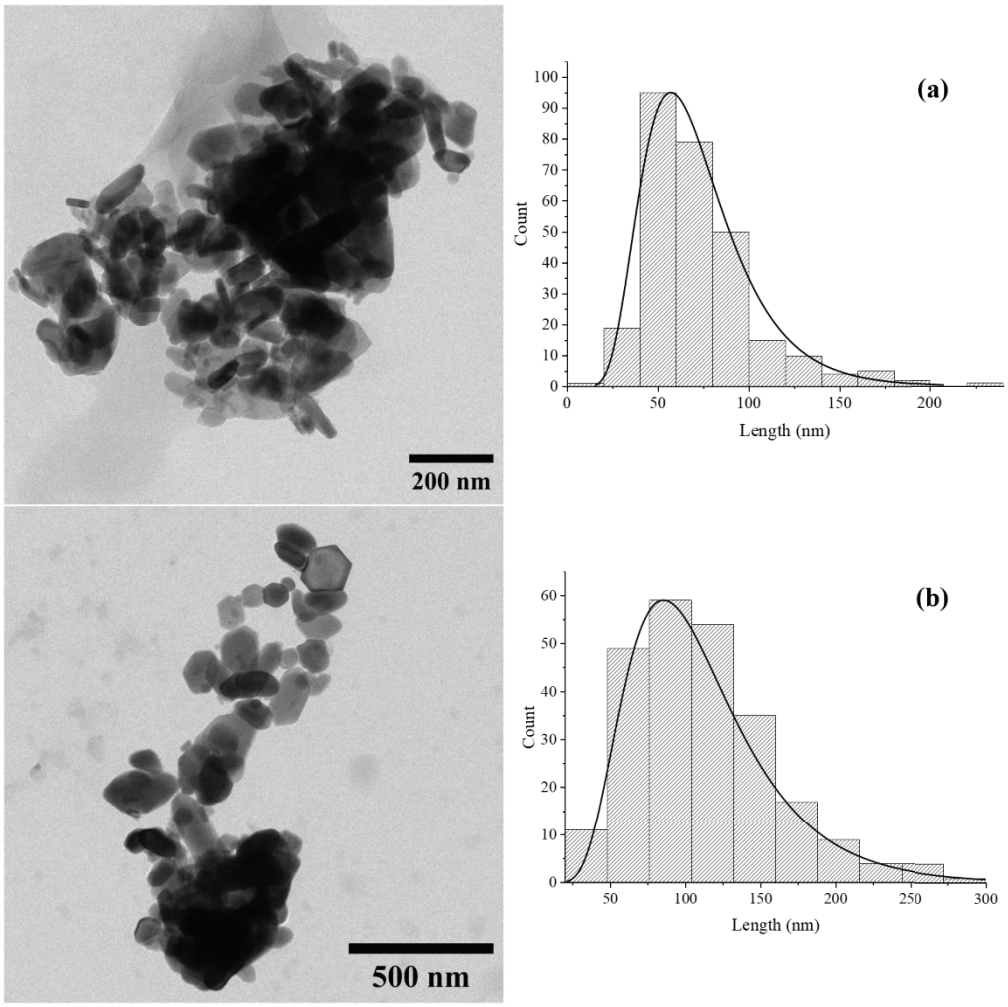


***Figure 2-9*** *TEM images and corresponding size distribution histogram of SrM samples produced by MSSR with stoichiometric NaOH: (a) $Fe^{3+}/Sr^{2+}$ = 10 and $Na^{+}/Sr^{2+}$ = 32; (b) $Fe^{3+}/Sr^{2+}$ = 12 and $Na^{+}/Sr^{2+}$ = 38. The histograms, fitted to a lognormal function, were estimated from: (a) over 100 particles; (b) over 200 particles.*

The hysteresis loops at 300 K (**Figure 2-10**) were collected by VSM, and the resultant magnetic properties are resumed in **Table 2-7**.

***Table 2-7*** *Saturation magnetization, remanence and coercivity obtained from the hysteresis loops at 300K of SrM samples produced by MSSR with stoichiometric NaOH.*

| Sample | $M_s$ ($Am^2kg^{-1}$) | $M_r$ ($Am^2kg^{-1}$) | $M_r/M_s$ | $\mu_0H_c$ (T) |
|---|---|---|---|---|
| **SrM_MSSR_R12/38** | 70 | 35 | 0.5 | 0.61 |
| **SrM_MSSR_R10/32** | 66 | 33 | 0.5 | 0.60 |

Even in this case, some noticeable differences were detected: the first was the increment of the coercivity of both SrM samples, with respect to the samples previously discussed [1]. Then, the saturation magnetization and remanence of SrM_MSSR_R12/32 was the highest among all the tests performed, despite of the size above 100 nm.

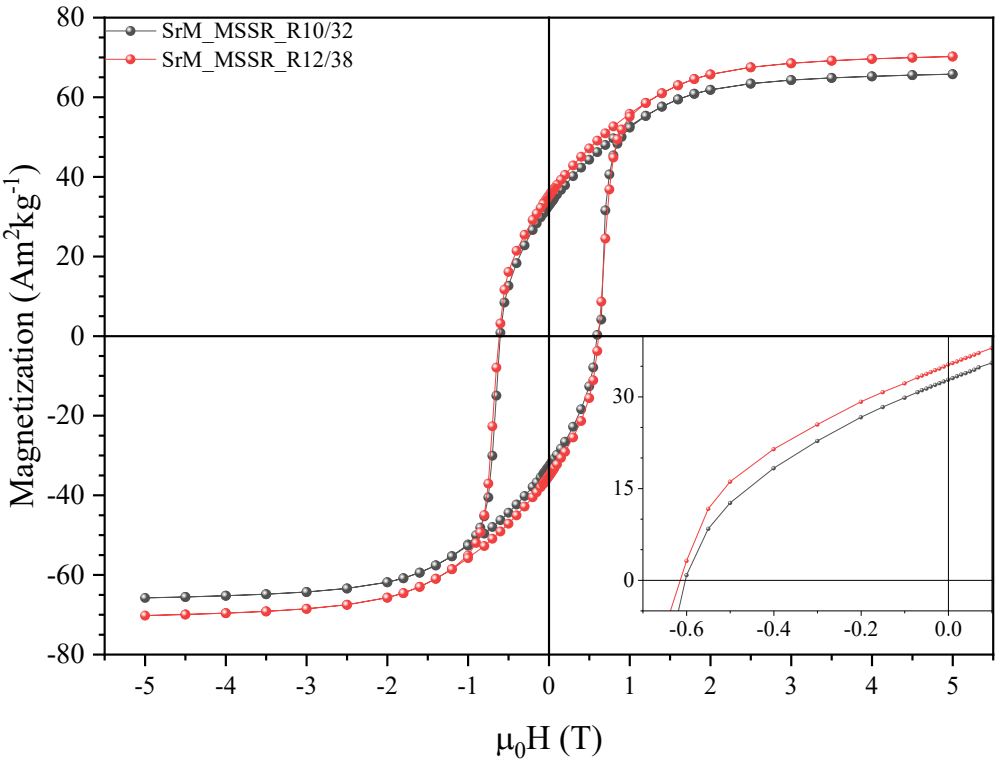


***Figure 2-10*** *Hysteresis loops at 300K of SrM samples produced by MSSR with stoichiometric NaOH.*

## 2.4.2 MSSR – Excess of sodium hydroxide

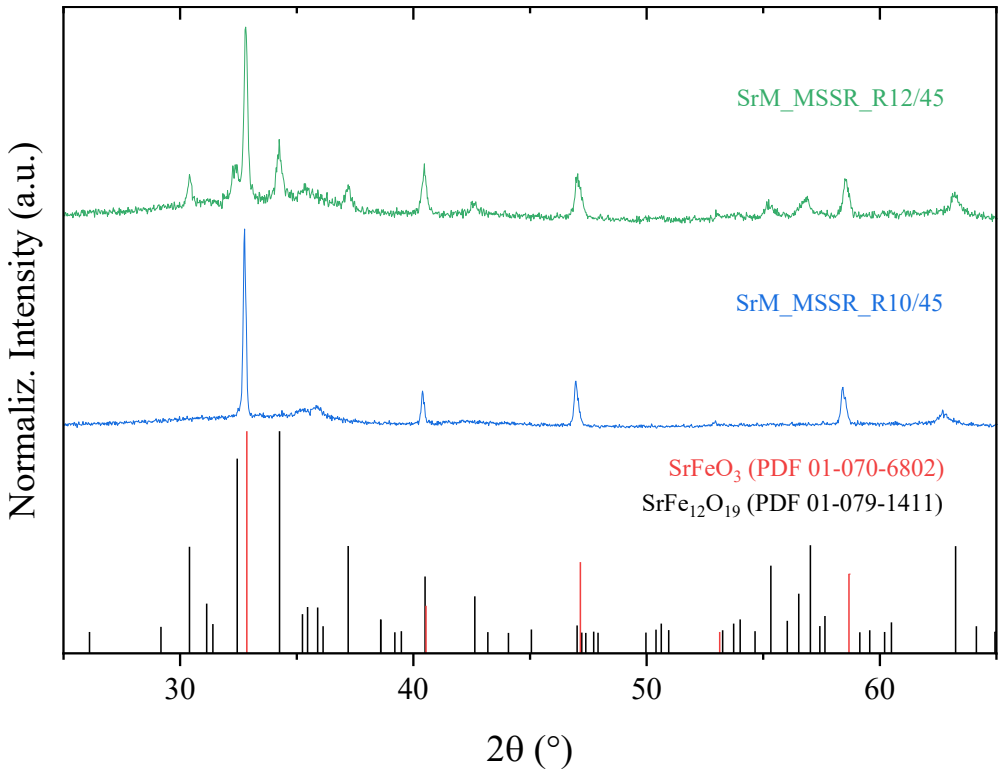


***Figure 2-11*** *PXRD diffractograms of SrM samples produced by MSSR in excess of NaOH. The samples were named SrM_Rx/y, indicating as x the $Fe^{3+}/Sr^{2+}$ ratio and y as the $Na^{+}/Sr^{2+}$ ratio.*

The PXRD diffractograms collected for SrM_MSSR_R12/45 and SrM_MSSR_R10/45 (**Figure 2-11**) showed patterns completely different from previous results. In the case of $Fe^{3+}/Sr^{2+}$ = 12, the peaks corresponding to the $SrFe_{12}O_{19}$ phase were broad and with a low intensity, indicating the low crystallinity of the prepared materials. Moreover, the pattern is dominated by the sharp and more intense peaks attributable to the $SrFeO_3$ phase. For SrM_MSSR_R10/45 only the latter phase can be discerned. It can be argued that NaOH during the calcination process can affect the stability of the precursors (i.e. $MO{\cdot}Fe_2O_3$, where M stands for the divalent cation), inducing

their decomposition, and consequently hindering the sintering process. Otherwise, NaOH can favor the formation of stable and soluble alkali hydroxometalates, which behave differently depending on the concentration and temperature conditions [2,22].

## 2.5 Conclusions

In this chapter, an in-depth investigation into the use of LTSSR method for the synthesis of SrM nanoparticles was conducted. The primary objective was to develop a cost-effective, scalable, and reproducible route for producing phase-pure SrM with desirable magnetic properties, appropriate particle size and which can be oriented by applying an external magnetic field. A temperature of 775 °C was identified as suitable for producing nanoparticles with a mean size below 100 nm, avoiding the significant grain growth observed at higher temperatures (837 °C and 900 °C) while still ensuring full conversion to the SrM phase. Interestingly, this temperature is far below those used in the conventional ceramic processes. The washing stage, and the corresponding pH of the washing solution, strongly impacts the characteristics of the final product. Washing to a neutral pH resulted in poor magnetic performance, while washing to a more basic pH led to the formation of impurity phases. A slightly basic pH of 7.5 was determined to be a good endpoint to obtain valuable magnetic properties ($M_s$ = 69 $Am^2kg^{-1}$, $\mu_0Hc$ = 0.59 T). Even the precursor molar ratio is a decisive factor: deviations from molar ratios $Fe^{3+}/Sr^{2+}$ = 10 and $Na^{+}/Sr^{2+}$ = 45 resulted in the formation of secondary phases (hematite in Fe-rich conditions, Sr-rich oxides in Sr-rich conditions). Despite optimizing these parameters, the LTSSR method suffered from poor reproducibility. Samples produced under identical conditions showed consistent structural properties but significant variations in the magnetic properties, particularly coercivity. This was attributed to the barely controllable leaching of water-soluble

strontium hydroxide during the washing step, which altered the final precursor stoichiometry. However, the major limitations of this technique consisted in the synthesis of individual nanoparticles with high crystallinity, single-phased, and size below 100 nm.

The main conclusion derived from these trials is that the pre-calcination washing step is the major weakness of the LTSSR method. To address this, a Modified Solid-State Reaction (MSSR) was proposed, where the washing step to remove NaCl by-product is performed after the calcination. This procedural change proved to be highly effective on retaining all precursors during the heat treatment, thus ensuring a correct stoichiometry. This approach successfully yielded a single-phase SrM product, completely free of additional phases that were consistently detected in the LTSSR samples. The samples produced via MSSR method exhibited enhanced magnetic properties, including a remarkable coercivity (up to 0.61 T) and the highest saturation magnetization (up to 70 $Am^2kg^{-1}$) achieved in this series of trials. The NaCl by-product acts as a solid-state matrix during calcination. This matrix can help to limit particle agglomeration and their growth, contributing to the formation of well-crystallized nanoparticles. Even in these conditions, a calcination temperature of 775 °C for 3 hours remains the best condition for achieving nanoscale particles. Based on this investigation, the MSSR method, using stoichiometric quantities of reagents, is concluded to be an advantageous synthesis route. A stoichiometric molar ratio of $Fe^{3+}/Sr^{2+} = 12$ and $Na^{+}/Sr^{2+} = 38$ led to a product with excellent magnetic properties, while a slightly Sr-rich molar ratio of $Fe^{3+}/Sr^{2+} = 10$ yielded smaller nanoparticles. Conversely, an excess of NaOH is detrimental, leading to the formation of other phases and amorphous material. Further investigations will focus on the reproducibility issue to ensure consistent results with the ones reported here.

# References


(1) Kiani, E.; Rozatian, A. S. H.; Yousefi, M. H. Synthesis and Characterization of SrFe12O19 Nanoparticles Produced by a Low-Temperature Solid-State Reaction Method. *Journal of Materials Science: Materials in Electronics* **2013**, *24* (7), 2485–2492. https://doi.org/10.1007/S10854-013-1122-5/FIGURES/9.

(2) Stäblein, H. Hard Ferrites and Plastoferrites. In *Handbook of Ferromagnetic Materials*; Elsevier, 1982; Vol. 3, pp 441–602. https://doi.org/10.1016/S1574-9304(05)80093-8.

(3) Pullar, R. C. Hexagonal Ferrites: A Review of the Synthesis, Properties and Applications of Hexaferrite Ceramics. *Prog Mater Sci* **2012**, *57* (7), 1191–1334. https://doi.org/10.1016/j.pmatsci.2012.04.001.

(4) Smit, J.; Wijn, H. P. J.; Luton, G. E. *Ferrites : Physical Properties of Ferrimagnetic Oxides in Relation to Their Technical Applications*; Philips' Technical Library, Ed.; 1959.

(5) Granados-Miralles, C.; Jenuš, P. On the Potential of Hard Ferrite Ceramics for Permanent Magnet Technology—a Review on Sintering Strategies. *J Phys D Appl Phys* **2021**, *54* (30), 303001. https://doi.org/10.1088/1361-6463/ABFAD4.

(6) Rahman, M. L.; Rahman, S.; Biswas, B.; Ahmed, M. F.; Rahman, M.; Sharmin, N. Investigation of Structural, Morphological and Magnetic Properties of Nanostructured Strontium Hexaferrite through Co-Precipitation Technique: Impacts of Annealing Temperature and Fe/Sr Ratio. *Heliyon* **2023**, *9* (3), e14532. https://doi.org/10.1016/J.HELIYON.2023.E14532.

(7) Bordia, R. K.; Camacho-Montes, H. Sintering: Fundamentals and Practice. In *Ceramics and Composites Processing Methods*; Wiley, 2012; pp 1–42. https://doi.org/10.1002/9781118176665.ch1.

(8) Pullar, R. C.; Taylor, M. D.; Bhattacharya, A. K. Halide Removal from BaM (BaFe 12 O 19 ) and SrM (SrFe 12 O 19 ) Ferrite Fibers via a Steaming Process. **2001**.

(9) Du, Y.; Gao, H.; Liu, X.; Wang, J.; Xu, P.; Han, X. Solvent-Free Synthesis of Hexagonal Barium Ferrite (BaFe12O 19) Particles. *J Mater Sci* **2010**, *45* (9), 2442–2448. https://doi.org/10.1007/S10853-010-4215-Z/FIGURES/7.

(10) Langhof, N.; Seifert, D.; Göbbels, M.; Töpfer, J. Reinvestigation of the Fe-Rich Part of the Pseudo-Binary System SrO–Fe2O3. *J Solid State Chem* **2009**, *182* (9), 2409–2416. https://doi.org/10.1016/j.jssc.2009.05.039.

(11) Kagotani, T.; Sugimoto, S.; M Okada; M Homma. Magnetic Properties of SrO-NFe2O3(0.5< N< 6.0) and Phase Diagram in SrO-Fe2O3 System. *IEEE Trans Magn* **1995**.

(12) Lide, D. CRC Handbook of Chemistry and Physics. **2004**.

(13) Verma, A.; Pandeyb, P.; Sharma, P. Strontium Ferrite Permanent Magnet-An Overview. *Indian Journal of Engineering & Materials Sciences* **2000**, *7*, 364–369.

(14) Coey, J. M. D.; Stuart, S. S. *Handbook of Magnetism and Magnetic Materials: Volume 1,2*; Springer International Publishing, 2021; Vol. 1–2. https://doi.org/10.1007/978-3-030-63210-6/COVER.

(15) Zijlstra, H. Permanent Magnets; Theory. In *Handbook of Ferromagnetic Materials*; Elsevier, 1982; Vol. 3, pp 37–105. https://doi.org/10.1016/S1574-9304(05)80088-4.

(16) de Julián Fernández, C.; Sangregorio, C.; de la Figuera, J.; Belec, B.; Makovec, D.; Quesada, A. Progress and Prospects of Hard Hexaferrites for Permanent Magnet Applications. *J Phys D Appl Phys* **2021**, *54* (15), 153001. https://doi.org/10.1088/1361-6463/ABD272.

(17) Arendt, R. H. The Molten Salt Synthesis of Single Magnetic Domain BaFe12O19 and SrFe12O19 Crystals. *J Solid State Chem* **1973**, *8* (4), 339–347. https://doi.org/10.1016/S0022-4596(73)80031-3.

(18) Liu, J. R.; Hong, R. Y.; Feng, W. G.; Badami, D.; Wang, Y. Q. Large-Scale Production of Strontium Ferrite by Molten-Salt-Assisted Coprecipitation. *Powder Technol* **2014**, *262*, 142–149. https://doi.org/10.1016/J.POWTEC.2014.04.076.

(19) Chin, T.-S.; Hsu, S. L.; Deng, M. C. Barium Ferrite Particulates Prepared by a Salt-Melt Method. *J Magn Magn Mater* **1993**, *120* (1–3), 64–68. https://doi.org/10.1016/0304-8853(93)91288-I.

(20) Guo, Z. B.; Ding, W. P.; Zhong, W.; Zhang, J. R.; Du, Y. W. Preparation and Magnetic Properties of SrFe12O19 Particles Prepared by the Salt-Melt Method. *J Magn Magn Mater* **1997**, *175* (3), 333–336. https://doi.org/10.1016/S0304-8853(97)00206-0.

(21) Patnaik, P. *Handbook of Inorganic Chemicals*; McGraw-Hill, 2003.

(22) Brauer, G. *Handbook of Preparative Inorganic Chemistry* ; 1965; Vol. 2.

# **Chapter 3 |** Synthesis of SrM nanoparticles by Modified Sol-Gel Synthesis (MSG)

In the previous chapter, the Low-Temperature solid state reaction method was investigated and optimized to synthesize SrM nanoparticles with an average size of ca. 100 nm. Nevertheless, a major limitation of this approach is the tendency of the nanoparticles to aggregate after the calcination step, which could hinder their application in the fabrication of an oriented bonded magnet.

Thus, in this thesis, another synthetic route was explored, that can be still suitable for industrial purposes, the *sol-gel* method. This technique is known to be effective for producing SrM nano-crystallites in the magnetic single-domain size range [1,2], with a narrow size distribution and very good magnetic properties, at relatively low calcination temperatures [3–5]. The key features and advantages of the *sol-gel* method include its energy efficiency, speed, low cost, and reproducibility, deriving from a relatively simple process with few synthesis steps[6,7]. However, a significant drawback, common to many other hexaferrite synthesis routes, is the high degree of particle agglomeration of resultant particles or, even sintering due to the elevated temperature needed for the calcination [4,8,9]. This can result in intergrown crystallites, rendering them unsuitable for alignment using pressure or applying a magnetic field. To address this, Sapoletova *et al*. [10] proposed a modified route that yielded plate-like, free-standing SrM crystallites with magnetic properties comparable to those prepared from conventional sol-gel methods. The method relies on the use of a NaCl matrix to prevent particle aggregation, an idea derived from

molten-salt reactions [11–14] or glass crystallization techniques, which instead employ $B_2O_3$ matrix [15–17].

In conventional sol-gel synthesis, the method typically involves the use of metal alkoxide solutions, which undergo hydrolysis and condensation-polymerization reactions to form a gel at room temperature. Subsequent heat treatment is necessary to remove volatile by-products to achieve the final crystalline state [18]. The modified sol-gel (MSG) synthesis, instead, generates a NaCl matrix in situ[19]. This derives directly from the reaction of metal chlorides with sodium carbonate in the precursor solution (*sol*) at 90 °C. Then, the free metal ions are coordinated through a citric acid solution which is subsequently dehydrated, forming a thick *gel*.

The MSG process here adopted involves two different heating treatments to yield the final product. The first one is at 450°C for one hour, which is a pre-calcination to burn off all the organic parts constituting the precursor gel [4,19–21]. The second one at 790°C (below the melting point of NaCl, 801 °C [28]) for another hour, instead, is the real calcination to crystallize the phase of interest, in this case SrM. The resulting product is washed once with $HNO_3$ 4 M and then several times with demineralized water, before finally being dried in an oven at 80°C.

Although some experimental works have been already reported in the literature about the MSG method, the way some synthesis parameters can influence the features of the resultant hexaferrite nanoparticles is still unclear. This, in this work we attempted to fill this gap by exploring the effect of the duration of the first pre-calcination step and of the temperature of the calcination step, the metal to salts molar ratio, and the amount of NaCl added to that already formed during the reaction. The synthesized nanoparticles were characterized by PXRD and TEM to detect additional phases and variations in size, ICP to

determine the effective stoichiometry, and VSM magnetometry to estimate the main magnetic properties.

## 3.1 The MSG synthesis for reduced agglomerates formation

Our initial synthesis trials were conducted considering the overall features of the SrM nanoparticles synthesized in previous work by Sapoletova *et al*. [10] and lately by Eikeland *et al.* [19] through this reaction. In these studies, they reported the synthesis of nanoparticles with a small number of agglomerates. This property was especially promising for future applications involving particle alignment to form anisotropic assemblies with improved remanence [22]. However, they obtained SrM particles with an average size larger than the one of our interest (below 100 nm). Thus, we tried to optimize this synthetic procedure with the aim of obtaining smaller SrM nanoparticles, with a very low degree of aggregation and good magnetic properties. Based on their considerations and other results in the literature, the following synthesis parameters were selected: a starting molar ratio $Fe^{3+}/Sr^{2+} = 9$ was chosen to mitigate the risk of hematite contamination found in a stoichiometric molar ratio of 12 [19,23,24]; the shortest time and lowest temperature for the calcination of the samples was sorted by a first step at 450°C for 1 h (pre-calcination) and a second one at 790°C for 1 h.

To detect the correct crystallographic phase and exclude the presence of other additional phases, a PXRD analysis was performed on the sample obtained after the thermal treatment and the appropriate washing procedure ($HNO_3$ 4 M and DM water). The resultant diffractogram are shown in **Figure 3-1**. The

diffraction patterns of the synthesized sample confirmed the presence of a single-phase corresponding to hexagonal $SrFe_{12}O_{19}$, and no other evident secondary phases were detected. Particularly, an enhancement in intensity of the diffraction plane (110) along the c-axis of the platelet was noticeable. To assess the consistency of the formed crystallographic phase, multiple experimental runs were performed to overcome the reproducibility issue encountered in the solid-state synthesis. From Pawley refinement of the diffractograms, the crystallite size and cell parameters were extracted, and the obtained values are reported in **Table 3-1**. The effective elemental composition revealed by ICP, within the experimental error of the measurement, resulted in a stoichiometry corresponding to $Sr_{1.07}Fe_{11.93}O_{19}$. Therefore, eventually additional phases such as $SrCO_3$, derived from the excess of $Sr^{2+}$, were removed by $HNO_3$ washing [19].

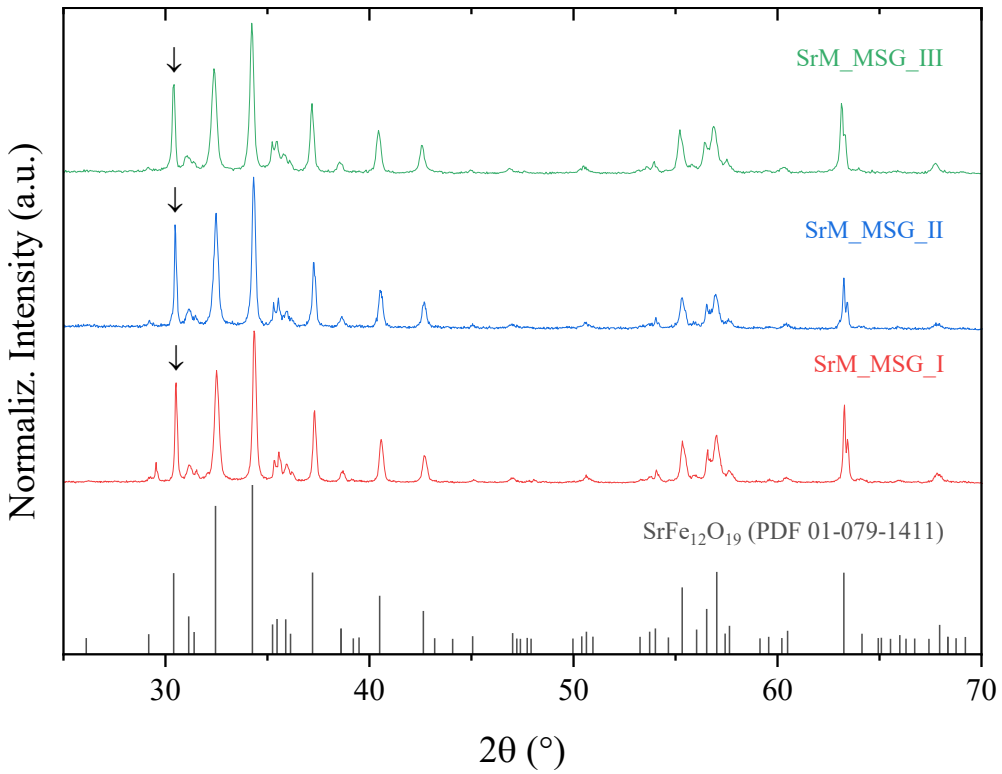


***Figure 3-1*** *PXRD diffractograms of SrM samples produced by MSG synthesis with molar ratio $Fe^{3+}/Sr^{2+}$ = 9, pre-calcination at 450 °C for 1 h and calcination at 790 °C for 1 h. The (110) diffraction planes are highlighted by the black arrow.*

***Table 3-1*** *Crystallite size and cell parameters (PXRD), mean size and standard deviation (TEM) of SrM samples produced by MSG synthesis with molar ratio $Fe^{3+}/Sr^{2+}$ = 9, pre-calcination at 450°C, 1 h, and calcination at 790°C, 1 h.*

| Sample | Cry.size (nm) | a (Å) | c (Å) | Mean Size (nm) | Std.Dev. (nm) |
|---|---|---|---|---|---|
| **SrM_MSG_I** | 58(1) | 5.8847(5) | 23.055(2) | 91 | 44 |
| **SrM_MSG _II** | 64(1) | 5.8841(4) | 23.049(2) | 91 | 40 |
| **SrM_MSG _III** | 60(1) | 5.8831(3) | 23.039(2) | 93 | 45 |

The results were consistent in all the series of tests, giving almost identical values for what concerns the crystallite size and cell parameters. Additionally, the mean sizes and the relative standard deviation, determined by the analysis

of TEM images (**Figure 3-2**), are in good agreement with each other. The nanoparticles presented a well-defined and distinguishable shape, corresponding to the characteristic platelet morphology of SrM. However, the discrepancy between the actual size from TEM and crystallite size from PXRD suggested the formation of polycrystalline samples. In the TEM images, the platelets appeared to be close to each other, but several nanoparticles showed a perpendicular orientation to the flat surface of the TEM grid. This arrangement could suggest the formation of individual nanoparticles free to rotate, with agglomerates rather due to magnetic and dipolar interactions than actually sintered together. To validate this hypothesis, a TEM grid was prepared while placed on the side of a permanent magnet, in a way that the magnetic field was applied horizontally to the grid. The resultant images, showed in **Figure 3-3**, showed a sort of alignment as a chain-assembly, more than overlapped irregular agglomerates. This further suggested that, at least partially, the platelets were susceptible to magnetic orientation.

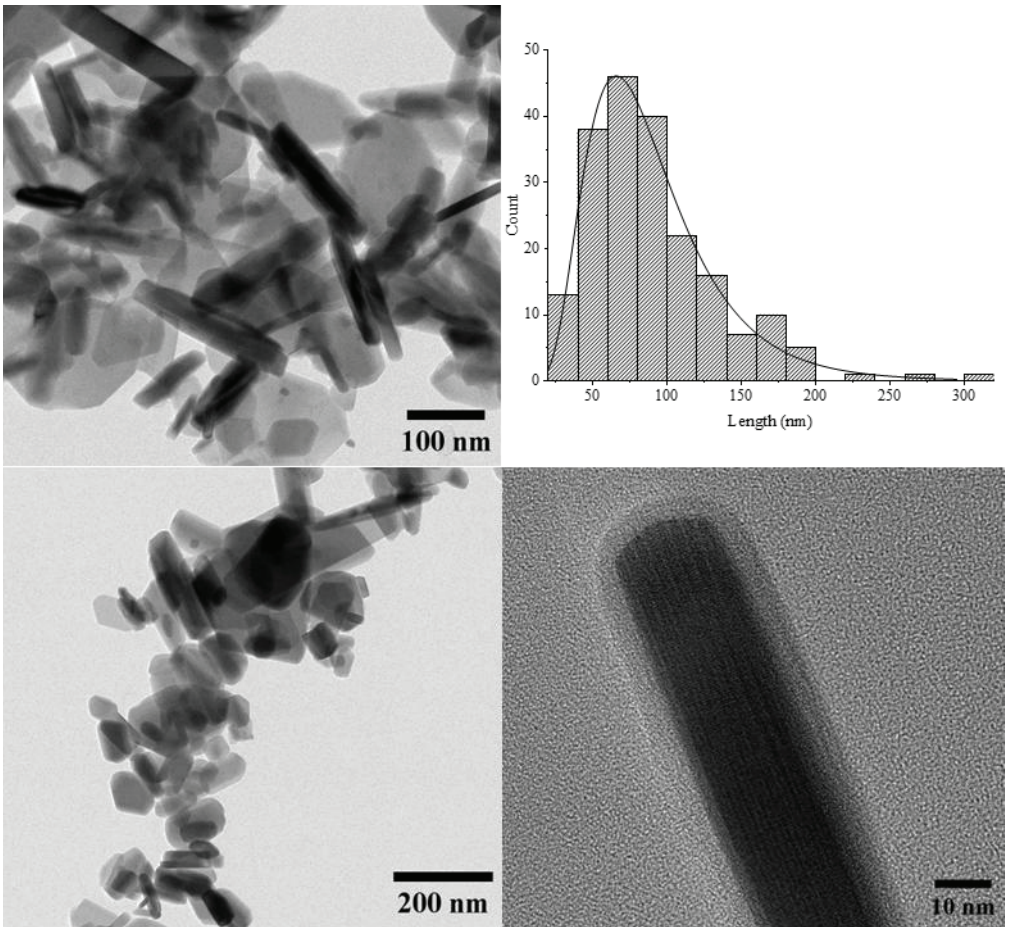


***Figure 3-2*** *Representative images and size distribution of SrM samples produced by MSG synthesis with molar ratio $Fe^{3+}/Sr^{2+}$ = 9, pre-calcination at 450°C, 1h, and calcination at 790°C, 1h. The histogram of size distribution was estimated from over 200 particles and fitted to a lognormal function.*

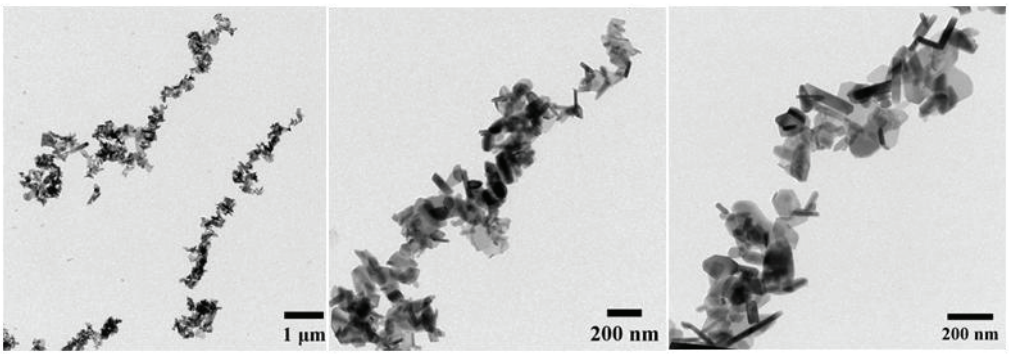


***Figure 3-3*** *TEM images of the oriented nanoparticles by deposition on TEM grid placed on the side of a permanent magnet.*

The corresponding hysteresis loops, collected at 300 K, are shown in **Figure 3-4**. The synthesized particles exhibited similar values of the main magnetic properties, summarized in **Table 3-2**, especially the remanence (average 29 ± 1 $Am^2kg^{-1}$) and the saturation magnetization (average 67 ± 1 $Am^2kg^{-1}$), the only difference being a slightly larger value of the coercivity of SrM_MSG _III.

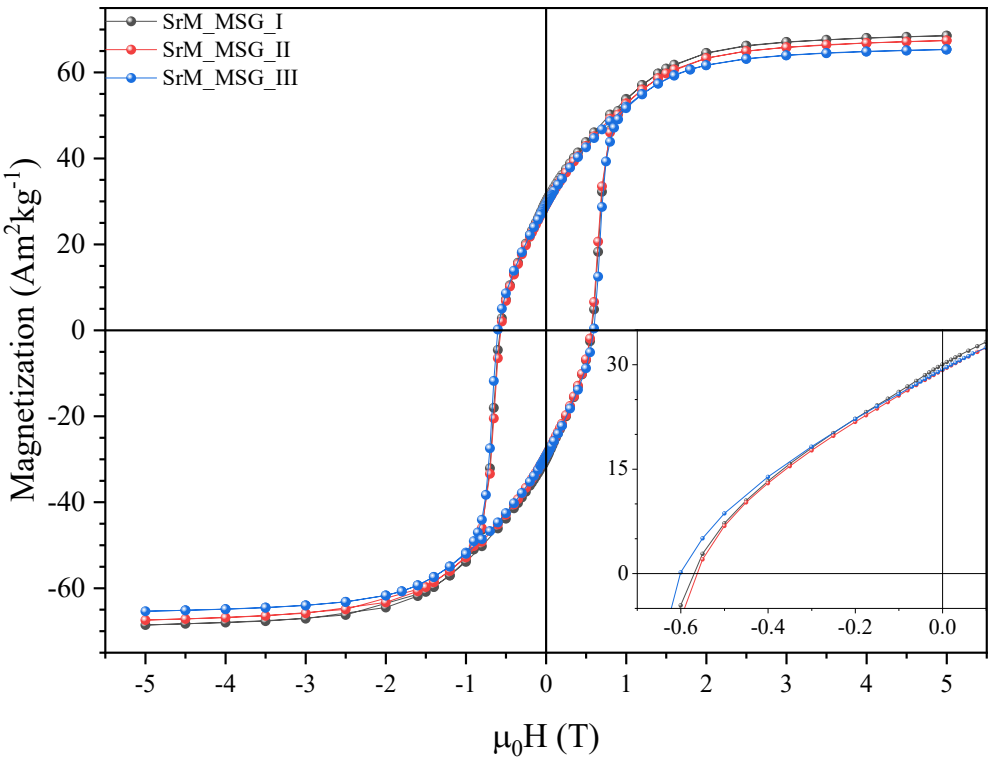


***Figure 3-4*** *Hysteresis loops at 300K of SrM samples produced by MSG synthesis with molar ratio* $Fe^{3+}/Sr^{2+}$ *= 9, pre-calcination at 450°C for 1 h and calcination at 790°C for 1 h.*

***Table 3-2*** *Magnetic parameters estimated from the hysteresis loops at 300 K of SrM samples produced by MSG synthesis with molar ratio $Fe^{3+}/Sr^{2+}$ = 9, pre-calcination at 450°C for 1h, and calcination at 790°C for 1h.*

| Sample | $M_s$ ($Am^2kg^{-1}$) | $M_r$ ($Am^2kg^{-1}$) | $M_r/M_s$ | $\mu_0H_c$ (T) |
|---|---|---|---|---|
| **SrM_MSG_I** | 69 | 30 | 0.44 | 0.57 |
| **SrM_MSG _II** | 67 | 29 | 0.43 | 0.56 |
| **SrM_MSG _III** | 65 | 29 | 0.45 | 0.60 |

# 3.2 Investigation into pre-calcination and calcination heating steps

To evaluate how the temperature steps in the calcination procedure influence the final nanoparticles' size, a series of samples was prepared by varying the holding time ($t_1$) at $T_1$ (pre-calcination temperature) and the temperature in $T_2$ (final calcination temperature) at fixed holding time $t_2$ (1 hour). In all the series the molar ratio between iron and strontium was kept equal to 9. The samples were named SrM_MSG_Ax/By, where "x" indicates $t_1$ at $T_1$ = 450°C, and "y" the $T_2$ temperature at fixed $t_2$ = 1 h. The samples were then analyzed by XRD and TEM.

## 3.2.1 MSG – Pre-calcination stage

Initially, slight variations in $t_1$ at $T_1$ = 450°C were explored: instead of one-hour as reported in the literature, the time intervals investigated were 50, 40 and 30 minutes. The selected temperature was kept fixed at 450 °C as a good compromise between efficiently burning the organic residues and avoiding the formation of some additional phases, like hematite ($\alpha$-$Fe_2O_3$) and strontium monoferrite ($SrFe_2O_4$) [20,25]. In **Figure 3-5** the PXRD diffractograms of the

synthesized samples are shown. All the most intense peaks were attributed to the main phase of M-type $SrFe_{12}O_{19}$, with no evident presence of additional phases.

In **Table 3-3** are reported the crystal size and lattice parameters of the resultant nanoparticles. Across the series, negligible variation was observed in the crystallographic features, including both the crystallite size and cell parameters. In the same table it is reported also the particles' mean size observed by TEM analysis, which confirms the polycrystalline nature of the synthesized nanoparticles. In TEM images, reported in Figure 3-6, the nanoparticles at different $t_1$ had the same appearance and size, similarly to those normally pre-calcined for one hour. This suggested that a different duration in the pre-calcination provided the right precursors even in shorter time, then fully converted into the main phase of SrM at $T_2$ = 790 °C [4,20].

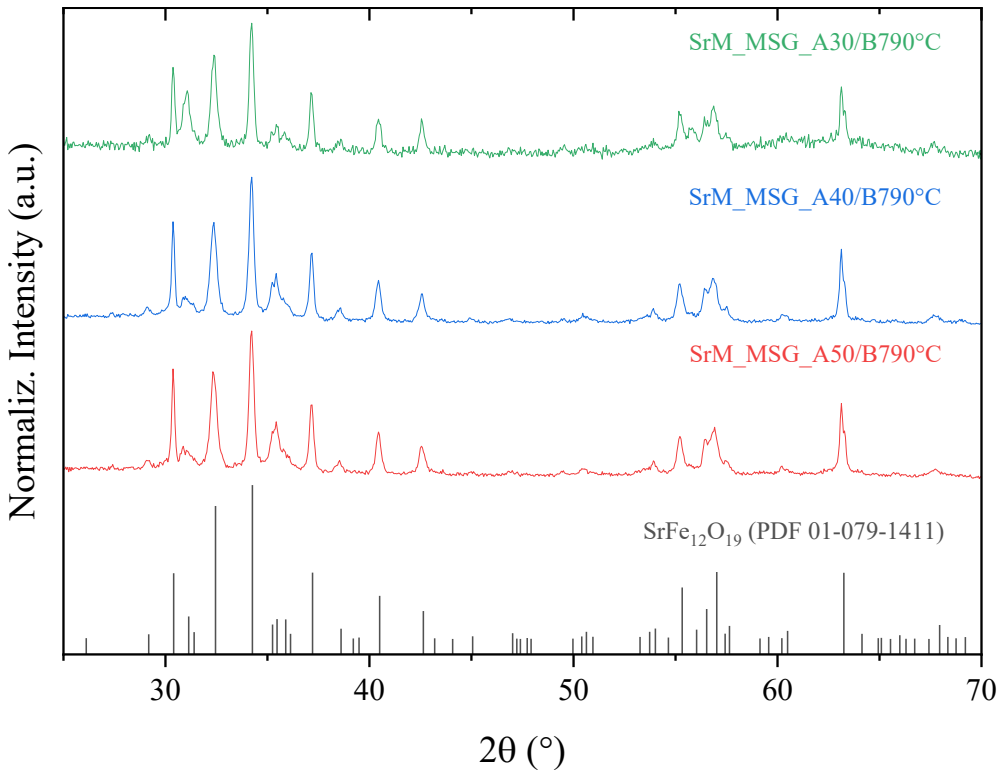


***Figure 3-5*** *PXRD diffractograms of SrM samples produced MSG synthesis with different $t_1$ at $T_1$ =450 °C.*

***Table 3-3*** *Crystallite size and cell parameters (PXRD), mean size and standard deviation (TEM) of SrM samples produced by MSG synthesis with different $t_1$ at $T_1$ = 450 °C.*

| Sample | Cry.size (nm) | a (Å) | c (Å) | Mean Size (nm) | Std.Dev. (nm) |
|---|---|---|---|---|---|
| **SrM_MSG_A50/B790** | 42(1) | 5.8852(3) | 23.046(2) | 83 | 34 |
| **SrM_MSG_A40/B790** | 43(1) | 5.8857(3) | 23.052(2) | 86 | 35 |
| **SrM_MSG_A30/B790** | 46(2) | 5.8844(5) | 23.049(3) | 88 | 37 |

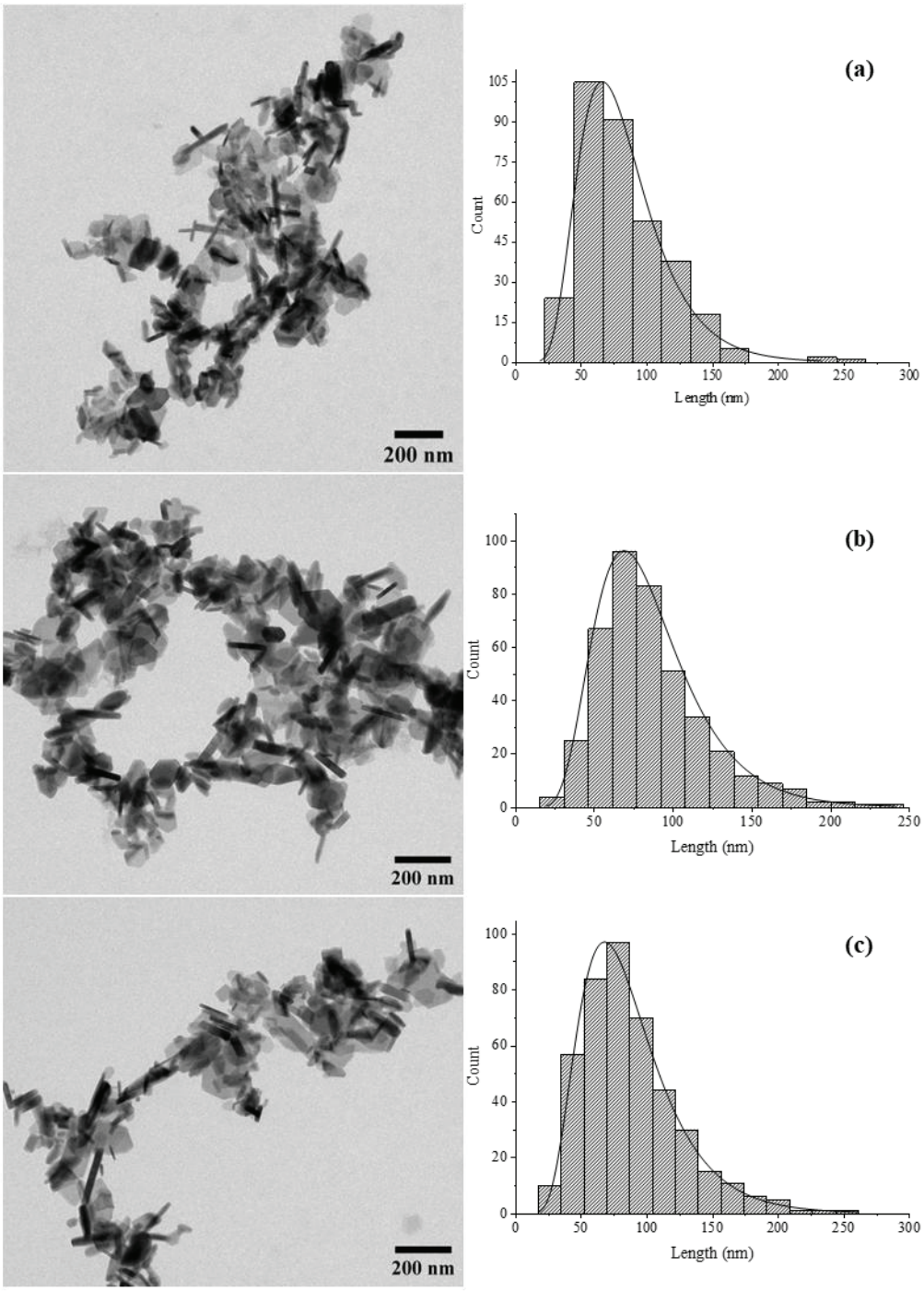


*Figure 3-6 TEM images of SrM samples produced by MSG synthesis at $T_1$ = 450° and different $t_1$: (a) 50 min; (b) 40 min; (c) 30 min. The size distributions were estimated from over 300 nanoparticles and fitted to a lognormal function.*

## 3.2.2 MSG – Calcination stage

To investigate the effect of the calcination temperature $T_2$, where the M-type $SrFe_{12}O_{19}$ phase is developed, two distinct temperature points were evaluated. The lower limit was set at 760 °C, which is above the temperature of 700 °C when SrM starts to crystallize from the amorphous phase [2,26] after the thermal decomposition of the citrate precursor at 600 °C [27], becoming prominent at 750 °C [20]. Conversely, 820 °C was selected as the upper limit in which the NaCl matrix is in liquid state (melting point of 801 °C) [28]. These temperatures are crucial for controlling both the crystallization degree and, particularly, the particle size [29]. The holding time $t_1$ and $t_2$ was fixed to 1 hour for both $T_1$ and $T_2$, as this duration proved to be enough for achieving a well-crystallized product without promoting excessive crystal growth. This approach aimed to directly correlate particle size differences with the final temperature $T_2$.

The PXRD diffractograms (**Figure 3-7**) confirmed the successful crystallization of the pure M-type $SrFe_{12}O_{19}$ phase without detectable secondary products, even at temperatures lower than 790 °C [10,22]. The difference between these samples was mainly found in the crystallite size estimated from the refinement of the diffractograms and the actual size of the nanoparticles derived from TEM analysis (**Table 3-4**), where a noticeable increase in both values was observed with increasing calcination temperature.

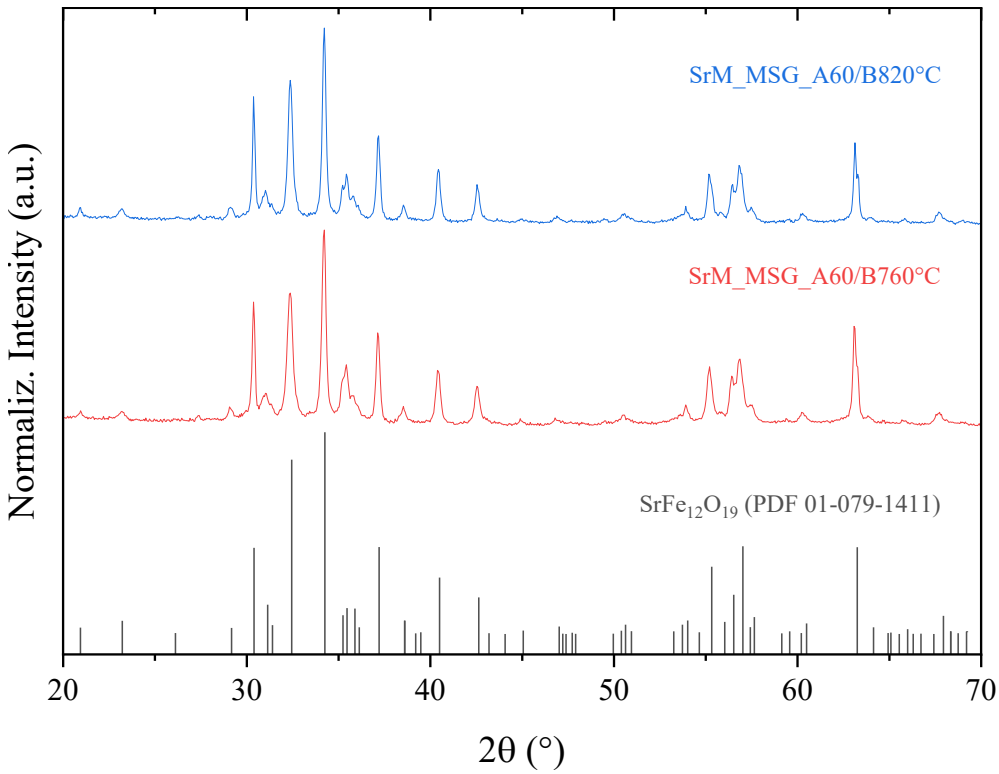


***Figure 3-7*** *PXRD diffractograms of SrM samples produced by MSG synthesis with different* $T_2$.

***Table 3-4*** *Crystallite size and cell parameters (PXRD), mean size and standard deviation (TEM) of SrM samples produced by MSG synthesis with different $T_2$.*

| Sample | Cry.size (nm) | a (Å) | c (Å) | Mean Size (nm) | Std.Dev. (nm) |
|---|---|---|---|---|---|
| **SrM_MSG_A60/B760** | 43(1) | 5.8909(8) | 23.074(3) | 72 | 42 |
| **SrM_MSG_A60/B820** | 54(1) | 5.8844(2) | 23.044(2) | 130 | 58 |

The elevated temperature was the primary factor in promoting a coherent enhancement in particle size [30,31]. In TEM images, the nanoparticles obtained at lower $T_2$ appeared to be slightly less defined along the edges of the platelets, differently to the shaper and more definite platelets of the sample at $T_2$ = 820 °C. This can be due to a smaller crystallinity degree due to the proximity of $T_2$ to 750°C, the temperature in which SrM phase becomes predominant. On the other hand, the aggregation of particles appeared independent of $T_2$, remaining similar as those observed in the normally calcined samples. Therefore, the liquid state of NaCl had minor influence in reducing aggregation, while higher $T_2$ enhanced the particle size.

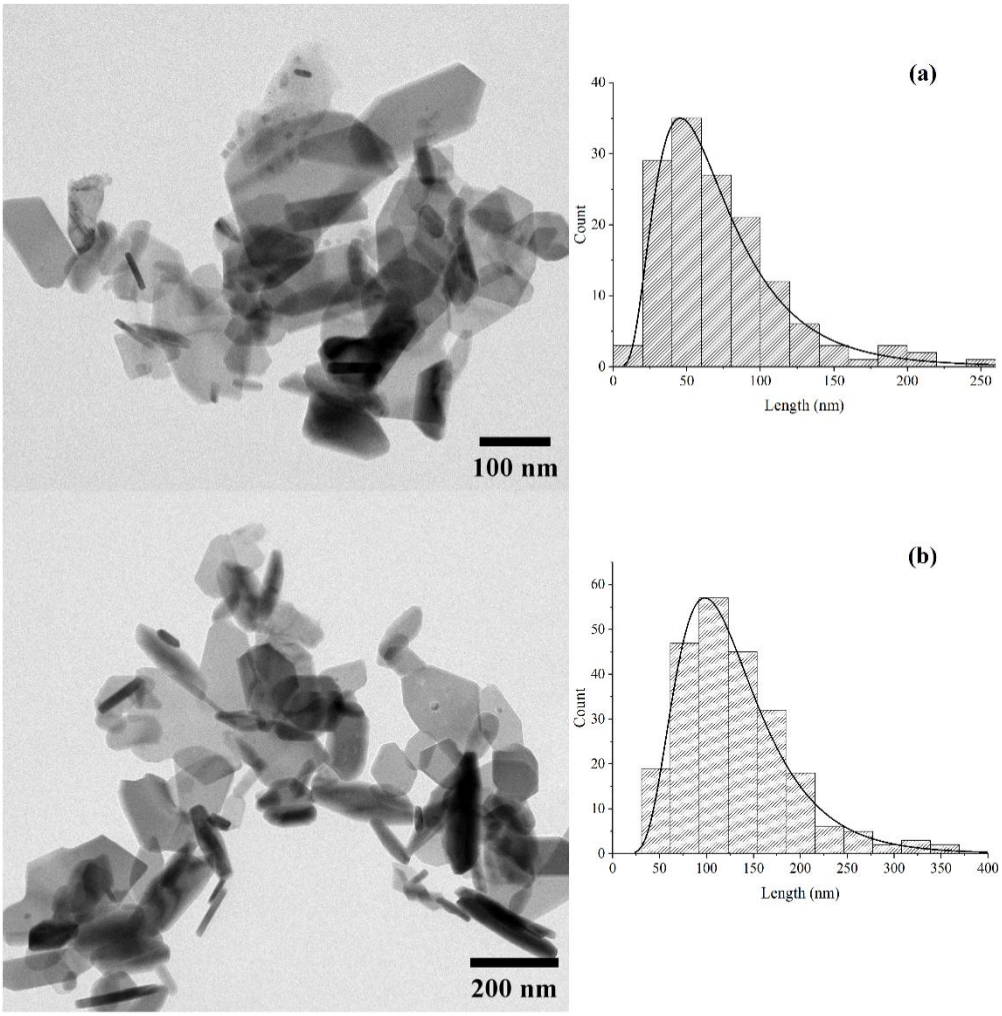


***Figure 3-8*** *TEM images and size distribution of SrM samples MSG synthesis with different temperature in the calcination step: (a) 760 °C (b) 820 °C. On the right, the histograms of size distribution, fitted to a lognormal function, were estimated from (a) over 100 particles, (b) over 200 particles.*

# 3.3 Evaluation of the increased NaCl matrix content on reducing the size

Since the MSG method proved to be reproducible, providing nanoparticles with desirable magnetic properties and no secondary phases, further studies focused on the role of the NaCl matrix, the key element of this procedure. In

particular, we aimed at assessing whether increasing the NaCl matrix content could further reduce nanoparticles' size or their agglomeration [10].

Thus, in addition to the NaCl, formed by the reaction of metal-chlorides and sodium carbonate, an increased amount of 100% by weight with respect to that formed during the synthesis, was added to the precursor gel in two different ways: by inclusion inside the *sol*, before the drying stage (sample SrM_MSG_100NaCl_SOL), or by addition to the dried *gel* while it is grinded in the mortar before calcination (sample SrM_MSG_100NaCl_GEL).

The PXRD diffractograms patterns of the as obtained samples displayed (**Figure 3-9**) no evidence of additional phases. The lattice parameters *a* and *c* seemed to be slightly enhanced when compared the sample with no NaCl addition, SrM_MSG_I (**Table 3-5**), while a decreased crystal size was estimated only for the sample SrM_MSG_100NaCl_GEL. The average particle size from TEM images (**Figure 3-10**) also differed. Both samples remained predominantly polycrystalline, leading to the conclusion that excess of NaCl, in the two approaches, did not contribute to further nanoparticles' size reduction. Neither a change nor reduction in the formed agglomerates were noticed adding extra NaCl, suggesting that an increased matrix content had a minor influence even in this regard.

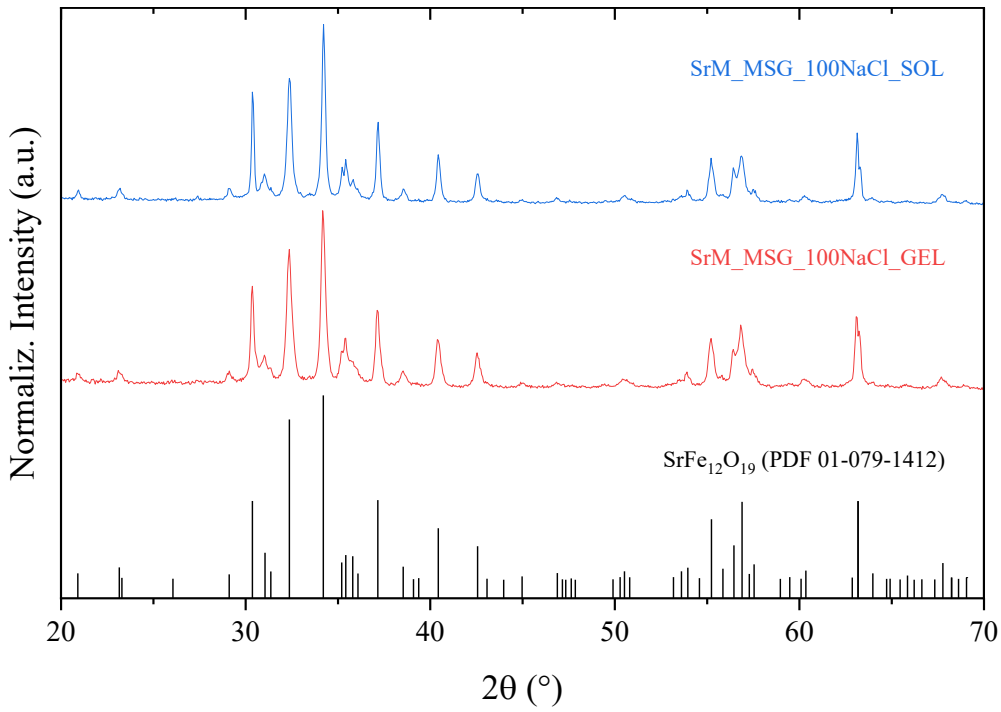


***Figure 3-9*** *PXRD diffractograms of SrM samples produced by MSG synthesis with $Fe^{3+}/Sr^{2+}$ = 9 and 100% extra NaCl added to the precursor in the dried gel (red line) and in the solution (blue line).*

***Table 3-5*** *Crystallite size and cell parameters (PXRD), mean size and standard deviation (TEM) of SrM samples produced by MSG synthesis with $Fe^{3+}/Sr^{2+}$ = 9 and 100% extra NaCl added to the precursor in the dried gel or in the sol. For comparison data of SrM_MSG_I having no extra NaCl are also reported.*

| Sample | Cry.size (nm) | a (Å) | c (Å) | Mean Size (nm) | Std.Dev. (nm) |
|---|---|---|---|---|---|
| **SrM_MSG_I** | 58(1) | 5.8847(5) | 23.055(2) | 91 | 44 |
| **SrM_MSG_100NaCl_SOL** | 58(1) | 5.8878(5) | 23.063(2) | 97 | 35 |
| **SrM_MSG_100NaCl_GEL** | 42 (1) | 5.8905(7) | 23.073(3) | 118 | 55 |

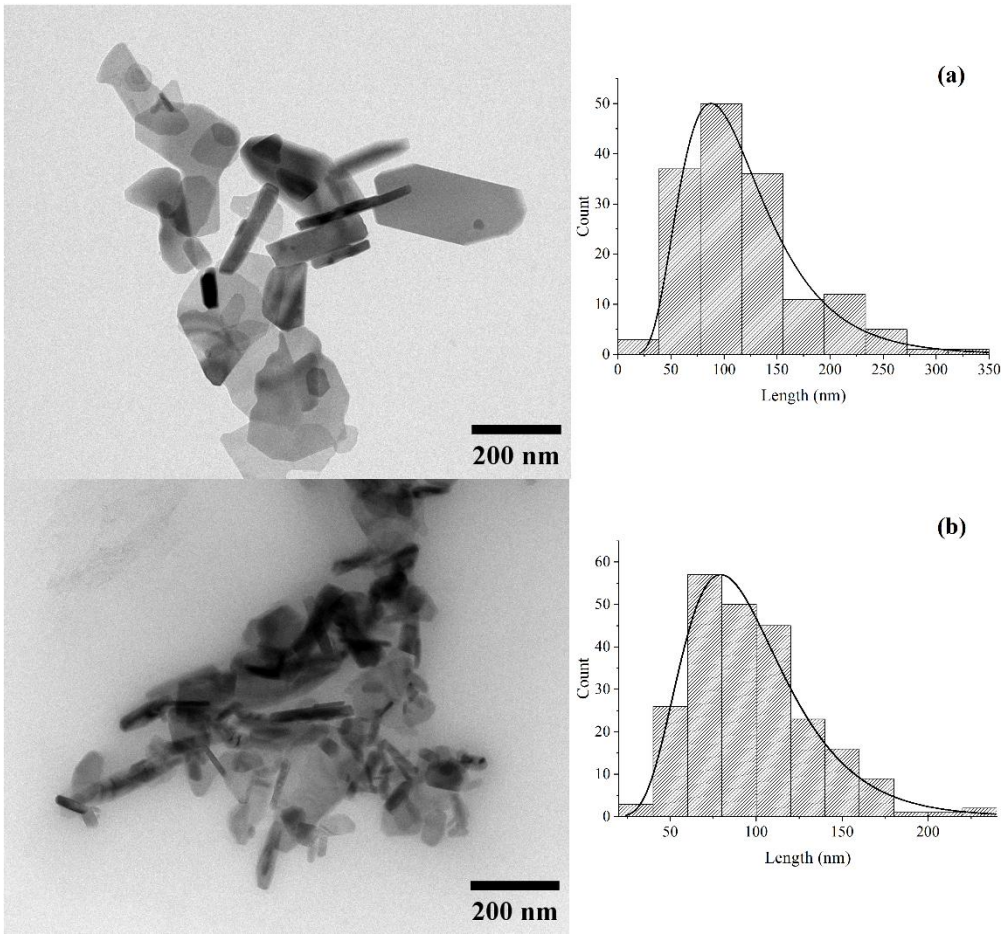


***Figure 3-10*** *TEM images and size distribution of SrM samples produced 100% extra NaCl added to the precursor (a) in the dried gel and (b) in the solution. On the right, the histograms of size distribution, fitted to a lognormal function, were estimated from: (a) over 100 particles; (b) over 200 particles.*

# 3.4 The influence of Fe/Sr molar ratios on the particle size

The initial trials were inspired by the work of Eikeland *et al.* [19], that synthesized SrM nanoparticles using this method to compare MSG with standard sol-gel synthesis, focusing on how crystallite morphology and aggregation affect alignment during compaction. Their results highlighted notable differences in

compaction behavior, likely due to an increased particles aspect ratio. Among the attested $Fe^{3+}/Sr^{2+}$ molar ratios (8-12), the ratio 9 was preferred for its lower risk of hematite formation (higher molar ratios resulted contaminated) and slightly smaller lattice parameters reported. While Eikeland et al. observed minimal changes in cell parameters across the ratio range and hypothesized an eventual oxygen-deficiency in the calcination stage for the appearance of α-$Fe_2O_3$ phase, other works reported the Fe/Sr ratio significantly impacts on particle size and composition, such in similar sol-gel processes [25,32,33], coprecipitation [34,35], hydrothermal [36] or milling [37], resulting slightly controversial. To assess possible variations in phase, size, and magnetic properties due to hematite contamination, as in the case of LTSSR synthesis, a $Fe^{3+}/Sr^{2+}$ molar ratio of 12 was also tested. The calcination parameters ($T_1$ = 450 °C; $T_2$ = 790 °C; $t_1$ and $t_2$ = 1 hour) and the afterward washing ($HNO_3$ 4M and DM water) were maintained constant.

The PXRD diffractograms of the samples with different $Fe^{3+}/Sr^{2+}$ molar ratios (in **Figure 3-11**) showed identical patterns, with all the main peaks corresponding to the M-type compound $SrFe_{12}O_{19}$, and no evident formation of secondary phases. Even increasing the $Fe^{3+}/Sr^{2+}$ molar ratio, no presence of hematite or other additional phases was detected. Also no differences in the main crystallographic parameters emerged from the refinement of the experimental patterns. Furthermore, the particle size distribution from TEM images were very similar in the two cases, in contrast to the MSSR synthesis, where a higher $Fe^{3+}/Sr^{2+}$ molar ratio resulted in larger particle sizes.

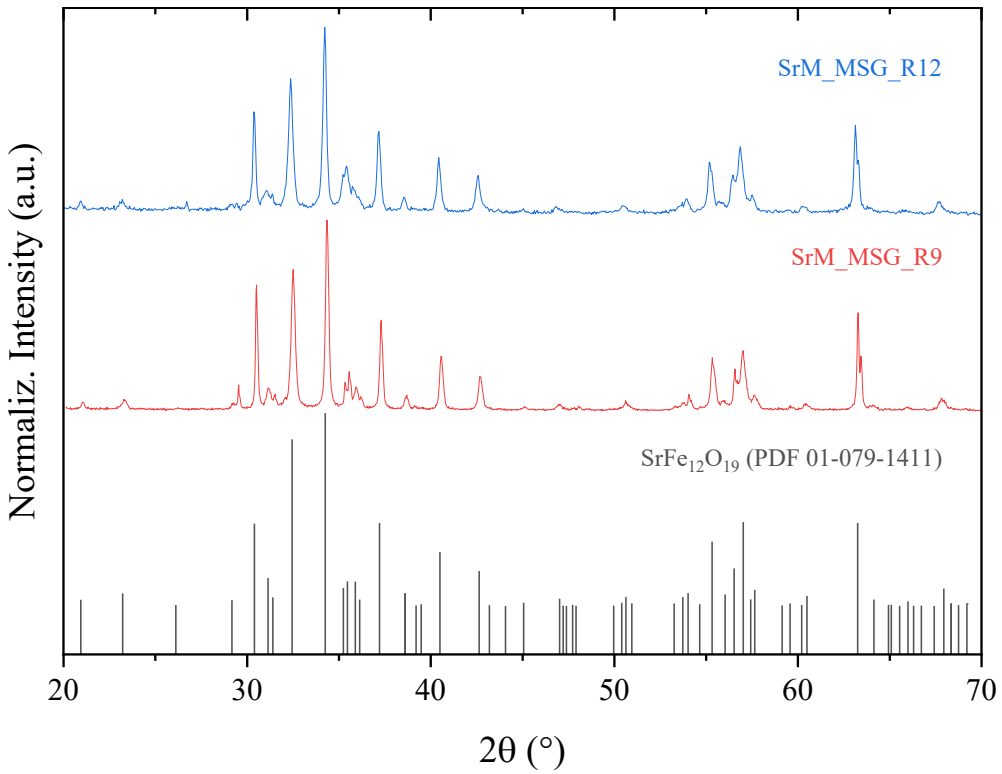


***Figure 3-11*** *PXRD diffractograms of SrM samples produced by MSG synthesis with different $Fe^{3+}/Sr^{2+}$ molar ratio.*

***Table 3-6*** *Crystallite size and cell parameters (PXRD), mean size and standard deviation (TEM) of SrM samples produced by MSG synthesis with different $Fe^{3+}/Sr^{2+}$ molar ratio.*

| Sample | Cry.size (nm) | a (Å) | c (Å) | Mean Size (nm) | Std.Dev. (nm) |
|---|---|---|---|---|---|
| **SrM_MSG_R12** | 58(1) | 5.8878(5) | 23.066(2) | 94 | 50 |
| **SrM_MSG_R9** | 58(1) | 5.8847(5) | 23.055(2) | 91 | 44 |

The elemental composition of the sample obtained by ICP analysis resulted in a stoichiometry of $Sr_{1.06}Fe_{11.94}O_{19}$ for molar ratio $Fe^{3+}/Sr^{2+}$ = 12 and $Sr_{1.07}Fe_{11.94}O_{19}$ for molar ratio $Fe^{3+}/Sr^{2+}$ = 9. These comparable results, within the experimental error, confirmed the correct formation of SrM.

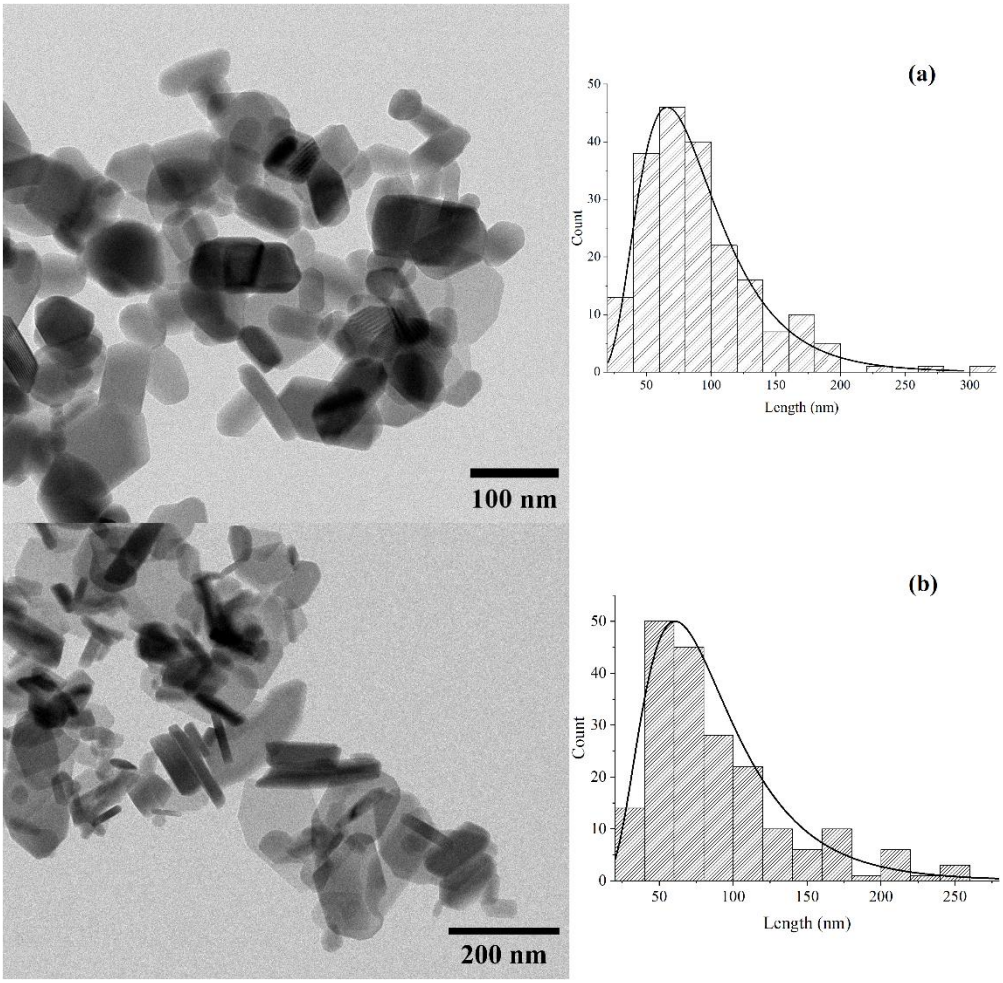


***Figure 3-12*** *TEM images and size distribution of SrM samples produced by MSG synthesis with different $Fe^{3+}/Sr^{2+}$ molar ratio: (a) SrM_MSG_R9 (b) SrM_MSG_R12. The histograms were estimated from over 200 nanoparticles and fitted to a lognormal function*

Only minor variations were observed in the main magnetic properties obtained from the hysteresis loops collected at 300 K (**Figure 3-13**), particularly in the $M_S$ and $M_R$ values (**Table 3-7**). However, coercivity slightly increased with a higher $Fe^{3+}/Sr^{2+}$ molar ratio. A similar effect was observed in Ref. [19] where it was ascribed to an increased shape anisotropy along the easy magnetization axis of the material. However, since this does not seem to be our case, we can argue that the increase in coercivity arises from the different arrangement of the nanoparticles in the powder, as indeed suggested by TEM images. The

latter, indeed, could generate a different internal field responsible for the increase of coercive force.

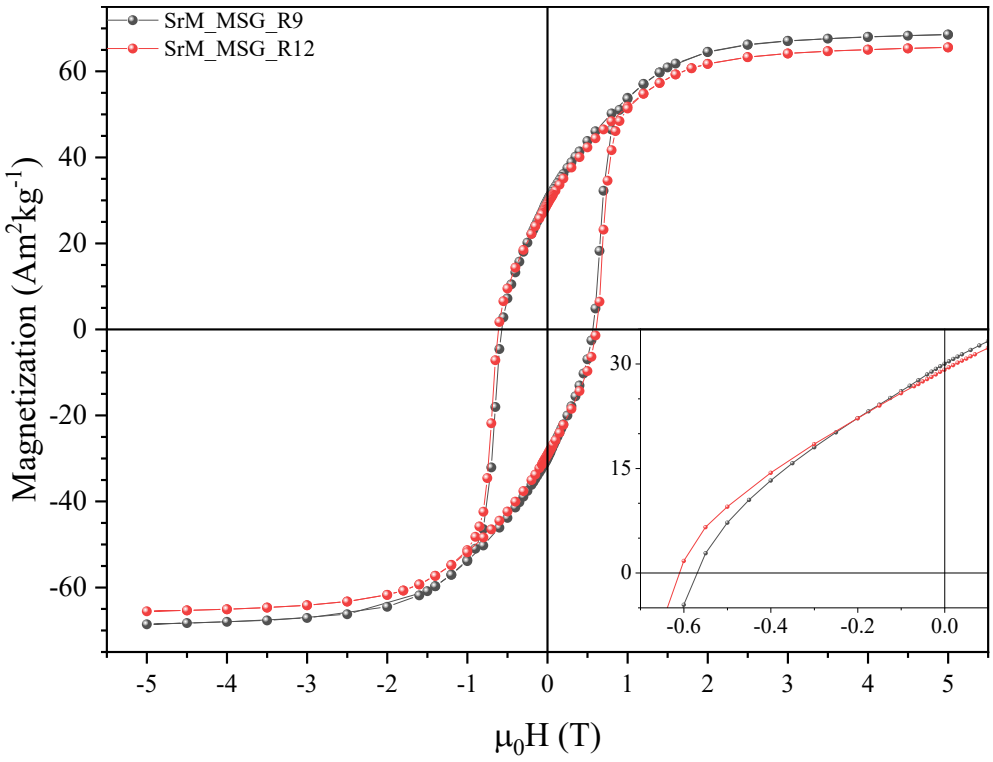


***Figure 3-13*** *Hysteresis loops at 300K of SrM samples produced by MSG synthesis with different $Fe^{3+}/Sr^{2+}$ molar ratio. The samples were named SrM_MSG_Rx, indicating as x the $Fe^{3+}/Sr^{2+}$ ratio.*

***Table 3-7*** *Magnetic properties derived from hysteresis loops at 300K of SrM samples produced by MSG synthesis with different $Fe^{3+}/Sr^{2+}$ molar ratio.*

| Sample | $M_s$ ($Am^2kg^{-1}$) | $M_r$ ($Am^2kg^{-1}$) | $M_r/M_s$ | $\mu_0H_c$ (T) |
|---|---|---|---|---|
| **SrM_MSG_R12** | 65 | 29 | 0.45 | 0.61 |
| **SrM_MSG_R9** | 68 | 30 | 0.44 | 0.57 |

## 3.5 Conclusions

The MSG synthesis was selected and evaluated to find the optimal conditions leading to individual nanograins suitable to be oriented, overcoming the main limitation of sintered aggregates obtained by solid-state synthesis. Although TEM images did not allow us to conclusively assess this aspect, the observed particles orientation suggested less strongly intergrown and agglomerated nanoparticles with respect to solid-state method. Moreover, the application of magnetic field showed a higher degree of individual particles capable of being partially aligned in chain-like arrangement. The SrM nanoparticles synthesized through this procedure consistently showed the obtainment of phase-pure strontium hexaferrite with no detectable amount of secondary phases, and ICP-AES analysis demonstrated that a correct stoichiometry of the compound was obtained for all the prepared samples. Single-phase SrM was successfully crystallized even at temperatures lower than the typical 800°C. The discrepancy between actual particle size from TEM and crystallite size from PXRD suggested the development of polycrystalline nanoparticles, with consistently high values of coercivity and magnetization. Nonetheless, some challenges could arise in preparing big batches to scale-up the reaction, differently from the solid-state route. While the reagents' solution was prepared in a relatively simple way, mixing them in water and in short time intervals, large volumes of liquid could be difficult in handling to ensure a homogenous dried gel, and time consuming without proper equipment. Additionally, the fume evolution from burning the carbonaceous residues of the precursor gel must be contained during the heating stages, and the yield of the final product is fairly lower compared to solid-state reactions. Variations in the pre-calcination holding time (from 30 to 60 minutes) at 450°C did not significantly impact the main crystallographic features or the mean particle size of the

resultant nanoparticles. The selected temperature of 450 °C effectively burned off organic residues and set the right precursors, without forming additional phases like hematite in the final calcination step. Conversely, the calcination temperature in the second heating step significantly influenced the particle size, as increasing the calcination temperature to 820 °C resulted in a noticeable increase in both crystallite size and mean particle size. The retained characteristic platelet shape indicated that the elevated temperature was the major factor promoting the particle size enlargement, while the liquid state of NaCl matrix seemed to have no influence. Increasing the NaCl matrix content, either added to the sol or to the dried gel, did not lead to a further reduction in nanoparticle size or in the formation of aggregates. Changing the $Fe^{3+}/Sr^{2+}$ molar ratio (from 9 to 12) showed minimal effect on the crystallographic phase, particle size, or main magnetic characteristics, and ICP analysis confirmed correct SrM formation for both ratios.

Altogether, these results demonstrated MSG is a more suited technique for the preparation of orientable, nanometric single crystal of hexagonal ferrite. Therefore, in the following we adopted this method to explore to further improve the properties of the nanoparticles through metal substitution.

# References


(1) Maltoni, P.; Ivanov, S. A.; Barucca, G.; Varvaro, G.; Peddis, D.; Mathieu, R. Complex Correlations between Microstructure and Magnetic Behavior in SrFe12O19 Hexaferrite Nanoparticles. *Scientific Reports 2021 11:1* **2021**, *11* (1), 1–8. https://doi.org/10.1038/s41598-021-02782-2.

(2) García-Cerda, L. A.; Rodríguez-Fernández, O. S.; Reséndiz-Hernández, P. J. Study of SrFe12O19 Synthesized by the Sol–Gel Method. *J Alloys Compd* **2004**, *369* (1–2), 182–184. https://doi.org/10.1016/J.JALLCOM.2003.09.099.

(3) Masoudpanah, S. M.; Seyyed Ebrahimi, S. A. Synthesis and Characterization of Nanostructured Strontium Hexaferrite Thin Films by the Sol–Gel Method. *J Magn Magn Mater* **2012**, *324* (14), 2239–2244. https://doi.org/10.1016/J.JMMM.2012.02.109.

(4) Nga, T. T. V.; Duong, N. P.; Loan, T. T.; Hien, T. D. Key Step in the Synthesis of Ultrafine Strontium Ferrite Powders (SrFe12O19) by Sol–Gel Method. *J Alloys Compd* **2014**, *610*, 630–634. https://doi.org/10.1016/j.jallcom.2014.04.193.

(5) Sürig, C.; Hempel, K. A.; Bonnenberg, D. Hexaferrite Particles Prepared by Sol—Gel Technique. *IEEE Trans Magn* **1994**, *30* (6), 4092–4094. https://doi.org/10.1109/20.333999.

(6) Bokov, D.; Turki Jalil, A.; Chupradit, S.; Suksatan, W.; Javed Ansari, M.; Shewael, I. H.; Valiev, G. H.; Kianfar, E. Nanomaterial by Sol-Gel Method: Synthesis and Application. *Advances in Materials Science and Engineering* **2021**, *2021* (1), 5102014. https://doi.org/10.1155/2021/5102014.

(7) Mackenzie, J. D. Applications of the Sol-Gel Process. *J Non Cryst Solids* **1988**, *100* (1–3), 162–168. https://doi.org/10.1016/0022-3093(88)90013-0.

(8) Mirkazemi, S. M.; Alamolhoda, S.; Ghiami, Z. Microstructure and Magnetic Properties of SrFe12O19 Nano-Sized Powders Prepared by Sol-Gel Auto-Combustion Method with CTAB Surfactant. *J Supercond Nov Magn* **2015**, *28* (5), 1543–1549. https://doi.org/10.1007/S10948-014-2872-X/FIGURES/9.

(9) Das, A.; Roychowdhury, A.; Pati, S. P.; Bandyopadhyay, S.; Das, D. Structural, Magnetic and Hyperfine Properties of Single-Phase SrFe12O19 Nanoparticles Prepared by a Sol–Gel Route. *Phys Scr* **2015**, *90* (2), 025802. https://doi.org/10.1088/0031-8949/90/2/025802.

(10) Sapoletova, N. A.; Kushnir, S. E.; Li, Y. H.; An, S. Y.; Seo, J. W.; Hur, K. H. Plate-like SrFe12O19 Particles Prepared by Modified Sol–Gel Method. *J*

*Magn Magn Mater* **2015**, *389*, 101–105. https://doi.org/10.1016/J.JMMM.2015.04.055.

(11) Arendt, R. H. The Molten Salt Synthesis of Single Magnetic Domain BaFe12O19 and SrFe12O19 Crystals. *J Solid State Chem* **1973**, *8* (4), 339–347. https://doi.org/10.1016/S0022-4596(73)80031-3.

(12) Liu, J. R.; Hong, R. Y.; Feng, W. G.; Badami, D.; Wang, Y. Q. Large-Scale Production of Strontium Ferrite by Molten-Salt-Assisted Coprecipitation. *Powder Technol* **2014**, *262*, 142–149. https://doi.org/10.1016/J.POWTEC.2014.04.076.

(13) Guo, Z. B.; Ding, W. P.; Zhong, W.; Zhang, J. R.; Du, Y. W. Preparation and Magnetic Properties of SrFe12O19 Particles Prepared by the Salt-Melt Method. *J Magn Magn Mater* **1997**, *175* (3), 333–336. https://doi.org/10.1016/S0304-8853(97)00206-0.

(14) Chin, T.-S.; Hsu, S. L.; Deng, M. C. Barium Ferrite Particulates Prepared by a Salt-Melt Method. *J Magn Magn Mater* **1993**, *120* (1–3), 64–68. https://doi.org/10.1016/0304-8853(93)91288-I.

(15) Zaitsev, D. D.; Kushnir, S. E.; Kazin, P. E.; Tretyakov, Y. D.; Jansen, M. Preparation of the SrFe12O19-Based Magnetic Composites via Boron Oxide Glass Devitrification. *J Magn Magn Mater* **2006**, *301* (2), 489–494. https://doi.org/10.1016/J.JMMM.2005.08.002.

(16) SHIRK, B. T.; BUESSEM, W. R. Magnetic Properties of Barium Ferrite Formed by Crystallization of a Glass. *Journal of the American Ceramic Society* **1970**, *53* (4), 192–196. https://doi.org/10.1111/J.1151-2916.1970.TB12069.X.

(17) Sato, H.; Umeda, T. Grain Growth of Strontium Ferrite Crystallized from Amorphous Phases. *Materials Transactions, JIM* **1993**, *34* (1), 76–81. https://doi.org/10.2320/MATERTRANS1989.34.76.

(18) Brinker, C. J.; W. Scherer, G. *Sol-Gel Science: The Physics and Chemistry of Sol-Gel Processing - C. Jeffrey Brinker, George W. Scherer - Google Books*; Academic Press, 2013.

(19) Eikeland, A. Z.; Stingaciu, M.; Mamakhel, A. H.; Saura-Múzquiz, M.; Christensen, M. Enhancement of Magnetic Properties through Morphology Control of SrFe12O19 Nanocrystallites. *Sci Rep* **2018**, *8* (1), 7325. https://doi.org/10.1038/s41598-018-25662-8.

(20) Zhong, W.; Ding, W.; Zhang, N.; Hong, J.; Yan, Q.; Du, Y. Key Step in Synthesis of Ultrafine BaFe12O19 by Sol-Gel Technique. *J Magn Magn Mater* **1997**, *168* (1–2), 196–202. https://doi.org/10.1016/S0304-8853(96)00664-6.

(21) Sankaranarayanan, V. K.; Pankhurst, Q. A.; Dickson, D. P. E.; Johnson, C. E. Ultrafine Particles of Barium Ferrite from a Citrate Precursor. *J Magn Magn Mater* **1993**, *120* (1–3), 73–75. https://doi.org/10.1016/0304-8853(93)91290-N.

(22) Eikeland, A. Z.; Gjørup, F. H.; Andersen, H. L.; Christensen, M. High-Performance Hexaferrite Magnets Tailored through Alignment of Shape-Controlled Nanocomposites. *RSC Adv* **2024**, *14* (15), 10790–10798. https://doi.org/10.1039/D3RA05634A.

(23) Rana, K.; Thakur, S.; Tomar, M.; Gupta, V.; Thakur, A. Effect of Low Sintering Temperature on the Structural and Magnetic Properties of M-Type Strontium Hexaferrite. *J Magn Magn Mater* **2023**, *587*, 171289. https://doi.org/10.1016/J.JMMM.2023.171289.

(24) Pullar, R. C. Hexagonal Ferrites: A Review of the Synthesis, Properties and Applications of Hexaferrite Ceramics. *Prog Mater Sci* **2012**, *57* (7), 1191–1334. https://doi.org/10.1016/j.pmatsci.2012.04.001.

(25) Pullar, R. C.; Bhattacharya, A. K. Crystallisation of Hexagonal M Ferrites from a Stoichiometric Sol–Gel Precursor, without Formation of the α-BaFe2O4

Intermediate Phase. *Mater Lett* **2002**, *57* (3), 537–542. https://doi.org/10.1016/S0167-577X(02)00825-X.

(26) Sankaranarayanan, V. K.; Khan, D. C. Mechanism of the Formation of Nanoscale M-Type Barium Hexaferrite in the Citrate Precursor Method. *J Magn Magn Mater* **1996**, *153* (3), 337–346. https://doi.org/10.1016/0304-8853(95)00537-4.

(27) Gajbhiyeo, N. S.; Vijayalakshmi, A. THERMAL DECOMPOSITION OF STRONTIUM IRON CITRATE. *Journal ofThermal Analysis* **1998**, *51*, 517–527.

(28) Pradyot Patnaik. Handbook of Inorganic Chemicals. *Choice Reviews Online* **2003**, *40* (11), 40-6428-40–6428. https://doi.org/10.5860/CHOICE.40-6428.

(29) Bordia, R. K.; Camacho-Montes, H. Sintering: Fundamentals and Practice. In *Ceramics and Composites Processing Methods*; Wiley, 2012; pp 1–42. https://doi.org/10.1002/9781118176665.ch1.

(30) Hölscher, J.; Saura-Múzquiz, M.; Ahlburg, J.; Mørch, M.; Grønseth, D. K.; Christensen, M. Controlling Structural and Magnetic Properties of SrFe12O19 Nanoplatelets by Synthesis Route and Calcination Time. *J Phys D Appl Phys* **2020**, *53* (47), 474002. https://doi.org/10.1088/1361-6463/ABAAE1.

(31) Lee, S. W.; An, S. Y.; Kim, S. J.; Shim, I. B.; Kim, C. S. The Annealing Temperature Dependence of Magnetic Properties in Sr-Ferrite Nanoparticles. *IEEE Trans Magn* **2003**, *39* (5 II), 2899–2901. https://doi.org/10.1109/TMAG.2003.815741.

(32) Wang, Y.; Li, Q.; Zhang, C.; Li, B. Effect of Fe/Sr Mole Ratios on the Formation and Magnetic Properties of SrFe12O19 Microtubules Prepared by Sol–Gel Method. *J Magn Magn Mater* **2009**, *321* (19), 3368–3372. https://doi.org/10.1016/J.JMMM.2009.05.066.

(33) Vijayalakshmi, A.; Gajbhiye, N. S. Magnetic Properties of Single-Domain SrFe12O19 Particles Synthesized by Citrate Precursor Technique. *J Appl Phys* **1998**, *83* (1), 400–406. https://doi.org/10.1063/1.366654.

(34) Hessien, M. M.; Rashad, M. M.; El-Barawy, K. Controlling the Composition and Magnetic Properties of Strontium Hexaferrite Synthesized by Co-Precipitation Method. *J Magn Magn Mater* **2008**, *320* (3–4), 336–343. https://doi.org/10.1016/J.JMMM.2007.06.009.

(35) Drmota, A.; Drofenik, M.; Žnidaršič, A. Synthesis and Characterization of Nano-Crystalline Strontium Hexaferrite Using the Co-Precipitation and Microemulsion Methods with Nitrate Precursors. *Ceram Int* **2012**, *38* (2), 973–979. https://doi.org/10.1016/j.ceramint.2011.08.018.

(36) Jean, M.; Nachbaur, V.; Bran, J.; Le Breton, J. M. Synthesis and Characterization of SrFe12O19 Powder Obtained by Hydrothermal Process. *J Alloys Compd* **2010**, *496* (1–2), 306–312. https://doi.org/10.1016/J.JALLCOM.2010.02.002.

(37) Chen, Y.; Xiong, C.; Li, Y.; Chen, Y.; Xiong, C.; Li, Y. Additive Manufacturing of Rare Earth Permanent Magnetic Materials: Research Status and Prospects. *Metals 2024, Vol. 14, Page 446* **2024**, *14* (4), 446. https://doi.org/10.3390/MET14040446.

# **Chapter 4 |** Enhancing magnetic properties of SrM with chemical modification: Doping

So far we have discussed how tuning the magnetic properties of M-type $SrFe_{12}O_{19}$, such as $M_R$ and $H_C$, through nanoscale microstructural engineering. Another effective strategy to reach the goal is to modify the magnetic structure of the ferrite via chemical doping [1–5] . This latter strategy involves substituting SrM's metal ions with other elements, which can significantly tune, and potentially enhance, its magnetic properties. Indeed, M-type hexagonal ferrites, like SrM, possess a structural flexibility that allows for a large variety of cation substitutions for both $Fe^{3+}$ and $Sr^{2+}$. Cation substitution aims at modifying the magnetization of the material and enhance the magnetocrystalline anisotropy by inducing local changes in crystallographic and chemical structures. However, predicting doping's effect on these properties is still complex, as evidenced in the literature [3].

As discussed in Chapter 1, the magnetic structure of M-ferrite arises from the occupancy of five distinct crystallographic sites by $Fe^{3+}$ ions and their coupling through oxygen-mediated superexchange interactions [1]. The net magnetic moment and magneto-crystalline anisotropy depend on the spin and orbital moments of the cations, influenced by their site symmetry, valence state and spin configuration (high spin, low spin, intermediate spin) [3]. The magnetic moment of SrM is determined from the coupling of 16 $Fe^{3+}$ spins aligned in the majority direction (2a, 2b, and 12k sites) and 8 in the minority direction

(4f1 and 4f2 sites). [6–8], [9,10]. Thus, doping strategies can either enhance the total magnetization or improve the anisotropy depending on the site occupied by the dopant [3,11]. Although both $Sr^{2+}$ and $Fe^{3+}$ ions can be replaced, this study focused on the substitution of $Fe^{3+}$ sites only with the aim to elucidate if dopants show site selectivity and how this could affect magnetic behavior. However, this replacement also affects super-exchange interaction and anisotropy, and their effects are not always predictable or monotonic with concentration [3].

In this thesis work, different dopants, namely $Al^{3+}$ and $Mn^{3+}$, were investigated to obtain SrM nanoparticles with improved magnetic properties exploitable to develop a more functional material for PMs avoiding the use of REE.

# 4.1 Synthesis of doped SrM nanoparticles through the modified sol-gel method

Among the synthesis approaches used in this research, the modified sol-gel synthesis (MSG) appeared to be the most promising [12,13]. The MSG reaction resulted, indeed, in almost all the trials, in a single product with reproducible morphological and magnetic properties. To better evaluate the effect of the iron substitution in the structure of SrM, a single-ion doping was preferred over more unpredictable combinations, and different doping concentrations were investigated for each ion in object: the dopant ion (M) was replaced according to the stoichiometric proportions in the general formula $M_xSrFe_{12-x}O_{19}$. The resultant powders were then characterized through PXRD to evaluate the presence of any additional phases besides SrM and eventual modification of the crystal lattice, TEM to detect the changes in the particle size or morphology, PPMS_VSM magnetometry to measure the magnetic properties,

and ICP-AES to assess the stoichiometry of the synthesized compound. Beyond doping strategies, the synthesis procedure was designed to be functional and cost-effective for manufacturing and scalability. Therefore, we adopted the MSG synthesis, avoiding elevated temperatures to prevent excessive crystallites growth and intergrowing agglomeration.

### 4.1.1 Effect of Aluminium doping on the morphological and magnetic properties of SrM

According to the literature, aluminum is one of the most studied cations for modifying the magnetic properties of M-type hexaferrites[14–20]. The Al-doped hexaferrites, in most of the cases, exhibited large coercivities with respect to the pristine material, and that can be useful in various applications, among which PMs, indeed. Depending on the site where substitution occurs, it can result in an increase of the magnetic anisotropy. Depending on the amount of $Fe^{3+}$ replaced by $Al^{3+}$, the resultant coercivities can increase up to over 1 T [21] [22,23]. An interesting feature of the resulting strong resistance to demagnetizing fields lies in the potential for integration with REE-based magnets in engineering applications. In some cases, increasing the magnetic anisotropy field, led to a decrease in magnetization and Curie temperature. This behavior is attributed to the site occupancy of $Al^{3+}$ cations among the five crystallographic sites of $Fe^{3+}$ in the SrM lattice. Theoretical calculations performed by Dixit *et al.* [1124] supported by experimental results [25–27], suggested a preferential occupancy for $Al^{3+}$ into the 12k or 2a octahedral site, both associated with spin-up alignment. Consequently, since $Al^{3+}$ is diamagnetic its introduction into these positions may lower the net magnetization and slightly weaken the super-exchange interactions, reducing the Curie temperature.

Nevertheless, by carefully controlling the doping concentration and site occupancy, it is possible to tailor the balance between coercivity, magnetization, and thermal stability—paving the way for customized strontium hexaferrites with improved performance and specific functional advantages.

Here, the MSG procedure was used to synthesis aluminum-doped SrM nanoparticles. To investigate the effect of $Al^{3+}$ doping on the morphological and magnetic properties of SrM, three Al-doped SrM samples with different $Al^{3+}$ concentrations were synthesized. The obtained precursors underwent two calcination steps: at 450 °C for 1 h followed by 790 °C for 1 h. The synthesized samples were named *Al(x)-SrM_MSG,* following the estimated molar ratio (*x*) in the formula corresponding to composition $Al_xSr_1Fe_{12-x}O_{19}$. The results were compared with the undoped SrM, named SrM_MSG_R12 (synthesis details in Chapter 3).

The stoichiometry of the obtained compound was checked by ICP-AES, confirming the presence of $Al^{3+}$ in the particles. However, $Al^{3+}$ concentration was systematically lower than the amount set in the synthesis: the effective molar ratio in the formula $Al_xSrFe_{12-x}O_{19}$ was 0.25 for the nominal ratio 0.5, 0.51 for the nominal ratio 1, and 0.38 for the nominal ratio 2. Instead, when the ICP-AES was performed on the powdered gel precursor, before the calcination step, the proper amount of $Al^{3+}$ was detected (Al = 1.18 for Al(1)-SrM). This discrepancy suggests that the diffusion rate of the ion into the lattice is limited under these operating conditions. Probably the low temperature calcination hindered the full conversion of precursors in Al-SrM [28]. The unreacted precursors, or other phases, such as spinel-like $Sr(Al, Fe)_2O_4$ and $Al_2O_3$, could have been removed during the subsequent washing stage with $HNO_3$ 4M and DM water in the MSG procedure [29].

***Table 4-1*** *Al, Sr, Fe content evaluated by elemental analysis (ICP-AES) reported as stoichiometric amount in the formula unit* $Al_xSr_1Fe_{(12-x)}O_{19}$.

| Sample | Element content | | |
|---|---|---|---|
| | Al | Sr | Fe |
| **SrM_MSG_R12** | 0 | 1.06 | 11.94 |
| **Al(0.5)-SrM_MSG** | 0.25 | 1.02 | 11.73 |
| **Al(1)-SrM_MSG** | 0.51 | 1.03 | 11.47 |
| **Al(2)-SrM_MSG** | 0.38 | 1.02 | 11.60 |

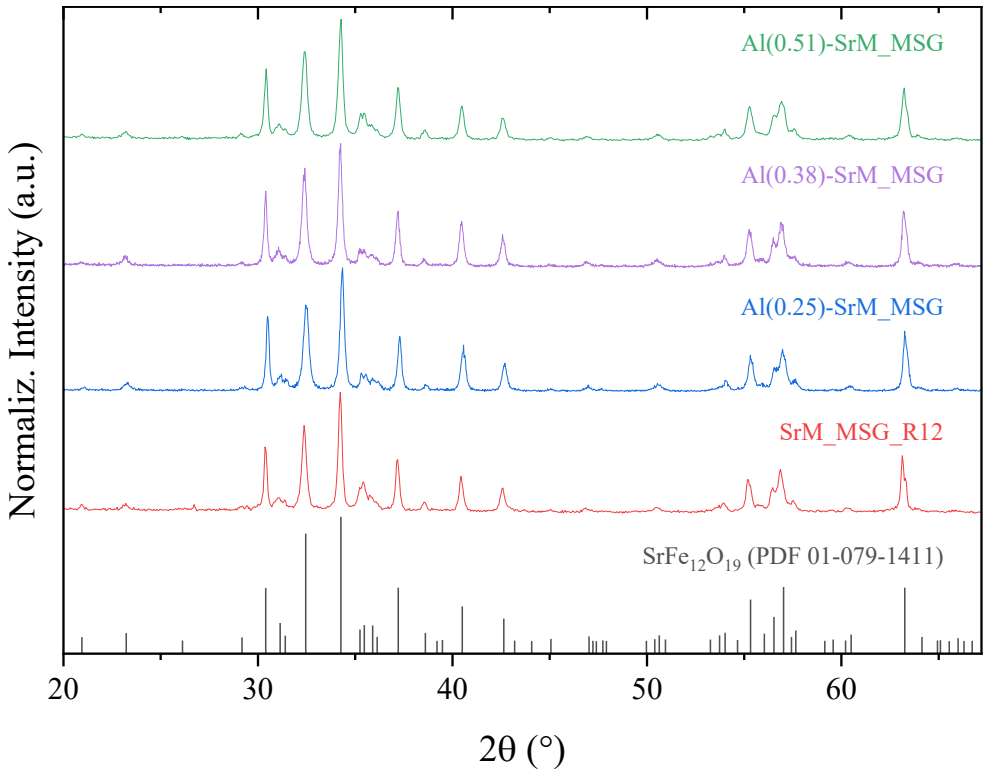


***Figure 4-1*** *PXRD diffractograms of SrM samples produced by MSG synthesis with different Al content. The samples were named Al(x)-SrM_MSG, indicating as x the Al molar ratio in the formula* $Al_{(x)}Sr_1Fe_{(12-x)}O_{19}$. *The sample SrM_MSG_R12 refers to the undoped SrM with molar ratio* $Fe^{3+}/Sr^{2+} = 12$ *made with the same procedure.*

In **Figure 4-1** are shown the diffraction patterns of the synthesized Al-SrM samples, in which the profiles correspond to the M-type $SrFe_{12}O_{19}$ structure with no presence of secondary phases. The Pawley refinement of the cell

parameters (**Table 4-2**), underlined the decrease in the crystallite size and in *a* and *c* values as the $Al^{3+}$ content is increased. This result is coherent with the smaller ionic radius of $Al^{3+}$ (0.535 Å) than $Fe^{3+}$ (0.645 Å).

***Table 4-2*** *Crystallite size and cell parameters (PXRD), and mean size and standard deviation (evaluated from over 200 particles in TEM images using ImageJ software) of SrM samples produced by MSG synthesis with different Al content. The sample SrM_MSG_R12 refers to the undoped SrM with molar ratio* $Fe^{3+}/Sr^{2+} = 12$ *made with the same procedure.*

| Sample | Cry.size (nm) | a (Å) | c (Å) | Mean Size (nm) | Std Dev. (nm) |
|---|---|---|---|---|---|
| **SrM_MSG_R12** | 58(1) | 5.8878(5) | 23.066(2) | 94 | 50 |
| **Al(0.25)-SrM_MSG** | 48(1) | 5.8852(5) | 23.055(2) | 80 | 30 |
| **Al(0.38)-SrM_MSG** | 50(1) | 5.8816(4) | 23.038(2) | 57 | 29 |
| **Al(0.51)-SrM_MSG** | 46(1) | 5.8813(5) | 23.040(2) | 66 | 27 |

Similarly, TEM images (**Figure 4-2**) revealed a progressive decrease in the average particle size as the $Al^{3+}$ content increases reaching a value of 57 nm for Al(0.38)-SrM, almost 40 nm less than the pristine SrM_MSG_R12. However, the nanoparticles in the Al-doped samples remain mostly polycrystalline, as suggested by the comparison of crystallite size and the actual size derived from TEM.

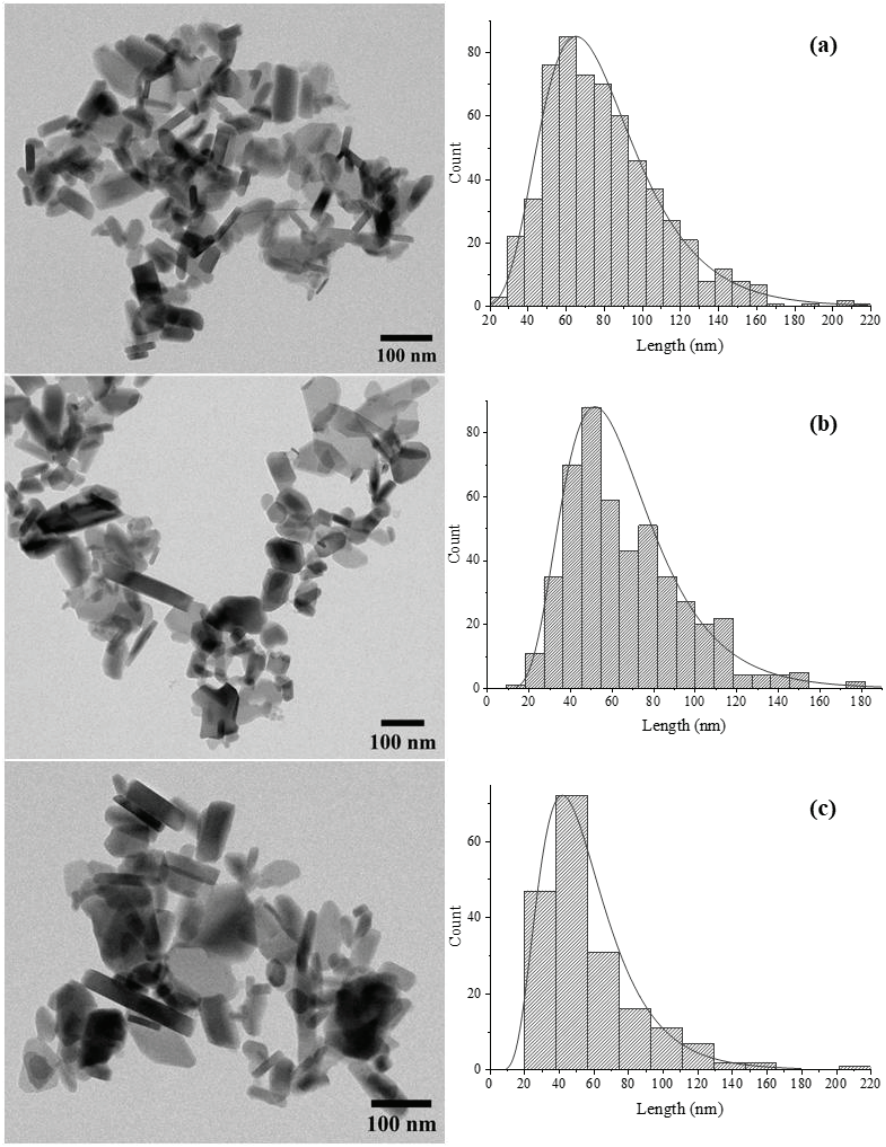


***Figure 4-2*** *TEM images of SrM samples produced by modified sol-gel (MSG) synthesis with different Al content: (a) Al(0.25)-SrM, (b) Al(0.51)-SrM, (c) Al(0.38)-SrM. On the right, the corresponding histograms of particle size distribution, estimated from over 200 nanoparticles and fitted with a lognormal function (black line).*

Magnetic properties of the proposed samples were studied recording hysteresis loops at 300 K (**Figure 4-3**), and the estimated values of remanence and coercivity were summarized in **Table 4-3**. Increasing the Al content in the

samples led clearly to an enhancement of the coercivity, reaching a really high value of 0.7 T for sample Al(0.51)-SrM. In combination with $H_C$ enhancement, a decrease in $M_S$ value came along with the increased doping, in accordance with the insertion of a non-magnetic ion in the spin-up sites and weakened super-exchange interactions [24]. The magnetic behavior of the three samples reflected the increasing amount of $Al^{3+}$ concentration in the SrM, as detected by ICP and further supported by the decreased crystallite size estimated from XRD. Therefore, the inclusion of Al, even if partial, allowed for the advantageous obtainment of hexaferrite nanoparticles with noticeably improved coercivity value.

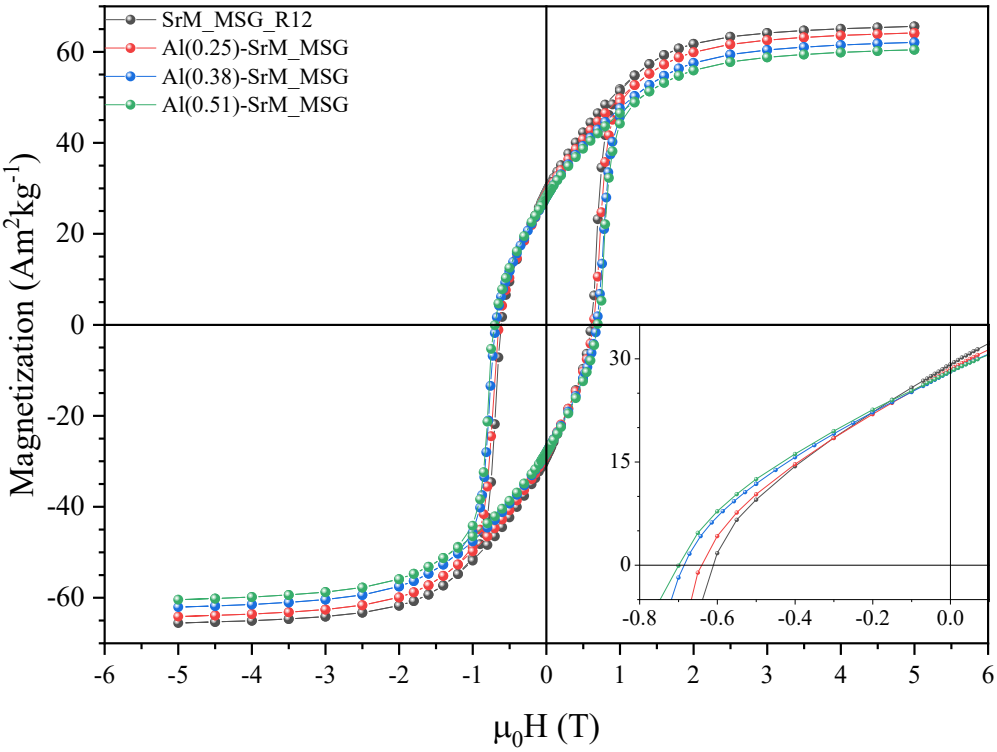


***Figure 4-3*** *Hysteresis loops at 300K of SrM samples produced by MSG synthesis with different Al content. In the inset, the enlargement at low field of the corresponding demagnetization curves is highlighted.*

***Table 4-3*** *Magnetic properties estimated from hysteresis loops at 300K of SrM samples produced by MSG synthesis with different Al content.*

| Sample | $M_s$ ($Am^2kg^{-1}$) | $M_r$ ($Am^2kg^{-1}$) | $M_r/M_s$ | $\mu_0H_c$ (T) |
|---|---|---|---|---|
| **SrM_MSG_R12** | 66 | 29 | 0.44 | 0.61 |
| **Al(0.25)-SrM_MSG** | 64 | 28 | 0.44 | 0.64 |
| **Al(0.38)-SrM_MSG** | 62 | 28 | 0.45 | 0.68 |
| **Al(0.51)-SrM_MSG** | 60 | 28 | 0.47 | 0.70 |

## 4.1.2 Effect of Manganese doping on the morphology and magnetic properties of SrM

Manganese is a transition metal that can present different valencies, and its cations possess ionic radii comparable to that of $Fe^{3+}$ (0.645 Å), particularly $Mn^{3+}$ (0.645 Å). This similarity facilitates the substitution of $Fe^{3+}$ ions at one or more of the five distinct crystallographic sites (12k, 4f1, 4f2, 2a, 2b) within the M-type hexagonal structure, without causing excessive lattice distortion. Differently from $Al^{3+}$, $Mn^{3+}$ ions carry their own magnetic moments, so their incorporation into the hexaferrite lattice, depending on the preferential site occupancy and oxidation state, can either enhance or reduce the net magnetization[30–32]. Some studies suggest Mn tends to occupy specific sites, while others indicate a more distributed substitution, often dependent on the Mn concentration and the synthesis conditions. In the case of $Mn^{3+}$, early work of Obradors et al [33] showed that the magnetic anisotropy field at low temperatures increases for high doping levels (x=9). Other studies reported Mn occupying first the spin up 12k and 2a sites and later the 4f2 sites [30,34]. Tenorio et al [30] outlined that the $Mn^{3+}$ ions occupy preferentially the 2a sites up to x=2. If the Mn content further increases, it occupies first the 12k position and then 4f1 and 4f2 sites. The occupancy in spin-up sites of $Mn^{3+}$ ion, which has a

smaller magnetic moment (3.5 μB) than $Fe^{3+}$ (5 μB), explains the decrease in overall magnetization. On the other hand, the same study reports that $H_C$ reaches 0.97 T for x = 5, but with a strong impact on $M_S$ (35 $Am^2kg^{-1}$) and the formation of large, aggregated particles with a size distribution of 250-600 nm, that is in a much larger size range than that we aim to address in this work.

Therefore, similarly to what was done with Al, the Mn-doped SrM nanoparticles were produced through MSG synthesis, with dopant molar ratios equal to 0.5, 1, and 1.5. The reagents were weighed in accordance, then the powders were calcined at 450 °C for 1 h followed by 790 °C for 1 h. The synthesized samples were named *Mn(x)-SrM_MSG,* following the estimated molar ratio (*x*) in the formula corresponding to composition $Mn_xSr_1Fe_{12-x}O_{19}$. To evaluate the effective stoichiometry, the samples were analyzed through ICP-AES. The obtained powders were subsequently characterized by PXRD and TEM to evaluate the crystallographic features and morphology, and VSM analysis was performed to investigate magnetic characteristics. The results were then compared with the undoped SrM having stoichiometric molar ratio ($Fe^{3+}/Sr^{2+}$= 12), prepared using the same process, named SrM_MSG_R12.

The ICP results showed that the effective manganese content matched its nominal value in the Mn(0.5)-SrM_MSG sample. Conversely, when the Mn concentration in the synthesis was raised, a lower Mn content was found in the final product (0.71 for the nominal value of 1, and 1.07 for the nominal value of 1.5). As hypothesized for the Al-doped series, probably the incorporation of Mn is not complete under these conditions, and the subsequent washing stage with $HNO_3$ and DM water could remove the unreacted reagents and by-products. In fact, even in this case the ICP analysis resulted in a correct Mn concentration (Mn =1) in the precursor gel.

***Table 4-4*** *Mn, Sr, Fe content evaluated by ICP-AES reported as stoichiometric amount per formula unit* $Mn_xSr_1Fe_{(12-x)}O_{19}$.

| Sample | Element content | | |
|---|---|---|---|
| | **Mn** | **Sr** | **Fe** |
| **SrM_MSG_R12** | 0 | 1.06 | 11.94 |
| **Mn(0.5)-SrM_MSG** | 0.51 | 1.08 | 11.41 |
| **Mn(1)-SrM_MSG** | 0.73 | 1.10 | 11.18 |
| **Mn(1.5)-SrM_MSG** | 1.07 | 1.08 | 10.85 |

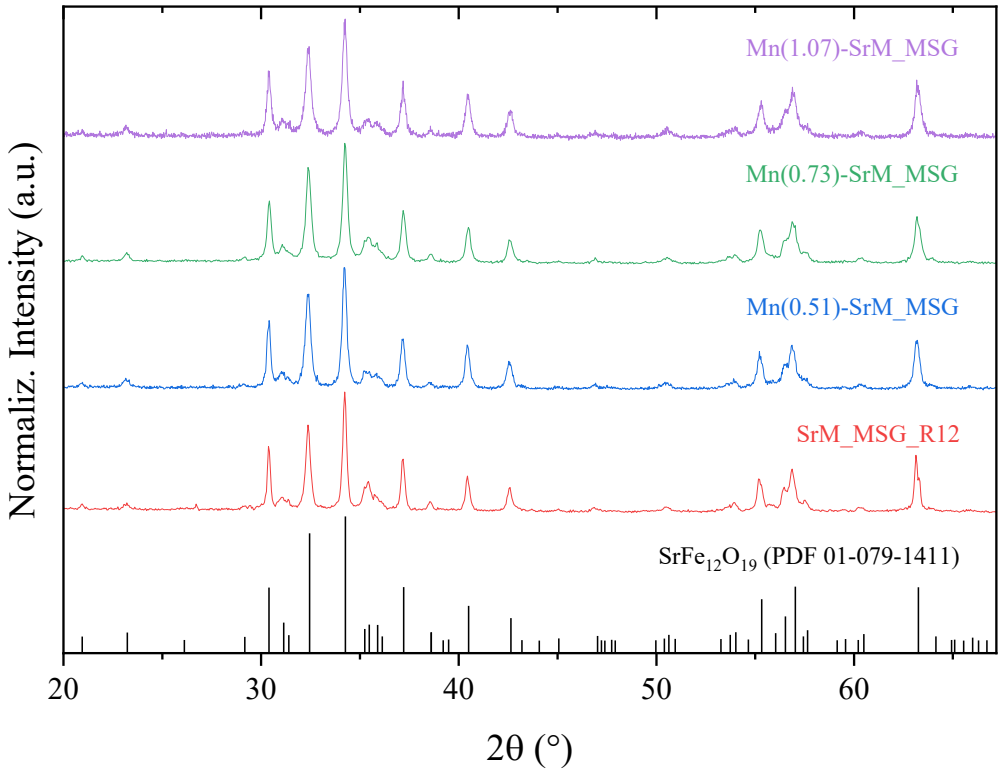


***Figure 4-4*** *PXRD diffractograms of SrM samples produced by MSG synthesis with different Mn content. The sample SrM_MSG_R12 refers to the undoped SrM with molar ratio* $Fe^{3+}/Sr^{2+}$ *= 12, made with the same procedure.*

***Table 4-5*** *Crystallite size and cell parameters (PXRD), mean size and standard deviation (evaluated from over 300 particles in TEM images using ImageJ software) of SrM samples produced by MSG synthesis with different Mn content.*

| Sample | Cry.size (nm) | a (Å) | c (Å) | Mean Size (nm) | Std. Dev. (nm) |
|---|---|---|---|---|---|
| **SrM_MSG_R12** | 58(1) | 5.8878(5) | 23.066(2) | 94 | 50 |
| **Mn(0.51)-SrM_MSG** | 41(1) | 5.8876(6) | 23.062(2) | 46 | 16 |
| **Mn(0.73)-SrM_MSG** | 41(1) | 5.8852(6) | 23.051(2) | 35 | 17 |
| **Mn(1.07)-SrM_MSG** | 35(1) | 5.8829(7) | 23.040(3) | 33 | 14 |

Only the M-type $SrFe_{12}O_{19}$ crystallographic phase can be observed in the PXRD patterns, suggesting the correct obtainment of a pure and single-phase product. No appreciable shift of the peaks was noticed after the dopant insertion, and this fact is coherent with the overlapping dimensions of $Fe^{3+}$ and $Mn^{3+}$ ionic radius. Consistently only a very small variation of the lattice parameters (*a* and *c*) is observed. A more remarkable variation was in the crystallite size, towards lower values with increasing Mn content. Additionally, the analysis of TEM images (**Figure 4-5**) displays the doped samples comprise smaller grains with respect to undoped sample. From that, it can be argued that the Mn insertion sensibly influences the mean physical particle size, reaching the half or even less with respect to the undoped SrM, and with much smaller standard deviation. Furthermore, the good agreement between the average dimensions obtained from TEM and the crystal grain size from XRD measurements of the Mn-doped particles indicates predominantly single-crystal nanoparticles, compared to all the other synthesized samples.

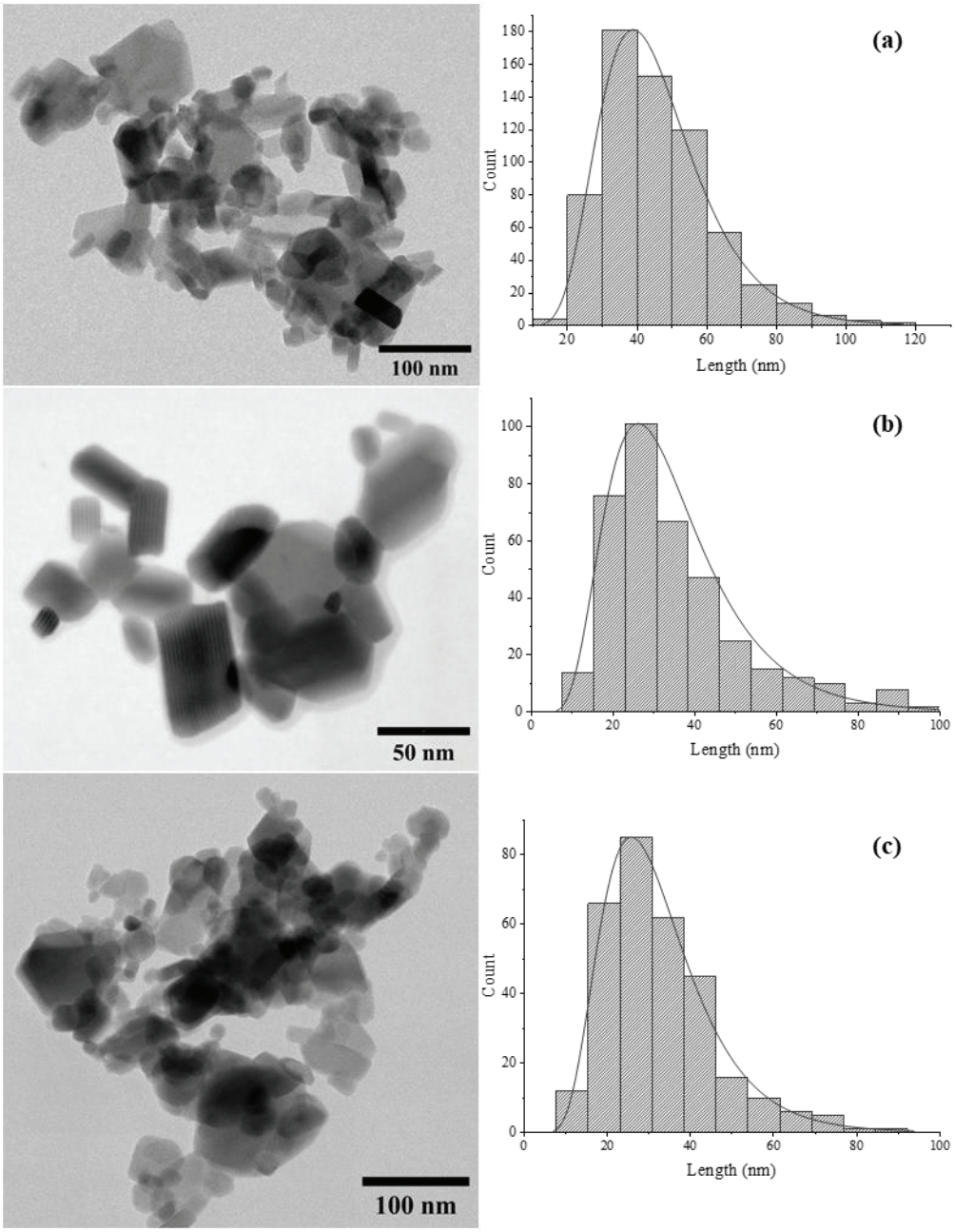


***Figure 4-5*** *TEM images of SrM samples produced by MSG synthesis with different Mn content: (a) Mn(0.51)-SrM, (b) Mn(0.73)-SrM, (c) Mn (1.07)-SrM.On the right, the corresponding histograms of particle size distribution, estimated from over 300 particles and fitted with a lognormal function (black line).*

Another noticeable difference was observed in the magnetic behavior of the synthesized Mn-doped SrM. The saturation magnetization value decreased progressively with the increasing Mn content, coherently with the preferential insertion of Mn in the 12k and 2a spin-up positions [30,35]. Conversely, the coercivity increased, reaching a maximum value of 0,65 T for x = 0.73, with an increase of 6.5% with respect to the pristine Sr-ferrite. Then, it decreased for higher doping values. The relative difference between these latter values is small and could derive from a partial physical alignment of the nanoparticles in the preparation of the sample for VSM measurement, which could also explain the small kink in the hysteresis curve when the magnetic field is removed. The literature is not univocal in addressing the effect the insertion of Mn in the lattice of hexagonal ferrites on the magnetic properties, from induced microstrains [30] to an increased magnetic dipole coupling [31]. Most of the samples reported so far are prepared derive from mechanosynthesis [33,34,36,37], thermal decomposition [38], or single crystal growth [38]. They mostly report, for substitutions over x = 1, a decreased value of the anisotropy constant caused by the lattice distortion, with weakened super-exchange interactions and disrupted spin collinearity. In our case, at lower Mn concentrations, we found that Mn-doping led to predominantly single-crystal hexaferrite nanoparticles with particularly small size (around 40 nm) and enhanced coercivity with respect to the undoped nanoparticles, although with only a small decrease of the remnant magnetization. Thus, in view of the scope of our work, the addition of Mn appeared definitely beneficial.

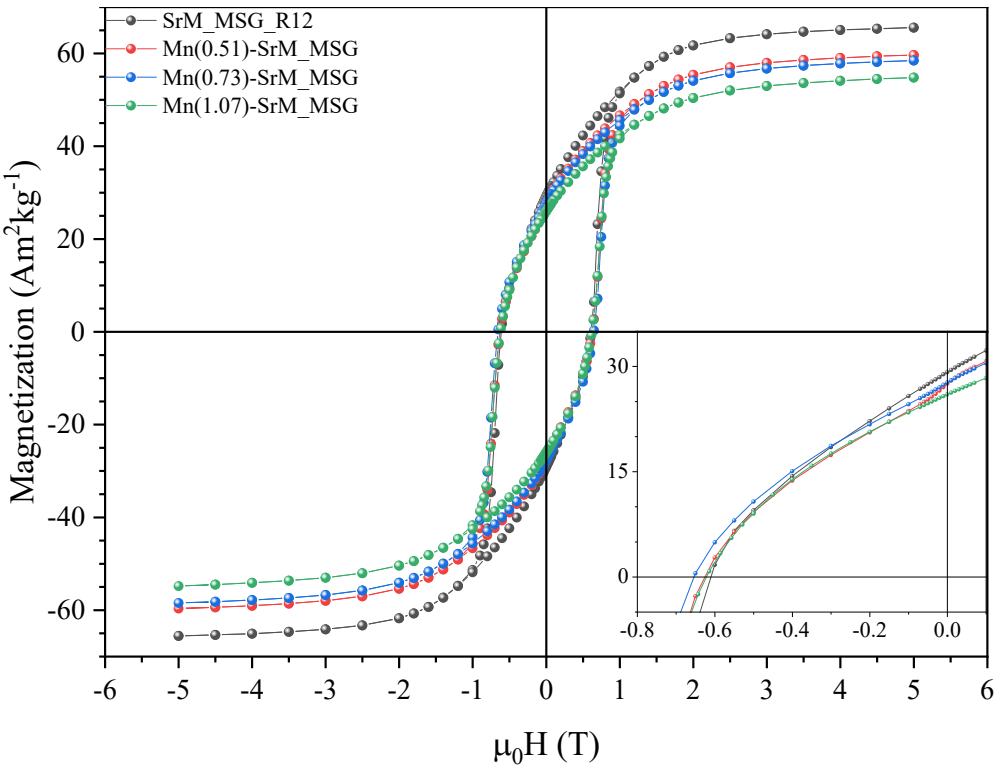


***Figure 4-6*** *Hysteresis loops at 300K of SrM samples produced by MSG synthesis with different Mn content. In the inset, the enlargement at low field of the corresponding demagnetization curves is highlighted.*

***Table 4-6*** *Magnetic properties derived from hysteresis loops at 300K of SrM samples produced by MSG synthesis with different Mn content.*

| Sample | $M_s$ ($Am^2kg^{-1}$) | $M_r$ ($Am^2kg^{-1}$) | $M_r/M_s$ | $\mu_0H_c$ (T) |
|---|---|---|---|---|
| **SrM_MSG_R12** | 66 | 29 | 0.44 | 0.61 |
| **Mn(0.51)-SrM_MSG** | 60 | 28 | 0.46 | 0.62 |
| **Mn(0.73)-SrM_MSG** | 58 | 28 | 0.47 | 0.65 |
| **Mn(1.07)-SrM_MSG** | 55 | 26 | 0.47 | 0.62 |

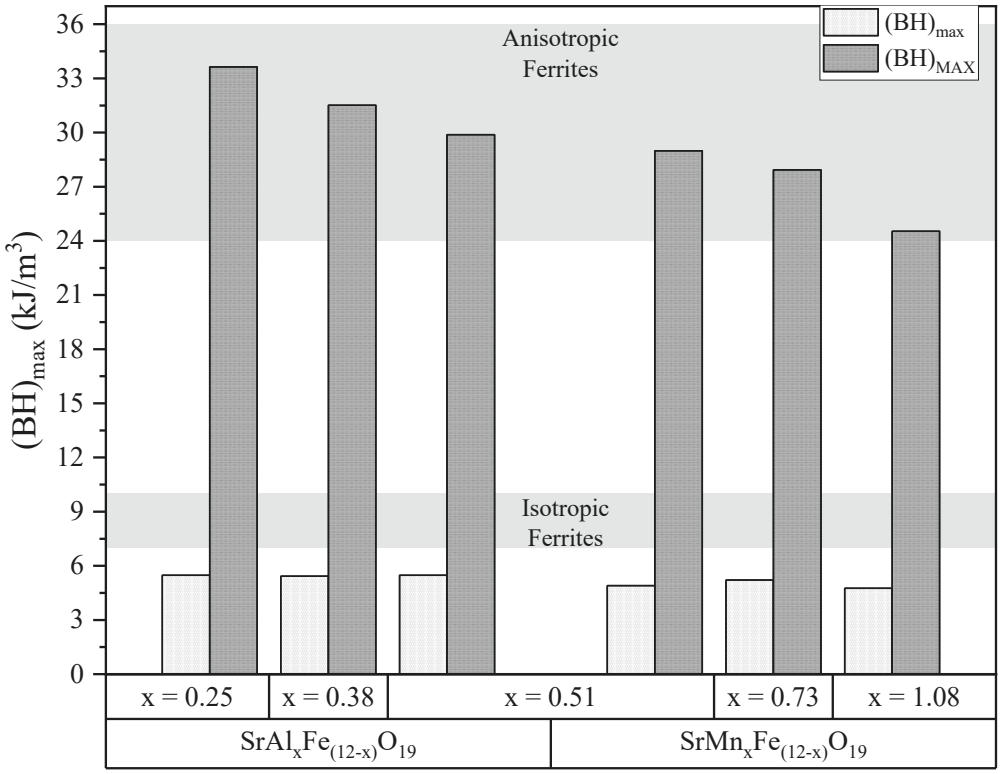


***Figure 4-7*** *Comparison between the measured $(BH)_{max}$ values (white columns) for Al- and Mn-doped SrM samples and the corresponding theoretical estimates $(BH)_{MAX}$ (grey columns) for fully-dense and oriented samples. Reference ranges for commercial isotropic ferrites (7–10 kJ/m³) and anisotropic ferrites (24–36 kJ/m³) are also reported.*

***Table 4-7*** *Magnetic parameters of Al- and Mn-doped SrM samples: remanence ($B_R$), normal coercivity ($H_{Cb}$), intrinsic coercivity ($H_{Ci}$), measured maximum energy product ($(BH)_{max}$), and theoretical maximum energy product ($(BH)_{MAX}$).*

| Sample | $B_R$ (mT) | $Hc_b$ (kA/m) | $Hc_i$ (kA/m) | $(BH)_{max}$ (kJ/m³) | $(BH)_{MAX}$ (kJ/m³) |
|---|---|---|---|---|---|
| **Al(0.25)-SrM_MSG** | 181 | 120 | 509 | 5.5 | 33.6 |
| **Al(0.38)-SrM_MSG** | 179 | 121 | 545 | 5.4 | 31.5 |
| **Al(0.51)-SrM_MSG** | 179 | 122 | 556 | 5.5 | 29.9 |
| **Mn(0.51)-SrM_MSG** | 175 | 114 | 497 | 4.9 | 29.0 |
| **Mn(0.73)-SrM_MSG** | 176 | 119 | 517 | 5.2 | 27.9 |
| **Mn(1.07)-SrM_MSG** | 165 | 114 | 494 | 4.8 | 24.5 |

The performances for each doped SrM sample were also evaluated (**Table 4-7**). The $(BH)_{max}$ was calculated by the hysteresis curves obtained from VSM measurements, adopting the X-ray crystallographic densities for the synthesized samples and a demagnetizing factor $N_x = 0.1$ for a thin disk pellet [39]. The resultant $(BH)_{max}$ values were found to be lower than commercial isotropic ferrite magnets, as shown in **Figure 4-7**, which values are in the range of 7-10 kJ/m$^3$ (around 1 MGOe)[40,41]. The increase in intrinsic coercivity did not directly translate into a proportional enhancement of $(BH)_{max}$ in isotropic samples, since the remanence and the squareness of the demagnetization curve remain limiting factors. Additionally, the ideal theoretical value, $(BH)_{MAX}$, was estimated through the equation $1/4\mu_0 M_S^2$ for a fully dense and perfectly oriented sample[42]. This highlights the intrinsic potential of the materials, falling in the range of commercial anisotropic ferrites[43,44]. Both in Al- and Mn-doped series, the theoretical $(BH)_{MAX}$ decreased with increasing dopant content, coherently with the reduced magnetization caused by the substitution of $Fe^{3+}$ cations. Nevertheless, the high intrinsic coercivity represents an important prerequisite for magnetic stability, ensuring resistance against external perturbations.

# 4.2 Conclusion

The synthesis of doped SrM nanoparticles with enhanced magnetic and morphological features by chemical modification was successfully achieved. Particularly, the MSG method allowed for the successful replacement of $Fe^{3+}$ ions with Al and Mn cations, although some discrepancy between the nominal and the effective content of the dopant were found. This was particularly noticeable in the Al-doped series, as the effective content incorporated into the hexagonal lattice was consistently lower than the targeted amounts, and to a minor extent even in the case of manganese. This suggests some limitations in

the diffusion rate of the cations under these specific synthesis conditions. Further investigations could regard a slight increase in the calcination temperature and duration to effectively determine if the dopant content can be enhanced, or if it is a limitation of the procedure itself. However, the synthesized doped particles presented remarkable differences in morphological and magnetic properties, in comparison with the undoped material obtained from the same procedure. The inclusion of Al resulted in a small decrease in the lattice parameters and mean particle size, coherently with the smaller ionic radius of Al, while the samples maintained a polycrystalline nature. Conversely, a different behavior was encountered as concerns the mean particle size of Mn-doped nanoparticles. In this case, the lattice parameters remained almost unchanged, in agreement with the similarity in ionic radii of $Mn^{3+}$ and $Fe^{3+}$. The crystallite size was decreased by the Mn incorporation, while at the same time the grain size remarkably decreased compared to Al doping, leading to considerably smaller nanoparticles (half or even less than undoped SrM). Moreover, the Mn-doped particles showed a good agreement between TEM and PXRD, indicating predominantly single-crystal nanoparticles, a notable improvement over the polycrystalline nature of undoped and Al-doped samples. Regarding the magnetic properties, the insertion of both cations affected the saturation magnetization. On the other hand, Al significantly enhanced the coercivity, reaching a remarkable value up to 0.7 T for Al(0.51)-SrM. The calculated $(BH)_{max}$ of the synthesized doped samples, although below than the commercial isotropic standard due to limited remanence and squareness in the isotropic powder, retained a significant theoretical potential comparable to anisotropic ferrites. The improved resistance to demagnetization, provided by the high intrinsic coercivities, could be practical for stable PM applications.

In summary, this test demonstrated that the chemical modification by doping can effectively enhance the structural, morphological and magnetic properties of the synthesized SrM nanoparticles, highlighting the potential for tailoring properties through precise dopant selection and control. The Al doping was particularly efficient to increase the coercivity of the material, while the Mn was determinant in yielding nanoparticles with notably reduced size. Future studies will regard the promising opportunity to combine these effects (co-doping strategy), while exploring the substitution with different metal cations to further enhance the SrM features.

# References


(1) Kojima, H. Fundamental Properties of Hexagonal Ferrites with Magnetoplumbite Structure. In *Handbook of Ferromagnetic Materials*; Elsevier, 1982; Vol. 3, pp 305–391. https://doi.org/10.1016/S1574-9304(05)80091-4.

(2) Pullar, R. C. Hexagonal Ferrites: A Review of the Synthesis, Properties and Applications of Hexaferrite Ceramics. *Prog Mater Sci* **2012**, *57* (7), 1191–1334. https://doi.org/10.1016/j.pmatsci.2012.04.001.

(3) de Julián Fernández, C.; Sangregorio, C.; de la Figuera, J.; Belec, B.; Makovec, D.; Quesada, A. Progress and Prospects of Hard Hexaferrites for Permanent Magnet Applications. *J Phys D Appl Phys* **2021**, *54* (15), 153001. https://doi.org/10.1088/1361-6463/ABD272.

(4) Lisjak, D.; Mertelj, A. Anisotropic Magnetic Nanoparticles: A Review of Their Properties, Syntheses and Potential Applications. *Prog Mater Sci* **2018**, *95*, 286–328. https://doi.org/10.1016/J.PMATSCI.2018.03.003.

(5) Mahmood, S. H.; Bsoul, I. Tuning the Magnetic Properties of M-Type Hexaferrites.

(6) Fang, C. M.; Kools, F.; Metselaar, R.; De With, G.; De Groot, R. A. Magnetic and Electronic Properties of Strontium Hexaferrite SrFe12O19from First-Principles Calculations. *Journal of Physics: Condensed Matter* **2003**, *15* (36), 6229. https://doi.org/10.1088/0953-8984/15/36/311.

(7) Soria, G. D.; Jenus, P.; Marco, J. F.; Mandziak, A.; Sanchez-Arenillas, M.; Moutinho, F.; Prieto, J. E.; Prieto, P.; Cerdá, J.; Tejera-Centeno, C.; Gallego, S.; Foerster, M.; Aballe, L.; Valvidares, M.; Vasili, H. B.; Pereiro, E.; Quesada, A.; de la Figuera, J. Strontium Hexaferrite Platelets: A Comprehensive Soft X-Ray Absorption and Mössbauer Spectroscopy Study. *Scientific Reports 2019 9:1* **2019**, *9* (1), 1–13. https://doi.org/10.1038/s41598-019-48010-w.

(8) Tejera-Centeno, C.; Gallego, S.; Cerdá, J. I. An Ab Initio Study of the Magnetic Properties of Strontium Hexaferrite. *Sci Rep* **2021**, *11* (1), 1964. https://doi.org/10.1038/s41598-021-81028-7.

(9) Smit, J.; Wijn, H. P. J.; Luton, G. E. *Ferrites : Physical Properties of Ferrimagnetic Oxides in Relation to Their Technical Applications*; Philips' Technical Library, Ed.; 1959.

(10) Obradors, X.; Solans, X.; Collomb, A.; Samaras, D.; Rodriguez, J.; Pernet, M.; Font-Altaba, M. Crystal Structure of Strontium Hexaferrite SrFe12O19. *J Solid State Chem* **1988**, *72* (2), 218–224. https://doi.org/10.1016/0022-4596(88)90025-4.

(11) Dixit, V.; Kim, S. G.; Park, J.; Hong, Y. K. Effect of Ionic Substitutions on the Magnetic Properties of Strontium Hexaferrite: A First Principles Study. *AIP Adv* **2017**, *7* (11). https://doi.org/10.1063/1.4995309/22415.

(12) Sapoletova, N. A.; Kushnir, S. E.; Li, Y. H.; An, S. Y.; Seo, J. W.; Hur, K. H. Plate-like SrFe12O19 Particles Prepared by Modified Sol–Gel Method. *J Magn Magn Mater* **2015**, *389*, 101–105. https://doi.org/10.1016/J.JMMM.2015.04.055.

(13) Eikeland, A. Z.; Stingaciu, M.; Mamakhel, A. H.; Saura-Múzquiz, M.; Christensen, M. Enhancement of Magnetic Properties through Morphology Control of SrFe12O19 Nanocrystallites. *Sci Rep* **2018**, *8* (1), 7325. https://doi.org/10.1038/s41598-018-25662-8.

(14) Rhein, F.; Karmazin, R.; Krispin, M.; Reimann, T.; Gutfleisch, O. Enhancement of Coercivity and Saturation Magnetization of Al3+ Substituted M-Type Sr-Hexaferrites. *J Alloys Compd* **2017**, *690*, 979–985. https://doi.org/10.1016/J.JALLCOM.2016.08.085.

(15) Ma, X.-M.; 马小梅; Liu, J.; 刘杰; Zhu, S.-Z.; 朱生志; Shi, H.-G.; 史慧刚. Tuning of Magnetic Properties of Aluminium-Doped Strontium Hexaferrite Powders. *Chinese Physics B* **2016**, *25* (12), 126102. https://doi.org/10.1088/1674-1056/25/12/126102.

(16) Maltoni, P.; Barucca, G.; Rutkowski, B.; Ivanov, S. A.; Yaacoub, N.; Mikheenkova, A.; Ek, G.; Eriksson, M.; Almqvist, B.; Vasilakaki, M.; Varvaro, G.; Sarkar, T.; De Toro, J. A.; Trohidou, K.; Peddis, D.; Mathieu, R. Engineering Hard Ferrite Composites by Combining Nanostructuring and Al3+ Substitution: From Nano to Dense Bulk Magnets. *Acta Mater* **2025**, *282*, 120491. https://doi.org/10.1016/j.actamat.2024.120491.

(17) Shirtcliffe, N. J.; Thompson, S.; O'Keefe, E. S.; Appleton, S.; Perry, C. C. Highly Aluminium Doped Barium and Strontium Ferrite Nanoparticles Prepared by Citrate Auto-Combustion Synthesis. *Mater Res Bull* **2007**, *42* (2), 281–287. https://doi.org/10.1016/j.materresbull.2006.06.001.

(18) Wang, H. Z.; Yao, B.; Xu, Y.; He, Q.; Wen, G. H.; Long, S. W.; Fan, J.; Li, G. D.; Shan, L.; Liu, B.; Jiang, L. N.; Gao, L. L. Improvement of the Coercivity of Strontium Hexaferrite Induced by Substitution of Al3+ Ions for Fe3+ Ions. *J Alloys Compd* **2012**, *537*, 43–49. https://doi.org/10.1016/J.JALLCOM.2012.05.063.

(19) Singhal, S.; Namgyal, T.; Singh, J.; Chandra, K.; Bansal, S. A Comparative Study on the Magnetic Properties of MFe12O19 and MAlFe11O19 (M = Sr, Ba and Pb) Hexaferrites with Different Morphologies. *Ceram Int* **2011**, *37* (6), 1833–1837. https://doi.org/10.1016/J.CERAMINT.2011.02.001.

(20) Liu, M.; Shen, X.; Song, F.; Xiang, J.; Meng, X. Microstructure and Magnetic Properties of Electrospun One-Dimensional Al3+-Substituted SrFe12O19 Nanofibers. *J Solid State Chem* **2011**, *184* (4), 871–876. https://doi.org/10.1016/j.jssc.2011.02.010.

(21) Luo, H.; Rai, B. K.; Mishra, S. R.; Nguyen, V. V.; Liu, J. P. Physical and Magnetic Properties of Highly Aluminum Doped Strontium Ferrite Nanoparticles Prepared by Auto-Combustion Route. *J Magn Magn Mater* **2012**, *324* (17), 2602–2608. https://doi.org/10.1016/j.jmmm.2012.02.106.

(22) Wang, S.; Ding, J.; Shi, Y.; Chen, Y. J. High Coercivity in Mechanically Alloyed BaFe10Al2O19. *J Magn Magn Mater* **2000**, *219* (2), 206–212. https://doi.org/10.1016/S0304-8853(00)00450-9.

(23) Wang, H. Z.; Hai, Y. N.; Yao, B.; Xu, Y.; Shan, L.; Xu, L.; Tang, J. L.; Wang, Q. H. Tailoring Structure and Magnetic Characteristics of Strontium Hexaferrite via Al Doping Engineering. *J Magn Magn Mater* **2017**, *422*, 204–208. https://doi.org/10.1016/j.jmmm.2016.08.066.

(24) Dixit, V.; Nandadasa, C. N.; Kim, S.-G.; Kim, S.; Park, J.; Hong, Y.-K.; Liyanage, L. S. I.; Moitra, A. Site Occupancy and Magnetic Properties of Al-Substituted M-Type Strontium Hexaferrite. *J Appl Phys* **2015**, *117* (24). https://doi.org/10.1063/1.4922867.

(25) Dhage, V. N.; Mane, M. L.; Keche, A. P.; Birajdar, C. T.; Jadhav, K. M. Structural and Magnetic Behaviour of Aluminium Doped Barium Hexaferrite Nanoparticles Synthesized by Solution Combustion Technique. *Physica B Condens Matter* **2011**, *406* (4), 789–793. https://doi.org/10.1016/J.PHYSB.2010.11.094.

(26) Behera, P.; Ravi, S. Influence of Al Substitution on Structural, Dielectric and Magnetic Properties of M-Type Barium Hexaferrite. *J Supercond Nov Magn* **2017**, *30* (6), 1453–1461. https://doi.org/10.1007/s10948-016-3924-1.

(27) Albanese, G.; Deriu, A. Magnetic Properties of Al, Ga, Sc, In Substituted Barium Ferrites: A Comparative Analysis. *Ceramurgia International* **1979**, *5* (1), 3–10. https://doi.org/10.1016/0390-5519(79)90002-4.

(28) Maltoni, P.; Barucca, G.; Rutkowski, B.; Ivanov, S. A.; Yaacoub, N.; Mikheenkova, A.; Ek, G.; Eriksson, M.; Almqvist, B.; Vasilakaki, M.; Varvaro, G.; Sarkar, T.; De Toro, J. A.; Trohidou, K.; Peddis, D.; Mathieu, R. Engineering Hard Ferrite Composites by Combining Nanostructuring and Al3+ Substitution: From Nano to Dense Bulk Magnets. *Acta Mater* **2025**, *282*, 120491. https://doi.org/10.1016/j.actamat.2024.120491.

(29) Pradyot Patnaik. Handbook of Inorganic Chemicals. *Choice Reviews Online* **2003**, *40* (11), 40-6428-40–6428. https://doi.org/10.5860/CHOICE.40-6428.

(30) Tenorio-González, F. N.; Bolarín-Miró, A. M.; Sánchez-De Jesús, F.; Vera-Serna, P.; Menéndez-González, N.; Sánchez-Marcos, J. Crystal Structure and Magnetic Properties of High Mn-Doped Strontium Hexaferrite. *J Alloys Compd* **2017**, *695*, 2083–2090. https://doi.org/10.1016/j.jallcom.2016.11.047.

(31) Silva, W. M. S.; Ferreira, N. S.; Soares, J. M.; Da Silva, R. B.; Macêdo, M. A. Investigation of Structural and Magnetic Properties of Nanocrystalline Mn-Doped SrFe12O19 Prepared by Proteic Sol–Gel Process. *J Magn Magn Mater* **2015**, *395*, 263–270. https://doi.org/10.1016/J.JMMM.2015.07.085.

(32) Gupta, A.; Roy, P. K. Improved Strontium Hexaferrites: An Overview of Current Progress in Synthesis, Properties, and Applications. *Materials Science and Engineering: B* **2024**, *306*, 117458. https://doi.org/10.1016/j.mseb.2024.117458.

(33) Obradors, X.; Collomb, A.; Pernet, M.; Joubert, J. C.; Isalgué, A. Structural and Magnetic Properties of BaFe12-XMnxO19 Hexagonal Ferrites. *J Magn*

*Magn Mater* **1984**, *44* (1–2), 118–128. https://doi.org/10.1016/0304-8853(84)90053-2.

(34) Sharma, P.; Rocha, R. A.; Medeiros, S. N.; Hallouche, B.; Paesano, A. Structural and Magnetic Studies on Mechanosynthesized BaFe12−xMnxO19. *J Magn Magn Mater* **2007**, *316* (1), 29–33. https://doi.org/10.1016/j.jmmm.2007.03.207.

(35) Collomb, A.; Obradors, X.; Isalgué, A.; Fruchart, D. Neutron Diffraction Study of the Crystallographic and Magnetic Structures of the BaFe12−xMnxO19 M-Type Hexagonal Ferrites. *J Magn Magn Mater* **1987**, *69* (3), 317–324. https://doi.org/10.1016/0304-8853(87)90259-9.

(36) Fu, H.; Zhai, H. R.; Zhang, Y. C.; Gu, B. X.; Li, J. Y. Magnetic Properties of Mn Substituted Barium Ferrite. *J Magn Magn Mater* **1986**, *54–57* (PART 2), 905–906. https://doi.org/10.1016/0304-8853(86)90307-0.

(37) Sharma, P.; Rocha, R. A.; De Medeiros, S. N.; Paesano, A.; Hallouche, B. Structural, Mössbauer and Magnetic Studies on Mn-Substituted Barium Hexaferrites Prepared by High Energy Ball Milling. *Hyperfine Interact* **2007**, *175* (1–3), 77–84. https://doi.org/10.1007/S10751-008-9591-2/METRICS.

(38) Lee, I. K.; Sur, J. C.; Shim, I. B.; Kim, C. S. The Effect of Manganese Substituted M-Type Hexagonal Ba-Ferrite. *Journal of Magnetics* **2009**, *14* (2), 93–96. https://doi.org/10.4283/JMAG.2009.14.2.093.

(39) Sato, M.; Ishii, Y. Simple and Approximate Expressions of Demagnetizing Factors of Uniformly Magnetized Rectangular Rod and Cylinder. *J Appl Phys* **1989**, *66* (2), 983–985. https://doi.org/10.1063/1.343481.

(40) *Grades of Ferrite | e-Magnets UK*. https://e-magnetsuk.com/ferrite-magnets/grades-of-ferrite/ (accessed 2025-10-23).

(41) *FERRITE DISCS - Italfit*. https://www.italfitmagneti.com/products/ferrite-permanent-magnet-alnico-smco/ferrite-discs (accessed 2025-10-23).

(42) Coey, J. M. D. Hard Magnetic Materials: A Perspective. *IEEE Trans Magn* **2011**, *47* (12), 4671–4681. https://doi.org/10.1109/TMAG.2011.2166975.

(43) Steel, K. S.; Steel, M. K.; Steel, N.; Al, A.-N.-C.-F.; Al-Ni-Co-Fe, -Ni-Co-Fe. Magnetic Characteristics Transition of TDK Ferrite Magnet (MG Oe) (KJ/m 3 ).

(44) *Imanes de Ferrita | IMA*. https://imamagnets.com/en/ferrite-magnets/ (accessed 2025-10-23).

# **Chapter 5 |** Innovative compaction and densification of SrM powders for PM applications

## 5.1 The aim of obtaining nanostructured PMs

Once obtained hexagonal ferrite nanograins with promising properties, the next step is to transform them in an oriented (anisotropic) and dense permanent magnet, while preserving the magnetic characteristics exhibited by the single nanoparticles. This is definitely not an easy task, as in conventional sintering processes elevated temperatures (up to 1350 °C) are employed to reduce porosity, attaining increased densities by coalescence of the nanoparticles [1–3]. The high temperatures required for densification and sintering are energy-intensive and make precise control over grain size and microstructure challenging, potentially leading to detrimental grain growth which can reduce coercivity [4]. Furthermore, during compaction the exchange intergranular interactions between magnetically aligned nanograins become prevalent, affecting the coercivity, and resembling a bulk-like magnetic structure [5].

To achieve this overarching goal, two different approaches for the compaction were envisaged. One was utilizing a high-pressure mechanical press with two different setups allowing to apply isotropic (multi-anvil) and uniaxial (piston cylinder) pressure at low temperature (below 300 °C). On the other hand, Spark Plasma Sintering, a novel densification technique which combines uniaxial pressure and short sintering times to minimize grain growth.

## 5.2 Multi-anvil and Piston cylinder press

Compaction tests were conducted at the Institute of Materials for Electronics and Magnetism of the National Research Council (IMEM-CNR[6]) which provided us the access to a 1000-ton oleodynamic press (Tecnoprecisa S.r.l.), equipped with:

- A Multi-anvil (M.A.) Walker-type press (Rockland Corps.) with P range from 2 GPa to 25 GPa and T range from room temperature to 2200 °C; the sample is placed in a hole within a pressure medium shaped into an octahedron and fabricated from ceramic material. The faces of the octahedron seat against the truncated corners of eight tungsten carbide (WC) cubic anvils. The cubes in turn are nested within cylindrical seats fabricated from steel and sectioned into segments that fit into a massively supported guide-block [7].
- End-loaded piston cylinder (P.C.) set of 1 inch (Enerpac and Danfoss) with P range from 0.05 GPa to 3.5 GPa and T range from room temperature to 1500 °C. The heart of the apparatus is the pressure vessel, which contains a tungsten carbide (WC) core supported by concentric rings of hardened steel. The force is provided by the main hydraulic ram acting against the sample assembly and stack top plate, which is confined by an end load applied by the upper hydraulic ram [7].

The powder assembly consisted of a NaCl cylindrical sleeve enclosing a cylindrical graphite furnace. The furnace provides energy by Joule effect to the centrally positioned sample, which was encapsulated within a cold-welded gold capsule (thickness 25 μm) and insulated by an MgO sleeve.

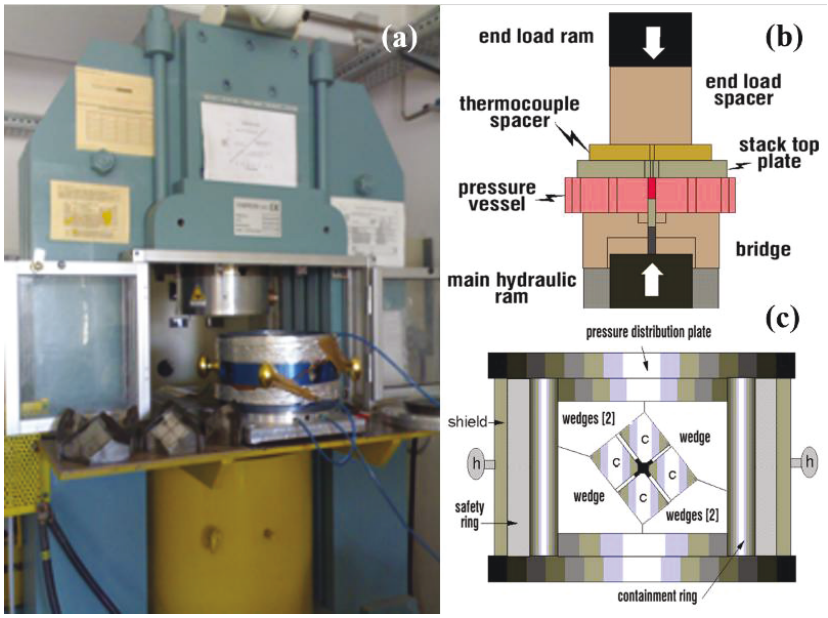


***Figure 5-1*** *Illustrative images of the high-pressure setup at IMEM: (a) 1000-tons oleodynamic press with multi-anvil module; (b) schematic representation of end-loaded piston cylinder press; (c) schematic representation of the multi-anvil Walker type press.*

Experiments were aimed at pursuing two main objectives. The first one was to investigate whether the synthesized nanometric SrM particles could be oriented (even partially) using the high uniaxial pressure provided by a piston cylinder system, which can promote mechanical crystallographic alignment of the platelet-like particles, whose plane lies perpendicular to the easy axis (c-axis) of magnetization [4]. The second was to explore whether the multi-anvil system could be employed to achieve high densification through application of quasi-isotropic thermodynamic conditions. In this case the goal was to maximize the density of the compacted SrM pellet by applying high pressure and low temperatures (below 300 °C), preserving the nanoparticles' size. Both procedures, enhancing densification and promoting grain alignment, should improve the SrM magnetic properties, especially the remanence [8]. High packing density also increases the total magnetic moment per volume, and enhances the mechanical strength by minimizing the porosity. An increased particle orientation allows for a significant improvement in remanence, enhancing it from half of the $M_S$, typical of randomly oriented particles [9], to values approaching $M_S$ when the field is applied in the direction of the easy axis, typical behavior of anisotropic magnets. Moreover, preserving the nanostructure of the grains is crucial to maintain high coercivity, which is dependent on the grain size. In fact, this is a typical drawback during sintering processes as the high temperatures, generally adopted to increase the density, cause an excessive grain growth [10].

Four powders were selected for this series of tests: SrM_LTSSR_R10/45 ($Fe^{3+}/Sr^{2+} = 10$, $Na^{+}/Sr^{2+} = 45$) calcined at 775 °C obtained from the solid-state reaction (for details *see* Chapter 2), as it presented the best compromise between particle size and good magnetic properties among the samples prepared by this synthesis procedure; SrM_MSG_R9 ($Fe^{3+}/Sr^{2+} = 9$) which

presented free-standing crystallites and valuable magnetic properties; the doped samples Al(0.5)-SrM_MSG and Mn(0.73)-SrM_MSG, obtained from MSG approach, which exhibited a remarkable increased coercivity and optimum size distribution, respectively.

Two samples were prepared from the powder SrM_LTSSR_R10/45, one with P.C. at 0.5 GPa and T= 250 °C, and the other with M.A. at 4GPa and 80 °C. The next two samples were produced with the undoped SrM_MSG_R9, one with M.A. at 4 GPa and 80 °C, and the other with P.C. at 1 GPa and 250 °C. For the last two samples, Al(0.5)_SrM_MSG and Mn(0.7)_SrM_MSG were pressed with P.C. at 3 GPa and 150 °C. These experimental conditions are summarized in **Table 5-1**. The obtained pellets had a cylindrical shape, about 4 mm in height and 3 mm in diameter (representative photo in **Figure 5-2**).

In this section, we reported the magnetic measurements done on the obtained compacted pellets, through a VSM magnetometer. The main focus is on evaluating the remanence ratio (squareness factor), which is a common indication of the alignment of domains from a magnetic point of view [11], and on the impact the performed treatment had on coercivity. The samples were labelled with *angle0*° or *angle90*°, corresponding to the field applied parallel or perpendicular, with respect to the axis of the pellet.

***Figure 5-2*** *Representative image of the obtained pellet from SrM_LTSSR_R10/45 powders after M.A. compaction at 80°C and 4 GPa.*

***Table 5-1*** *Summary of experimental parameters in powder densification through M.A. and P.C press.*

| Sample | Technique | P (GPa) | T (°C) |
|---|---|---|---|
| **SrM_LTSSR_P.C.** | Piston Cylinder | 0.5 | 250 |
| **SrM_LTSSR_M.A.** | Multi-Anvil | 4 | 80 |
| **SrM_MSG_P.C.** | Piston Cylinder | 1 | 250 |
| **SrM_MSG_M.A.** | Multi-Anvil | 4 | 80 |
| **Al(0.5)-SrM_MSG_P.C.** | Piston Cylinder | 3 | 150 |
| **Mn(0.7)-SrM_MSG_P.C.** | Piston Cylinder | 3 | 150 |

## 5.2.1 SrM powders from LTSSR synthesis

The first tests were performed with the powder from LTSSR synthesis. The intent was to see if, despite the dense agglomerates noticed in TEM images, a degree of alignment could be achieved by the means of high uniaxial pressure. Therefore, the P.C. was employed, and the experimental conditions were fixed

at 0.5 GPa and 250 °C, where the heating was provided to facilitate the mobility of the grains.

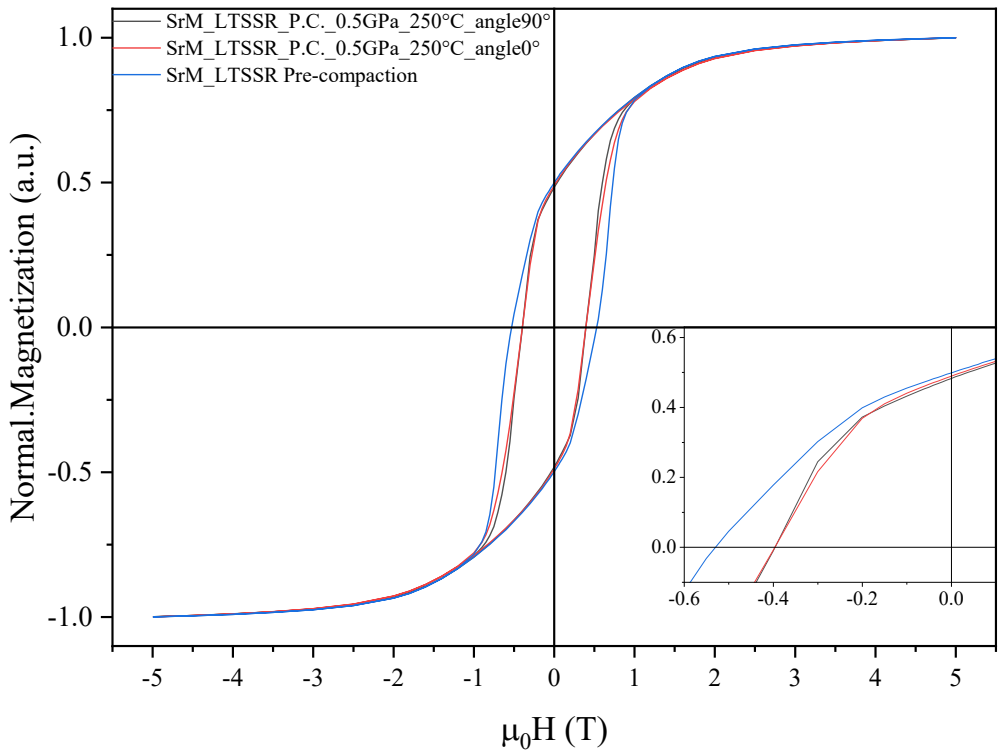


***Figure 5-3*** *Hysteresis loops collected at room temperature on the SrM_LTSSR_P.C_0.5GPa_250 °C. The sample is positioned with the c-axis parallel (angle 0°) or perpendicular (angle 90°) to the applied magnetic field.*

From the hysteresis loops collected at 300 K (**Figure 5-3**) it can be noticed that the shape of the loops is unvaried, suggesting that even in this conditions the grains inside the pellet did not aligned and showed an isotropic behavior. What the compaction affected the most is the coercivity, which decreased its value by around 25% from the pristine powder (values are summarized in **Table 5-2**). This effect can be due to increased magnetic interaction deriving from the close proximity of the grains [12]. Induced directional stress and strain on the randomly oriented nanograins, plastic deformation, or some other defects introduced by

the unidirectional compaction process [13] can also contribute to lower the coercivity[12].

***Table 5-2*** *Remanence ratio ($M_R/M_S$) and coercivity ($H_C$) of SrM_LTSSR_P.C_0.5GPa _250 °C. The sample is positioned with the c-axis parallel (angle 0°) or perpendicular (angle 90°) to the applied magnetic field in VSM.*

| **Sample** | **$M_R/M_S$** | **$\mu_0 H_C$ (T)** |
|---|---|---|
| **SrM_LTSSR pre-compaction** | 0.50 | 0.53 |
| **SrM_LTSSR_P.C. _0.5GPa_250°C_angle90°** | 0.48 | 0.4 |
| **SrM_LTSSR_P.C. _0.5GPa_250°C_angle0°** | 0.49 | 0.4 |

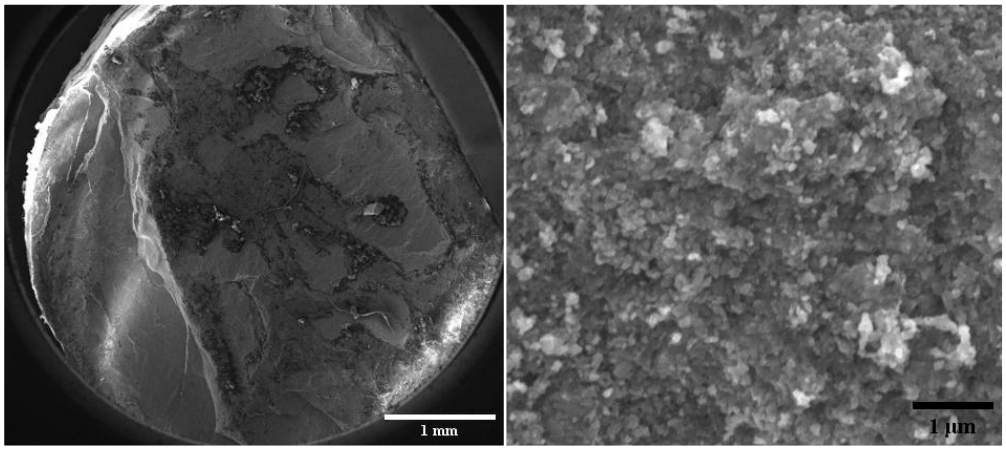


***Figure 5-4*** *SEM images showing the flat face of SrM_LTSSR_P.C_0.5GPa _250 °C.*

Observing the SEM images (**Figure 5-4**) of the pellet surface it could be noticed that the general microstructure of the powder was efficiently maintained, preserving the grains in a nanosized range. From this point, we tried to maximize the density of the pellet to get a nanostructured PM.

In a second attempt, the multi-anvil system was employed, applying a high pressure of 4 GPa in quasi-isotropic conditions, and a low heating temperature of 80°C. The density of the as obtained magnet was determined to be 4.67 g/cm$^3$, which is 92% of the bulk density (5.101 g/cm$^3$) of SrM [1]. This value

found was significantly high, especially considering the very low temperature adopted [4,11,14,15]. The corresponding hysteresis loops are reported in **Figure 5-5**.

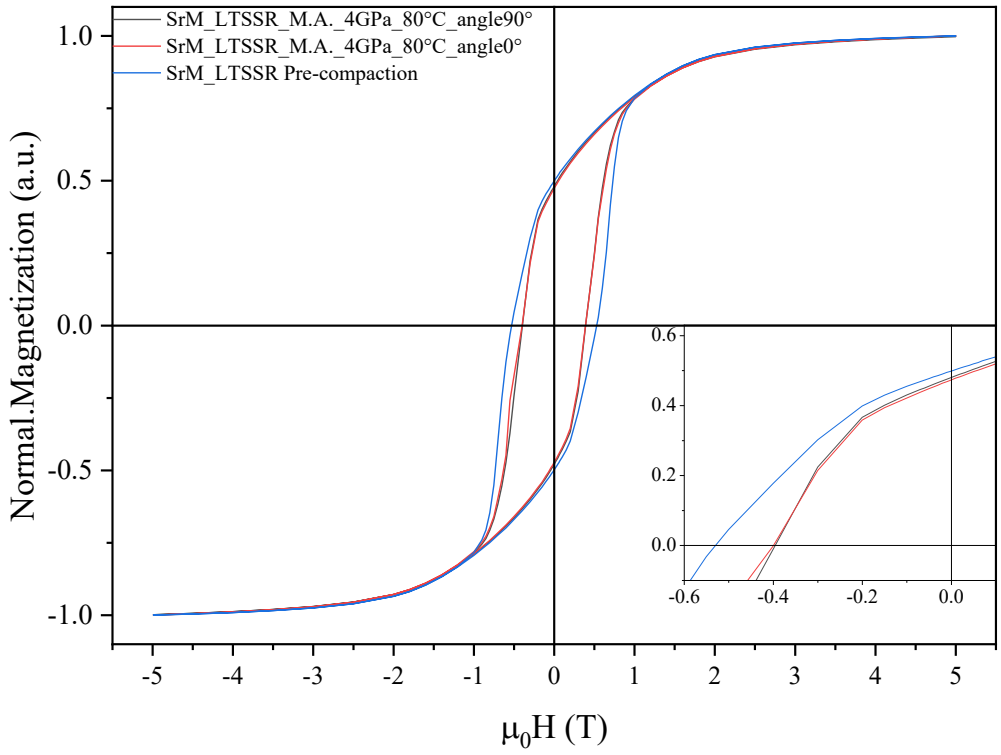


***Figure 5-5*** *Hysteresis loops collected at room temperature of SrM_LTSSR_M.A_4GPa _80°C. The sample is positioned with the axis parallel (angle 0°) or perpendicular (angle 90°) to the applied magnetic field in VSM.*

As expected, the $M_R/M_S$ value remained unchanged from the starting powder, while coercivity decreased by approximately 26% with respect to the pre-compaction powder (**Table 5-3**). The lowered coercivity value was ascribed to stronger exchange interaction effect between the nanograins, associated with the increased density.

***Table 5-3*** *Remanence ratio ($M_R/M_S$) and coercivity ($H_C$) of SrM_LTSSR_M.A._4GPa _80°C. The sample is positioned with the c-axis parallel (angle 0°) or perpendicular (angle 90°) to the applied magnetic field in VSM.*

| Sample | $M_R/M_S$ | $\mu_0 H_C$ (T) |
|---|---|---|
| **SrM_LTSSR pre-compaction** | 0.50 | 0.53 |
| **SrM_LTSSR_M.A._4GPa _80°C_angle90°** | 0.48 | 0.39 |
| **SrM_LTSSR_M.A._4GPa _80°C_angle0°** | 0.47 | 0.39 |

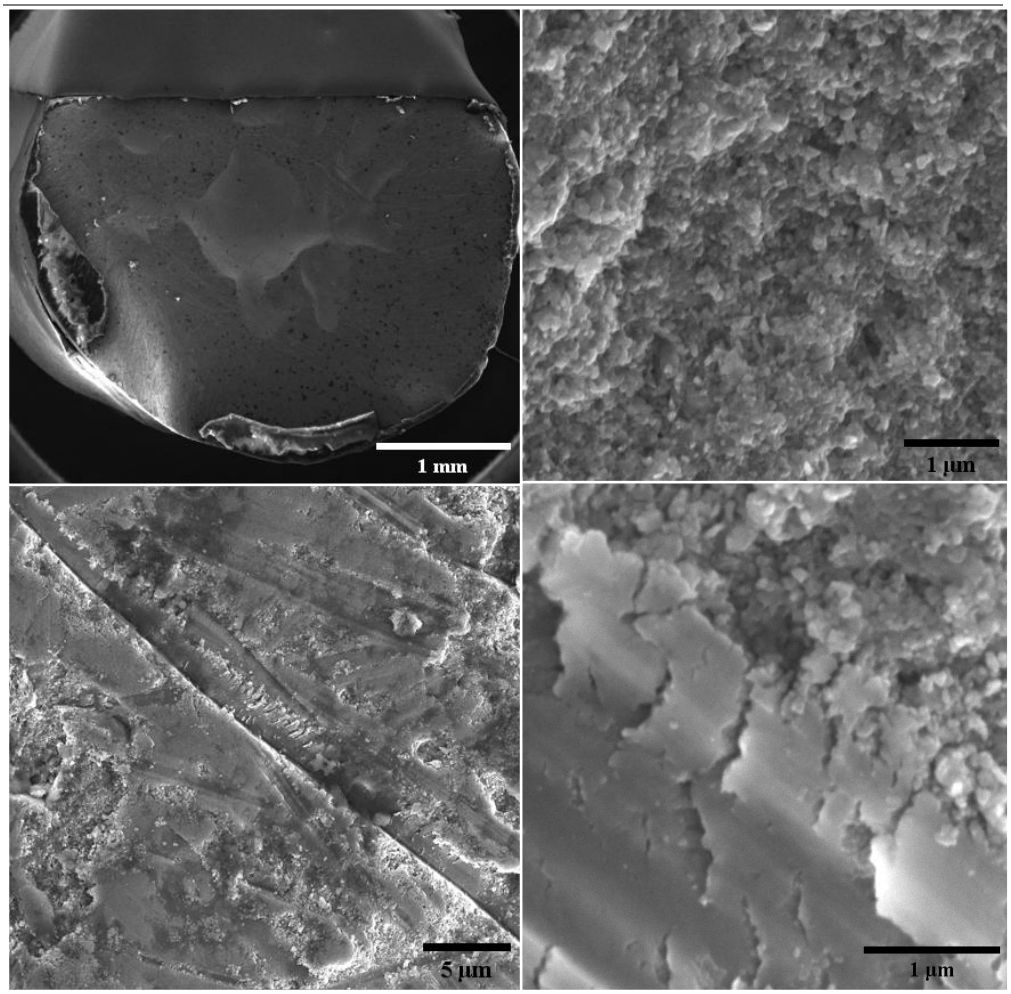


***Figure 5-6*** *SEM images showing the flat face of the SrM_LTSSR_M.A._4GPa _80°C.*

The SEM images of the M.A.-compacted pellet showed that the nanostructure is generally preserved, except in some local areas where some coalescence or plastic deformation appears on the surface, which can be attributed to the non-perfectly isotropic high pressure applied. Moreover, these regions are located on the pellet's external surface, at the interface with the sample holder and in contact with the gold encapsulating layer that contains the powder. This is confirmed by XRD measurements performed on the surface of the pellet or scanning the internal part, once it was cut in half (**Figure 5-7**).

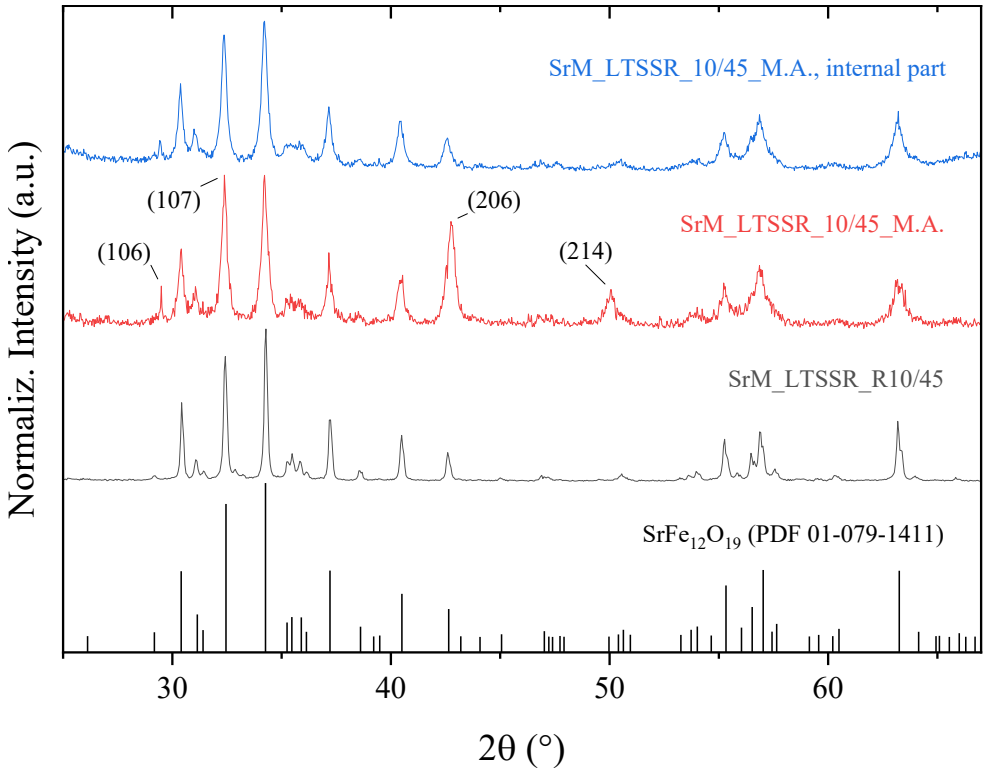


***Figure 5-7** XRD diffraction patterns of SrM_LTSSR_M.A._4 GPa_80°C. One scan was taken from the flat face (red line) of the pellet, and another from the internal part (blue line) once cut in half. The black line is the pattern of the as-synthesized powder.*

The scan of the flat face presented some preferred orientation, as shown by the higher intensities of the reflections (106), (107), (206), and (214), a behavior which is not present in the diffraction pattern of the internal part of

the pattern, where the relative intensities are in accordance with an isotropic sample without any preferred orientation. This suggested a certain degree of alignment on the pellet surface, while no such orientation was detected in its internal part. Therefore, the applied pressure was not totally isotropic in M.A. system.

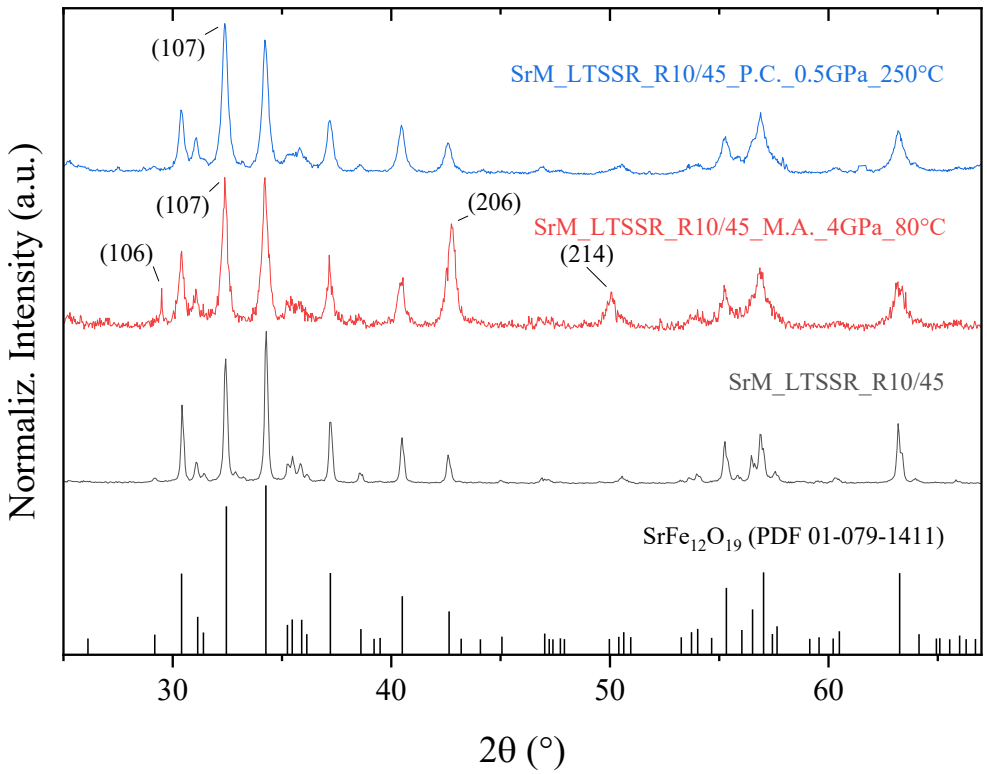


***Figure 5-8*** *XRD diffraction patterns of: SrM_LTSSR_M.A._4GPa_80°C (red line), SrM_LTSSR_P.C._0.5GPa_250 °C (blue line), and compared with the as-synthesized powder (black line).*

In the diffraction pattern of the pellet compacted through the piston cylinder appeared only a minor enhanced intensity of the reflection plane (107), which is in line with the lower, unidirectional pressure applied. The enhanced alignment on the surface in the M.A pellet obtained from the same powder, suggested that probably a higher uniaxial pressure could be beneficial to further align the powders synthesized by LTSSR.

## 5.2.2 SrM powders from MSG synthesis

The subsequent trials were based on the powders deriving from MSG synthesis. The initial conditions tested, in order to achieve the same high density found in previous trials, were through the multi-anvil system. Therefore, a pressure of 4 GPa and a temperature of 80 °C were applied. The resulting pellet presented a lower density of 3.91 g/cm$^3$, corresponding to 77% of the bulk density. This value, even if lower than the pellet from LTSSR, is remarkably high for this material under the given operative conditions[11,16].

This shift in final density can be attributed to a different porosity in the powders produced by the different synthesis routes, despite of the comparable nanoparticles size: MSG synthesis yielded mostly individual crystallites with a low degree of aggregation. Their high specific surface area can hinder efficient packing and increase resistance to densification. Conversely, the nanoparticles produced by LTSSR synthesis formed large, consolidated aggregates during calcination. These aggregates have reduced surface, grain boundary energy and potential energy elastically stored in the lattice, consequent to the partial sintering already undergone by the nanoparticles [3,13,17,18].

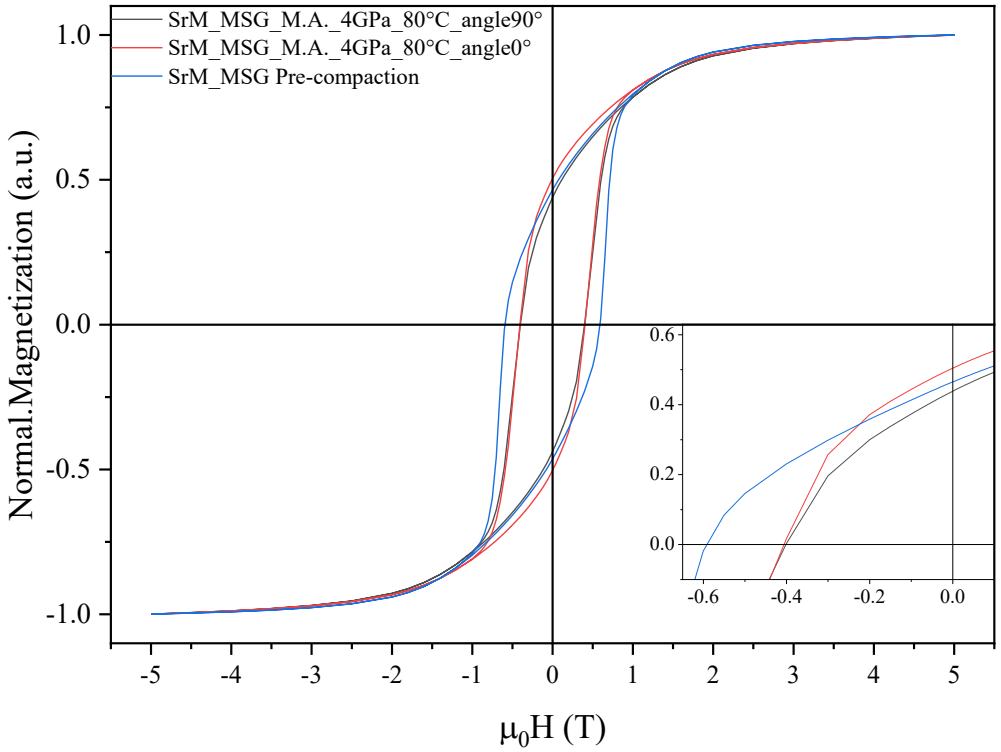


***Figure 5-9*** *Hysteresis loops collected at 300 K of the SrM_MSG_M.A._4GPa_80°C. The sample is positioned with the c-axis parallel (angle 0°) or perpendicular (angle 90°) to the applied magnetic field in VSM.*

The hysteresis loops at 300 K, reported in **Figure 5-9**, showed a small increase in the remanence when the sample was measured with the axis along the magnetic field (angle 0°), suggesting a small degree of orientation of the crystallites' easy axis along this direction. Regarding the magnetic properties (**Table 5-4**) the coercivity is lowered with respect to the powder by 33%. This is in line with the hypothesis of demagnetizing internal effects from proximity interactions, consequent to the pressing procedure and the increased density, [12,13].

***Table 5-4*** *Remanence ratio ($M_R/M_S$) and coercivity ($H_C$) of the SrM_MSG_M.A._4GPa_80°C. The sample is positioned with the c-axis parallel (angle 0°) or perpendicular (angle 90°) to the applied magnetic field in VSM.*

| **Sample** | **$M_R/M_S$** | **$\mu_0 H_C$ (T)** |
|---|---|---|
| **SrM_MSG pre-compaction** | 0.45 | 0.60 |
| **SrM_MSG_M.A. _4GPa_80°C_angle90°** | 0.44 | 0.40 |
| **SrM_MSG_M.A._4GPa_80°C_angle0°** | 0.51 | 0.41 |

This was confirmed by the relative intensity of the peaks in the diffraction pattern (**Figure 5-10**) which display an increase in the relative intensities of the peaks (107), (206), (1011), (208), and (0014). Particularly, the enhancement of the (0014) reflection is indicative of the c-axis orientation of the crystallites parallel to the cylinder axis, which produces as an increase in (00*l*) peak intensity [19], belonging to the family of basal planes. In accordance with this alignment, the axes of easy magnetization lie perpendicular to the flat face of the pellet and thus to the direction of the magnetic field, thereby explaining the remanence enhancement. As mentioned in reference [13], even commercial isotropic specimens exhibit slight directional orientation, deriving from the anisometric particle shape and the rheological phenomena during manufacture.

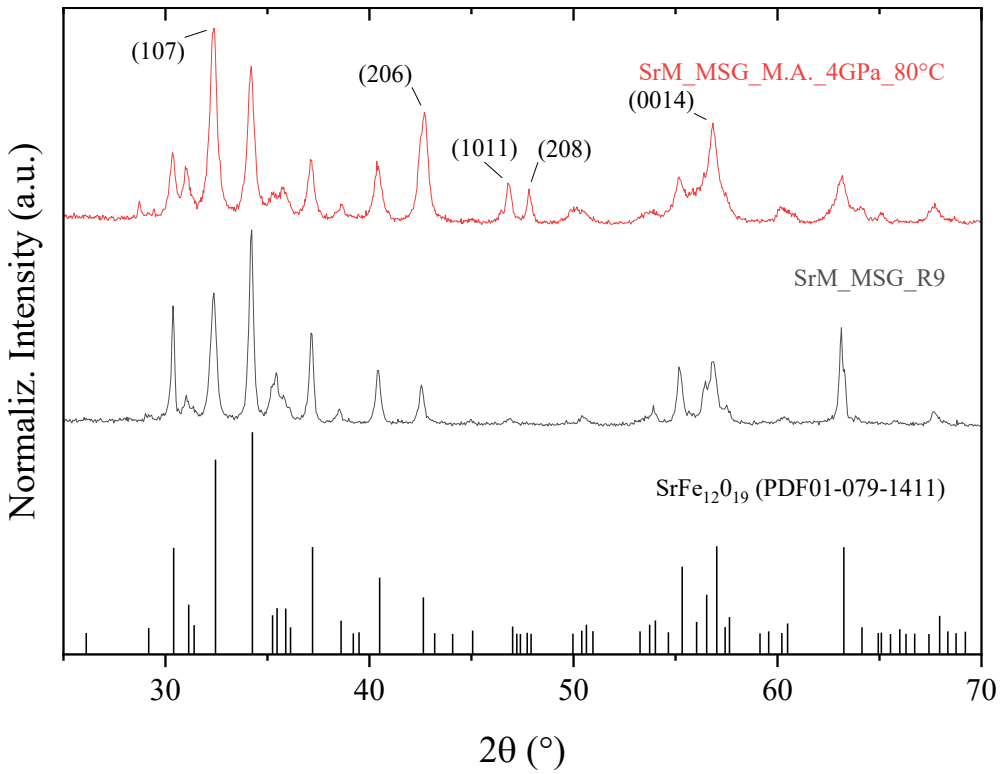


***Figure 5-10*** *XRD diffraction patterns of the SrM_MSG_M.A._4GPa_80°C. The scan was taken from the flat face of the pellet (red line) and compared with the as-synthesized powder.*

The undoped SrM_MSG_R9 showed interesting features of anisotropic behavior with the application of high isotropic pressure in the multi-anvil system, as shown in the previous section. The powder was thus pressed by applying the unidirectional pressure (1 GPa) of the piston cylinder and a heating temperature of 250 °C, to promote the necessary microstructural mobility for alignment and densification.

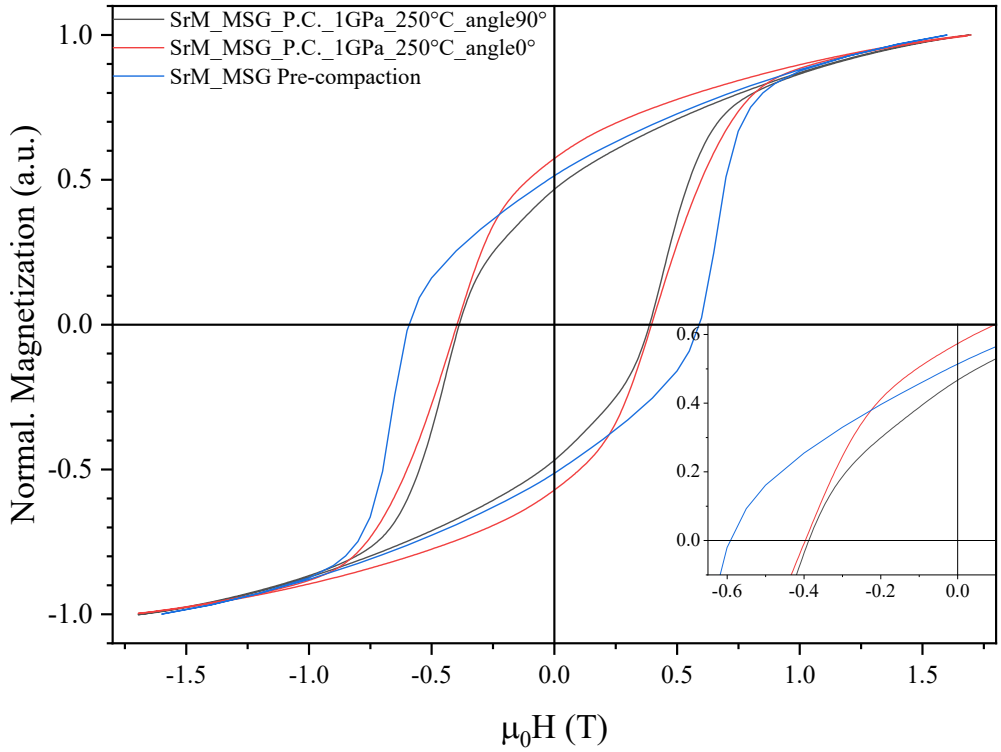


***Figure 5-11*** *Hysteresis loops collected at r.t. of SrM_MSG_P.C._1GPa_250°C. The sample is positioned with the c-axis parallel (angle 0°) or perpendicular (angle 90°) to the applied magnetic field in VSM.*

From the observation of the corresponding hysteresis loops (**Figure 5-11**) it can be appreciated that the remanence increase, already partially seen after multi-anvil pressing, is larger than the powder and different in the two orientations (**Table 5-5**), indicating a good degree of orientation of the crystallites. This is in agreement with the correct alignment of the nanograins with the application of uniaxial pressure, as the compression exerted by the piston forces the nanoplatelets to stay in the plane of the resulting flat face of the pellet, and the c-axis of easy magnetization of the crystallites matches with the c-axis of the cylinder. The coercivity, instead, presented the same loss entity of the previous tests, decreasing by 33% from the initial value, supporting the hypothesis of internal demagnetizing factors and variations related to the

compaction process. However, a promising result was obtained with an effective remanence enhancement. This further confirms the obtainment of nanoparticles capable to be aligned through this synthesis method.

***Table 5-5*** *Remanence ratio ($M_R/M_S$) and coercivity ($\mu_0 H_C$) of SrM_MSG_P.C._1GPa_250°C. The sample is positioned with the axis parallel (angle 0°) or perpendicular (angle 90°) to the applied magnetic field in VSM.*

| Sample | $M_R/M_S$ | $\mu_0 H_C$ (T) |
|---|---|---|
| **SrM_MSG pre-compaction** | 0.51 | 0.60 |
| **SrM_MSG_P.C._1GPa_250°C_angle90°** | 0.46 | 0.39 |
| **SrM_MSG_P.C._1GPa_250°C_angle0°** | 0.57 | 0.40 |

In summary, two different outcomes could be noticed. While it was not possible to align the powders from LTSSR synthesis with the P.C., a remarkable relative density of 91 % was obtained with the M.A setup. On the other hand, powders from MSG synthesis were more suitable for the application of uniaxial pressure of the P.C., showing promising features for the development of anisotropic magnets.

## 5.2.3 Doped SrM from MSG synthesis

Since the doped nanoparticles were significantly smaller (66 ± 27 nm for Al(0.5)-SRM_MSG and 39 ± 19 nm for Mn(0.7)-SrM_MSG, versus 88 ± 36 nm of SrM_MSG_R9) an increase in uniaxial pressure was necessary to enhance sample densification. While the pressure was increased to 3 GPa, the heating temperature was lowered (150 °C) to minimize grain growth and preserve their nanometric dimensions. The hysteresis loops at room temperature of both pellets are shown in **Figure 5-12** for Al-doped SrM and in **Figure 5-13** for Mn-doped SrM.

Before compaction, the Al-doped SrM exhibited a high coercivity of 0.7 T, while after, the coercivity loss was estimated to be around 28%, consistent with previous uniaxial and isotropic trials. However, the remanence ratio slightly increased (around 7% at angle 0°), indicating a partial crystallite alignment. These values are summarized in **Table 5-6**.

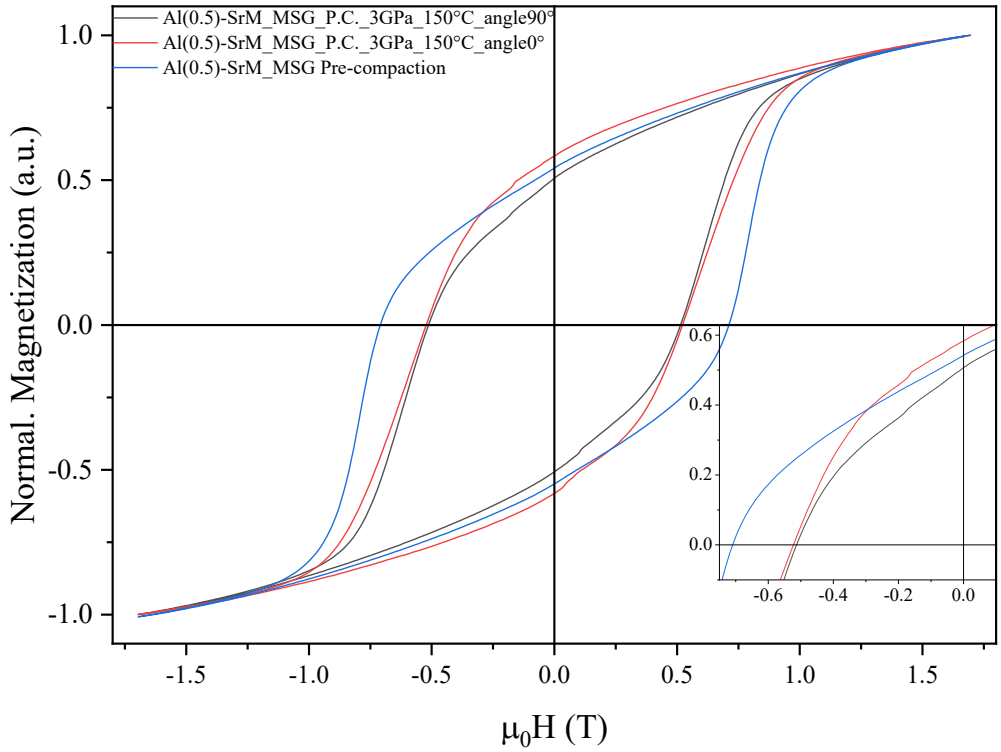


***Figure 5-12*** *Hysteresis loops collected at r.t. of Al(0.5)_SrM_MSG_P.C._3GPa_150°C. The sample is positioned with the c-axis parallel (angle 0°) or perpendicular (angle 90°) to the applied magnetic field in VSM.*

***Table 5-6*** *Remanence ratio ($M_R/M_S$) and coercivity ($H_C$) of Al(0.5)_SrM_MSG_P.C._3GPa_150°C. The sample is positioned with the c-axis parallel (angle 0°) or perpendicular (angle 90°) to the applied magnetic field in VSM.*

| **Sample** | **$M_R/M_S$** | **$\mu_0 H_C$ (T)** |
|---|---|---|
| **Al(0.5)-SrM_MSG pre-compaction** | 0.54 | 0.71 |
| **Al(0.5)-SrM_MSG_P.C._3GPa_150°C_angle90°** | 0.51 | 0.51 |
| **Al(0.5)-SrM_MSG_P.C._3GPa_150°C_angle0°** | 0.58 | 0.52 |

In contrast, the Mn-doped SrM pellet displayed a different behavior. The remanence was minimally affected by the compaction process (**Table 5-7**), showing just 4% variation between the two orientations. The limited changes in coercivity and remanence (compared to the 12 % $M_R/M_S$ variation in the Al-doped sample) suggest that the current operative conditions were insufficient to achieve significant alignment and densification, due to the small particle size, that hinders an effective compaction.

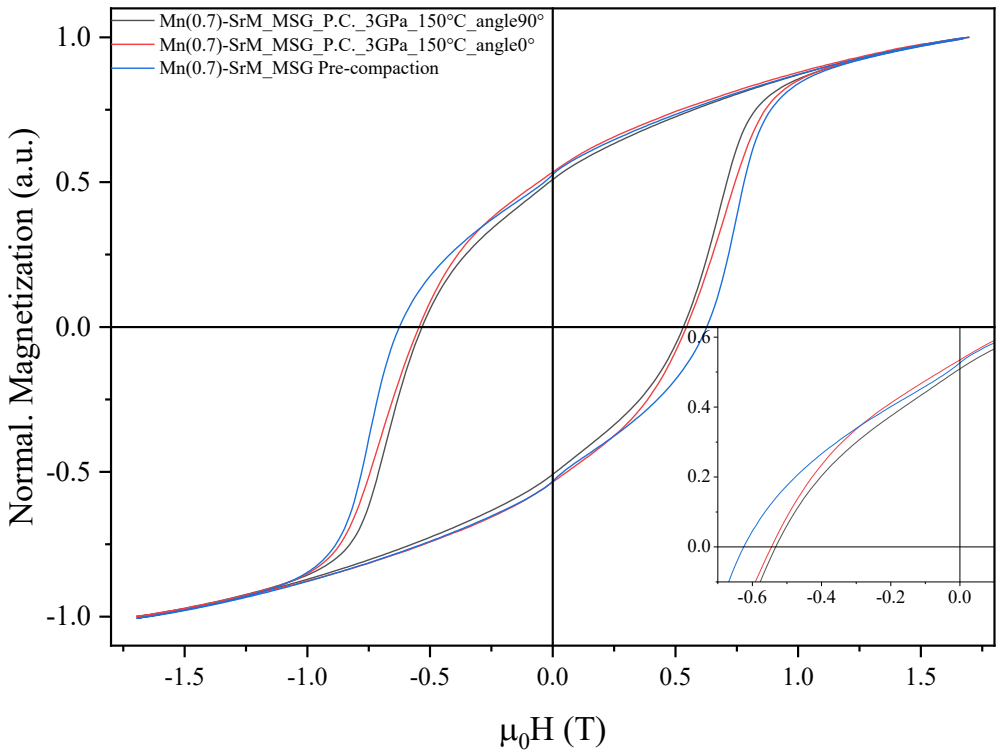


***Figure 5-13*** *Hysteresis loops collected at r.t. of Mn(0.7)_SrM_MSG_P.C._3GPa_150°C. The sample is positioned with the c-axis parallel (angle 0°) or perpendicular (angle 90°) to the applied magnetic field in VSM.*

***Table 5-7*** *Remanence ratio ($M_R/M_S$) and coercivity ($H_C$) of Mn(0.7)_SrM_MSG_P.C._3GPa_150°C. The sample is positioned with the c-axis parallel (angle 0°) or perpendicular (angle 90°) to the applied magnetic field in VSM.*

| **Sample** | **$M_R/M_S$** | **$\mu_0 H_C$ (T)** |
|---|---|---|
| **Mn(0.7)-SrM_MSG pre-compaction** | 0.52 | 0.63 |
| **Mn(0.7)-SrM_MSG_P.C._3GPa_150°C_angle90°** | 0.51 | 0.53 |
| **Mn(0.7)-SrM_MSG_P.C._ 3GPa_150°C_angle0°** | 0.53 | 0.54 |

This last hypothesis was further supported by magnetic field alignment test, performed by mixing doped SrM powder with suitable melted adhesive (Crystalbond [20]). VSM analysis (**Figure 5-14**) revealed distinct alignment tendencies: Al-doped powder showed moderate orientation ($M_R/M_S$ of 0.51 for angle 90° and 0.60 for angle 0°), while Mn-doped powder displayed a significantly higher degree of alignment ($M_R/M_S$ value of 0.14 for angle 90° and 0.93 for angle 0°). These results highlight a noteworthy potential of the Mn-doped SrM powder and suggest that, with optimized compaction parameters, they hold great promises for developing highly anisotropic bonded magnets.

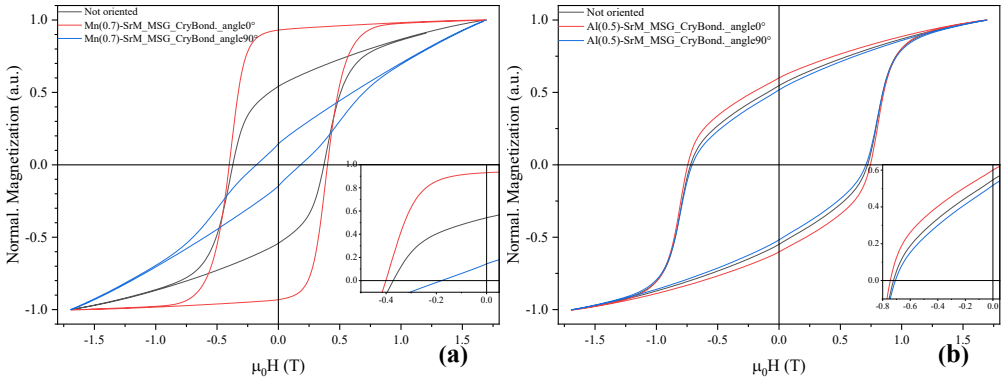


***Figure 5-14*** *Normalized hysteresis loops at room temperature of the doped SrM powders (a) Mn(0.7)-SrM_MSG, (b) Al(05)-SrM_MSG. The samples were dispersed in Crystalbond and measured without orientation (black line) or aligned in a magnetic field (red and blue line). The red line refers to parallel orientation (angle 0°) and the blue line to perpendicular (angle 90 °) with respect to the applied field in VSM.*

# 5.3 Spark plasma sintering (SPS)

Recently, Spark Plasma Sintering (SPS) has been proposed as a promising technique for the fabrication of dense magnetic materials from fine powders. SPS, indeed, offers several advantages over traditional sintering methods which can be very appealing for the consolidation of SrM powders [4,21–25]. The technique operates through the simultaneous application of electrical current and uniaxial pressure, which generates unique heating mechanisms. These mechanisms are different from those characterizing common thermal processing or microwave sintering, enabling exceptionally fast heating rates, shorter sintering times, and lower sintering temperatures [4,26]. Specifically, in SPS, a pulsed direct current passes through the conductive die (generally made of graphite) and through the sample, heating it via the Joule effect. This rapid heating, primarily at particle surfaces, minimizes coarsening, thereby enabling the achievement of high densities. This allows sintering of nano-sized powders

without significant grain growth, diverging from conventional sintering processes [27,28], as the combined mechanical pressure and rapid Joule heating facilitate particle rearrangement and diffusion, thereby merging the compaction and sintering stages into a single operation. Furthermore, the high heating rates, short sintering times, and lower sintering temperatures compared to conventional methods (approximately 200 °C less) render SPS an economically advantageous technique [28]. The limited grain growth offered by this technique is particularly appealing, as it enables densification while preserving the nanostructure, thus preventing the coercivity degradation. Moreover, the application of uniaxial pressure is expected to be beneficial to the magnetic properties, especially regarding remanence, by inducing preferential orientation of the platelet-shaped SrM nanograins.

Given the above advantages, we explored the SPS technique as a viable technique for the consolidation of synthesized SrM powders. The tests were conducted at the Jožef Stefan Institute (JSI) in Ljubljana, Slovenia, thanks to the collaboration with Dr. Petra Jenuš Belec and her team. All the samples were sintered under the same conditions, based on the previous work of Jenuš *et al* [22] temperature of 900 °C, with a holding time of 5 min, and an applied pressure of 92 MPa. Four powders were investigated, the undoped SrM_MSG_R9, the doped Al(0.5)-SrM_MSG and Mn(0.7)-SrM_MSG obtained from MSG, and SrM_LTSSR_R10/45_775°C obtained from LTSSR. The resulting pellets produced by SPS from these powders were labelled with "*_SPS*".

The attained densities of the SPS-compacted pellets were 5.03 g/cm$^3$ for the undoped SrM from MSG synthesis, 4.3 g/cm$^3$ for the Al-doped SrM and 4.7 g/cm$^3$ for the Mn-doped SrM, corresponding to a relative density of 97%, 83% and 91%, compared to SrM bulk density [1]. Conversely, the pellet from LTSSR synthesis was delaminated, therefore it was not possible to estimate its density.

Although the morpho-structural characterization of the samples is still in progress, here we wish to present and preliminary discuss the magnetic properties exhibited by the pellets prepared by SPS. The hysteresis loops were collected at room temperature at the JSI facility through VSM magnetometry (**Figure 5-15**) and were compared to those of the same powder pressed in pellets with similar geometry and sample weight before SPS treatment

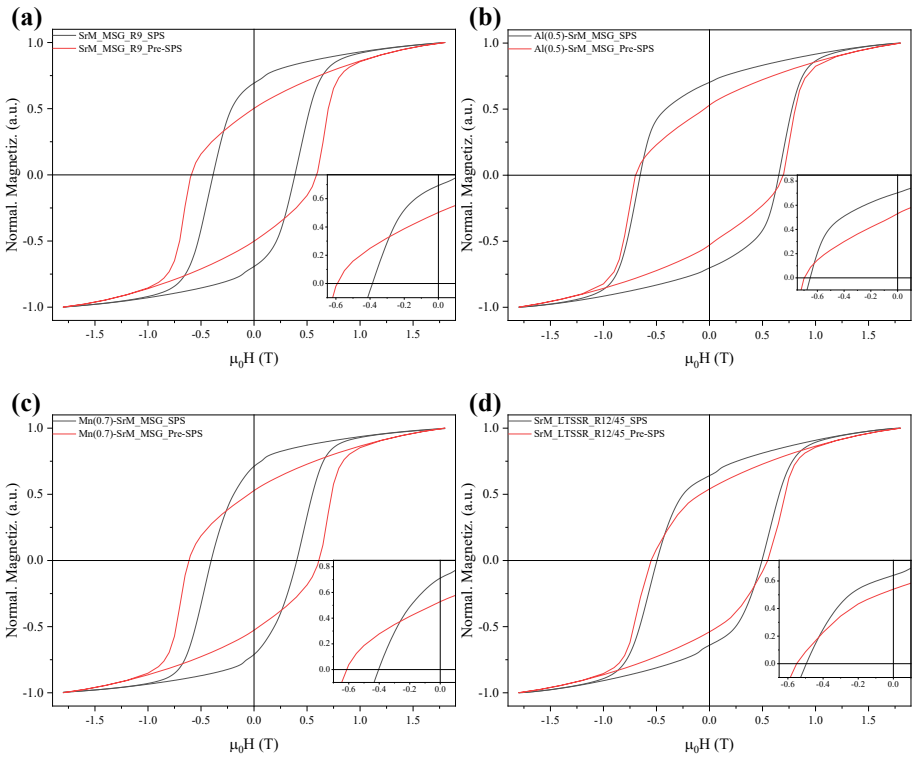


**Figure 5-16**). The main magnetic parameters extracted from the loops are summarized in **Table 5-8**. All the measurements were performed with the axis of the pellet aligned parallel to the applied magnetic field (angle 0°). The loop of the pellet prepared by SPS clearly presented an increased squareness due to the enhanced remanence, which indicates a certain degree of alignment was attained. The small kinks observed at low field for same samples probably arise from a not entirely aligned nanograins due to not enough pressure applied,

which makes the magnetization reversal behavior act as two independent phases.

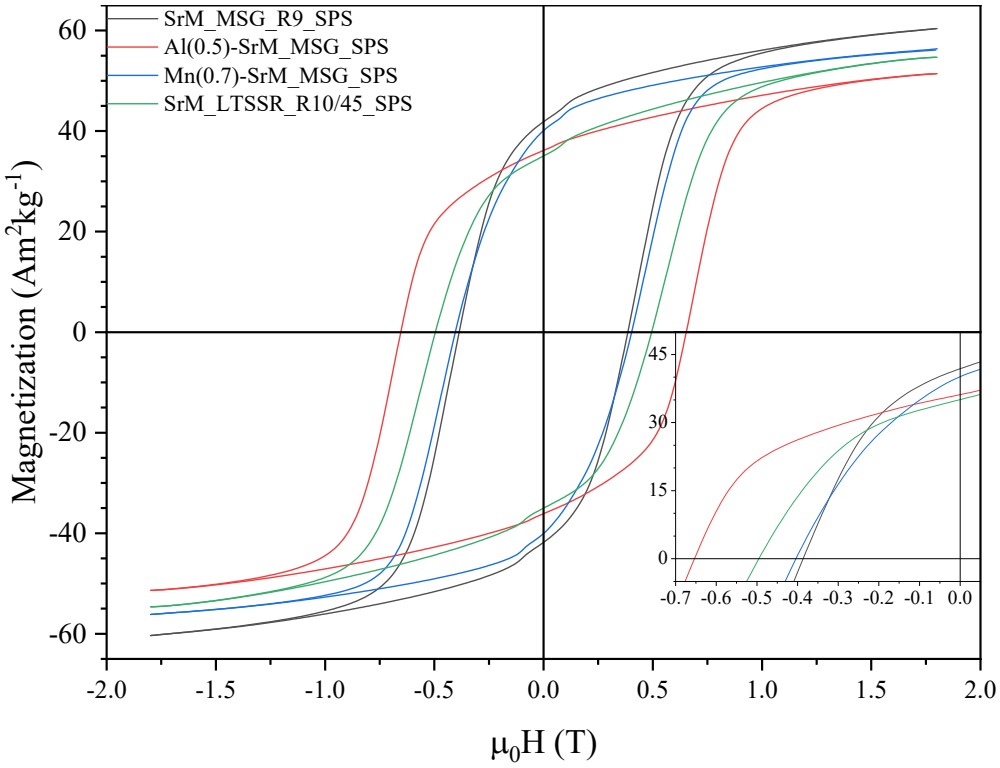


***Figure 5-15*** *Hysteresis loops at room temperature of SrM pellets obtained from SPS of undoped SrM_R9, doped Al(0.5)-SrM and Mn(0.7)-SrM from MSG synthesis and SrM_R10/45_775°C from LTSSR synthesis. The samples were measured with the axis of the pellet aligned parallel to the applied magnetic field (angle 0°). The inset displays the low field region enlargement.*

SrM_MSG_R9_SPS presented a large increase in remanence (32%), but a significant decrease of the coercivity (-34% down to 0.39 T). The latter is consistent with the higher internal demagnetization caused by the nearly full densification reached (97%), although a partial growth of the nanograins above the single to multidomain critical size cannot be excluded. Both these

mechanisms can facilitate incoherent reversal modes characterized by lower energy for the demagnetization.

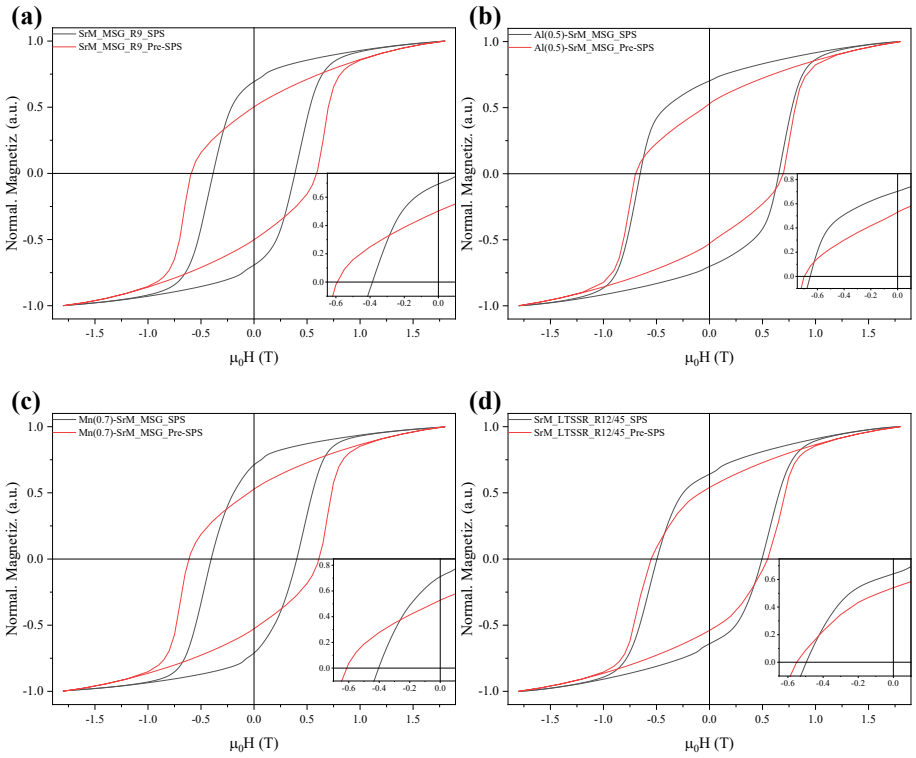


***Figure 5-16*** *Normalized hysteresis loops collected at room temperature for pellets of SrM with same geometry before (red line) and after (black line) SPS treatment: a) SrM_MSG_R9; b) Al(0.5)-SrM_MSG; c) Mn(0.7)-SrM_MSG; d) SrM_LTSSR_R10/45_775°C. The samples were measured with the axis of the pellet aligned parallel to the applied magnetic field (angle 0°).*

***Table 5-8*** *Remanence and coercivity of SrM pellets sintered by SPS, derived from different syntheses: undoped SrM_R9, doped Al(0.5)-SrM and Mn(0.7)-SrM from MSG synthesis and SrM_R10/45_775°C from LTSSR synthesis. The samples were measured with the axis of the pellet aligned parallel to the applied magnetic field (angle 0°). The table additionally reports the corresponding values of pellets of the starting powders and the relative variation of* $M_R$ *and* $H_C$ *following SPS.*

| **Sample** | $\mathbf{M_R}$ **($Am^2kg^{-1}$)** | $\mathbf{\mu_0 H_c}$ **(T)** | $\mathbf{\Delta_{MR}}$ | $\mathbf{\Delta_{Hc}}$ |
|---|---|---|---|---|
| **SrM_MSG_R9 Pre-SPS** | 32 | 0.59 | | |
| **SrM_MSG_R9_SPS** | 42 | 0.39 | +32% | -34% |
| **Al(0.5)-SrM_MSG Pre-SPS** | 30 | 0.70 | | |
| **Al(0.5)-SrM_MSG_SPS** | 36 | 0.65 | +22% | -7% |
| **Mn(0.7)-SrM_MSG Pre-SPS** | 29 | 0.61 | | |
| **Mn(0.7)-SrM_MSG_SPS** | 40 | 0.40 | +36% | -34% |
| **SrM_LTSSR_R10/45 Pre-SPS** | 31 | 0.55 | | |
| **SrM_LTSSR_R10/45_SPS** | 35 | 0.49 | +12% | -11% |

The application of SPS on Mn-doped nanoparticles produced a sample with similar alignment and decrease of coercivity, consistent with its high density. Conversely, the sample obtained from Al-doped nanoparticles, although presented a smaller increase of remanence (32%) still preserved a notably high coercivity (0.65 T) close to that of the not sintered powder. Additionally, the hysteresis curve did not present the same kink of the other samples. This behavior indicates that under these conditions the alignment is efficient, while, due to the lower density (83%), internal interaction effects are limited.

Finally, the powders from LTSSR synthesis showed the lowest alignment degree (19% increase of $M_R$) and coercivity of 0,40 T. In conclusion, although largely preliminary, magnetic properties of the samples prepared by SPS are

very promising (particularly the high density and remanence of SrM_MSG_R9_SPS and the large coercivity of Al(0.5)-SrM_MSG_SPS) and clearly suggests that further efforts must be paid to optimize the parameters of the process to prepare compacted magnets with enhanced energy product.

## 5.4 Conclusions

In this chapter are presented key advancements in the compaction and densification of SrM powders for PM applications, offering an interesting alternative to conventional high-temperature and energy-intensive sintering methods. Both M.A. and P.C. systems proved efficacy in achieving high densification at relatively low temperatures. The M.A. system excelled for its ability to reach exceptional densities under quasi-isotropic conditions while preserving the nanostructure of the powders. Meanwhile, the piston cylinder press demonstrated a clear advantage in promoting crystallographic alignment in platelet-shaped SrM particles under uniaxial pressure, a crucial factor for enhancing magnetic anisotropy. While a slight reduction in coercivity was generally observed after compaction, due to lattice stress, plastic deformation, and internal demagnetizing fields, the primary objective of improving remanence through grain orientation was successfully accomplished, particularly for MSG-synthesized powders pressed uniaxially. Remarkably, a relative density of 91% was attained using LTSSR nanometric powder compacted with M.A. system at just 80 °C, showcasing the feasibility of ultra-low-temperature densification.

The SPS technique also showed promising results, yielding near-full densification and significant particle alignment in both undoped and Mn-doped MSG powders. Despite minor losses in coercivity in hysteresis loops, SPS

confirmed its potential to produce high-performance anisotropic magnets at reduced sintering temperatures.

The contrasting behaviors of LTSSR and MSG powders in terms of densification and orientation capability underlined the decisive influence of the synthesis route and particle morphology on the final magnetic properties. Future work should focus on fine-tuning compaction parameters to preserve coercivity while maximizing density and orientation, potentially through hybrid synthesis approaches (e.g. MSSR synthesis) or targeted post-compaction treatments to fully unlock the magnetic potential of these nanostructured materials.

# 5.5 References


(1) Pullar, R. C. Hexagonal Ferrites: A Review of the Synthesis, Properties and Applications of Hexaferrite Ceramics. *Prog Mater Sci* **2012**, *57* (7), 1191–1334. https://doi.org/10.1016/j.pmatsci.2012.04.001.

(2) Bansal, N. P.; Boccaccini, A. R. *Ceramics and Composites Processing Methods*; Bansal, N. P., Boccaccini, A. R., Eds.; Wiley, 2012. https://doi.org/10.1002/9781118176665.

(3) Bordia, R. K.; Camacho-Montes, H. Sintering: Fundamentals and Practice. In *Ceramics and Composites Processing Methods*; Wiley, 2012; pp 1–42. https://doi.org/10.1002/9781118176665.ch1.

(4) Granados-Miralles, C.; Jenuš, P. On the Potential of Hard Ferrite Ceramics for Permanent Magnet Technology—a Review on Sintering Strategies. *J Phys D Appl Phys* **2021**, *54* (30), 303001. https://doi.org/10.1088/1361-6463/ABFAD4.

(5) Coey, J. M. D.; Stuart, S. S. *Handbook of Magnetism and Magnetic Materials: Volume 1,2*; Springer International Publishing, 2021; Vol. 1–2. https://doi.org/10.1007/978-3-030-63210-6/COVER.

(6) *Magnetic and Multiferroic Materials | IMEM-CNR*. https://www.imem.cnr.it/en/AdR/4/Magnetic-and-Multiferroic-Materials/intro (accessed 2025-05-30).

(7) *Rockland Research Corporation*. https://rocklandresearch.com/ (accessed 2025-05-30).

(8) Coey, J. M. D. Permanent Magnets: Plugging the Gap. *Scr Mater* **2012**, *67* (6), 524–529. https://doi.org/10.1016/j.scriptamat.2012.04.036.

(9) Stoner, E. C.; Wohlfarth, E. P. A Mechanism of Magnetic Hysteresis in Heterogeneous Alloys. *IEEE Trans Magn* **1991**, *27* (4), 3475–3518. https://doi.org/10.1109/TMAG.1991.1183750.

(10) Dho, J.; Lee, E. K.; Park, J. Y.; Hur, N. H. Effects of the Grain Boundary on the Coercivity of Barium Ferrite BaFe12O19. *J Magn Magn Mater* **2005**, *285* (1–2), 164–168. https://doi.org/10.1016/J.JMMM.2004.07.033.

(11) Valentin, J. L.; Gjørup, F. H.; Knudsen, C. G.; Christensen, M. Grain Alignment in Hexaferrite Permanent Magnets by Compaction at Room and Elevated Temperatures. *Nanoscale* **2024**, *16* (45), 21106–21117. https://doi.org/10.1039/D4NR02738H.

(12) Kojima, H. Fundamental Properties of Hexagonal Ferrites with Magnetoplumbite Structure. In *Handbook of Ferromagnetic Materials*; Elsevier, 1982; Vol. 3, pp 305–391. https://doi.org/10.1016/S1574-9304(05)80091-4.

(13) Stäblein, H. Hard Ferrites and Plastoferrites. In *Handbook of Ferromagnetic Materials*; Elsevier, 1982; Vol. 3, pp 441–602. https://doi.org/10.1016/S1574-9304(05)80093-8.

(14) Widodo, R. D.; Darsono, F. B.; Fitriyana, D. F.; Rusiyanto; Widayat, W.; Nuryanta, M. I.; Kriswanto; Rudianto, I. Effect of Compaction Pressure on Shrinkage, Density, and Hardness of Strontium Hexaferrite. *J Phys Conf Ser* **2024**, *2900* (1), 012049. https://doi.org/10.1088/1742-6596/2900/1/012049.

(15) García-Martín, E.; Granados-Miralles, C.; Ruiz-Gómez, S.; Pérez, L.; Del Campo, A.; Carlos Guzmán-Mínguez, J.; De Julián Fernández, C.; Quesada, A.; Fernández, J. F.; Serrano, A. Dense Strontium Hexaferrite-Based Permanent Magnet Composites Assisted by Cold Sintering Process. **2022**. https://doi.org/10.1016/j.jallcom.2022.165531.

(16) Serrano, A.; García-Martín, E.; Granados-Miralles, C.; Gorni, G.; López-Sánchez, J.; Ruiz-Gómez, S.; Pérez, L.; Quesada, A.; Fernández, J. F. Hexaferrite-Based Permanent Magnets with Upper Magnetic Properties by Cold Sintering Process via a Non-Aqueous Solvent. *Acta Mater* **2021**, *219*, 117262. https://doi.org/10.1016/J.ACTAMAT.2021.117262.

(17) Cui, J.; Ormerod, J.; Parker, D.; Ott, R.; Palasyuk, A.; Mccall, S.; Paranthaman, M. P.; Kesler, M. S.; McGuire, M. A.; Nlebedim, I. C.; Pan, C.; Lograsso, T. Manufacturing Processes for Permanent Magnets: Part I—Sintering and Casting. *JOM* **2022**, *74* (4), 1279–1295. https://doi.org/10.1007/S11837-022-05156-9/FIGURES/14.

(18) Chaim, R.; Levin, M.; Shlayer, A.; Estournes, C. Sintering and Densification of Nanocrystalline Ceramic Oxide Powders: A Review. https://doi.org/10.1179/174367508X297812.

(19) Zlatkov, B. S.; Nikolic, M. V.; Aleksic, O.; Danninger, H.; Halwax, E. A Study of Magneto-Crystalline Alignment in Sintered Barium Hexaferrite Fabricated by Powder Injection Molding. *J Magn Magn Mater* **2009**, *321* (4), 330–335. https://doi.org/10.1016/J.JMMM.2008.09.014.

(20) *Crystalbond Adhesives*. https://www.agarscientific.com/crystalbond-adhesives (accessed 2025-05-30).

(21) Saura-Múzquiz, M.; Eikeland, A. Z.; Stingaciu, M.; Andersen, H. L.; Granados-Miralles, C.; Avdeev, M.; Luzin, V.; Christensen, M. Elucidating the Relationship between Nanoparticle Morphology, Nuclear/Magnetic Texture and Magnetic Performance of Sintered SrFe12O19 Magnets. *Nanoscale* **2020**, *12* (17), 9481–9494. https://doi.org/10.1039/D0NR01728K.

(22) Jenuš, P.; Topole, M.; McGuiness, P.; Granados-Miralles, C.; Stingaciu, M.; Christensen, M.; Kobe, S.; Žužek Rožman, K.; Belik, A. Ferrite-Based Exchange-Coupled Hard–Soft Magnets Fabricated by Spark Plasma Sintering. *Journal of the American Ceramic Society* **2016**, *99* (6), 1927–1934. https://doi.org/10.1111/JACE.14193.

(23) Stingaciu, M.; Topole, M.; McGuiness, P.; Christensen, M. Magnetic Properties of Ball-Milled SrFe12O19 Particles Consolidated by Spark-Plasma Sintering. *Scientific Reports 2015 5:1* **2015**, *5* (1), 1–8. https://doi.org/10.1038/srep14112.

(24) Breitwieser, R.; Acevedo, U.; Ammar, S.; Valenzuela, R. Ferrite Nanostructures Consolidated by Spark Plasma Sintering (SPS). In *Nanostructured Materials - Fabrication to Applications*; InTech, 2017. https://doi.org/10.5772/68017.

(25) Jenuš, P.; Učakar, A.; Repše, S.; Sangregorio, C.; Petrecca, M.; Albino, M.; Cabassi, R.; De Julián Fernández, C.; Belec, B. Magnetic Performance of SrFe12O19–Zn0.2Fe2.8O4 Hybrid Magnets Prepared by Spark Plasma Sintering. *J Phys D Appl Phys* **2021**, *54* (20), 204002. https://doi.org/10.1088/1361-6463/ABDF96.

(26) Stingaciu, M.; Eikeland, A. Z.; Gjørup, F. H.; Deledda, S.; Christensen, M. Optimization of Magnetic Properties in Fast Consolidated SrFe12O19 Nanocrystallites. *RSC Adv* **2019**, *9* (23), 12968–12976. https://doi.org/10.1039/C9RA02440A.

(27) Biesuz, M.; Grasso, S.; Sglavo, V. M. What's New in Ceramics Sintering? A Short Report on the Latest Trends and Future Prospects. *Curr Opin Solid State Mater Sci* **2020**, *24* (5), 100868. https://doi.org/10.1016/J.COSSMS.2020.100868.

(28) Cavaliere, P.; Sadeghi, B.; Shabani, A. Spark Plasma Sintering: Process Fundamentals. In *Spark Plasma Sintering of Materials*; Springer International Publishing: Cham, 2019; pp 3–20. https://doi.org/10.1007/978-3-030-05327-7_1.

# **Chapter 6 |** Nanocomposites based on $Fe^0$ nanowires and SrM for innovative PMs

Among the different strategies proposed to increase the energy product of standard hexagonal ferrites, combining soft and hard magnetic phases at the nanoscale to create novel magnetic materials with enhanced properties has emerged as a highly promising research direction[1–5]. This concept is primarily based on the principle of exchange-coupling, first proposed by Kneller and Hawig [6]. When a soft magnetic phase and a hard magnetic phase are brought into intimate contact at the nanoscale, typically below the domain wall width of the hard phase [7], magnetic exchange interactions at their interface can lead to a synergistic improvement in the magnetic properties. Ideally, an exchange-coupled nanocomposite (NC) magnet can exhibit a high saturation magnetization (contributed by the soft phase) and a high coercivity (contributed by the hard phase), potentially surpassing the performance of individual components and leading to a significantly enhanced maximum energy product $(BH)_{max}$[8–10]. The effectiveness of exchange-coupling is critically dependent on several factors, including the intrinsic magnetic properties of the constituent phases, their volume fractions, the size and morphology of the nanostructures, the degree of interfacial contact, and the crystallographic alignment of the grains [2,4,11]. Being an interface-related effect, even in this case, reaching the nanoscale can be beneficial as the particles' surface area to volume ratio can be maximized, while focusing on the SD size range and avoiding the SPM state[12]. When coupled, the spins of the soft phase align with those of the hard phase, and the magnetization direction can thus

rotate coherently. This interaction can significantly influence the shape of the hysteresis loop, resulting in a single-phase magnetization behavior even if multiple magnetic phases are present. In the absence of exchange-coupling, there is the possibility of exploiting the magnetodipolar interactions inside the magnetic material to align the spins of both phases [13]. Normally, the internal dipolar interactions and the demagnetizing fields, especially of the high magnetization soft phases, normally lead to a substantial decrease of both remanence and coercivity [14]. However, in certain conditions, the interphase dipolar interactions have been reported to lead to a horizontal and vertical shift in the hysteresis loop that entails an increase in remanence and energy product [15,16]. The idea is that mixing hard and soft with appropriate material´s parameters, particle sizes, shapes and distribution, a certain fraction of the soft spins aligns with the effective H field created by the aligned SrM particles. A competition between the self-demagnetizing field of the soft and the effective 'external' field of the hard occurs [17,18].

In this framework, we attempted to prepare a nanocomposite where the best SrM nanoparticles developed in this work and discussed in the previous Chapter, are coupled with a high magnetization, anisotropic soft phase, constituted by $Fe^0$ nanowires (NWs). The underlying principle is to leverage the high $M_S$ of $Fe^0$ NWs to improve the remanence of the NC, while the hard phase, in this case SrM, provides the high coercivity.

# 6.1 Synthesis of the soft phase: metal Iron Nanowires

Among the diverse nanostructures, one-dimensional nanomaterials, such as nanowires (NWs), have garnered significant attention due to their unique anisotropic shape and high surface area-to-volume ratios, which grant for potential applications in diverse fields [19–21]. Magnetic zero-valent iron ($Fe^0$) NWs, in particular, stand out owing to their strong intrinsic magnetization and cost-effectiveness, in combination with the anisotropy derived from the elongated shape of the wire [22,23]. The magnetic properties of $Fe^0$ NWs are significantly influenced by their dimensions, morphology, crystal structure, and surface characteristics, making their controlled synthesis a critical aspect of their application [24–29]. This section focuses on the synthesis and characterization of $Fe^0$ NWs, tailored for the subsequent preparation of SrM/$Fe^0$ NCs. The objective is to understand the fundamental relationships between the physical and magnetic characteristics of the Fe NWs, and their efficacy in promoting intimate interfacial contact, and possibly exchange-coupling, with nanosized SrM.

To synthesize $Fe^0$ NWs we explored a wet-chemistry approach, the chemical reduction of metal salts with sodium borohydride ($NaBH_4$) in aqueous environment [30–32]. The key feature of the chemical reduction is the simplicity, the low cost, and environmental sustainability, providing a route for scalable production [33]. Since $Fe^0$ is prone to oxidize, all the procedures for its synthesis need to be performed under protected environment of inert gas ($N_2$) and with manipulation techniques for handling air-sensitive compounds ($H_2$ development during the reaction). However, this method, especially regarding morphology and size distribution, is still not standardized, even if these factors

can significantly influence the ultimate reactivity of the NWs [34,35]. The characteristics of the final product are influenced by several factors, like the solvent, the volume of $NaBH_4$ and the addition rate [30,36] and the aging conditions [37,38]. To be in line with a green procedure, the chosen solvent was water, as it is the most appropriate to be inserted in a sustainable and cost-effective reaction to be scaled to industrial production. In the typical process, the metal salts are dissolved in DM water to give a resultant concentration of 0.09 M for iron (III) chloride hexahydrate ($FeCl_3.6H_2O$) and 0.19 M for $NaBH_4$. All the solvents were adequately degassed through $N_2$-purging (bubbling) to minimize oxygen availability [39]. The reaction was performed inside a $N_2$-filled glovebag (FeNWs_I), or alternatively through a $N_2$ Schlenk-line (FeNWs_II). The as-prepared $NaBH_4$ solution was added to the iron chloride solution quickly, then the precipitated $Fe^0$ was washed thoroughly with degassed ethanol and collected with the help of a magnet, to be finally dried in a $N_2$ flux. The resulting $Fe^0$ NWs were characterized using various analytical techniques, including XRD for phase identification, SEM and TEM for morphological and structural analysis, and VSM or SQUID magnetometry for magnetic property evaluation.

As it can be seen in the TEM images reported in **Figure 6-1**, the experimental trials resulted in aggregated nanoparticles assembled in a chain-like superstructure with lengths up to 5 μm and a mean diameter of 87 ± 22 nm. The particles are not perfectly round, and their diameter varies moving along the wires, thinning out towards the edges. In the magnification of TEM images, the formation of a core-shell structure can be evidenced [40], where a thin oxide shell (few nanometers) of markedly less contrast covers the inner core of iron. This is a very characteristic feature of the applied synthesis method, even when strictly controlled inert conditions are adopted, due to uncomplete degassing of the aqueous environment [41,42]. The layer is made out of amorphous iron

oxide which exact composition is hard to be determined [43,44]. The most relevant fact in our case is the modification of the magnetic properties of the $Fe^0$ nanoparticles caused by the shell, which provides a much lower contribution to the saturation magnetization compared to metal iron. Since our intent is to try to maximize the $M_S$ value to be beneficial during the coupling with SrM, the shell thickness must be kept as thinner as possible. This is not an easy task, since the high surface-to-volume ratio makes the small particles extremely reactive enhancing the intrinsic sensitivity of $Fe^0$ towards oxygen, air and water.

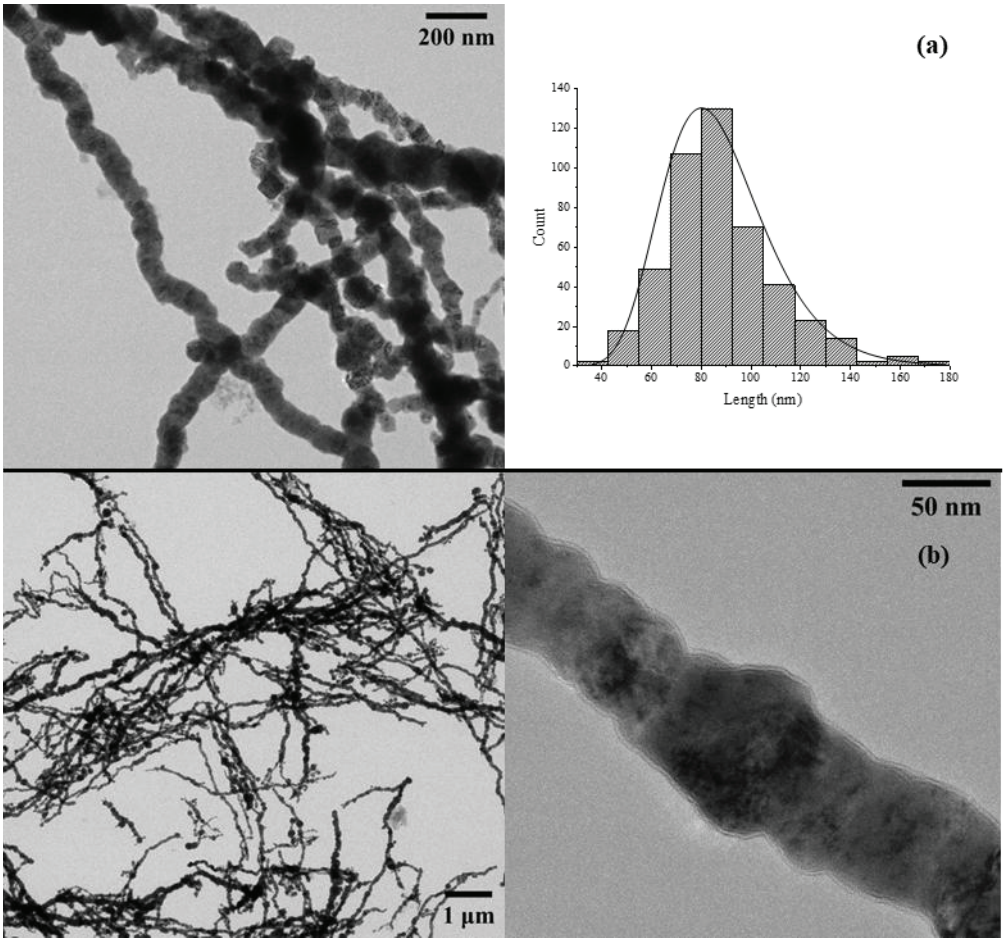


***Figure 6-1*** *Representative TEM images of: (a) synthesized samples of $Fe^0$ NWs and corresponding diameter distribution histogram; (b) overall and magnified images of the wires.*

In the experimental XRD pattern (**Figure 6-2**), measured under a thin film of Kapton to prevent air exposure, the primary peaks of metal iron can be recognized, indicative of the successful synthesis of $Fe^0$ NWs. However, the peak broadness suggests a partial amorphous nature of iron. In addition to the main peaks, the diffractogram evidenced the small presence of a secondary phase, which can be identified by the peak at 2θ = 35°, suggesting the iron oxide shell is probably constituted by a spinel ferrite oxide (see the maghemite reference in the figure). The low intensity of this secondary phase can be also due to the Kapton film background, which reduces the intensity of the signal.

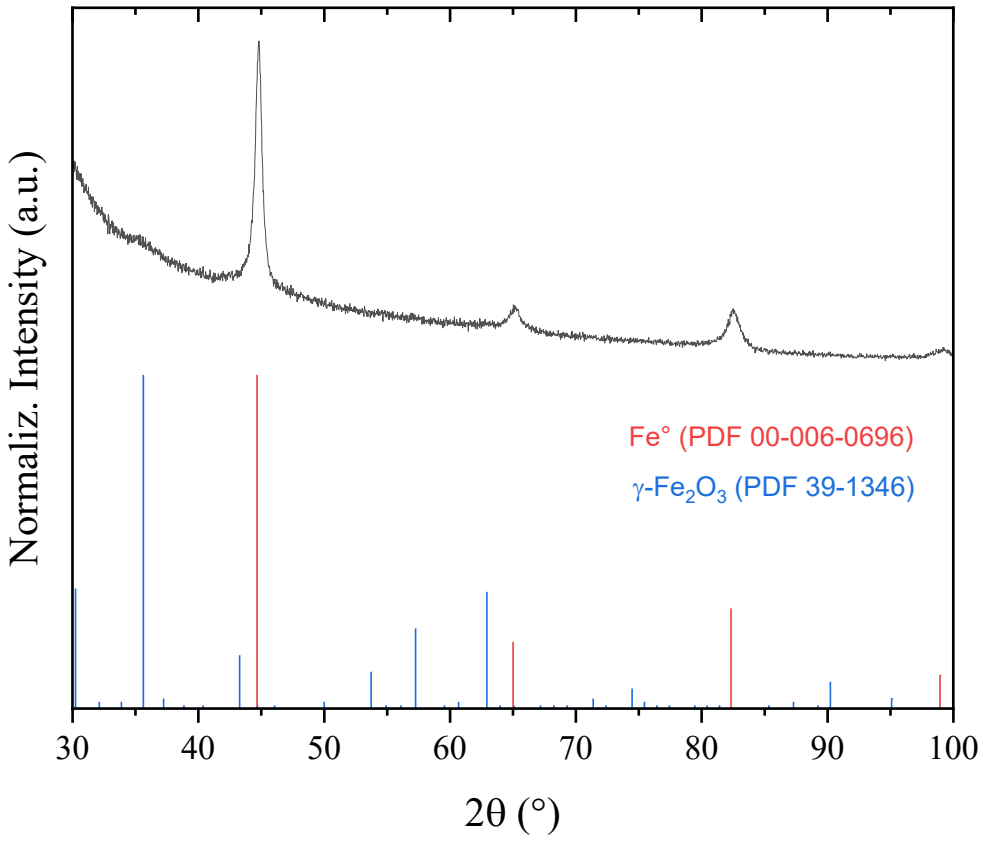


***Figure 6-2*** *Representative PXRD diffraction pattern of $Fe^0$ NWs samples. The diffractogram of samples was collected under a protective film of Kapton.*

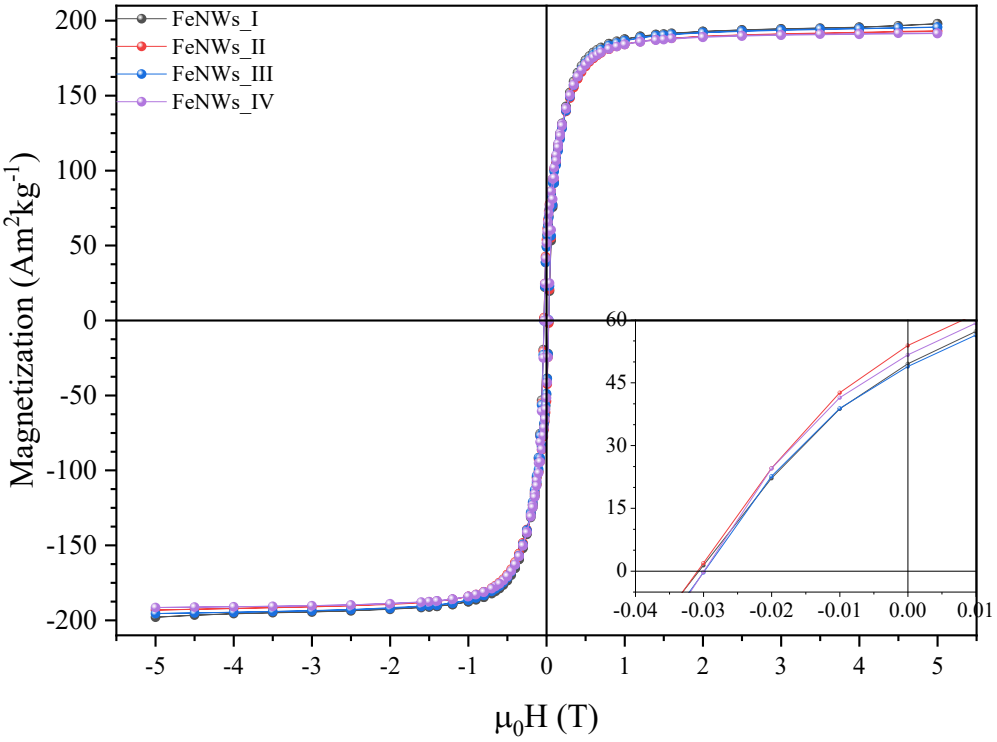


***Figure 6-3*** *Hysteresis loops at 300K of different samples of the synthesized $Fe^0$ NWs. All the samples were produced inside the glovebag, except for sample FeNWs_II which was prepared in a Schlenk line.*

In order to verify the reproducibility of the preparation technique, the magnetic properties of 4 samples, 3 prepared produced inside the glovebag (FeNWs_I, FeNWs_III, and FeNWs_IV) and one in a Schlenk line (FeNWs_II), were investigated. From the analysis of the hysteresis loops collected at 300 K (**Table 6-1**), it emerges that the synthesis is highly reproducible as the properties are very similar one to each other. The $M_S$ reached in the best samples was considerably high, reaching values near to 200 $Am^2kg^{-1}$. These values are close to the $M_S$ of bulk iron, which is around 220 $Am^2kg^{-1}$ [45]. In our case the slightly lower Ms can be ascribed to the presence of the oxide shell.

Despite adequate protection, samples with high magnetization (up to 203 $Am^2kg^{-1}$ at 5K) showed a 9-13% decrease after just one day, with average value dropping to 170-175 $Am^2kg^{-1}$. This behavior underlines the poor stability of the synthesized product, suggesting some modifications in the synthesis procedure.

***Table 6-1*** *Magnetic values obtained from hysteresis at 300K of the synthesized $Fe^0$ NWs. Samples FeNWs_I, FeNWs_III, FeNWs_IV were made inside a glovebag, sample FeNWs_II in a Schlenk line.*

| Sample | $M_s$ ($Am^2kg^{-1}$) | $M_r$ ($Am^2kg^{-1}$) | $M_r/M_s$ | $H_c$ (Oe) |
|---|---|---|---|---|
| **FeNWs_I** | 198 | 50 | 0.25 | 305 |
| **FeNWs_II** | 193 | 54 | 0.28 | 310 |
| **FeNWs_III** | 196 | 56 | 0.29 | 300 |
| **FeNWs_IV** | 192 | 52 | 0.27 | 300 |

## 6.1.1 The effect of PVP as capping agent

One of the strategies to improve the NWs' surface stability to air exposure, relied on the surface modification of bare-iron NWs. Polyvinylpyrrolidone (PVP), an environmentally friendly, low-cost and water-soluble dispersant, has been widely used in nanoparticles synthesis to provide steric and electrostatic stabilization [31,46,47]. To provide a protective layer towards oxidation, two different PVP percentages (12%, 2% w/w over the $Fe^{3+}$ precursor) were added in the solution before the addition of $NaBH_4$.

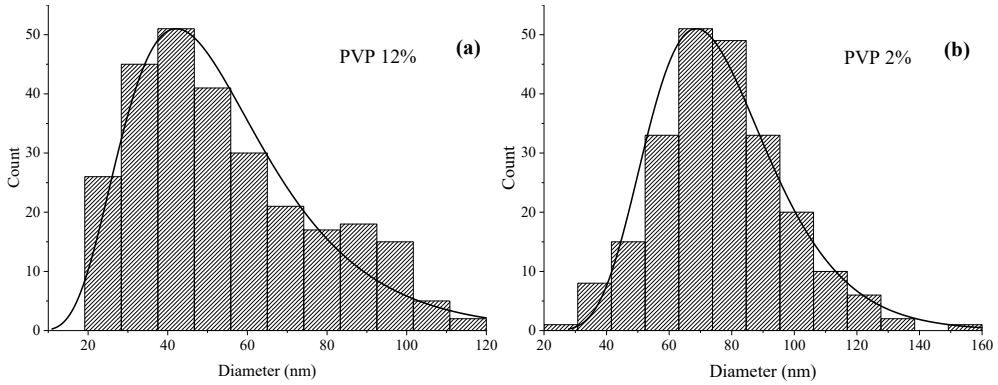


***Figure 6-4*** *Histogram of the diameter distribution of FeNWs synthesized with different PVP concentration: (a) 12%; (b) 2%*

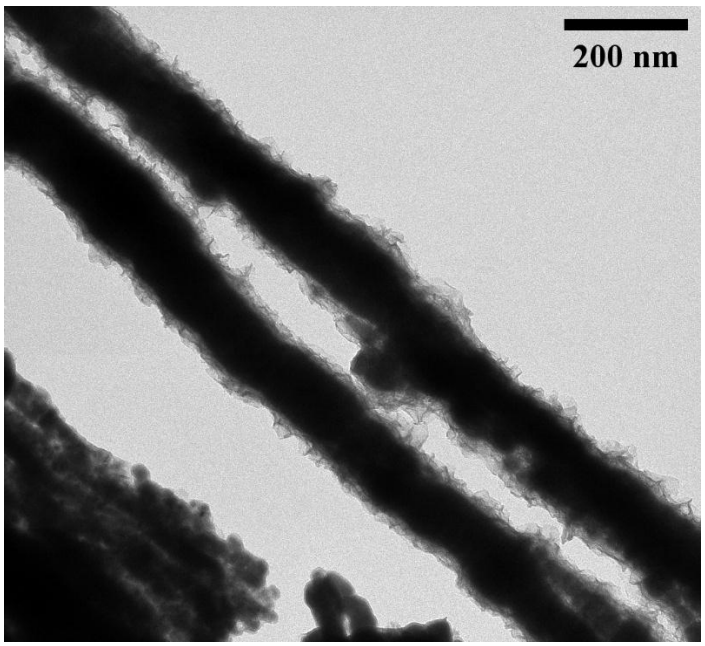


***Figure 6-5*** *Representative image of the synthesized $Fe^0$ NWs capped with PVP.*

In both cases, the inclusion of the PVP affected the size distribution of the resultant NWs (**Figure 6-4**). The surfactant caused a shrinkage in the mean particle size, reducing it to 76 ± 20 nm in the case of 2% PVP addition, or it is reduced even more in the case of 12% PVP, reaching a mean of 54 ± 22 nm.

Through the hysteresis loop collected at 300 K ( **Figure 6-6** ), the impact on the main magnetic properties can be also appreciated.

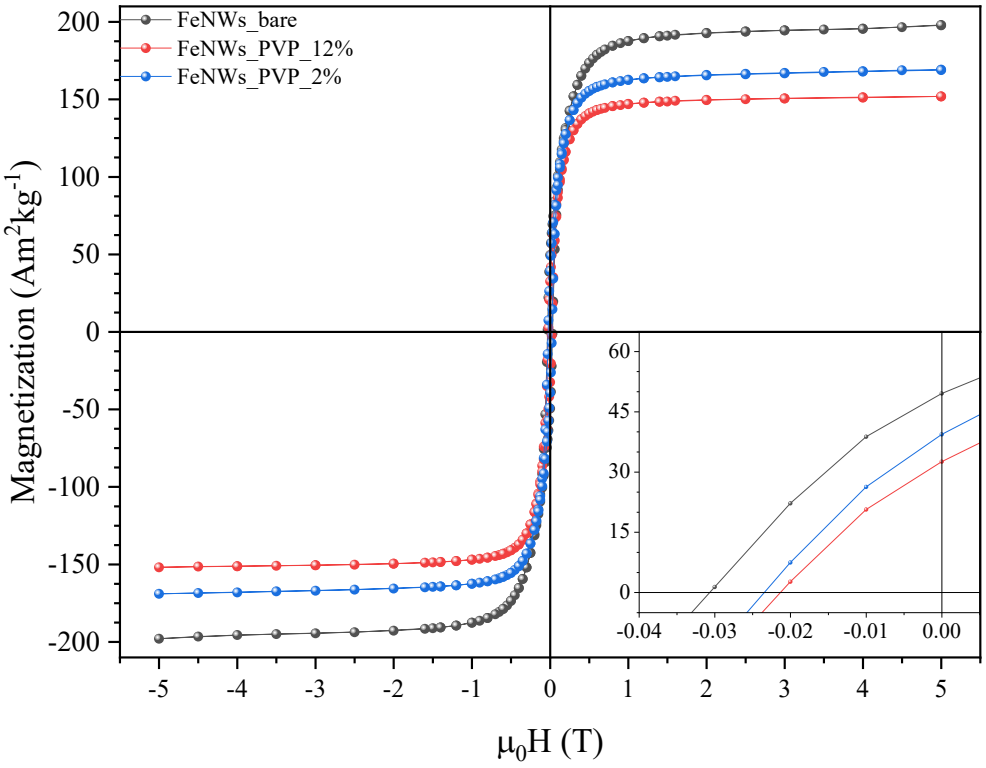


***Figure 6-6*** *Hysteresis loops collected at 300 K of $Fe^0$ NWs samples synthesized with different PVP concentrations: 12% (red curve); 2% (blue curve). The samples are compared to uncoated $Fe^0$ NWs (black curve).*

The effect of PVP coating reflected even in the magnetization of the NWs, lowering its value. The magnetization reduction can be ascribed to the presence of a non-magnetic layer of polymer (PVP) on the surface of the nanoparticles and the diminished diameter, therefore enhancing the surface-to-volume ratio. On the surface the number of defects, cation vacancies, etc., are large in comparison to the inside core region of the particles, and all these effects contribute negatively to the overall magnetization [48–50]. The observed values of Ms (**Table 6-2**), compared with the highest value obtained from the synthesized bare $Fe^0$ NWs (197 $Am^2kg^{-1}$), presented a magnetization loss of

23% in case of Fe NWs coated with 12% PVP and 14% in the case of 2% PVP addition. Once the data are scaled for the effective amount of metal iron present in the NWs $M_S$ decreases 172 $Am^2kg^{-1}$, which however is around 12% lower than the best value obtained for the bare $Fe^0$ NWs. Moreover, a decrease of $H_C$ is also observed.

***Table 6-2*** *Magnetic values obtained from hysteresis at 300K of the synthesized bare and PVP-coated $Fe^0$ NWs. The data were corrected by removing the magnetic contribution of PVP.*

| Sample | $M_s$ ($Am^2kg^{-1}$) | $M_r$ ($Am^2kg^{-1}$) | $M_r/M_s$ | $H_c$ (Oe) |
|---|---|---|---|---|
| **FeNWs_bare** | 198 | 50 | 0.25 | 305 |
| **FeNWs_PVP_12%** | 152 | 33 | 0.21 | 210 |
| **FeNWs_PVP_2%** | 169 | 39 | 0.23 | 235 |

All together these data underline that PVP does not provide an effective protection able to prevent oxidation of the NWs. As a future work, other surface modifications must be tested, employing organic or inorganic coatings, which can be suitable for preserving the optimal magnetic properties of the synthesized $Fe^0$ NWs [51-54]

## 6.1.2 The impact of high temperature treatment

As an alternative road to stabilize the NWs and in order to increase the magnetic contribution of the shell, we explored the possibility to promote the crystallization of the amorphous phase by applying a heat treatment [55]. According to the literature, the crystallization of the α-Fe phase from the amorphous structure is observed at temperatures around 450–500 °C [56-57]. For this reason, some Fe NWs, owning an initial $M_S$ of 188 $Am^2kg^{-1}$, were subjected to thermal annealing in a tubular furnace under inert atmosphere ($N_2$) at 500 °C for 2 hours. In **Figure 6-7** is shown the resultant XRD diffractogram, where the main diffraction peak of $Fe^0$ after thermal annealing appears

narrowed and surrounded by less background noise, indicating a successful transition from amorphous to crystalline state. However, TEM images (**Figure 6-8**) revealed an enlargement of the grain size, with an increase in the mean value, that almost doubled (167 nm for annealed samples), and the loss of the wire arrangement, with the formation of really large particles and randomly sized aggregates.

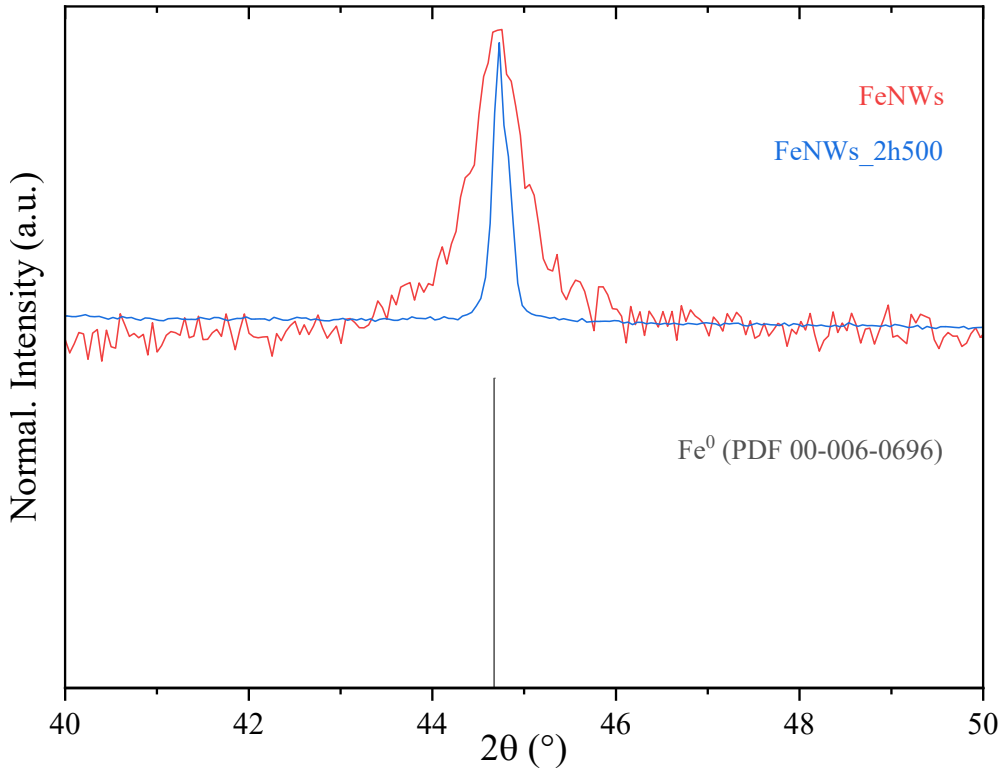


***Figure 6-7*** *PXRD diffraction pattern of as-synthesized $Fe^0$ NWs (red line) and after thermal annealing at 500 °C, 2h (blue line).*

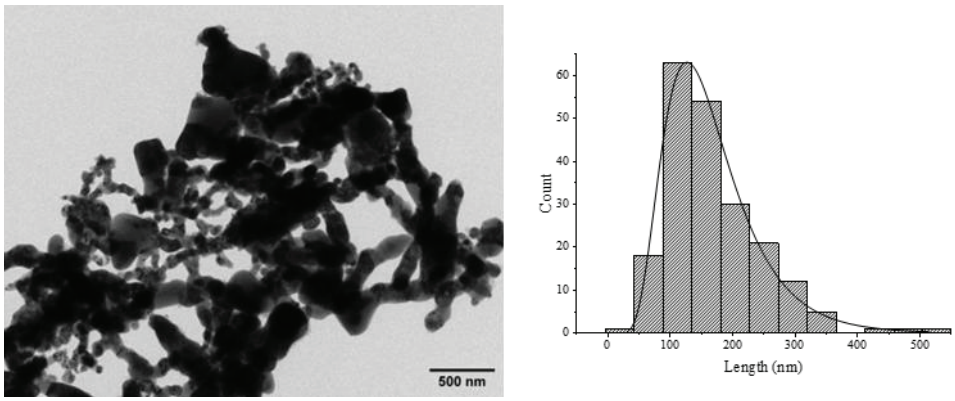


***Figure 6-8*** *TEM images and distribution plot of the sample of $Fe^0$ NWs thermally annealed at 500 °C, 2h.*

On the other hand, no variation was observed in the $M_S$ values at 300 K (from 188 $Am^2kg^{-1}$ to 185 $Am^2kg^{-1}$) while remanence and the coercivity were significantly reduced down to 12 $Am^2kg^{-1}$ and 95 Oe, respectively, in accordance with the change in morphology. Interestingly, the $M_S$ value remained almost stable even after 8 days of air exposure (182 ± 3 $Am^2kg^{-1}$). This stability is a promising indicator of the material's resistance to oxidation. Further studies will investigate heat treatments at lower temperatures to prevent material deformation, aimed at preserving the wire structure and maintaining consistent morphology.

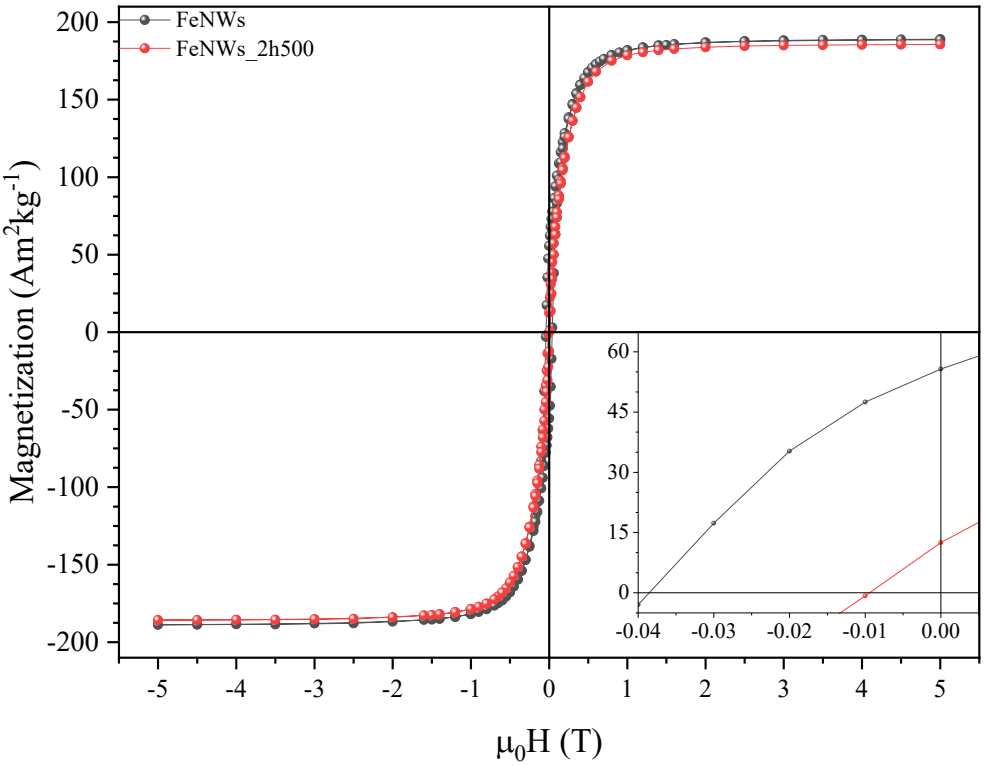


***Figure 6-9*** *Hysteresis loops collected at 300 K of as-synthesized $Fe^0$ NWs (black curve) and after thermal annealing at 500 °C for 2 h (red curve). The inset displays the enlargement of the low field region.*

To conclude, the different strategies explored to mitigate the harmful effects of oxidation on NWs stability, present some limitations. Future studies will focus on refining and improving these approaches to further enhance the air stability of the NWs, aiming to achieve an optimized material suitable for coupling with SrM and for the development of advanced NCs.

## 6.2 The realization of SrM - $Fe^0$ NWs nanocomposites for improved SrM

In order to prepare hard-soft composites different strategies were explored. The employed techniques involved the physical mixing of the hard and soft components through sonication in degassed EtOH, grinding the powders in an agate mortar, or alternatively to this second step, the annealing of the mixed powders at different temperatures. Different ratios of the two phases were evaluated, starting from 70% in SrM content by weight to 95%. In the following the NCs will be named *NC_x/y*, where "x" and "y" represent the relative percentage of SrM_MB and $Fe^0$ NWs, respectively. All the procedures were performed under protected $N_2$ environment to prevent the oxidation of $Fe^0$. Then, the mixed powders were dispersed in docosane wax and aligned in a magnetic field of 0.5 T, to favor the orientation of nanograins. As a first attempt we explored the combination of the synthesized $Fe^0$ NWs described above with a commercial micrometric powder of SrM, produced by Max Baermann Gmbh, (SrM_MB) [58].

The physical arrangement of the micrometric platelets into the array of the iron wires was investigated by TEM and SEM images. The analysis of the acquired images for sample NC_70/30_MB_$Fe^0$ revealed a recurrent pattern with oriented SrM platelets aligned with the main axis of iron NWs (representative TEM and SEM images are shown in **Figure 6-10** and **Figure 6-11**). Moreover, this specific arrangement was consistently observed across the entire range of investigated SrM/$Fe^0$ ratios. This observed feature indicates a possible non-uniform distribution of magnetic dipoles within the NWs, with a preferential localization of the SrM at their extremities [59-60].

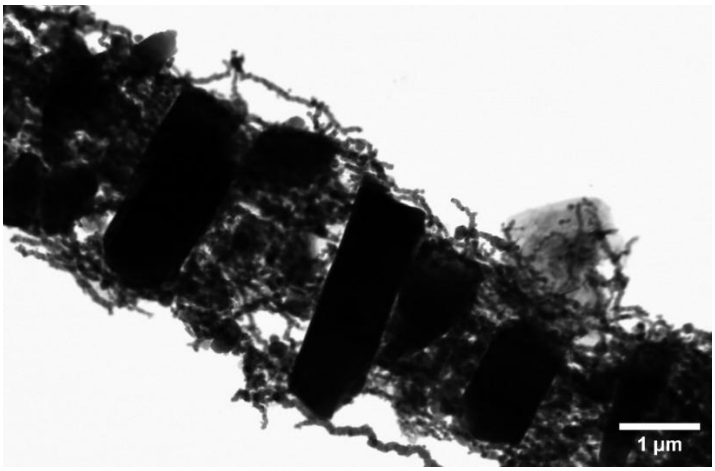


***Figure 6-10*** *Representative TEM image of the NC obtained by combining micrometric SrM_MB (70%) with synthesized $Fe^0$ NWs (30%) and aligned in docosane wax.*

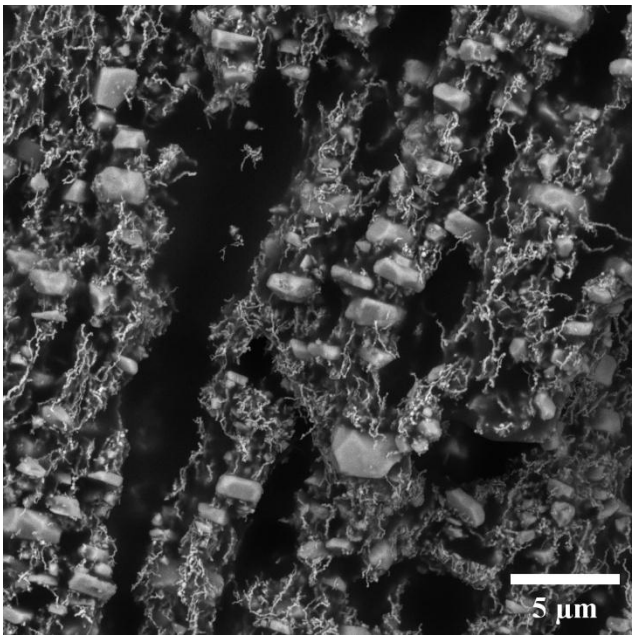


***Figure 6-11*** *Representative SEM image of the NC obtained by combining micrometric SrM_MB (70%) with synthesized $Fe^0$ NWs (30%) and aligned in docosane wax.*

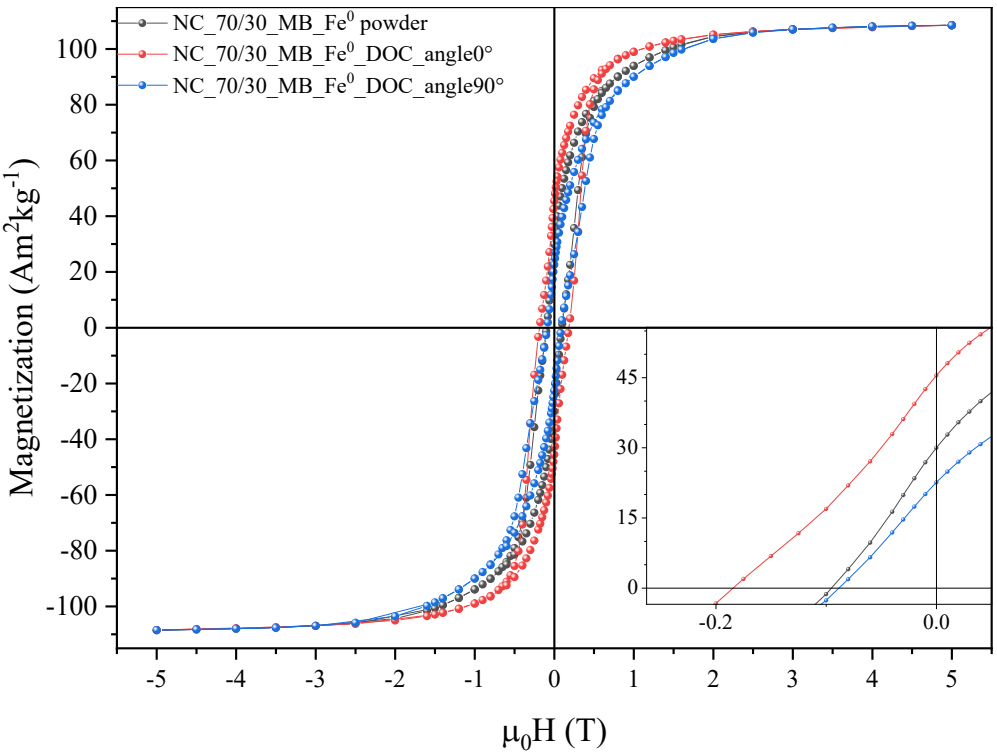


***Figure 6-12*** *Hysteresis loop recorded at room temperature of the NC obtained by combining SrM_MB with $Fe^0$ NWs. The powder was aligned in docosane (DOC) in a magnetic field of 0.5 T and measured parallel (angle 0°) and perpendicular (angle 90°) to the magnetic field. The black line refers to the not aligned powder.*

The magnetic properties of the NCs are summarized in **Table 6-3** and shown in **Figure 6-13** as a function of the metal content. As expected, the addition of $Fe^0$ NWs led to an increase of $M_S$ and a decrease of the coercivity. NC_70/30 exhibited the highest $M_S = 108\ Am^2kg^{-1}$ and lowest $H_C = 0.10$ T, corresponding to an increase of 53% in $M_S$ and a decrease of 64% in $H_C$ with respect to the pure SrM powder, while the fall in remanence was instead of 32%. The shape of the hysteresis loop, reported in **Figure 6-12** denoted a partially decoupled system, suggesting that under these experimental conditions no effective exchange coupling was obtained. On the other hand, the comparison of the

loops measured by applying the field parallel or perpendicular to the alignment direction demonstrates a partial degree of alignment.

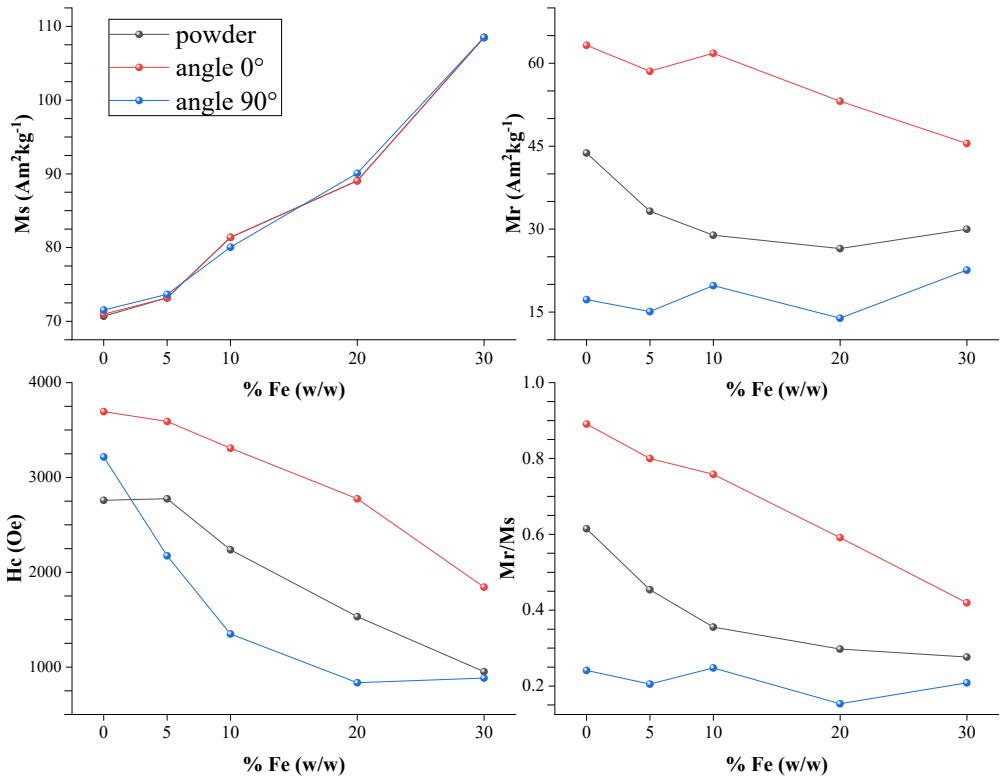


***Figure 6-13*** *Evolution of the main magnetic properties of SrM_MB in function of the $Fe^0$ NW concentration. The label "powder" refers to the physical mix. The aligned powder in docosane was measured parallel (angle 0°) and perpendicular (angle 90°) to the magnetic field in SQUID.*

NC_95/5 powders exhibit magnetic parameters close to those of the pure SrM sample ($H_C$ decreased by 3%, and $M_R$ by 7%). Particularly, the remanence of NC_90/10 decreased by only 2% for the parallel case. Interestingly, the $M_R$ values were in accordance with the calculated values from the linear combination of $M_R$ contributions of the two phases ($M_R$ of $Fe^0$ NWs was 48 $Am^2kg^{-1}$). Although, given the existence of magnetostatic interacting fields

between all particles, we cannot exclude this agreement may just be a coincidence as the exact magnetic state of each phase is unknown [18], it suggests a dipolar interaction is activated in the magnetically oriented state, similarly to what discovered by Guzmán-Minguez in another work on hard-soft bonded magnet prepared through injection moulding [16].

***Table 6-3*** *Main magnetic properties from the hysteresis loops at 300 K of the NCs obtained by combining SrM_MB with synthesized $Fe^0$ NWs, where the label "_powders" refers to the physical mix. The aligned powder in docosane was measured parallel (angle 0°) and perpendicular (angle 90°) to the magnetic field in SQUID.*

| | $M_s$ ($Am^2kg^{-1}$) | $M_r$ ($Am^2kg^{-1}$) | $M_r/M_s$ | $\mu_0H_c$ (T) |
|---|---|---|---|---|
| **SrM_MB_powder** | 70 | 44 | 0.61 | 0.28 |
| **NC_95/05_powder** | 73 | 33 | 0.45 | 0.28 |
| **NC_90/10_powder** | 81 | 29 | 0.36 | 0.22 |
| **NC_80/20_powder** | 89 | 26 | 0.30 | 0.15 |
| **NC_70/30_powder** | 108 | 30 | 0.28 | 0.10 |
| **SrM_MB_angle0°** | 71 | 63 | 0.89 | 0.37 |
| **NC_95/05_angle0°** | 73 | 59 | 0.80 | 0.36 |
| **NC_90/10_angle0°** | 81 | 62 | 0.76 | 0.33 |
| **NC_80/20_angle0°** | 89 | 53 | 0.59 | 0.28 |
| **NC_70/30_angle0°** | 108 | 45 | 0.42 | 0.18 |
| **SrM_MB_angle90°** | 72 | 17 | 0.24 | 0.32 |
| **NC_95/05_angle90°** | 74 | 15 | 0.20 | 0.22 |
| **NC_90/10_angle90°** | 80 | 20 | 0.25 | 0.13 |
| **NC_80/20_angle90°** | 90 | 14 | 0.15 | 0.08 |
| **NC_70/30_angle90°** | 108 | 23 | 0.21 | 0.09 |

## 6.3 Conclusions

In this chapter, the development of SrM/Fe⁰ nanocomposites was investigated with the aim of achieving exchange-coupling to enhance SrM's magnetic properties. The synthesis of the soft magnetic phase successfully yielded Fe⁰ NWs with high $M_S$ values, close to those bulk iron, using a sustainable and scalable method, an encouraging result for future applications. While the intrinsic instability and tendency to oxidize of $Fe^0$ NWs remains a challenge, the outcomes provide a solid foundation for further improvements. Although strategies such as PVP coating and thermal annealing did not fully preserve the desired magnetic and morphological properties, they offer valuable insight into the system's behavior and guide for future optimization. Further strategies could regard controlled thermal or chemical oxidation, the employment of different coatings, either organic or inorganic, to evaluate suitable paths to preserve the inherent characteristics of the NWs.

Although initials attempts to combine Fe⁰ NWs with commercial micro-SrM did not result in a clear exchange coupling, as evidenced by the observed decoupled magnetic behavior in the hysteresis, a particularly promising outcome was found in the system comprising commercial SrM and Fe⁰ nanowires at a 90/10 ratio. The enhanced remanence in this composition suggested the presence of beneficial magnetostatic dipolar interactions, opening new possibilities for performances enhancement even in the absence of full exchange coupling. These results point to interesting prospects: by optimizing dipolar interactions, especially in aligned magnet configurations, and by fine-tuning the SrM/$Fe^0$ ratio, it may lead to peculiar magnetic behavior. The development of more advanced magnet samples, namely a bonded

magnet, can be beneficial in this context, combining high pressure application and embedding a suitable matrix to adequately protect the $Fe^0$.

# References


(1) Xu, X.; Hong, Y. K.; Park, J.; Lee, W.; Lane, A. M. Exchange Coupled SrFe12O19/Fe-Co Core/Shell Particles with Different Shell Thickness. *Electronic Materials Letters* **2015**, *11* (6), 1021–1027. https://doi.org/10.1007/S13391-015-5163-1/METRICS.

(2) Granados-Miralles, C.; Saura-Múzquiz, M.; Andersen, H. L.; Quesada, A.; Ahlburg, J. V.; Dippel, A. C.; Canévet, E.; Christensen, M. Approaching Ferrite-Based Exchange-Coupled Nanocomposites as Permanent Magnets. *ACS Appl Nano Mater* **2018**, *1* (7), 3693–3704. https://doi.org/10.1021/ACSANM.8B00808/ASSET/IMAGES/LARGE/AN-2018-00808N_0008.JPEG.

(3) Maltoni, P.; Sarkar, T.; Barucca, G.; Varvaro, G.; Locardi, F.; Peddis, D.; Mathieu, R. Tuning the Magnetic Properties of Hard-Soft SrFe12O19/CoFe2O4 Nanostructures via Composition/Interphase Coupling. *Journal of Physical Chemistry C* **2021**, *125* (10), 5927–5936. https://doi.org/10.1021/ACS.JPCC.1C00355/ASSET/IMAGES/LARGE/JP1C00355_0005.JPEG.

(4) Liu, F.; Hou, Y.; Gao, S. Exchange-Coupled Nanocomposites: Chemical Synthesis, Characterization and Applications. *Chem Soc Rev* **2014**, *43* (23), 8098–8113. https://doi.org/10.1039/C4CS00162A.

(5) Jenuš, P.; Topole, M.; McGuiness, P.; Granados-Miralles, C.; Stingaciu, M.; Christensen, M.; Kobe, S.; Žužek Rožman, K.; Belik, A. Ferrite-Based Exchange-Coupled Hard–Soft Magnets Fabricated by Spark Plasma Sintering. *Journal of the American Ceramic Society* **2016**, *99* (6), 1927–1934. https://doi.org/10.1111/JACE.14193.

(6) Kneller, E. F.; Hawig, R. The Exchange-Spring Magnet: A New Material Principle for Permanent Magnets. *IEEE Trans Magn* **1991**, *27* (4), 3588–3600. https://doi.org/10.1109/20.102931.

(7) Schrefl, T.; Kronmüller, H.; Fidler, J. Exchange Hardening in Nano-Structured Two-Phase Permanent Magnets. *J Magn Magn Mater* **1993**, *127* (3), L273–L277. https://doi.org/10.1016/0304-8853(93)90042-Z.

(8) Skomski, R.; Coey, J. M. D. Giant Energy Product in Nanostructured Two-Phase Magnets. *Phys Rev B* **1993**, *48* (21), 15812. https://doi.org/10.1103/PhysRevB.48.15812.

(9) Coehoorn, R.; de Mooij, D. B.; de Waard, C. Meltspun Permanent Magnet Materials Containing Fe3B as the Main Phase. *J Magn Magn Mater* **1989**, *80* (1), 101–104. https://doi.org/10.1016/0304-8853(89)90333-8.

(10) Skomski, R.; Coey, J. M. D. Exchange Coupling and Energy Product in Random Two-Phase Aligned Magnets. *IEEE Trans Magn* **1994**, *30* (2), 607–609. https://doi.org/10.1109/20.312350.

(11) Asti, G.; Solzi, M.; Ghidini, M.; Neri, F. M. Micromagnetic Analysis of Exchange-Coupled Hard-Soft Planar Nanocomposites. *Phys Rev B* **2004**, *69* (17), 174401. https://doi.org/10.1103/PhysRevB.69.174401.

(12) Skomski, R. Nanomagnetics. *Journal of Physics: Condensed Matter* **2003**, *15* (20), R841. https://doi.org/10.1088/0953-8984/15/20/202.

(13) Montero, M. I.; Cebollada, F.; Morales, M. P.; González, J. M.; Hernando, A. Magnetic Interactions in Fe–Ba Hexaferrite Nanocomposite Materials. *J Appl Phys* **1998**, *83* (11), 6277–6279. https://doi.org/10.1063/1.367774.

(14) de Julián Fernández, C.; Sangregorio, C.; de la Figuera, J.; Belec, B.; Makovec, D.; Quesada, A. Progress and Prospects of Hard Hexaferrites for Permanent Magnet Applications. *J Phys D Appl Phys* **2021**, *54* (15), 153001. https://doi.org/10.1088/1361-6463/ABD272.

(15) González, J. M.; Montero, M. I.; Raposo, V.; Crespo, P.; Marín, P.; Hernando, A. Dipolar Interactions in Hard-Soft Nanocomposites. *IEEE Trans Magn* **2000**, *36* (5 I), 3342–3344. https://doi.org/10.1109/20.908794.

(16) Guzmán-Mínguez, J. C.; Granados-Miralles, C.; Kuntschke, P.; de Julián Fernández, C.; Erokhin, S.; Berkov, D.; Schliesch, T.; Fernández, J. F.; Quesada, A. Remanence Increase in SrFe12O19/Fe Exchange-Decoupled Hard-Soft Composite Magnets Owing to Dipolar Interactions. *Nanomaterials 2023, Vol. 13, Page 2097* **2023**, *13* (14), 2097. https://doi.org/10.3390/NANO13142097.

(17) González, J. M.; Montero, M. I.; Raposo, V.; Hernando, A. On the Relationship between the Hysteresis Loop Shift and the Dipolar Interactions in Hard–Soft Nanocomposite Samples. *J Magn Magn Mater* **2000**, *221* (1–2), 187–195. https://doi.org/10.1016/S0304-8853(00)00526-6.

(18) Guzman-Mínguez, J. C.; Ruiz-Gomez, S.; Vicente-Arche, L. M.; Granados-Miralles, C.; Fernandez-Gonzalez, C.; Mompean, F.; García-Hernandez, M.; Erohkin, S.; Berkov, D.; Mishra, D.; De Julian Fernandez, C.; Fernandez, J. F.; Perez, L.; Quesada, A. FeCo Nanowire−strontium Ferrite Powder Composites for Permanent Magnets with High-Energy Products. *ACS Appl Nano Mater* **2020**, *3* (10), 9842–9851. https://doi.org/10.1021/ACSANM.0C01905/ASSET/IMAGES/LARGE/AN0C01905_0007.JPEG.

(19) Fert, A.; Piraux, L. Magnetic Nanowires. *J Magn Magn Mater* **1999**, *200* (1–3), 338–358. https://doi.org/10.1016/S0304-8853(99)00375-3.

(20) Murphy, C. J.; Jana, N. R. Controlling the Aspect Ratio of Inorganic Nanorods and Nanowires. https://doi.org/10.1002/1521-4095.

(21) Xue, S. H.; Wang, Z. D. Metal Nanorod Arrays and Their Magnetic Properties. *Materials Science and Engineering: B* **2006**, *135* (1), 74–77. https://doi.org/10.1016/J.MSEB.2006.08.037.

(22) Lisjak, D.; Mertelj, A. Anisotropic Magnetic Nanoparticles: A Review of Their Properties, Syntheses and Potential Applications. *Prog Mater Sci* **2018**, *95*, 286–328. https://doi.org/10.1016/J.PMATSCI.2018.03.003.

(23) Huber, D. L. Synthesis, Properties, and Applications of Iron Nanoparticles. *Small* **2005**, *1* (5), 482–501. https://doi.org/10.1002/SMLL.200500006.

(24) Park, S. J.; Kim, S.; Lee, S.; Khim, Z. G.; Char, K.; Hyeon, T. Synthesis and Magnetic Studies of Uniform Iron Nanorods and Nanospheres [12]. *J Am Chem Soc* **2000**, *122* (35), 8581–8582. https://doi.org/10.1021/JA001628C/SUPPL_FILE/JA001628C_S.PDF.

(25) Xu, W.; Yang, T.; Liu, S.; Du, L.; Chen, Q.; Li, X.; Dong, J.; Zhang, Z.; Lu, S.; Gong, Y.; Zhou, L.; Liu, Y.; Tan, X. Insights into the Synthesis, Types and Application of Iron Nanoparticles: The Overlooked Significance of Environmental Effects. *Environ Int* **2022**, *158*, 106980. https://doi.org/10.1016/J.ENVINT.2021.106980.

(26) Pasinszki, T.; Krebsz, M. Synthesis and Application of Zero-Valent Iron Nanoparticles in Water Treatment, Environmental Remediation, Catalysis, and Their Biological Effects. *Nanomaterials* **2020**, *10* (5), 917. https://doi.org/10.3390/nano10050917.

(27) Li, L.; Hu, J.; Shi, X.; Fan, M.; Luo, J.; Wei, X. Nanoscale Zero-Valent Metals: A Review of Synthesis, Characterization, and Applications to Environmental Remediation. *Environmental Science and Pollution Research 2016 23:18* **2016**, *23* (18), 17880–17900. https://doi.org/10.1007/S11356-016-6626-0.

(28) Zhu, Y.; Liu, X.; Hu, Y.; Wang, R.; Chen, M.; Wu, J.; Wang, Y.; Kang, S.; Sun, Y.; Zhu, M. Behavior, Remediation Effect and Toxicity of Nanomaterials in Water Environments. **2019**. https://doi.org/10.1016/j.envres.2019.04.014.

(29) Zhang, W. X. Nanoscale Iron Particles for Environmental Remediation: An Overview. *Journal of Nanoparticle Research* **2003**, *5* (3–4), 323–332. https://doi.org/10.1023/A:1025520116015/METRICS.

(30) Glavee, G. N.; Klabunde, K. J.; Sorensen, C. M.; Hadjipanayis, G. C. Chemistry of Borohydride Reduction of Iron(II) and Iron(III) Ions in Aqueous and Nonaqueous Media. Formation of Nanoscale Fe, FeB, and Fe2B Powders. *Inorg Chem* **1995**, *34* (1), 28–35. https://doi.org/10.1021/IC00105A009/ASSET/IC00105A009.FP.PNG_V03.

(31) Wang, C. B.; Zhang, W. X. Synthesizing Nanoscale Iron Particles for Rapid and Complete Dechlorination of TCE and PCBs. *Environ Sci Technol* **1997**, *31* (7), 2154–2156. https://doi.org/10.1021/ES970039C/ASSET/IMAGES/MEDIUM/ES970039CE00002.GIF.

(32) Sun, Y. P.; Li, X. qin; Cao, J.; Zhang, W. xian; Wang, H. P. Characterization of Zero-Valent Iron Nanoparticles. *Adv Colloid Interface Sci* **2006**, *120* (1–3), 47–56. https://doi.org/10.1016/J.CIS.2006.03.001.

(33) Ravikumar, K. V. G.; Dubey, S.; pulimi, M.; Chandrasekaran, N.; Mukherjee, A. Scale-up Synthesis of Zero-Valent Iron Nanoparticles and Their Applications for Synergistic Degradation of Pollutants with Sodium Borohydride. *J Mol Liq* **2016**, *224*, 589–598. https://doi.org/10.1016/J.MOLLIQ.2016.10.040.

(34) Wang, Q.; Kanel, S. R.; Park, H.; Ryu, A.; Choi, H. Controllable Synthesis, Characterization, and Magnetic Properties of Nanoscale Zerovalent Iron with Specific High Brunauer-Emmett-Teller Surface Area. *Journal of Nanoparticle Research* **2009**, *11* (3), 749–755. https://doi.org/10.1007/S11051-008-9524-7/FIGURES/7.

(35) Liou, Y. H.; Lo, S. L.; Kuan, W. H.; Lin, C. J.; Weng, S. C. Effect of Precursor Concentration on the Characteristics of Nanoscale Zerovalent Iron and Its Reactivity of Nitrate. *Water Res* **2006**, *40* (13), 2485–2492. https://doi.org/10.1016/J.WATRES.2006.04.048.

(36) Brown, H. C.; Mead, E. J.; Rao, B. C. S. A Study of Solvents for Sodium Borohydride and the Effect of Solvent and the Metal Ion on Borohydride Reductions. *J Am Chem Soc* **1955**, *77* (23), 6209–6213. https://doi.org/10.1021/JA01628A044/ASSET/JA01628A044.FP.PNG_V03.

(37) Wang, Q.; Lee, S.; Choi, H. Aging Study on the Structure of Fe0-Nanoparticles: Stabilization, Characterization, and Reactivity. *Journal of Physical Chemistry C* **2010**, *114* (5), 2027–2033. https://doi.org/10.1021/JP909137F/SUPPL_FILE/JP909137F_SI_001.PDF.

(38) Ribas, D.; Černík, M.; Benito, J. A.; Filip, J.; Marti, V. Activation Process of Air Stable Nanoscale Zero-Valent Iron Particles. *Chemical Engineering Journal* **2017**, *320*, 290–299. https://doi.org/10.1016/J.CEJ.2017.03.056.

(39) Butler, I. Removal of Dissolved Oxygen from Water: A Comparison of Four Common Techniques. *Talanta* **1994**, *41* (2), 211–215. https://doi.org/10.1016/0039-9140(94)80110-X.

(40) Kumar, N.; Auffan, M.; Gattacceca, J.; Rose, J.; Olivi, L.; Borschneck, D.; Kvapil, P.; Jublot, M.; Kaifas, D.; Malleret, L.; Doumenq, P.; Bottero, J. Y. Molecular Insights of Oxidation Process of Iron Nanoparticles: Spectroscopic, Magnetic, and Microscopic Evidence. *Environ Sci Technol* **2014**, *48* (23), 13888–13894. https://doi.org/10.1021/ES503154Q/SUPPL_FILE/ES503154Q_SI_001.PDF.

(41) Krajewski, M.; Lin, W. S.; Lin, H. M.; Brzozka, K.; Lewinska, S.; Nedelko, N.; Slawska-Waniewska, A.; Borysiuk, J.; Wasik, D. Structural and Magnetic Properties of Iron Nanowires and Iron Nanoparticles Fabricated through a Reduction Reaction. *Beilstein Journal of Nanotechnology 6:167* **2015**, *6* (1), 1652–1660. https://doi.org/10.3762/BJNANO.6.167.

(42) Martin, J. E.; Herzing, A. A.; Yan, W.; Li, X. Q.; Koel, B. E.; Kiely, C. J.; Zhang, W. X. Determination of the Oxide Layer Thickness in Core-Shell Zerovalent Iron Nanoparticles. *Langmuir* **2008**, *24* (8), 4329–4334.

https://doi.org/10.1021/LA703689K/ASSET/IMAGES/LARGE/LA703689KF00008.JPEG.

(43) Yan, W.; Herzing, A. A.; Kiely, C. J.; Zhang, W. X. Nanoscale Zero-Valent Iron (NZVI): Aspects of the Core-Shell Structure and Reactions with Inorganic Species in Water. *J Contam Hydrol* **2010**, *118* (3–4), 96–104. https://doi.org/10.1016/J.JCONHYD.2010.09.003.

(44) Wang, C.; Baer, D. R.; Amonette, J. E.; Engelhard, M. H.; Antony, J.; Qiang, Y. Morphology and Electronic Structure of the Oxide Shell on the Surface of Iron Nanoparticles. https://doi.org/10.1021/ja900353f.

(45) Lide, D. CRC Handbook of Chemistry and Physics. **2004**.

(46) Liang, B.; Xie, Y.; Fang, Z.; Tsang, E. P. Assessment of the Transport of Polyvinylpyrrolidone-Stabilised Zero-Valent Iron Nanoparticles in a Silica Sand Medium. *Journal of Nanoparticle Research* **2014**, *16* (7), 1–11. https://doi.org/10.1007/S11051-014-2485-0/TABLES/3.

(47) Yang, X. Y.; Yang, B.; Li, X. P.; Cao, Y.; Yu, R. H. Structural-Controlled Chemical Synthesis of Nanosized Amorphous Fe Particles and Their Improved Performances. *J Alloys Compd* **2015**, *651*, 551–556. https://doi.org/10.1016/J.JALLCOM.2015.08.156.

(48) Zulfiqar; Khan, R.; Rahman, M. U.; Iqbal, Z. Variation of Structural, Dielectric and Magnetic Properties of PVP Coated γ-Fe2O3 Nanoparticles. *Journal of Materials Science: Materials in Electronics* **2016**, *27* (12), 12490–12498. https://doi.org/10.1007/S10854-016-5634-7/FIGURES/11.

(49) Zulfiqar; Afzal, S.; Khan, R.; Zeb, T.; Rahman, M. ur; Burhanullah; Ali, S.; Khan, G.; Rahman, Z. ur; Hussain, A. Structural, Optical, Dielectric and Magnetic Properties of PVP Coated Magnetite (Fe3O4) Nanoparticles. *Journal of Materials Science: Materials in Electronics* **2018**, *29* (23), 20040–20050. https://doi.org/10.1007/S10854-018-0134-6/FIGURES/11.

(50) Vadivel, M.; Babu, R. R.; Ramamurthi, K.; Arivanandhan, M. Effect of PVP Concentrations on the Structural, Morphological, Dielectric and Magnetic Properties of CoFe2O4 Magnetic Nanoparticles. *Nano-Structures & Nano-Objects* **2017**, *11*, 112–123. https://doi.org/10.1016/J.NANOSO.2017.08.005.

(51) Zhang, D.; Ni, X.; Zheng, H. Surfactant-Controlled Synthesis of Fe Nanorods in Solution. *J Colloid Interface Sci* **2005**, *292* (2), 410–412. https://doi.org/10.1016/J.JCIS.2005.05.086.

(52) Lee, Y. C.; Kim, C. W.; Lee, J. Y.; Shin, H. J.; Yang, J. W. Characterization of Nanoscale Zero Valent Iron Modified by Nonionic Surfactant for Trichloroethylene Removal in the Presence of Humic Acid: A Research Note. *Desalination Water Treat* **2009**, *10* (1–3), 33–38. https://doi.org/10.5004/DWT.2009.722.

(53) Rončević, S.; Nemet, I.; Ferri, T. Z.; Matković-Čalogović, D. Characterization of NZVI Nanoparticles Functionalized by EDTA and Dipicolinic Acid: A Comparative Study of Metal Ion Removal from Aqueous Solutions. *RSC Adv* **2019**, *9* (53), 31043–31051. https://doi.org/10.1039/C9RA04831F.

(54) Mehdipour, M.; Gloag, L.; Lian, J.; Tilley, R. D.; Gooding, J. J. Zero-Valent Iron Core–Iron Oxide Shell Nanoparticles Coated with Silica and Gold with High Saturation Magnetization. *Chemical Communications* **2021**, *57* (97), 13142–13145. https://doi.org/10.1039/D1CC05165B.

(55) Krajewski, M.; Lin, W. S.; Lin, H. M.; Tokarczyk, M.; Lewinska, S.; Nedelko, N.; Slawska-Waniewska, A.; Kowalski, G.; Borysiuk, J.; Wasik, D. High Temperature Annealing of Iron Nanowires. *physica status solidi (a)* **2015**, *212* (4), 862–866. https://doi.org/10.1002/PSSA.201431843.

(56) Vasić, M. M.; Minić, D. M.; Minić, D. M.; Vasić, M. M.; Minić, D. M.; Minić, D. M. Thermal Stability and Phase Transformations of Multicomponent Iron-Based Amorphous Alloys. *Metallic Glasses* **2020**. https://doi.org/10.5772/INTECHOPEN.88260.

(57) Falqui, A.; Loche, D.; Casu, A. In Situ TEM Crystallization of Amorphous Iron Particles. https://doi.org/10.3390/cryst10010041.

(58) *Max Baermann GmbH*. https://www.max-baermann.de/en/ (accessed 2025-05-31).

(59) Skomski, R.; Zeng, H.; Zheng, M.; Sellmyer, D. Magnetic Localization in Transition-Metal Nanowires. *Phys Rev B* **2000**, *62* (6), 3900. https://doi.org/10.1103/PhysRevB.62.3900.

(60) Peng, Y.; Zhang, H. L.; Pan, S. L.; Li, H. L. Magnetic Properties and Magnetization Reversal of α-Fe Nanowires Deposited in Alumina Film. *J Appl Phys* **2000**, *87* (10), 7405–7408. https://doi.org/10.1063/1.373001.

# **Chapter 7 |** The industrial experience in Kolektor: material development for bonded magnets

Part of the activity of this thesis project was conducted in collaboration with Kolektor, a prominent industrial partner specialized in hard magnetic materials based on ferrites and NdFeB [1]. Among the several technologies they are involved in, the company focuses primarily on the development and production of bonded magnets, mostly employed for the realization of automotive components. The activity here described was carried out in Kolektor KFH production plant, located in Logatec, Slovenia and in Idrija, Slovenia, where the company's headquarters are located.

In Kolektor KFH facility, the fabrication of test samples and their preliminary evaluation were conducted, a key stage before the large-scale production of PM materials, which takes place in the same plant. Given the considerable amounts of powder necessary for the realization of test samples in the industrial machinery, it was not possible to use the SrM nanoparticles synthesized within this thesis work. Indeed, even if at the laboratory scale the proposed synthesis for SrM was already optimized to obtain 5 g of product, such amount was not large enough for the industrial fabrication of the ca. 20 test samples required for only one, full-comprehensive evaluation. Therefore, my efforts in this facility were mainly dedicated to tuning optimized parameters and define the requirements for employing in the next future the nanocomposites produced in this work for production on an industrial scale of bonded magnets.

At the same time, efforts were devoted to explore the production of bonded magnet exploiting recycled powders of NdFeB PMs, recovered by hydrogen processing (HPMS) [2], and hexaferrite PMs from milling manufacturing waste[3].

# 7.1 Industrial procedures for testing and producing bonded PMs

Currently, bonded magnets constitute a significant and growing fraction of 20% of PM market share [4]. In bonded magnets, or plastomagnets, the magnetic powders are embedded within a non-magnetic polymer or binder matrix [5,6]. This approach offers significant advantages in designing flexible and complex geometries, despite the lower volume of magnetic material compared to fully dense sintered magnets due to the presence of the binder [7]. Through the optimization of the processing parameters, features such as elasticity, physical strength, resistance to fracture and impact, dimensional tolerance, or reduced density and orientation can be tuned to have the desired performances [8–10]. Bonding magnetic powders in polymers allows for low weight, resistance to corrosion, ease of machining and forming, and capability for high production rates [11]. These advantages make them useful materials for applications requiring miniaturized parts with precise and complex shapes and structure [7,12].

In Kolektor facility, the procedure employed for the fabrication of bonded magnets, relies on two-step, extrusion and injection moulding. The extrusion is the stage where the various constituents are combined, while the injection moulding gives the compound the final shape. A schematic representation of the whole procedure is reported in **Figure 7-1**. The injection moulding process allows to have fast production, good dimensional control and surface finish, with little post-production scraps [13,14]. The industrial philosophy is to

repurpose even the manufacturing side scraps, minimizing waste and ensuring a circular economy of the production line.

Three different raw materials are the fundamental constituents of the final plastomagnets. The main part is the magnetic powder, either NdFeB or ferrites, which accounts for 80-90% by weight, determining the fundamental magnetic properties of the final product. The polymer (binder), which can be polyphenylene sulfide (PPS) or polyamide (PA6 or PA12), along with some additives, completes the composition. The relative combination of the different starting materials relies on the desired magnetic or mechanical properties that the material must have [15]. In particular, the polymer determines the mechanical and physical properties, and thus the applications, of the final magnet [16]. For example, PPS mixed with some glass fibers ensures the mechanical strength but harms the material's flowability. Polyamide guarantees better flowability in the moulding process but presents some water permeability issues (PA6). The role of additives, mainly lubricants, allows for improved mechanical and rheological properties when the powders are subsequently combined [17].

The extrusion process is performed in a compounder (Brabender OHG Duisburg), constituted by two co-rotating screw shafts in an elongated heating assembly. This assembly has seven different heating zones, each with a selectable temperature, tailored to the melting point of the polymer (around 300 °C for PPS and 220-230 °C for PA). The appropriate amounts of polymer, additives, and magnetic powders are preventively mixed in a biaxial mixer and then fed to the compounder, which melts the polymer and combines all the components. The resultant product is cooled in air, pelletized, and homogeneously collected.

To ensure the material has proper flowability features, the melting flow index (MFI) is measured with an appropriate instrument (Dynisco LMI 5000). The

material is then transferred into the machine (Demag Ergotech) for injection moulding. In this stage, high temperatures and pressure are applied to form the test samples. The temperatures employed are slightly higher than extrusion (around 350 °C for PPS and 280 °C for PA), to guarantee the material's flowability, but not excessively to avoid burning the polymer while keeping a good viscosity. The charged material is thus melted again and injected into the press, with pressure ranging from 2000 to 2700 bar. Once the pressure is released, the final test sample is obtained. The test sample has the shape of a bar with four cylinders attached. This shape consents to perform, once the components are separated, the necessary mechanical stress tests on the tensile bar and magnetic characterization on the cylinders. During the pressing stage in the injection moulding, a magnetic field is applied in some of the molding cavities for the cylinders, to make isotropic and anisotropic samples of PMs.

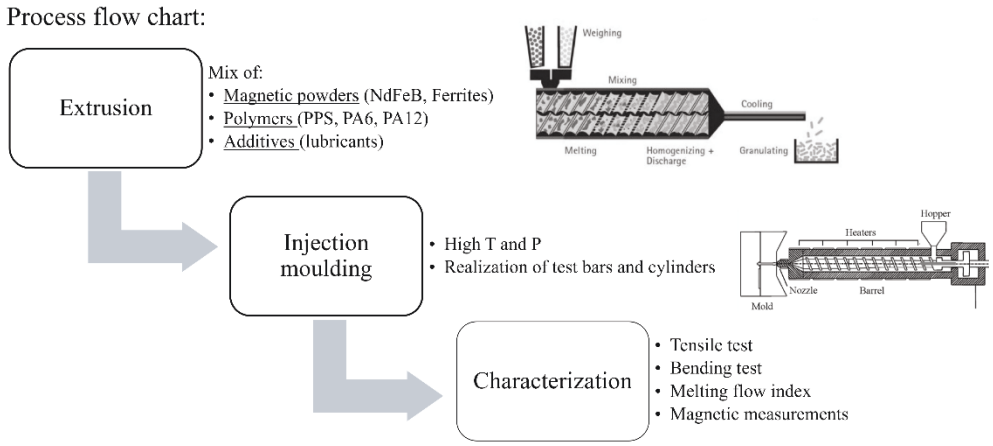


***Figure 7-1*** *Schematic representation of the process flow chart to produce bonded magnets in Kolektor.*

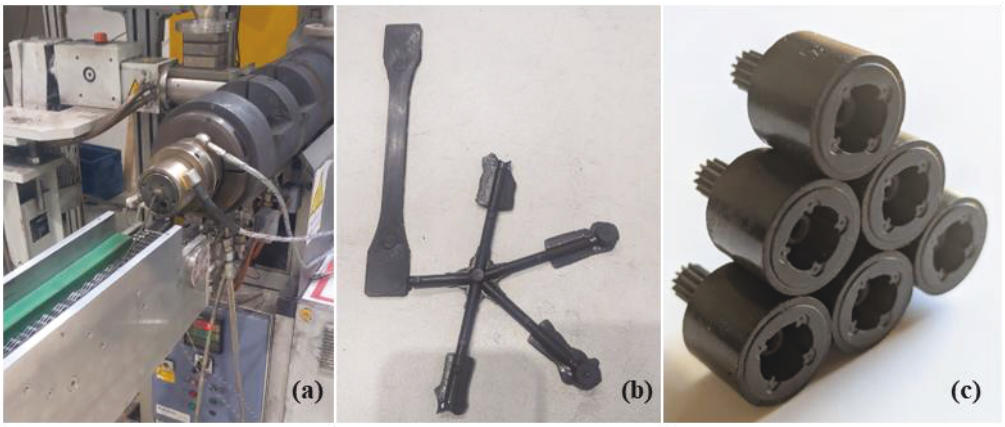


***Figure 7-2*** *Some pictures taken from Kolektor KFH production plant: (a) the compounder employed for extrusion;(b) representative image of test samples produced; (c) example of injected moulded final device, e.g. rotors for window lifters.*

The NdFeB or hexaferrite powders of various grades, normally employed in the production of PMs in Kolektor, are usually purchased in the worldwide PM market. After the manufacturing process, the test samples are fully characterized. The tensile bars are subject to stress tests with two different instruments, one applying bending force (KARG Industrietechnik) and one stretching force (Zwick-Roell), with an average batch of 10 bars for each measure. The mechanical properties measured regarding the tensile strength comprise the Young's modulus ($E_t$), the ultimate tensile strength ($\sigma_m$), and the relative deformation ($\varepsilon_m$) on the sample length. The flexural tests, instead, measure the maximum deflection at the peak of applied force ($sF_{max}$), and the magnitude of the force when the bar breaks ($F_y$). The density of five cylinders, for both isotropic and anisotropic magnets, is measured on an analytical balance (buoyancy method). Then, the magnetic properties are evaluated for sample magnets with the lowest and highest density through a permeameter (Magnet-Physik), which calculates the hysteresis loops and extrapolates the

main magnetic properties. The properties of interest measured are the remanent induction ($B_{R)}$), the intrinsic ($H_{Cj}$) and normal ($H_{Cb}$) coercivities, and the maximum energy product $BH_{(max)}$. Typical values of commercial NdFeB and hexaferrite magnets produced in Kolektor are reported in **Table 7-1**.

***Table 7-1*** *Magnetic properties and density of the most valuable bonded PMs based on NdFeB and ferrite powders in PPS or PA12, produced in Kolektor. From [1].*

| **Material** | **$B_R$ (mT)** | **$BH_{(max)}$ (kJ/m$^3$)** | **$H_{Cb}$ (kA/m)** | **$H_{Cj}$ (kA/m)** | **ρ (g/cm$^3$)** |
|---|---|---|---|---|---|
| **NdFeB in PPS Neocomp I 51/65 PS** | 576 | 53.1 | 363 | 650 | 5.14 |
| **NdFeB in PA12 Neocomp 49/67 PA** | 575 | 54.0 | 375 | 695 | 5.15 |
| **Ferrite in PPS Ferrocomp 11/18 PS** | 253 | 12.2 | 178 | 265 | 3.57 |
| **Ferrite in PA12 Ferrocomp 15/21 PA** | 283 | 15.4 | 199 | 254 | 3.70 |

As a future prospect, it would be definitely promising to implement the SrM nanoparticles, obtained from our synthesis, in this production line. The realization of bonded magnets could further expand the possibility of tuning the final features of the material by mixing a wide array of polymer and additives employed at industrial level.

# 7.2 The evaluation of NdFeB and Ferrite PMs from recycled content

Recycling has become an integral part of modern sustainability efforts, with increasing global initiatives for a more sustainable future. However, the full recycling of REEs remains a significant challenge. Most REEs recycling

feedstock originates from manufacturing losses, while end-of-life (EOL) PMs are constrained by low collection rates and challenging economics [18]. These motivations explain why recycling NdFeB is considered a “key enabling technology” to insert REEs in circular economy. On the other hand, the development of affordable routes for recycling of EOL PMs, particularly from e-waste such as computer hard drives, electric motors, and wind turbines, represents another active research area. Recycling, indeed, offers the potential to create a secure, secondary stream of REEs, reducing reliance on mining and its associated environmental impact [19]. However, the recycling of NdFeB magnets faces significant technical and economic challenges. These include the difficulty of collecting and dismantling complex products, the presence of protective coatings, and the need for sophisticated, high-cost processes (e.g., hydrometallurgy or pyrometallurgy) to separate and recover the rare earth elements in a pure, reusable form [20]. Despite these barriers, ongoing research is focused on developing more efficient and commercially viable recycling routes to insert REEs in circular economy [21].

### 7.2.1 Recycling routes for NdFeB magnets

The different techniques available to recycle NdFeB magnets can be divided into reusing, reprocessing, and remelting. The most economically viable route is to repurpose EOL magnets without changing the chemical structure. However, this approach is limited to not- oxidized, large and accessible PMs (wind turbines, large motors and generators in electric vehicles), and the already defined shape and properties render them useful only in the same application [19,21]. Remelting the PMs is a direct route with no waste generation, typically employed by manufacturers to put back the magnetic material in the production line. In the case of waste electronic goods, which contain a large fraction of permanent magnets (PMs), the low collection rate, due to the

difficulty of removal or losses during shredding, makes the melting process inefficient for recovering the high content of REE-oxides and other materials [22,23]. Hydrometallurgical methods involve using strong mineral acids to dissolve the magnet alloys and selectively precipitate REEs in the form of sulfates, oxalates or fluorides [24–26]. This procedure requires huge amounts of chemicals and wastewater, and even some other elements and contaminants are inevitably dissolved. Pyrometallurgy, employing high-temperature processes to recover REEs and alloys, is energy-intensive and necessitates further purification [25,27,28]. To address these challenges and eliminate all the processing steps of conventional recycling, an environmentally friendly process based on hydrogen decrepitation is getting interest. It consists in a differential volume expansion by $H_2$ absorption in the NdFeB phase resulting in friable, coarse and demagnetized powder [19,29,30].

The European project INSPIRES (Innovative Solutions for Permanent Magnet Recycling and Sustainability) [31], which includes part of the activity conducted in this PhD thesis, addresses the critical need for the sustainable management of PMs, particularly those found in EOL home appliances. The project focuses on the systematic dismantling of home appliances to enable the extraction of NdFeB magnets and on their recycling. The recovered materials are then re-utilized in the subsequent magnet production phase, and the new PMs synthesized from recycled content are then implemented in new machines (electric motors or home appliances) and tested, ensuring they meet the required specifications for various applications [21]. To pursue this aim, the pathway for obtaining recycled powders suitable for PM application comprises several advanced technologies. Among these, Hydrogen-Processing of Magnetic Scrap (HPMS), a patented process developed by researchers at the University of Birmingham [30], was adopted to remove the protective anti-corrosion coatings generally employed in the fabrication of sintered NdFeB

magnets, and efficiently recover their Nd-rich phases [2,19]. Spark plasma sintering (SPS), previously explained, was utilized to sinter the recovered and jet-milled powders into dense magnets [32,33].

In parallel with RE-based PMs, the project also focused on the recycling of hexaferrites. As explained in the introduction, indeed, some of the inherent characteristics of this material are advantageous even for recycling, e.g., the corrosion resistance. The recycling process for hexaferrites is relatively straightforward, involving milling, annealing, and re-fabrication, and does not require the complex separation steps needed for RE PMs. Few studies are currently on this topic, [34] probably due to the convenience of buying new components instead of putting effort into recycling cheap material. Nevertheless, the industrial implications are quite relevant, and economically and environmentally profitable. The opportunity to develop a circular line of production and recycling within the same industrial plant, indeed, is a promising perspective. This is particularly true when the processing steps are limited, and the manufacturing allows obtaining a recycled final product that is comparable to the starting material. The bonded magnets investigated by Berja *et al* [3], containing 50 wt.% recycled material and fabricated in Kolektor, exhibited mechanical and magnetic properties very close to those of commercially available injection moulded magnets, making the process very promising. As a further example, the magnetic properties of two test samples, one isotropic and one anisotropic, made entirely by purchased recycled ferrites, are shown in **Table 7-2**. The recycled ferrite content in the compounder was 86%, with the addition of 14% of PPS. Even in this case, the resultant magnetic properties, compared with a commercial grade ferrite from Kolektor, and considering the powders came from a recycled source, were noticeably promising.

***Table 7-2*** *Magnetic properties of isotropic and anisotropic test samples of recycled ferrites made by injection moulding, compared with the commercial Ferrocomp I 9/18 PS-3 from Kolektor., The recycled ferrite content in the compounder was 86%, with the addition of 14% of PPS.*

| **Material** | **$B_R$ (mT)** | **$BH_{(max)}$ ($kJ/m^3$)** | **$H_{Cb}$ (kA/m)** | **$H_{Cj}$ (kA/m)** |
|---|---|---|---|---|
| **Ferrocomp I 9/18 PS-3, anisotropic** | 235 | 10.7 | 177.6 | 264.5 |
| **Ferrite_14%PPS Recycled, isotropic** | 151 | 4.1 | 107.4 | 352 |
| **Ferrite_14%PPS Recycled, anisotropic** | 227 | 9.9 | 167 | 385 |

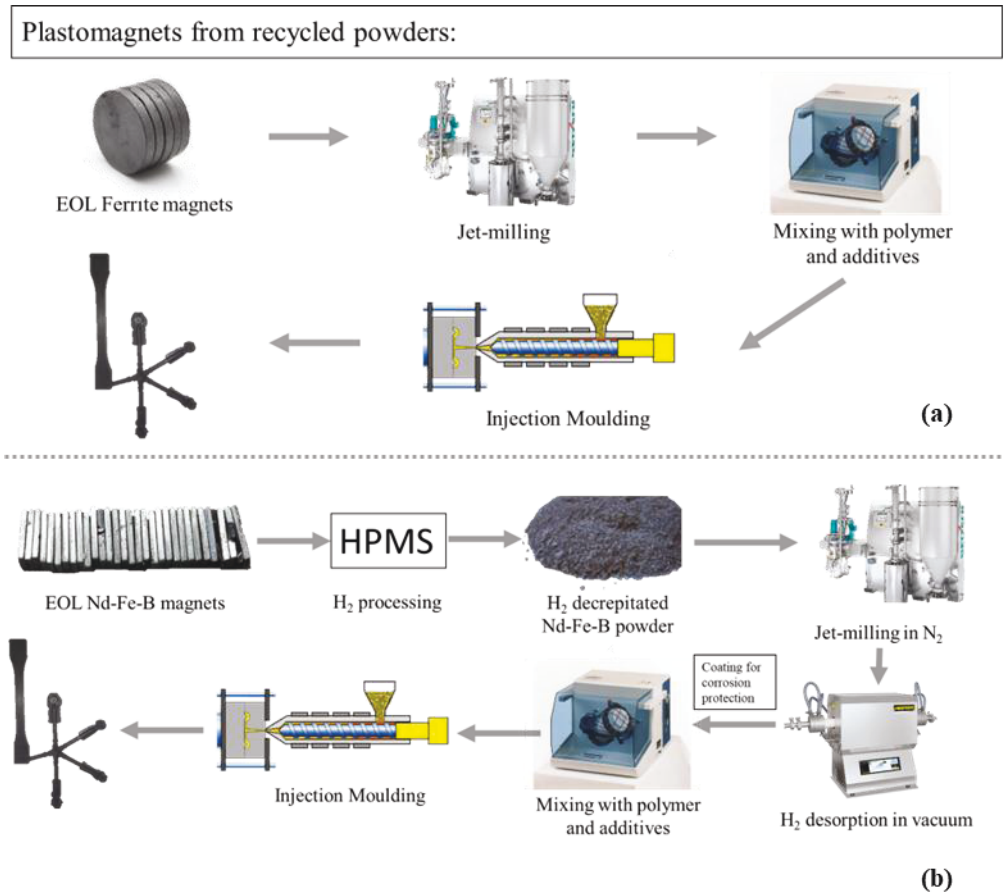


***Figure 7-3*** *Comparison between the recycling process of EOL ferrite magnets (a) and EOL NdFeB magnets (b) for the development of new bonded magnets.*

# 7.3 Conclusions

This chapter detailed the activity carried out at Kolektor, a leading manufacturer of bonded magnets, providing insights into the large-scale production processes for hard magnetic materials. The initial objective of testing lab-synthesized powders was adapted due to the material volume requirements of industrial machinery. Consequently, the focus shifted to the

engagement with Kolektor's established manufacturing workflow for verifying the viability of introducing in the future the nanocomposites investigated in this thesis work or incorporating recycled materials, in the context of the European project INSPIRES.

The work involved the key stages of bonded magnet production: the compounding of magnetic powders (ferrites or NdFeB) with polymer binders (PPS or PA12) via extrusion, and the subsequent high-pressure injection moulding to form both test samples and final components.

A remarkable outcome of this activity was the successful demonstration of a circular economy approach for ferrite PMs. Test samples were fabricated using recycled ferrite powders sourced from manufacturing waste. The resulting anisotropic bonded magnets, composed of 86% recycled ferrite and 14% PPS binder, exhibited magnetic properties that were significantly comparable to Kolektor's commercial-grade magnets made from virgin materials. In conclusion, this industrial study validates that recycled ferrite powders can be effectively integrated into the existing production line for bonded magnets, without a significant compromise in magnetic performance. This finding is a promising step towards establishing a more sustainable and resource-efficient manufacturing cycle for PMs. It underscores the potential for recycled materials to meet the high-performance demands of industrial applications, thereby contributing to the economic and environmental goals of a circular economy.

# References

(1) *Kolektor* . https://www.kolektor.com/en (accessed 2025-06-01).

(2) Grau, L.; Fleissner, P.; Kobe, S.; Burkhardt, C. Processability and Separability of Commercial Anti-Corrosion Coatings Produced by In Situ Hydrogen-

Processing of Magnetic Scrap (HPMS) Recycling of NdFeB. *Materials 2024, Vol. 17, Page 2487* **2024**, *17* (11), 2487. https://doi.org/10.3390/MA17112487.

(3) Berja, A.; Casaleiz, D.; Granados-Miralles, C.; Kosmač, K.; Saje, B.; Frangež, T.; Dvoršak, S.; Samardžija, Z.; Podmiljšak, B.; Fernández, J. F.; Quesada, A. A Simple and Industrially Scalable Process for Recycling Hexaferrite Ceramic Magnets. *Open Ceramics* **2025**, *21*, 100724. https://doi.org/10.1016/j.oceram.2024.100724.

(4) Coey, J. M. D. Perspective and Prospects for Rare Earth Permanent Magnets. *Engineering* **2020**, *6* (2), 119–131. https://doi.org/10.1016/J.ENG.2018.11.034.

(5) Stäblein, H. Hard Ferrites and Plastoferrites. In *Handbook of Ferromagnetic Materials*; Elsevier, 1982; Vol. 3, pp 441–602. https://doi.org/10.1016/S1574-9304(05)80093-8.

(6) Cui, J.; Ormerod, J.; Parker, D. S.; Ott, R.; Palasyuk, A.; McCall, S.; Paranthaman, M. P.; Kesler, M. S.; McGuire, M. A.; Nlebedim, C.; Pan, C.; Lograsso, T. Manufacturing Processes for Permanent Magnets: Part II—Bonding and Emerging Methods. *JOM* **2022**, *74* (6), 2492–2506. https://doi.org/10.1007/S11837-022-05188-1/FIGURES/1.

(7) Croat, J. J. Current Status and Future Outlook for Bonded Neodymium Permanent Magnets (Invited). *J Appl Phys* **1997**, *81* (8), 4804–4809. https://doi.org/10.1063/1.365469.

(8) Coey, J. M. D. Hard Magnetic Materials: A Perspective. *IEEE Trans Magn* **2011**, *47* (12), 4671–4681. https://doi.org/10.1109/TMAG.2011.2166975.

(9) Ormerod, J.; Constantinides, S. Bonded Permanent Magnets: Current Status and Future Opportunities (Invited). *J Appl Phys* **1997**, *81* (8), 4816–4820. https://doi.org/10.1063/1.365471.

(10) Kurth, K. H.; Drummer, D. Improvement of the Magnetic Properties of Injection Molded Polymer Bonded Magnets. In *2013 3rd International Electric Drives Production Conference (EDPC)*; IEEE, 2013; pp 1–5. https://doi.org/10.1109/EDPC.2013.6689718.

(11) Otaigbe, J. U.; Kim, H. S.; Xiao, J. Effect of Coupling Agent and Filler Particle Size on Melt Rheology of Polymer-Bonded Nd-Fe-B Magnets. *Polym Compos* **1999**, *20* (5), 697–704. https://doi.org/10.1002/PC.10393.

(12) Grönefeld, M. Review on Bonded Magnets. *Bonded Magnets* **2003**, 1–12. https://doi.org/10.1007/978-94-007-1090-0_1.

(13) Basir, A.; Sulong, A. B.; Jamadon, N. H.; Muhamad, N.; Emeka, U. B. Process Parameters Used in Macro/Micro Powder Injection Molding: An Overview. *Metals and Materials International* **2021**, *27* (7), 2023–2045. https://doi.org/10.1007/S12540-020-00767-W/FIGURES/9.

(14) Piotter, V.; Bauer, W.; Knitter, R.; Mueller, M.; Mueller, T.; Plewa, K. Powder Injection Moulding of Metallic and Ceramic Micro Parts. *Microsystem Technologies* **2011**, *17* (2), 251–263. https://doi.org/10.1007/S00542-011-1274-2/FIGURES/18.

(15) Rösel, U.; Drummer, D. Understanding the Effect of Material Parameters on the Processability of Injection-Molded Thermoset-Based Bonded Magnets. *Magnetism 2022, Vol. 2, Pages 211-228* **2022**, *2* (3), 211–228. https://doi.org/10.3390/MAGNETISM2030016.

(16) CHENG, X. hua; YU, X. jun. Effect of Binder and Additives on Properties of NdFeB Bonded Magnets by Injection Moulding. *Journal of Iron and Steel Research, International* **2006**, *13* (SUPPL. 1), 282–285. https://doi.org/10.1016/S1006-706X(08)60195-8.

(17) Hung, Y. C.; Ko, W. S.; Tung, M. J.; Chen, L. K.; Chang, W. C. Effects of Additives on the Orientation and Strength of Plastic Ferrite Magnet. *IEEE Trans Magn* **1989**, *25* (5), 3287–3289. https://doi.org/10.1109/20.42280.

(18) *Executive Summary – Recycling of Critical Minerals – Analysis - IEA*. https://www.iea.org/reports/recycling-of-critical-minerals/executive-summary (accessed 2025-06-19).

(19) Binnemans, K.; Jones, P. T.; Blanpain, B.; Van Gerven, T.; Yang, Y.; Walton, A.; Buchert, M. Recycling of Rare Earths: A Critical Review. *J Clean Prod* **2013**, *51*, 1–22. https://doi.org/10.1016/j.jclepro.2012.12.037.

(20) Liang, B.; Gu, J.; Zeng, X.; Yuan, W.; Rao, M.; Xiao, B.; Hu, H. A Review of the Occurrence and Recovery of Rare Earth Elements from Electronic Waste. *Molecules 2024, Vol. 29, Page 4624* **2024**, *29* (19), 4624. https://doi.org/10.3390/MOLECULES29194624.

(21) Podmiljšak, B.; Saje, B.; Jenuš, P.; Tomše, T.; Kobe, S.; Žužek, K.; Šturm, S. The Future of Permanent-Magnet-Based Electric Motors: How Will Rare Earths Affect Electrification? *Materials* **2024**, *17* (4), 848. https://doi.org/10.3390/ma17040848.

(22) Yang, Y.; Walton, A.; Sheridan, R.; Güth, K.; Gauß, R.; Gutfleisch, O.; Buchert, M.; Steenari, B. M.; Van Gerven, T.; Jones, P. T.; Binnemans, K. REE Recovery from End-of-Life NdFeB Permanent Magnet Scrap: A Critical Review. *Journal of Sustainable Metallurgy* **2017**, *3* (1), 122–149. https://doi.org/10.1007/S40831-016-0090-4/FIGURES/2.

(23) Yang, Y.; Walton, A.; Sheridan, R.; Güth, K.; Gauß, R.; Gutfleisch, O.; Buchert, M.; Steenari, B. M.; Van Gerven, T.; Jones, P. T.; Binnemans, K. REE Recovery from End-of-Life NdFeB Permanent Magnet Scrap: A Critical Review. *Journal of Sustainable Metallurgy* **2017**, *3* (1), 122–149. https://doi.org/10.1007/S40831-016-0090-4/FIGURES/2.

(24) Yoon, H. S.; Kim, C. J.; Chung, K. W.; Kim, S. D.; Lee, J. Y.; Kumar, J. R. Solvent Extraction, Separation and Recovery of Dysprosium (Dy) and Neodymium (Nd) from Aqueous Solutions: Waste Recycling Strategies for

Permanent Magnet Processing. *Hydrometallurgy* **2016**, *165*, 27–43. https://doi.org/10.1016/J.HYDROMET.2016.01.028.

(25) Kumari, A.; Sahu, S. K. A Comprehensive Review on Recycling of Critical Raw Materials from Spent Neodymium Iron Boron (NdFeB) Magnet. *Sep Purif Technol* **2023**, *317*, 123527. https://doi.org/10.1016/J.SEPPUR.2023.123527.

(26) Önal, M. A. R.; Borra, C. R.; Guo, M.; Blanpain, B.; Van Gerven, T. Hydrometallurgical Recycling of NdFeB Magnets: Complete Leaching, Iron Removal and Electrolysis. *Journal of Rare Earths* **2017**, *35* (6), 574–584. https://doi.org/10.1016/S1002-0721(17)60950-5.

(27) Kaya, M. An Overview of NdFeB Magnets Recycling Technologies. *Curr Opin Green Sustain Chem* **2024**, *46*, 100884. https://doi.org/10.1016/J.COGSC.2024.100884.

(28) Takeda, O.; Okabe, T. H. Current Status on Resource and Recycling Technology for Rare Earths. *Metallurgical and Materials Transactions E 2014 1:2* **2014**, *1* (2), 160–173. https://doi.org/10.1007/S40553-014-0016-7.

(29) Burkhardt, C.; van Nielen, S.; Awais, M.; Bartolozzi, F.; Blomgren, J.; Ortiz, P.; Xicotencatl, M. B.; Degri, M.; Nayebossadri, S.; Walton, A. An Overview of Hydrogen Assisted (Direct) Recycling of Rare Earth Permanent Magnets. *J Magn Magn Mater* **2023**, *588*, 171475. https://doi.org/10.1016/J.JMMM.2023.171475.

(30) Walton, A.; Williams, A. Rare Earth Recovery. *Materials World* **2011**, *19* (8), 24–26.

(31) *Home Page - Inspires*. https://inspires-magnet.eu/ (accessed 2025-06-02).

(32) Tomše, T.; Samardžija, Z.; Scherf, L.; Kessler, R.; Kobe, S.; Žužek Rožman, K.; Šturm, S. A Spark-Plasma-Sintering Approach to the Manufacture of

Anisotropic Nd-Fe-B Permanent Magnets. *J Magn Magn Mater* **2020**, *502*, 166504. https://doi.org/10.1016/J.JMMM.2020.166504.

(33) Tomše, T.; Tremelling, D.; Kessler, R.; Christen, T.; Scherf, L.; Simon, R. A.; Greuter, F.; Herrmann, L.; Dubois, J. M.; Kobe, S.; Jaćimović, J. Multicomponent Permanent Magnets for Enhanced Electrical Device Efficiency. *J Magn Magn Mater* **2020**, *494*, 165750. https://doi.org/10.1016/J.JMMM.2019.165750.

(34) Bollero, A.; Rial, J.; Villanueva, M.; Golasinski, K. M.; Seoane, A.; Almunia, J.; Altimira, R. Recycling of Strontium Ferrite Waste in a Permanent Magnet Manufacturing Plant. *ACS Sustain Chem Eng* **2017**, *5* (4), 3243–3249. https://doi.org/10.1021/ACSSUSCHEMENG.6B03053/ASSET/IMAGES/LARGE/SC-2016-03053U_0008.JPEG.

# **Chapter 8 |** Conclusions and perspectives

The experimental work, here presented, was devoted to the synthesis, characterization, and processing of SrM nanomaterials for REE-free PM applications. The overall research encompassed the optimization of sustainable and viable synthesis routes for industrial employment, the chemical modification via doping, advanced compaction techniques, and the exploration of hard-soft nanocomposite structures. This work culminated in a real industry experience, where laboratory-scale research was elevated to large-scale manufacturing of PMs.

First, the research focused on establishing a cost-effective, scalable, and reproducible methodology for producing single-phase SrM nanoparticles with suitable properties. The investigation began with the LTSSR synthesis, identifying the best conditions across the evaluated parameters in a molar ratio of $Fe^{3+}/Sr^{2+}$ of 10, a calcination temperature of 775 °C, and a narrowly basic pH in the washing stage. This allowed to obtain SrM nanoparticles under 100 nm, while minimizing the impurity phases. However, the method presented low reproducibility for precise stoichiometry control, particularly affecting the coercivity value. To overcome the drainage of water-soluble strontium hydroxide, the MSSR method was developed. The procedural modification proved to be highly effective, ensuring a correct stoichiometry by retaining all precursors during the heat treatment. The MSSR successfully yielded phase-pure SrM nanoparticles with enhanced magnetic properties, including the highest $H_C$ and $M_S$ achieved in the solid-state series. In this regard, MSSR stands out as a convenient and promising synthesis route, therefore future work should focus on a rigorous reproducibility assessment and a more detailed investigation on further optimizations, such as $Fe^{3+}/Sr^{2+}$ molar ratios and

calcination temperature or duration, to confirm its potentiality in refining SrM nanoparticle size and magnetic properties.

Proceeding with the research on nanosized particles with the least degree of agglomeration, the MSG synthesis was explored. The clear advantages of this method were the consistent reproducibility of single-phase, polycrystalline SrM particles with noteworthy magnetic properties at relatively low temperatures of 790 °C. The study confirmed that the calcination temperature significantly influenced the particle size, which was instead less affected by variations in the $Fe^{3+}/Sr^{2+}$ molar ratio, the addition of extra NaCl matrix, or the pre-calcination time at 450 °C. Nevertheless, this latter stage is recommended to limit the development of additional phases. The reliability of the procedure renders the MSG synthesis an excellent candidate for further optimization, including a finer range of calcination temperatures or intermediate metals' molar ratios, to achieve greater handling over the particle morphology, size distribution, and magnetic features. The attested consistency of MSG provided a solid foundation for the subsequent investigation on doping studies, where precise control over the magnetic properties of SrM was essential.

Therefore, work progressed to modifying the intrinsic SrM magnetoplumbite structure. The inclusion of Al and Mn as dopants successfully altered the structural, morphological, and magnetic features of the SrM magnetic array. Despite the effective content detected in the samples was inferior to the nominal content expected, doping with these cations exerted remarkable effects. Al-doping significantly enhanced the coercivity, reaching a value of 0.7 T, although with an expected decrease in magnetization due to preferential insertion in 12k and 2a spin-up positions. The nanoparticles remained largely polycrystalline with a minor decrease in particle size. Conversely, Mn doping had a strong impact on this regard. Mn was notably effective in reducing the

particle size to the range of 40 nm and promoted the formation of predominantly single-crystal nanoparticles. Its inclusion in the crystal structure under MSG synthesis conditions was more efficient than that of Al, as denoted by the ICP analysis. Furthermore, it provided a moderate increase in coercivity, while $M_S$ decreased for the same preferential crystallographic spin-up sites of Al. Future investigations could explore other non-REE dopants and co-doping strategies to include the benefits of each inserted element. Moreover, the MSG procedure, especially the calcination temperature or duration, could be modified to enhance the dopant diffusion into the lattice. The successful incorporation of these dopants demonstrates the significant potential for tailoring magnetic anisotropy and further material engineering.

The comparison in **Table 8-1** highlights that the isotropic SrM nanoparticles synthesized in this work ($(BH)_{max}$: 5–8 kJ/m$^3$, $B_R$: 0.18–0.21 T) already match the performance range of isotropic hexaferrites reported in the literature, confirming the robustness of the adopted synthesis routes and the quality of phase-pure nanosized compounds. Within this framework, MSSR samples stand out with the highest energy product, while Mn/Al doping successfully enhances coercivity, demonstrating the tunability of these materials. Although commercial anisotropic ferrites (24–36 kJ/m$^3$) still outperform isotropic powders, the present results underline the potential of phase-pure SrM nanoparticles in further improvements through densification and texturing.

***Table 8-1*** *Key magnetic parameters of isotropic SrM powders synthesized in this work, grouped by synthesis route, and compared with representative values from literature and commercial benchmark magnets: remanent induction ($B_R$), normal coercivity ($H_{Cb}$), intrinsic coercivity ($H_{Ci}$) and measured maximum energy product ($(BH)_{max}$).*

| **Material / Source** | **$B_R$ (T)** | **$Hc_b$ (kA/m)** | **$Hc_i$ (kA/m)** | **$(BH)_{max}$ (kJ/m$^3$)** |
|---|---|---|---|---|
| **SrM_LTSSR** | 0.21-0.22 | 138-144 | 422-470 | 7.1-7.9 |
| **SrM_MSSR** | 0.21-0.22 | 150-140 | 478-489 | 7.3-8.5 |
| **SrM_MSG** | 0.18-0.19 | 121-123 | 447-485 | 5.7-5.9 |
| **Doped (Al, Mn) SrM_MSG** | 0.17-0.18 | 114-122 | 494-556 | 4.8-5.5 |
| **Isotropic hexaferrites (literature)** | 0.18-0.22 | 100-150 | 450-600 | 5-10 |
| **Anisotropic hexaferrites (sintered)** | 0.35-0.40 | 250-350 | 250-350 | 24-36 |
| **NdFeB (sintered)** | 1.20-1.40 | 800-1200 | 1000-2000 | 200-400 |
| **SmCo (sintered)** | 0.90-1.10 | 600-1000 | 1500-2000 | 150-250 |

To transform the synthesized powders into bulk magnets, improved compaction and densification techniques were involved as alternatives to traditional high-temperature sintering. The multi-anvil and piston cylinder presses were capable of attaining high densities at considerably low temperatures, maintaining the nanostructure and the main SrM phase intact. The multi-anvil system achieved an impressive relative density of nearly 92% at merely 80 °C, employing the powder synthesized by LTSSR. The particular

platelet shape of the nanoparticles induced a certain degree of alignment even under isotropic pressure, which was further confirmed by application of uniaxial pressure using the piston cylinder. In this latter case, the nanoparticles produced by MSG synthesis demonstrated a more pronounced tendency to be aligned, owing to mostly individual crystallites and less consolidated aggregates. For the same reason, the Al-doped and Mn-doped nanoparticles produced by the same procedure showed an identical behaviour, even if the degree of alignment can be further improved. A significant grain alignment can be obtained by SPS (average Mr/Ms of 0.7), reaching almost full densification for undoped SrM_MSG. Achieving discrete, non-agglomerated crystallites is crucial for enhancing remanence through effective platelet piling. However, the operative conditions still need to be optimised to prevent misalignment of the magnetisation c-axis and, therefore, the distribution of reversal fields.

To explore whether the high $H_C$ of hard SrM could be combined with the high $M_S$ of a soft magnetic phase s as $Fe^0$ NWs, an investigation into exchange-coupled nanocomposites was undertaken. A scalable, aqueous synthesis for $Fe^0$ NWs was developed, reaching remarkable $M_S$ values close to bulk iron. However, the extreme reactivity and propensity for oxidation of the $Fe^0$ NWs presented a significant challenge to entirely preserve the pristine features. In this regard, future research should comprise more robust strategies to maintain the most a notable magnetization. Furthermore, attempts to create an effective exchange-coupled nanocomposite combining the NWs with synthesized nanometric SrM were unsuccessful, resulting in a magnetically decoupled system. Nonetheless, a noteworthy result emerged from the study employing the commercial micro-particulate SrM. While still decoupled, the composite with a SrM/$Fe^0$ ratio of 90/10 showed promising maintenance of remanence in the aligned state, suggesting the presence of beneficial magnetostatic dipolar interactions. Moreover, a 95/5 ratio had a minimal impact on the magnetic

properties of the original SrM. This evidence warrants a deeper investigation, specifically by fine-tuning the in between ratios to evaluate if an even more prominent interaction could be denoted. Other promising options rely on the employment of SrM nanoparticles successively synthesized in a NaCl matrix. They presented defined capabilities to be aligned, similar to the micrometric SrM and conversely to the consolidated aggregates formed by LTSSR. As observed for Mn-doped SrM, a high degree of alignment with the application of a magnetic field was noticeable, and the increased surface area related to the small particle size can be further advantageous in a mutual interaction with $Fe^0$ NWs. Additionally, the fabrication of a bonded magnet could integrate the understanding of how these interactions manifest in a practical magnet while providing a protective matrix for $Fe^0$.

The final phase of this research consisted of an industrial experience conducted at Kolektor in Slovenia, providing invaluable insights into the industrial-scale manufacturing of bonded magnets. The acquired notions were multifaceted, spanning from gained familiarity with materials, techniques, and machinery employed in a magnet production line to the rigorous demands of industrial processes and related quality control. Furthermore, a remarkable outcome was the successful validation of a circular economy model for ferrite magnets. Test samples composed of 100% recycled ferrite powders from manufacturing waste demonstrated, indeed, functionalities comparable to brand-new commercial-grade magnets. This finding further validates the potential of ferrites for sustainable PM manufacturing, highlighting a significant step towards creating a more resource-efficient and environmentally responsible engineering.

From an industrial perspective, the synthesis routes explored in this work are based on inexpensive and widely available reagents (metal chlorides, sodium

hydroxide, citric acid, sodium carbonate) and predominantly water as solvent, with nitric acid required only in one stage under controlled conditions (handling and neutralization of residues). Both the solid-state and the modified sol-gel methods are scalable, the latter offering the potential adaptation to continuous reactors. Calcination was performed at the lowest effective temperature, reducing energy demand, while densification strategies such as high-pressure compaction and SPS demonstrate viable routes to achieve higher density at reduced thermal efforts. Moreover, the chance of implementing additives as sintering aids or applying a magnetic field can further expand the possible outcomes. However, potential bottlenecks include fine tuning of the processing parameters to achieve good texture and orientation, and eventual cost of SPS for large-scale production. Nevertheless, the environmental footprint of the present routes is favourable compared REE-magnet production, and the intrinsic chemical and thermal stability of SrM ensures long-term durability. These considerations highlight that SrM nanoparticles provide a reliable basis for their future industrial development as a sustainable, REE-free alternative.

This thesis demonstrates that the advancement of PM technology is not a singular pursuit but a multi-scale challenge, requiring innovation from the atomic level to the final manufactured component. Through the systematic optimization of synthesis, targeted chemical modification, and novel low-temperature densification, this research has established a comprehensive framework for tailoring the properties of SrM. The journey from designing a nanoparticle to validating recycled materials on an industrial production line underscores the critical relevance of practical solutions that will drive the future development of more resilient and sustainable ferrite-based magnetic materials.

Although the present work has focused on SrM for PM applications, the intrinsic properties of hexaferrites suggest potential applications that extend beyond PMs, opening perspectives in several emerging fields. Their strong magnetocrystalline anisotropy and tunable magnetic properties make them promising candidates for spintronic devices, where control of spin-polarized currents is essential. In the microwave regime, hexaferrites are widely investigated for use in filters, circulators, and electromagnetic absorbers due to their ferromagnetic resonance characteristics. While these directions were beyond the scope this thesis, they highlight the broader technological relevance of hexaferrites and suggest profitable avenues for future research.

# Appendix

## Starting materials and chemicals

All the samples were synthesized using commercially available reagents.

Iron (III) chloride hexahydrate ($FeCl_3 \cdot 6H_2O$, ≥98%); Strontium chloride hexahydrate ($SrCl_2 \cdot 6H_2O$, 99%); Manganese (II) chloride tetrahydrate ($MnCl_2 \cdot 4H_2O$, ≥ 98%); Aluminium chloride ($AlCl_3$, 99%); Sodium carbonate ($Na_2CO_3$, ≥ 99.5%); Citric acid ($C_6H_8O_7$ ≥ 99.5%); Sodium hydroxide (NaOH, ≥ 98%); Sodium borohydride ($NaBH_4$ ≥ 98%); Ethanol (EtOH, ≥ 99.5%); Nitric acid ($HNO_3$, 65%). All the starting materials were purchased from Sigma-Aldrich and used without further purification.

## Synthesis of SrM nanoparticles by low temperature solid-state reaction (LTSSR)

**LTSSR.** In a typical synthesis, $FeCl_3 \cdot 6H_2O$ and $SrCl_2 \cdot 6H_2O$ (molar ratio $Fe^{3+}/Sr^{2+}$ = 10) were crushed, mixed and added to finely ground NaOH (molar ratio $Na^+/Sr^{2+}$ = 45) in a mortar. The immediate and exothermic reaction, producing minor fumes, resulted in a brownish amorphous paste. The mixture was ground for 20 min and washed thoroughly with demineralized (DM) water on a Büchner funnel, until a chloride assay (using $AgNO_3/HNO_3$) confirmed the absence of $Cl^-$ ions and a pH of 7.5 was reached. The wet paste was then dried at 80 °C overnight in oven, ground to a fine powder, and calcined at 775 °C for 3 h (heating rate 10 °C/min).

**MSSR.** In the stoichiometric modified version, the molar ratios were $Fe^{3+}/Sr^{2+}$ = 10 and $Na^+/Sr^{2+}$ = 32 or $Fe^{3+}/Sr^{2+}$ = 12 and $Na^+/Sr^{2+}$ = 38. The reagents were

ground for 20 min in a mortar as the LTSSR method. The unwashed amorphous paste was dried in oven at 80 °C overnight, powdered, and calcined at 775 °C for 3 h (heating rate 10 °C/min). The resultant powder was washed five times with DM water ensuring a neutral pH, and finally dried in oven at 80 °C.

# Synthesis of SrM nanoparticles by modified sol-gel synthesis (MSG)

In a typical synthesis, $FeCl_3 \cdot 6H_2O$ and $SrCl_2 \cdot 6H_2O$ (molar ratio $Fe^{3+}/Sr^{2+} = 9$) were dissolved in DM water to give a $Sr^{2+}$ concentration of 0.1 M. The metal ion solution was added to a 1 M solution of $Na_2CO_3$ (molar ratio $Na^+/Cl^- = 1$) under constant stirring at 90 °C on a hot plate. After 5 min, a 5.5 M solution of $C_6H_8O_7$ (molar ratio $C_6H_8O_7/Na^+ = 1.5$) was added and the mixture was left to stir 20 min. The resulting *sol* was dried in oven at 90 °C overnight. The dried *gel* was ground in a mortar and calcined at 450 °C for 1 h and 790 °C for 1 h, with a constant heating rate of 10 °C/min. The product was washed once with $HNO_3$ and four times with DM water, then dried in oven at 80 °C.

**DOPING.** For the doped SrM nanoparticles, the dopant concentration *x* (either from $MnCl_2 \cdot 4H_2O$ or $AlCl_3$) was adjusted to achieve a molar ratio $(Fe^{3+} + x)/Sr^{2+} = 12$, with a $Sr^{2+}$ concentration of 0.1 M in the metal ion solution. The procedure then followed the MSG protocol.

# Synthesis of $Fe^0$ nanowires via aqueous chemical reduction

A typical reaction was performed under the protected environment provided by a $N_2$-filled glovebag. A 0.09 M solution of $FeCl_3 \cdot 6H_2O$ in DM water, DM water for $NaBH_4$, and EtOH for washing were adequately degassed through $N_2$

purging (bubbling) prior to the reaction. Inside the purged glovebag, a freshly made 0.19 M solution of $NaBH_4$ was quickly added to the 0.09 M solution of $FeCl_3 \cdot 6H_2O$. The precipitated $Fe^0$ was separated with a permanent magnet and washed several times with degassed EtOH. The product was then dried in a $N_2$ flux under protected environment.

**PVP Coating.** The weighed amount of PVP (2%, 12%) was dissolved in the 0.09 M solution of $FeCl_3 \cdot 6H_2O$ while degassing, then the procedure followed the same protocol inside the glovebag.


La borsa di dottorato è stata cofinanziata con risorse del
Programma Operativo Nazionale Ricerca e Innovazione 2014-2020, risorse FSE REACT-EU
Azione IV.4 “Dottorati e contratti di ricerca su tematiche dell’innovazione”
e Azione IV.5 “Dottorati su tematiche Green”